

2

GL-TR-90-0211

AD-A229 306

Wave Dynamics in the Mesospheric Hydroxyl Layer DTIC FILE COPY

Hitoshi Yoshimoto

Utah State University  
Space Dynamics Laboratory  
UMC 4140  
Logan, UT 84322

1 August 1990

DTIC  
ELECTE  
NOV 14 1990  
S D

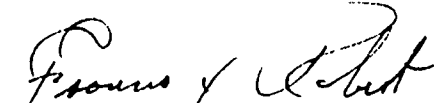
Scientific Report No. 1

APPROVED FOR PUBLIC RELEASE; DISTRIBUTION UNLIMITED

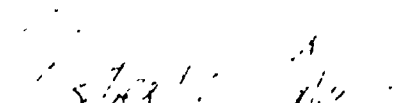
90 11 13 057

GEOPHYSICS LABORATORY  
AIR FORCE SYSTEMS COMMAND  
UNITED STATES AIR FORCE  
HANSOM AIR FORCE BASE, MASSACHUSETTS 01731-5000

"This technical report has been reviewed and is approved for publication"

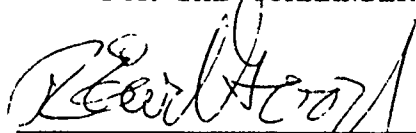


FRANCIS X. ROBERT  
Contract Manager



ROBERT R. O'NEIL, Chief  
Atmospheric Effects Branch  
Optical/Infrared Technology Div.

FOR THE COMMANDER



R. EARL GOOD, SES, Director  
Optical/Infrared Technology Division

This report has been reviewed by the ESD Public Affairs office (PA) and is releasable to the National Technical Information Service (NTIS).

Qualified requestors may obtain additional copies from the Defense Technical Information Center. All others should apply to the National Technical Information Service.

If your address has changed, or if you wish to be removed from the mailing list, or if the addressee is no longer employed by your organization, please notify GL/IMA, Hanscom AFB, MA 01731. This will assist us in maintaining a current mailing list.

Do not return copies of this report unless contractual obligations or notices on a specific document requires that it be returned.

Unclassified

SECURITY CLASSIFICATION OF THIS PAGE

REPORT DOCUMENTATION PAGE				Form Approved GMB No. 274-108	
1a REPORT SECURITY CLASSIFICATION <b>Unclassified</b>			1b RESTRICTIVE MARKINGS		
2a SECURITY CLASSIFICATION AUTHORITY			3 DISTRIBUTION AVAILABILITY OF REPORT <b>Approved for public release; Distribution unlimited</b>		
2b DECLASSIFICATION/DOWNGRADING SCHEDULE					
4 PERFORMING ORGANIZATION REPORT NUMBER(S) <b>SDL/90-049</b>			5 MONITORING ORGANIZATION REPORT NUMBER(S) <b>GL-TR-90-0211</b>		
6a NAME OF PERFORMING ORGANIZATION <b>Utah State University</b>		6b OFFICE SYMBOL (If applicable)	7a NAME OF MONITORING ORGANIZATION <b>Office of Naval Research</b>		
6c ADDRESS (City, State, and ZIP Code) <b>Space Dynamics Laboratory UMC 4140 Logan, UT 84322</b>			7b ADDRESS (City, State, and ZIP Code) <b>University District Building, Rm 315 1107 NE 45th Street Seattle, WA 98105-4631</b>		
8a NAME OF FUNDING/SPONSORING ORGANIZATION <b>Geophysics Laboratory</b>		8b OFFICE SYMBOL (If applicable) <b>OPB</b>	9 PROCUREMENT INSTRUMENT IDENTIFICATION NUMBER <b>F19628-87-C-0100</b>		
8c ADDRESS (City, State, and ZIP Code) <b>Hanscom AFB Massachusetts 01731-5000</b>			10 SOURCE OF FUNDING NUMBERS		11 TITLE (Include Security Classification) <b>Wave Dynamics in the Mesospheric Hydroxyl Layer</b>
			PROGRAM ELEMENT NO <b>62101F</b>	PROJECT NO <b>S322</b>	
			TASK NO <b>01</b>	ACQUISITION NO <b>AC</b>	
12 PERSONAL AUTHOR(S) <b>Hitoshi Yoshimoto</b>					
13a TYPE OF REPORT <b>Scientific #1</b>		13b TIME COVERED FROM _____ TO _____		14 DATE OF REPORT (Year, Month, Day) <b>1990 August 1</b>	
15 PAC: COUNT <b>214</b>					
16 SUPPLEMENTARY NOTATION					
17 COSATI CODES			18 SUBJECT TERMS (Continue on reverse if necessary and identify by block number)		
FIELD	GROUP	SUB GROUP	<b>Wave dynamics Mesosphere</b>		
19 ABSTRACT (Continue on reverse if necessary and identify by block number) <b>Due to the improvement of infrared-measuring instruments, it is possible to observe the middle atmospheric airglow directly from ground-based sites with fine temporal and spatial resolution. In such studies, temporal and spatial fluctuations are found in two major observables: emission intensity and rotational temperature. One possible cause of such fluctuations is passing atmospheric disturbances, known as internal gravity waves. There have been considerable theoretical modeling efforts and experimental investigations to test this hypothesis. This paper attempts to develop a theoretical model of the mesospheric airglow observables. The model uses underlying physical and chemical processes to derive the following physical entities as functions of altitude: the concentrations of major species and minor but influential species and the kinetic temperature of the neutral atmosphere. The model also incorporates geometrical configurations in order to estimate the following observables: the infrared emission intensity for a particular vibrational</b>					
20 DISTRIBUTION/AVAILABILITY OF ABSTRACT <input type="checkbox"/> UNCLASSIFIED/UNLIMITED <input type="checkbox"/> SAME AS RPT <input type="checkbox"/> DTIC USERS			21 ABSTRACT SECURITY CLASSIFICATION <b>Unclassified</b>		
22a NAME OF RESPONSIBLE INDIVIDUAL <b>Frank Robert</b>			22b TELEPHONE (Include Area Code)		22c OFFICE SYMBOL <b>GL/OPB</b>

Cont of Block 19:

(72) band and the rotational emission-line intensities for a particular vibrational band. Many theoretical models assume that gravity waves are monochromatically sinusoidal. This study asserts that such an assumption is not valid, based upon the propagation characteristics of the waves. Results of the model indicate that the frequencies of such waves vary. It can also be shown that the geometrical configuration of a ground-based optical observation has a significant effect, especially on the estimation of the rotational temperature. The apparent intensities have strong asymmetrical distribution among rotational lines so that temperature-fitting methods which are based upon Gaussian line distribution are inadequate. A theoretical model has been developed to optimize the experimental data estimation.

This paper also discusses a numerical signal processing system which has been developed so that the expected observables, based upon the aforementioned model, can be optimally processed using experimental data. The signal processing system takes into account observational limitations and is optimized for inclusion of experimental results in the theoretical model. Observed signals should be analyzed in the time domain as well as in the frequency domain. Performance of the signal processing system is demonstrated using experimental data gathered in relatively poor conditions. Optimal experimental configurations for the theoretical model are suggested.

## FOREWORD

Middle Atmospheric Periodic-Structure-Associated Radiance (MAPSTAR) is a AFOSR (2310G201)/Geophysics Laboratory sponsored program. MAPSTAR is a continuation of a series of ground-based experiments designed to measure and characterize time-dependent mesospheric emissions above large-area terrains of interest (e.g., oceans, mountains, and plains). Data from these experiments will be used to develop a middle-atmospheric dynamic structure data base for Air Force modelers and systems designers. Space Dynamics Laboratory (SDL) at Utah State University (USU) participates in this program under Geophysics Laboratory contract F19628-87-C-0100.

The scientific report that follows develops a model of mesospheric airglow observables.

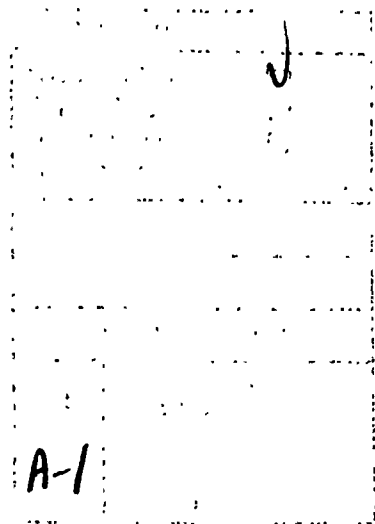


## TABLE OF CONTENTS

FOREWORD . . . . .	iii
TABLE OF CONTENTS . . . . .	v
LIST OF TABLES . . . . .	vii
LIST OF FIGURES . . . . .	viii

### Chapter

I. INTRODUCTION . . . . .	1
Introduction . . . . .	1
Dynamics of Upper Atmosphere . . . . .	1
The Hydroxyl Emission Layer . . . . .	4
Wave Structure in the Mesospheric Hydroxyl Emission Layer . . . . .	5
Scope and Objectives . . . . .	7
II. BASIC MODEL FORMULATION . . . . .	9
Emission Layer Formulation . . . . .	9
Chemical Model . . . . .	12
Thermodynamic Equation . . . . .	19
Internal Gravity Wave . . . . .	21
Geometric Effect . . . . .	23
Krassovsky's Parameter Eta . . . . .	36
III. DYNAMIC MODEL . . . . .	55
Computational Dynamic Model . . . . .	55
Model Calculation Examples . . . . .	74
Long Range Dynamics of IGW . . . . .	75
Model Results . . . . .	80
IV. GEOMETRIC EFFECT . . . . .	96
Geometric Effect Model . . . . .	96
Geometric Effect on Rotational Temperature . . . . .	98
Geometric Effect for Vertical Observations . . . . .	114
Geometric Effect for Off-Zenith Observations . . . . .	98

TABLE OF CONTENTS  
(Continued)

Chapter

V.	DATA PROCESSING TECHNIQUE .....	122
	Data Reduction System .....	122
	Spectral Analysis Techniques .....	123
	Digital Filter .....	128
	Time Domain Analysis .....	135
	Example Data Analysis .....	140
VI.	DISCUSSION .....	149
	Data Processing and Interpretation .....	149
	Observables .....	165
	Discussion on Eta .....	167
VII.	CONCLUSIONS .....	175
	Summary .....	175
	Conclusions .....	177
	Recommendations .....	179
	REFERENCES .....	182
	APPENDICES .....	185
	Appendix A. Theory of the Internal Gravity	
	Waves .....	186
	Appendix B. Rotational Temperature .....	196
	Appendix C. Linearization of the Adiabatic	
	State Equation .....	200
	VITA .....	204

# LIST OF TABLES

Table		
I.	Typical Physical Quantities in Mesosphere .....	10
II.	Chemical Reactions Related to the Formation of Hydroxyl Layer .....	12
III.	Constants Used in the Model .....	16
IV.	Matrix A and Vector B .....	20
V.	Dynamic IGW Equations .....	23
VI.	Wave Period and Slant Angle $\theta$ .....	28
VII.	Observed Wave Parameters .....	30
VIII.	Limiting T and $L_x$ as a Function of $\alpha$ .....	92
IX.	Rotational Temperature Fit Statistics .....	110
X.	Rotational Line Parameters .....	111
XI.	Estimate for Fig. 4-5 .....	112
XII.	Polarization Relations [13] .....	194



## LIST OF FIGURES

Figure		
1-1.	Upper atmosphere .....	2
2-1.	Propagation property of IGW [13] .....	23
2-2.	Propagation modes of IGW [13], [18] .....	24
2-3.	Ground-based observation geometry .....	27
2-4.	Geometric effect in emission .....	29
2-5.	Geometric effect in rotational temperature .....	31
2-6.	Model temperatures .....	33
2-7.	Function Y .....	35
2-8.	Relation between temperature models .....	36
2-9.	Example of measured data .....	53
3-1.	MSIS model results for various entities: day 001 and 222 of 1986 were used as representatives for the winter and summer respectively .....	57
3-2.	Airglow layer model results .....	64
3-3.	Measured airglow layer profile .....	65
3-4.	Numerical model calculation .....	76
3-5.	IGW phase plane .....	80
3-6.	Packet velocity vs. elevation angle .....	81
3-7.	IGW dispersion relation [18] .....	83
3-8.	Chirp signal .....	84
3-9.	Limiting period and elevation angle .....	86
3-10.	Packet velocity .....	89
3-11.	Frequency chirp (shown with period) .....	92
4-1.	Layer model (day 86001) .....	104
4-2.	Layer model (day 86222) .....	105

4-3.	Temperature model (day 86001) .....	106
4-4.	Temperature model (day 86222) .....	107
4-5.	Rotational temperature fit .....	109
4-6.	Intensity distribution as a function of temperature .....	113
4-7.	3D geometric effect .....	117
4-8.	Special case geometric effect .....	119
5-1.	Observed chirp in airglow emission .....	126
5-2.	Effect of high-pass filter .....	131
5-3.	Effect of low-pass filter .....	133
5-4.	Time domain analysis .....	136
5-5.	Signal processing .....	141
6-1.	Effect of windows of different lengths .....	153
6-2.	Day 86223 MEM spectrum .....	158
6-3.	Fourier spectrum .....	159
6-4.	Wavelength, frequency and travel distance .....	168
6-5.	Time domain analysis .....	171
A-1.	Permissible IGWs .....	191
A-2.	IGW topography .....	192
A-3.	Filtering of IGW [13] .....	194
B-1.	Hydroxyl model [10] .....	197

## CHAPTER I

### INTRODUCTION

#### Introduction

This is a study about the dynamics of the mesospheric hydroxyl infrared-emitting layer. In this chapter, a brief background of the upper atmosphere study is presented, followed by a short introduction to the mesospheric hydroxyl emission layer. Emphasis then shifts to a geometric consideration for the ground-based passive optical observation of the layer, leading to a rarely studied effect in which apparent oscillations occur in observational data which do not represent any physical property of the layer but are caused purely by the geometric effect. Finally, the objectives of this study are presented along with the technical approaches which will be developed in the following chapters.

#### Dynamics of the Upper Atmosphere

In the last several decades, studies on chemical and thermodynamic properties of the upper atmosphere have included both physical measurements and theoretical modeling. Our current understanding of the earth's upper atmosphere, derived from physical measurements to date, is summarized in Fig. 1-1 [1]. The atmospheric regions depicted in this diagram are classified according to altitudinal variations in temperature. The major focus of this study is the mesospheric region, which extends in altitude from 60 to 90 km. In this region, several atmospheric species exhibit special properties not found in other altitude regions. For example, chemically reactive

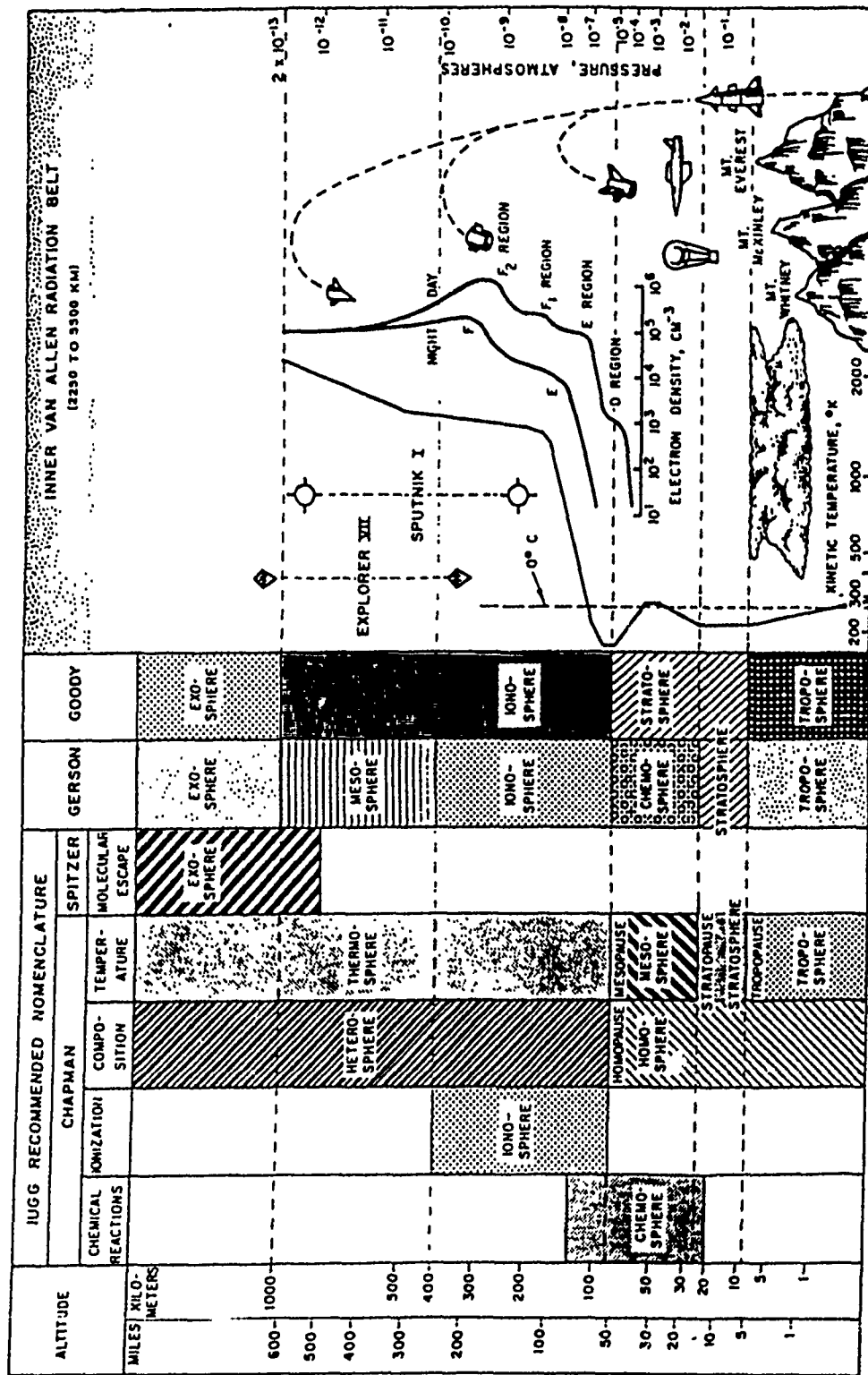


Fig. 1-1. Upper atmosphere

species like hydroxyl (OH) form an infrared-emitting layer as a result of complicated chemical processes.

In the first-order approximation, the gravitationally bound atmospheric species are in hydrostatic equilibrium. This approximation fails in the stratosphere and the thermosphere due to a rise in local temperature, induced from the generation of energetic species by solar radiation. In the stratosphere, the kinetic energy is produced by the ultraviolet photodissociation of ozone according to the reaction [2], [3]:



which provides the heat source. The ozone is recycled as:



where M is an arbitrary third body. In the thermosphere, energetic atomic nitrogen N and atomic oxygen O, together with their ionized species, are the major products. These ionized products are more chemically reactive than their neutral counterparts.

The mesopause is the boundary between the turbosphere and the homosphere, in other words, the boundary between the fluid atmosphere below and the molecular flow above [1]. The mesosphere is referred to as the region immediately below the mesopause. At the mesopause, about 86 km in altitude, lies the thin hydroxyl (OH) emission layer, which is only a few kilometers thick. The formation of this layer is

governed by the photochemistry and dynamics of active oxygen and active hydrogen species, including O, O<sub>3</sub>, H and HO<sub>2</sub>, as well as by a change in pressure and temperature of the major species, namely N<sub>2</sub> and O<sub>2</sub>. The concentrations and temperatures of the major species can be evaluated by the thermodynamic equation of state, which determines the active species' concentrations by the cascading chemical reactions. These concentrations can be used to calculate the amount of the hydroxyl with appropriate chemical reactions. This process is discussed in detail in Chapter II.

#### The Hydroxyl Emission Layer

In the night sky, the major source of infrared emission is the hydroxyl (OH) layer described above. Because the lower atmosphere is transparent to portions of the near-infrared region, studies on the upper atmosphere have been conducted by ground-based optical observation of infrared emissions from the layer. The fact that the air density in the layer region is too thin for aircraft to maintain altitude but too thick for artificial satellites to maintain orbits also made the remote observation the most common method of studying the dynamics of the mesosphere. Among those mesospheric studies, a number of reports show the existence of patchiness and wave-like structures in emissions from this layer [4], [5], [6]. Several theoretical studies ascertain the formation mechanisms of these spatial structures [7]. Evidence has accumulated in support of the theory that the so-called atmospheric internal gravity wave is the principal wave-formation mechanism in many cases [5], [6]. A detailed theory of the atmospheric gravity wave is presented in Appendix A.

The consensus now is that the internal gravity wave is also important in the dynamics and heating of other mesospheric species, including the turbulent transport of O and O<sub>3</sub> [8].

#### Wave Structures in the Mesospheric Hydroxyl Emission Layer

An observable from the mesospheric hydroxyl layer is the spectral radiance of the infrared emissions from which the rotational temperature can be calculated. A detailed theory of the rotational temperature is given in Appendix B [9]. The OH rotational temperature is assumed to be representative of the kinetic temperature in the mesosphere [10]. Both the calculated rotational temperature and the emission intensity of the OH layer show temporal variations. These variations often exhibit ordered, wave-like forms which are functions of time and space.

In early studies of mesospheric hydroxyl dynamics, a parameter usually denoted as  $\eta$  (eta) was introduced by Krassovsky [4] and used by others [7], [11] to characterize the sinusoid oscillations. The  $\eta$  is defined as:

$$\eta = \frac{dI/I}{dT/T} \quad (\text{unitless}) \quad (1.3)$$

where T is the stationary temperature, I is the stationary emission intensity and dT and dI are their oscillation amplitudes. The absolute value of  $\eta$ , first evaluated to have a value of about 5 [4], has recently been extended to a complex number based upon model

calculations [7], [11]. This extension allows phase shifts between the oscillations in temperature and emission intensity to be taken into account. This phase shift has been observed in some cases [12].

In this paper presents a possible mechanism for the phase relationship between the temperature and intensity. The first approach is to show that the geometrical observational set-up provides a relative phase shift between intensity and temperature oscillations. Under typical conditions, the temperature oscillation contains a spurious frequency component, an observable oscillation which is an artifact of the geometric effect. The second approach uses a set of chemical and thermodynamical equations to model the layer. The theory of the internal gravity wave is included to describe the characteristics of the wave itself as well as its effect upon the OH layer. This approach is based upon those used in several previous studies [11], [13]. The two methods can be combined and extended into more general modeling, allowing simulations of observed emission oscillations with off-zenith observational configurations. This model extension is unique to this study and will serve to facilitate many practical experimental setups. Based upon such model evaluations, recommendations for experimental setups which will achieve better scientific understanding of the mesospheric dynamics will be presented.

It is assumed in the definition of  $\eta$  that the wave is monochromatic sinusoid. In Chapter III, such assumption is tested. It is found that the dynamic model predicts that the wave frequency varies as a function of time. This finding is used to construct the signal processing system in Chapter V.



The concept of  $\eta$  was introduced using simple data of low temporal resolution. It is not obvious which quantity should be used to calculate  $\eta$  in the higher resolution data available today. Several mathematical considerations and tools are introduced to process such data in a way useful for theoretical model evaluation. Some discussion about  $\eta$  is presented in Chapter VI.

### Scope and Objectives

The specific objectives of this study are summarized as follows:

1. To discuss Krassovsky's theoretical  $\eta$  using linearized chemical equations and dynamic internal gravity wave models, taking into account the geometric effect.
2. To develop a procedure to simulate off-zenith observations using the model for zenith observations with geometric effect modifications.
3. To relate the  $\eta$  calculated from theoretical models with the values calculated from the measurement data, taking into account both magnitude and phase of oscillations.
4. To formulate an appropriate signal processing technique that makes possible a reasonable estimation of gravity wave parameters from observational data.
5. To perform an evaluation of dynamic hydroxyl emission layer models.
6. To determine the relevancy of the concept of a complex  $\eta$  and the associated dynamic models.
7. To consider the possibility of improving the acquisition of

knowledge of the hydroxyl layer dynamics and, if such improvement is found, to make appropriate recommendations for further study.

## CHAPTER II

## BASIC MODEL FORMULATION

This chapter describes a detailed development of the chemical model and a brief introduction of the overall picture of the problem.

Emission Layer Formulation

In this section, a set of chemical and photochemical reactions based upon an equation set with the updated reaction rate constants used for ozone model calculations is presented [3], [14]. As introduced in Chapter I, the mesopause is the narrow, upper region of the mesosphere in which the ratio of the major odd oxygen constituents, atomic oxygen and ozone, changes [3], [15]. The atomic oxygen is created by photo dissociation



during the daytime. The ozone is created by the reaction [3]:



where M is a third body such as  $\text{N}_2$ ,  $\text{O}_2$  or O. The atomic oxygen created by reaction (2.1) is the major constituent of the upper atmosphere above 220 km [1]. Table I summarizes typical values of physical importance in the mesospheric region [1], [3]. As can be evaluated from the values given in Table I and using equation (2.2),

TABLE I  
Typical Physical Quantities in Mesosphere [3].

Species	Concentration ( $\text{cm}^{-3}$ )
---------	------------------------------------

$\text{N}_2$	$10^{14}$
--------------	-----------

$\text{O}_2$	$10^{13}$
--------------	-----------

$\text{O}$	$10^{10}$
------------	-----------

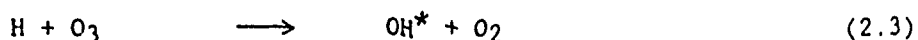
$\text{O}_3$	$10^8$
--------------	--------

Temperature	150 K (Summer)	220 K (Winter)
-------------	----------------	----------------

the atomic oxygen has a lifetime of 10 to 15 hours at 85 to 95 km. Consequently, the concentration of this species can be regarded as constant, even during the nighttime.

The ozone-creation profile resulting from (2.2), which is identical to its concentration profile, has a sharp peak because the creation mechanism of ozone is similar to the formation of the Chapman layer which has a gaussian-type distribution. This ozone peak occurs in the stratosphere, at an altitude of about 50 to 70 km [1]. From (2.2) the creation of ozone occurs with the destruction of atomic oxygen. Therefore, there is a transition of the major odd oxygen

component from ozone to atomic oxygen with increasing altitude. This transition occurs in a narrow region at the mesopause [3]. In this region, one particular reaction is the major contributor to the formation of the hydroxyl layer [3], [15]. This reaction is the hydration of ozone [15]



The vibrationally-excited hydroxyl in the ground electronic state, denoted as  $\text{OH}^*$ , can emit photons. The wavelengths of the resultant photon emissions fall in the infrared and visible spectral regions. Since the hydroxyl concentration is determined by the balance of the atomic oxygen and the ozone, both of which are highly chemically active, the hydroxyl forms into a relatively thin layer at the transient region of the odd oxygen species. Most investigators report the infrared emission region to be a relatively thin layer, usually about 7 km thick [10], consistent with the dynamic model.

Formation of the hydroxyl airglow layer can be numerically simulated using a computer; that is, successive values of the concentrations of the species of interest can be calculated by employing a small time step  $\Delta t$  in the equations. This approach is explained in detail in Chapter III. Simplifications of the process are discussed in the following section. Table II summarizes the most important chemical reactions related to the mesospheric hydroxyl airglow layer [3].

TABLE II  
Chemical Reactions Related to the Formation of Hydroxyl Layer [3].

REACTION NUMBER as in [3]		REACTION COEFFICIENT T: temperature (K)
R13	$O + O_2 + O \rightarrow O_3 + O$	$2.15E-34 e^{(345/T)}$
R14	$O + O_2 + O_2 \rightarrow O_3 + O_2$	$2.15E-34 e^{(345/T)}$
R15	$O + O_2 + N_2 \rightarrow O_3 + N_2$	$8.82E-35 e^{(575/T)}$
R17	$O + OH \rightarrow O_2 + H$	$2.3E-11 e^{(-90/T)}$
R29	$H + O_3 \rightarrow OH^* + O_2$	$1.4E-10 e^{(-270/T)}$

### Chemical Model

#### Simplified Model

In the simplified chemical model, the principal reactions are as follows [3]:



where  $i, j = 0 \dots 9$  are vibrational states and  $OH_i^*$  represents the hydroxyl which is vibrationally excited to state  $i$ . Equation (2.5) represents the quenching, a transition between states without photon

emission. Equation (2.6) represents the photo emissive transitions which give rise to the mesospheric airglow layer. The coefficients  $l_{ij}$  are known as Einstein coefficients [10]. The following set of equations follow:

$$\frac{d[OH_i^*]}{dt} = g_i[H][O_3] \quad (2.7)$$

$$\frac{d[OH_i^*]}{dt} = - \sum_{j=0}^{i-1} k_{ij}[M][OH_i^*] \quad (2.8)$$

$$\frac{d[OH_i^*]}{dt} = \sum_{j=0}^{i-1} l_{ij} [OH_j^*] \quad (2.9)$$

This set can be represented by a 10 by 11 matrix; however, with the following assumptions, most of the off-diagonal elements can be neglected:

- 1] Production of  $OH_i^*$  occurs only for  $i=7,8$  and 9.
- 2] Quenching shown by (2.5) occurs only when  $i-j = 1$ .

These assumptions are represented by the following relationships:

$$g_i = \begin{cases} 0 & (i > 6) \\ 0 & (\text{otherwise}) \end{cases} \quad (2.10)$$

$$k_{ij} = \begin{cases} 0 & (i-j=1) \\ 0 & (\text{otherwise}) \end{cases} \quad (2.11)$$

With these constraints, equations (2.7), (2.8) and (2.9) are reduced to the following set:

$$\frac{d[OH_i^*]}{dt} = - [OH_i^*] \left( \sum_{j=0}^{i-1} (l_{ij}) + k_{ii-1}[M] \right) + g_i[H][O_3] \quad (2.12)$$

This matrix equation can be expressed as follows:

$$\frac{dX}{dt} = AX + B \quad (2.13)$$

where

$$A = \left( \sum_{j=0}^{i-1} (l_{ij}) + k_{ii-1} [M] \right)$$

$$B = ( g_i[H][O_3] )$$

$$X = ( [OH_i^*] ) \quad (2.14)$$

This has a solution of:

$$X = \exp[-\int A(t)dt] \exp(-\int A(t)dt) \int \exp(\int A(t)dt) B(t)dt X(0) \quad (2.15)$$

where  $X(0)$  is the temporal initial values set. Equation (2.15) can be reduced to the following form with (2.13):

$$X = \exp(At) X(0) - \exp(At) A^{-1}B + A^{-1}B \quad (2.16)$$

where  $A^{-1}$  represents the inverse matrix of  $A$ .

Further simplification is possible. Previous studies have shown that the reactions (2.8) and (2.9) have time constants on the order of tens of milliseconds. The observational data are discrete time series with tens of seconds time steps. Because this is almost one thousand



times longer than the time constants of (2.8) and (2.9), the concentration of excited hydroxyl of all levels,  $[OH_i^*]$   $i=1-9$ , can be approximated to be at equilibrium for all data points. This is equivalent to taking the  $\exp(At)$  in (2.16) as zero which gives the following simple solution for X:

$$X = A^{-1}B \quad (2.17)$$

#### Elements of A and B

The elements of the transition matrix A, defined in the previous section, are deduced from the Einstein coefficients for the excited hydroxyl (the emissive transition rates among the excited states) and the quenching rates for each of the states. These numbers are provided in Table III [15]. Note that the matrix A is upper-half triangular with non-zero diagonal elements.

The elements of the column vector B are the reaction rates  $g_i$  of equation (2.4), which have non-zero values only for  $i=7,8,9$ . However, a recent study indicates that the elements of B may be non-zero for other levels as well, including  $i=4-9$  [15]. These values are also included in Table III.

#### Model Extension

The simple model described in the previous section is extendable according to the following rules, allowing for the formulation of appropriate models under different assumptions: first, to add an additional chemical reaction to the model, there are three cases which depend on whether the OH itself is involved in the reaction.

TABLE III  
Constants Used in the Model

Quenching Rate  $\times 10^{-13}$

v	1	2	3	4	5	6	7	8	9
	0.000	0.003	0.23	1.1	3.5	6.5	9.6	11.5	8.9

Generation Ratio (%)

v	1	2	3	4	5	6	7	8	9
	0.0	0.0	0.0	0.0	0.0	0.0	15.0	31.0	38.0

Einstein Coefficient

v'	1	2	3	4	5	6	7	8	9
v' =									
0	-31.7	40.6	67.9	13.5	2.81	0.59	0.13	0.03	0.01
1	0.0	-67.0	35.0	116.3	28.5	7.39	1.82	0.46	0.13
2	0.0	0.0	-106.8	22.1	165.9	47.4	14.9	4.43	1.24
3	0.0	0.0	0.0	-152.4	8.33	213.5	68.5	24.8	8.90
4	0.0	0.0	0.0	0.0	-205.6	0.31	256.4	90.7	36.9
5	0.0	0.0	0.0	0.0	0.0	-269.2	5.12	291.8	110.2
6	0.0	0.0	0.0	0.0	0.0	0.0	-346.9	31.1	322.8
7	0.0	0.0	0.0	0.0	0.0	0.0	0.0	-443.3	90.5
8	0.0	0.0	0.0	0.0	0.0	0.0	0.0	0.0	-570.6

Case 1:  $\text{OH}^*$  is in the product only.



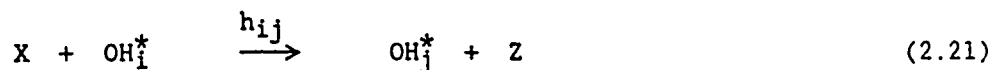
where  $i$  is the appropriate vibrational level. This equation leads to the following equation:

$$\frac{d(\text{OH}_i^*)}{dt} = h_i [X][Y] \quad (2.19)$$

The modification is performed on the vector B by adding the term  $h_i[X][Y]$  to the i-th row.

$$b_i = b_i + h_i[X][Y] \quad (2.20)$$

Case 2:  $\text{OH}^*$  is both in the reactant and in the product.



which leads to the following equation set:

$$\frac{d(\text{OH}_i^*)}{dt} = -h_{ij} [X][\text{OH}_i^*] \quad (2.22)$$

$$\frac{d(\text{OH}_j^*)}{dt} = h_{ij} [X][\text{OH}_i^*] \quad (2.23)$$

The modification is then performed on the matrix A by adding  $-h_{ij}[X]$  to its  $a_{ij}$  element:

$$a_{ij} = a_{ij} - h_{ij}[X] \quad (2.24)$$

Case 3:  $\text{OH}^*$  is in the reactant only.



which leads to the following equation:

$$\frac{d[OH_j^*]}{dt} = -h_j[X][OH_j^*] \quad (2.26)$$

This is accomplished by adding  $-h_j[X]$  to the  $a_{jj}$  element of the matrix A:

$$a_{jj} = a_{jj} - h_j[X] \quad (2.27)$$

Using these techniques, the previous model can be simplified as follows. This simpler model is appropriate when the time scale of interest is on the order of hours, but may suffer some problems when the time scale is less than 30 minutes. The reaction R29 has a time constant of about 10 minutes. Therefore, when the time scale of interest is much larger than 10 minutes, on the order of hours, the concentration of ozone can be regarded at its equilibrium value. In such a case, the reactions R13, 14 and 15 can be substituted as the production of OH instead of R29 [15]. This simplifies the model because the reliable observational data on  $[O_3]$  and  $[H]$  are not readily available. In this case, vector B in the equation (2.14) is replaced by:

$$B = (g'_1[O][O_2][M]) \quad (2.28)$$

where  $g'$  denotes the appropriate coefficient and  $[M]$  is either  $O_2$ ,  $O$  or  $N_2$ , depending upon which reactions are to be used. The complete expression is provided in Table IV.

#### Thermodynamic Equation

The thermodynamic equation of state is represented as:

$$\frac{N}{V} = \frac{P}{R T} \quad (2.29)$$

where  $N$  is the number of molecules in volume  $V$ ,  $p$  is the pressure,  $R$  is the gas constant,  $8.314 \text{ J/mol K}$ , and  $T$  is the temperature. Under the adiabatic condition, this equation reduces to [4]:

$$T V^{\gamma-1} = K \quad (2.30)$$

where  $\gamma$  is the ratio of the constant-pressure specific heat  $C_p$  to the constant-volume specific heat  $C_v$  and  $K$  is a constant. For future uses, the following formula provides an alternative expression for the adiabatic state equation:

$$\rho^{\gamma-1} = \frac{k' R T}{m} \quad (2.31)$$

where  $k'$  is a constant of proportionality,  $m$  is the average molecular mass of air and  $\rho$  is the average mass density of the air ( $\text{kg/cm}^3$ ). The expression (2.31) is useful for detailed modeling because it

TABLE IV  
Matrix A and Vector B

$i$	1	2	3	4	5	6	7	8	9
$A(1,i)$	$-l_{10}-k_{10}[M]$	$l_{1j}+k_{21}[M]$	$l_{31}$	$l_{41}$	$l_{51}$	$l_{61}$	$l_{71}$	$l_{81}$	$l_{91}$
$A(2,i)$	0	$-\sum_{j=0}^1 l_{2j}-k_{21}[M]$	$l_{32}+k_{32}[M]$	$l_{42}$	$l_{52}$	$l_{62}$	$l_{72}$	$l_{82}$	$l_{92}$
$A(3,i)$	0	0	$-\sum_{j=0}^2 l_{3j}-k_{32}[M]$	$l_{43}+k_{43}[M]$	$l_{53}$	$l_{63}$	$l_{73}$	$l_{83}$	$l_{93}$
$A(4,i)$	0	0	0	$-\sum_{j=0}^3 l_{4j}-k_{43}[M]$	$l_{54}+k_{54}[M]$	$l_{64}$	$l_{74}$	$l_{84}$	$l_{94}$
$A(5,i)$	0	0	0	0	$-\sum_{j=0}^4 l_{5j}-k_{54}[M]$	$l_{65}+k_{65}[M]$	$l_{75}$	$l_{85}$	$l_{95}$
$A(6,i)$	0	0	0	0	0	$-\sum_{j=0}^5 l_{6j}-k_{65}[M]$	$l_{76}+k_{76}[M]$	$l_{86}$	$l_{96}$
$A(7,i)$	0	0	0	0	0	0	$-\sum_{j=0}^6 l_{7j}-k_{76}[M]$	$l_{87}+k_{87}[M]$	$l_{97}$
$A(8,i)$	0	0	0	0	0	0	0	$-\sum_{j=0}^7 l_{8j}-k_{87}[M]$	$l_{98}+k_{98}[M]$
$A(9,i)$	0	0	0	0	0	0	0	0	$-\sum_{j=0}^8 l_{9j}-k_{98}[M]$

$i$	1	2	3	4	5	6	7	8	9
$B(i)$	0	0	0	0	0	0	0	0	0

involves only the observable quantities in the mesopause region.

### Internal Gravity Wave

Evidence suggests that the so-called atmospheric internal gravity wave (IGW) is the source of spatial and temporal oscillations observed in hydroxyl infrared emissions in the mesospheric layer [5], [16], [17]. Hines summarized linearized IGW model (Appendix A) [13], [18]. Major characteristics of IGW related to study of the mesospheric layer can be summarized as follows:

1. IGWs are dispersive. This means a wave's packet and phase velocity depend upon its oscillation frequency. This property sets an upper limit to the oscillation frequency that can reach to mesospheric altitudes.
2. The propagation speed of the IGW depends upon its propagation direction and the frequency, suggesting that the observed IGW at a certain height is almost monochromatic [13], [18].
3. The temperature inversion below the mesosphere prevents short-period components of IGW originating at lower altitudes from propagating upward further into the mesosphere. This makes the upper limit of allowed frequencies of IGWs in the mesosphere smaller than the Brunt-Vaisala frequency.
4. Energy loss due to viscosity becomes significant for IGWs with short wavelengths.
5. The phase velocity and group velocity are almost perpendicular to each other. Therefore, an IGW originated at a lower altitude and propagating upward to the mesopause region at group

velocity, appears locally to propagate downward at phase velocity. Most observations measuring only a few periods of oscillation are likely to observe the phase velocity, or "phase trace speed" as Hines defined [18].

These properties of IGWs put limits on the characteristics of a particular IGW that can reach in the mesospheric OH airglow layer region, such as the oscillation period, horizontal and vertical wavelengths and propagation direction. Table V provides equations regarding properties of an IGW in general as well as additional equations that model the characteristics of IGWs in the mesospheric region [13], [18], [19]. Fig. 2-1 depicts the general propagation property of IGWs described by those equations [13]. The family of ellipsoids represents the acoustic-wave solutions to the equations in Table V. The family of hyperbolas represents the IGWs. Each curve is marked by oscillation periods in minutes. In this example,  $\gamma$  is 1.4,  $g$  is 9.5 ( $\text{m/s}^2$ ),  $\omega_A$  corresponds to 4.4 minutes and  $\omega_g$  is 4.9 minutes. The expected characteristics of an IGW in the mesospheric region are shown in Fig. 2-2 [13], [18]. Fig. 2-2(a) and (b) depict the parameters of the IGW's that can propagate through the atmosphere between the troposphere and mesosphere [13]. Fig. 2-2(c) depicts the relationship between the oscillation period, group velocity, propagation elevation angle and phase velocity of an IGW [18]. Fig. 2-2(a) illustrates the spectrum of wavelengths available at 90 km, following propagation from the lower atmosphere, shown by the unhatched area [13]. Fig. 2-2(b) depicts propagation modes at meteor heights. The periods, measured in minutes, are shown in boxes on the corresponding constant-period



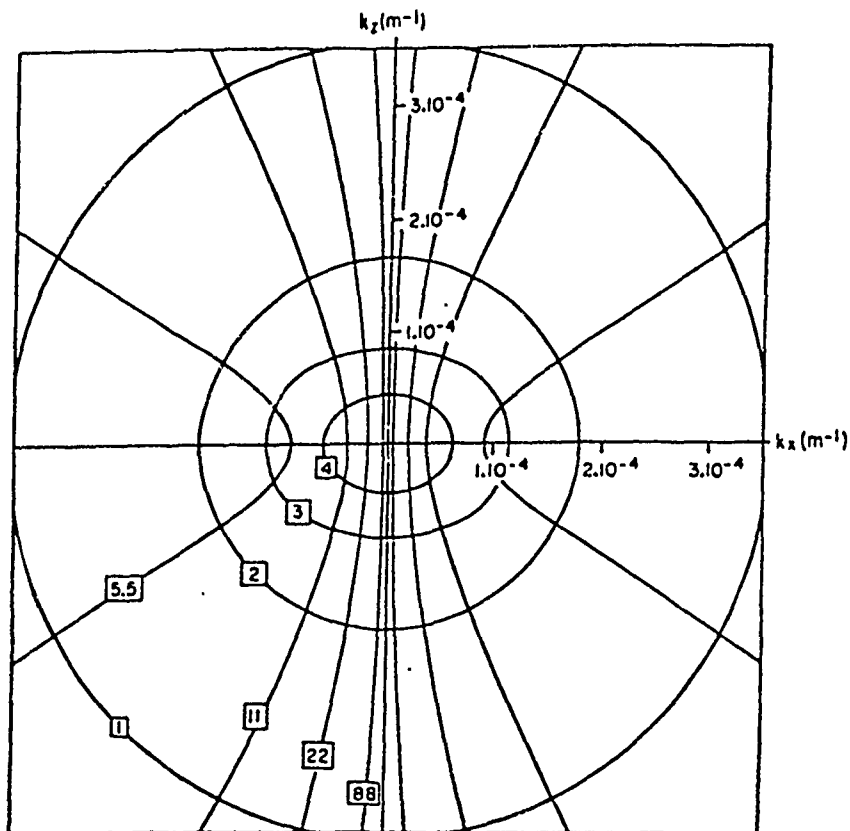


Fig. 2-1. Propagation property of IGW [13]

TABLE V  
Dynamic IGW Equations [13]

$$\omega^4 - \omega^2 c^2 (k_x^2 + k_z^2) + (\gamma - 1) g^2 k_x^2 - \frac{\gamma^2 g^2 \omega^2}{4c^2} = 0$$

$$\frac{(\omega^2 - \omega_A^2)}{c^2} \omega^2 - \omega^2 (k_x^2 + k_z^2) + \omega_g k_x^2 = 0$$

TABLE V  
Dynamic IGW Equations [13] (continued)

$$\omega_A = \gamma g / 2c$$

$$\omega_g = \sqrt{\gamma - 1} \, g / c$$

$$\omega^2 = c^2 (k_x^2 + k_z^2) \quad \text{Acoustic Wave}$$

$$\omega^2 = \frac{\omega_g^2 k_x^2}{(k_x^2 + k_z^2)^2} \quad \text{IGW}$$

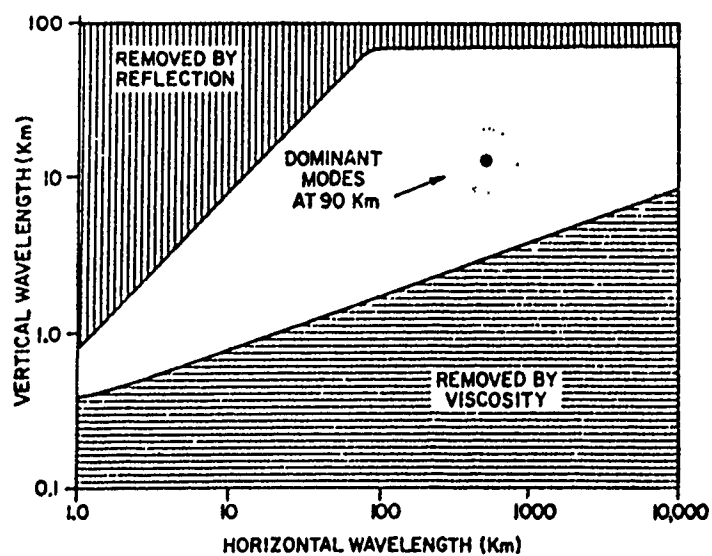


Fig. 2-2. Propagation modes of IGW [13], [18]

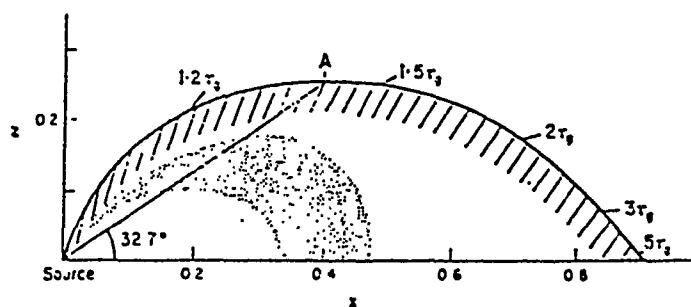
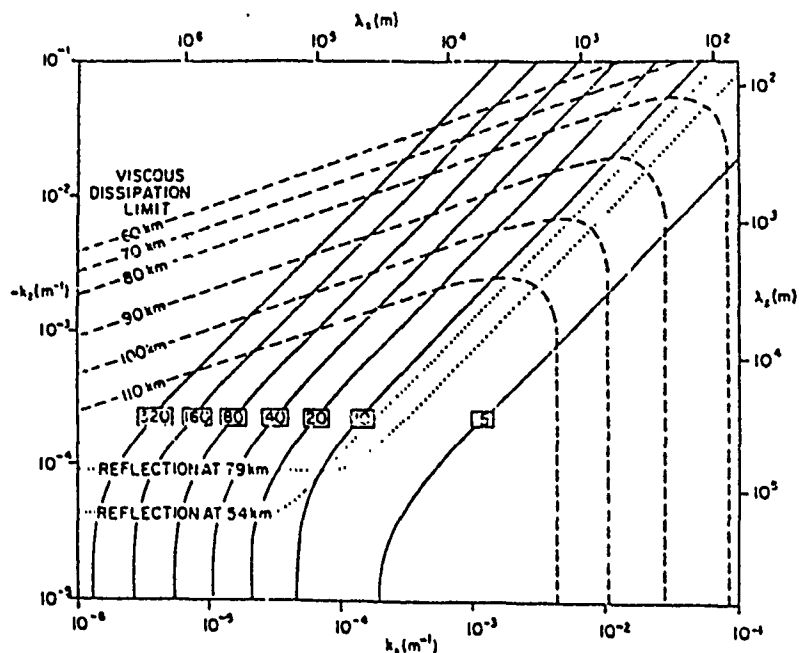


Fig. 2-2. Propagation modes of IGW [13], [18] (continued)

contours (solid lines). The limits of the permitted spectrum, as determined by viscous damping, are shown for several heights by broken curves. Modes lying above and to the right of these curves are excluded. The modes subject to reflection are shown by dotted lines. Modes lying below these curves cannot proceed from the lower atmosphere to the upper [13]. Fig. 2-2(c) depicts an IGW front (bold curve) in the course of expansion from a point source at the origin of coordinates [18]. It is depicted at unit time after its

emission, if the spatial coordinates are taken to be measured in units such that the speed of sound is 1. The wave period at the front is indicated by multiples of  $\tau_g = 2\pi/\omega_g$  at various points along the front. Inclined line segments behind the advancing front indicate planes of constant phase immediately behind the front. The bulk of some observable disturbances may proceed more slowly than the frontal speeds and may be confined at this particular moment of time to a region such as the shaded region [18]. As a first-order approximation that the hydroxyl layer is horizontal with a constant height, the pattern can be represented by the intersection of this curve and the layer plane. In a more accurate approximation, one must take into account the chemical reactions governing the hydroxyl concentration involving the odd oxygen constituents whose concentrations are first changed by the incoming IGW.

#### Geometric Effect

Because this study involves a comparison of theoretical models with ground-based optical observational data, the geometric effect must be taken into account. The problems associated with observational geometry has been pointed out briefly [11] but not worked out in great detail. The approach will be illustrated here using a simplified model. A more elaborate model will be introduced in chapter IV.

In ground-based optical measurements, the instrument is often oriented to look up at the sky in the near zenith, resulting in a geometric configuration like the one shown in Fig. 2-3. Since the OH airglow layer is about 5 to 10 km thick, the observation is not

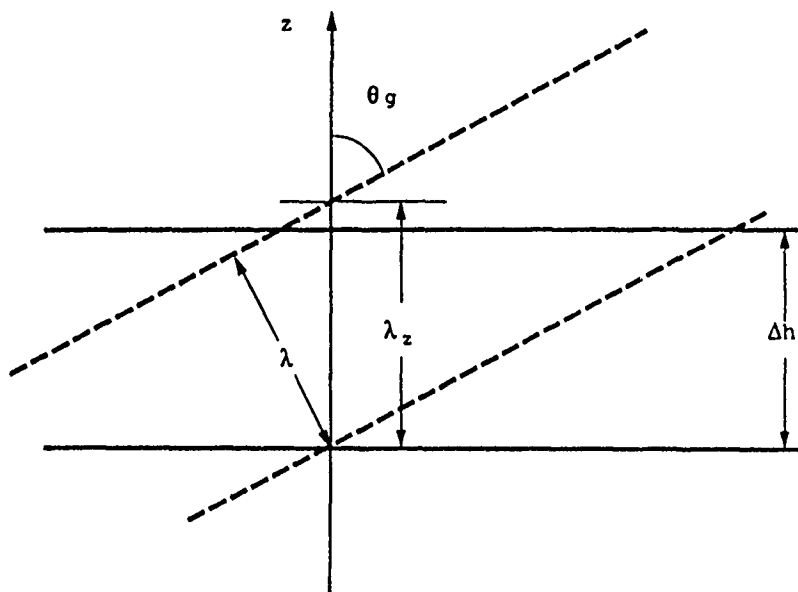


Fig. 2-3. Ground-based observation geometry

an emission from a localized small volume but rather of the integrated volume emission within the field of view along the line of sight. The combination of a linearized IGW model [13] and experimental airglow data [4] can be used to demonstrate the significance of this geometrical effect.

A simple linearized-IGW theory includes a directional dispersion relation [20]:

$$\frac{\omega}{\Omega} = \cos \theta \quad (2.32)$$

where  $\omega$  is the frequency and  $\theta$  is the angle of the packet velocity relative to the zenith and  $\Omega$  is the Brunt-Vaisala frequency [20].

The phase velocity is perpendicular to the packet velocity, that is, perpendicular to the phase plane. Table VI and Fig. 2-4 demonstrate several values of  $\theta$  with typical values of  $\omega$ . Table VII illustrates several characteristics for an airglow observation [5]. This example shows an IGW with a period of 11 minutes and a wavelength of 14 km in the vertical direction. If the wave is represented by:

$$I(t, z) = I_0 + \Delta I \sin(\omega t - k_z z) \quad (2.33)$$

where  $I_0$  is a constant, or a DC component, and  $\Delta I$  is the amplitude of the oscillation, then the observed airglow intensity is:

$$\begin{aligned} I_{\text{obs}}(t) &= \int_0^{\Delta h} I(t, z) dz \\ &= I_0 \Delta h + \Delta I \int_0^{\Delta h} \sin(\omega t - k_z z) dz \end{aligned} \quad (2.34)$$

instead of:

$$I_{\text{ref}}(t) = I_0 \Delta h + \Delta I \Delta h \sin(\omega t - k_z z) \quad (2.35)$$

TABLE VI  
Wave Period and Slant Angle  $\theta$

Period (min)	$\theta$ (degree)
10	60.0
20	75.5
30	80.4
60	85.2

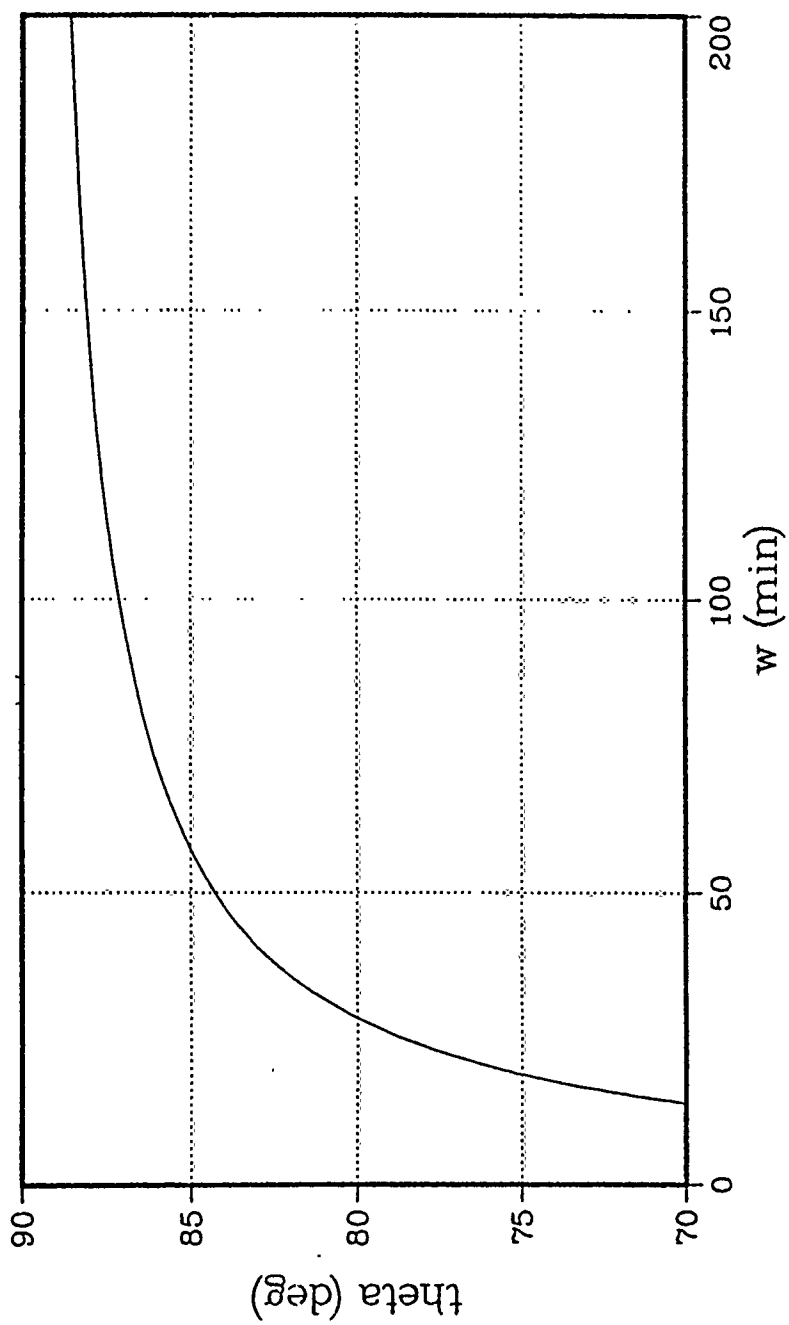


Fig. 2-4. Geometric effect in emission

TABLE VII  
Observed Wave Parameters [5]

$\lambda_x$	$26.0 \pm 0.3$	km
$v_x$	$38.0 \pm 2.0$	m/s
$\lambda_z$	$14.5 \pm 2.0$	km
$v_z$	$21.0 \pm 3.0$	m/s
$\frac{\lambda_x}{v_x}$	$11.4 \pm 0.6$	min

From (2.32),  $\theta$  is about 57 degrees for a typical value of  $\Omega$ , the Brunt-Vaisala frequency. If the layer is approximated by a 5km-thick horizontal slab, the vertical line of sight will integrate about 5/14 of one oscillation period, or about 128 degrees of a 360 degrees phase. Under these conditions, the integration of (2.34) is:

$$I_{\text{obs}}(\tau) = I_0 \Delta h + \frac{\Delta I}{k_z} [2(1 - \cos(k_z \Delta h))]^{1/2} \sin(\omega \tau + \Psi) \quad (2.36)$$

$$\Psi = \arctan\left(\frac{\cos(k_z \Delta h) - 1}{\sin(k_z \Delta h)}\right) = -\frac{k_z \Delta h}{2} \quad (2.37)$$

Fig. 2-5 is a plot of the apparent amplitude and phase as functions of the thickness of the emitting layer. At  $\Delta h = 5$  km,  $\Psi$  is about -55 degrees and the amplitude is about 85% of  $I_{\text{ref}}$ . Since  $\Delta h$  is usually unknown and therefore needs to be estimated, the geometric effect can cause considerable uncertainty in both the amplitude and phase of the apparent emissions. The effect could



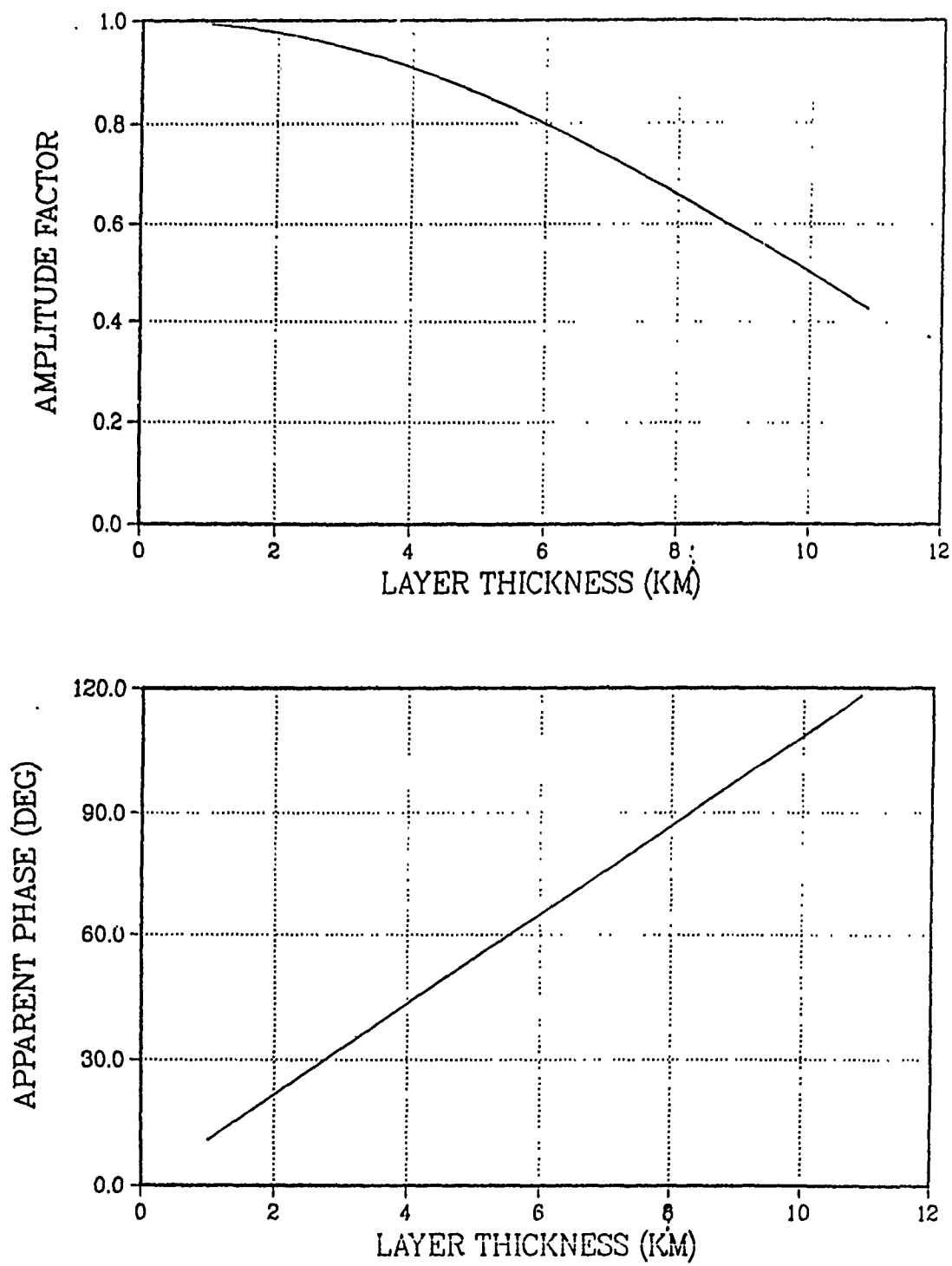


Fig. 2-5. Geometric effect in rotational temperature

mask out amplitude and phase modifications caused by other factors such as chemical reaction-rate dependencies. Therefore, further study of the geometric effect is needed in order to model mesospheric dynamics and to compare the model with experimental data.

Similarly, it is possible to assess the geometric effect on the apparent temperature of the layer. The rotational temperature, calculated from observational data, is assumed to be equal to the local kinetic temperature. The actual observed value is "brightness-weighted temperature" through the layer along the line of sight. In each of three cases depicted in Fig. 2-6, a temperature is assumed to be a constant at a same altitude. The temperature at height  $h$  is approximated by the following equation:

$$T(h) = T_{\max} - \frac{T_{\max} - T_{\min}}{\Delta h} (h - h_0) \quad (2.38)$$

The observed temperature, the brightness-weighted average temperature, is therefore:

$$T_{\text{obs}}(\tau) = \frac{\int_{h_0}^{h_0 + \Delta h} T(h) I(h) dh}{\int_{h_0}^{h_0 + \Delta h} I(h) dh} \quad (2.39)$$

This integral can be evaluated as:

$$T_{\text{obs}}(\tau) = \frac{I_0 \Delta h \frac{(T_{\max} + T_{\min})}{2} + \frac{\Delta I}{k_z} A \sin(\omega \tau + \Psi)}{I_0 \Delta h + \frac{\Delta I}{k_z} B \sin(\omega \tau + \Phi)} \quad (2.40)$$

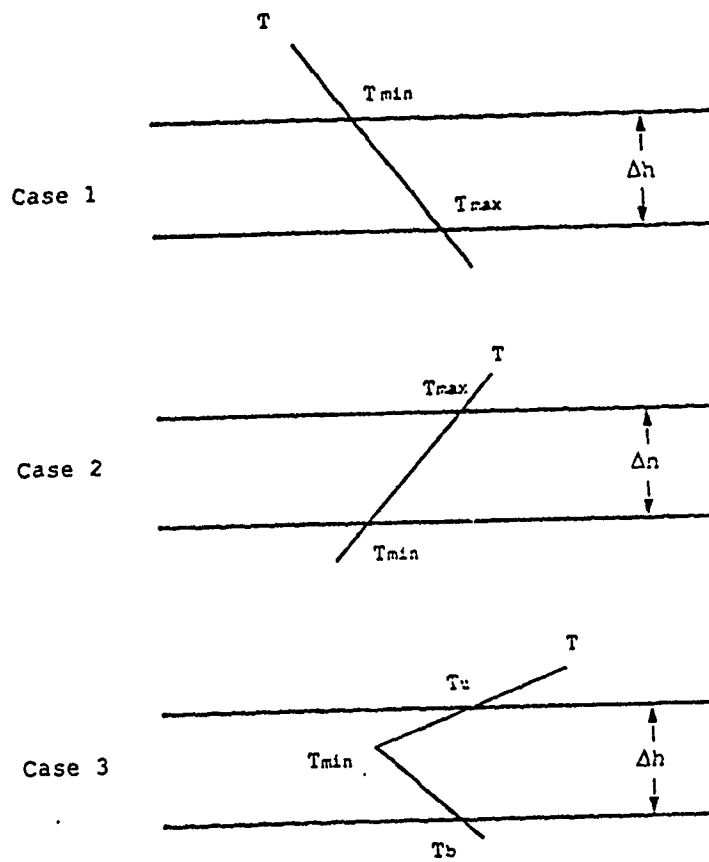


Fig. 2-6. Model temperatures

where

$$A^2 = T_{\max}^2 + T_{\min}^2 + \frac{2\Delta T^2}{(k_z \Delta h)^2} (1 - \cos(k_z \Delta h)) + \frac{2\Delta T^2}{k_z \Delta h} \sin(k_z \Delta h) - 2T_{\max} T_{\min} \cos(k_z \Delta h) \quad (2.41)$$

$$\psi = \tan^{-1} \frac{T_{\max} k_z \Delta h \cos(k_z \Delta h) - T_{\min} k_z \Delta h - \Delta T \sin(k_z \Delta h)}{T_{\max} k_z \Delta h \sin(k_z \Delta h) + \Delta T (\cos(k_z \Delta h) - 1)} \quad (2.42)$$

$$\Delta T = T_{\max} - T_{\min} \quad (2.43)$$

Fig. 2-7 shows a family of curves of the function:

$$Y = \frac{-5 + \sin(T)}{5 + \sin(T+\Phi)} \quad (2.44)$$

where  $\Phi$  is taken as 0, 30, 60, 90 and 180 degrees. Since (2.44) is a generalized normal form of (2.40), this illustrates the form of  $T_{\text{obs}}(t)$  for several phase shifts between  $\psi$  and  $\Phi$ . Note that in the presence of a sinusoidal IGW, even when there is no local oscillation in temperature, the observed temperature shows non-sinusoidal oscillation at the same frequency as the IGW. Case 2 is the same equation with  $T_{\max}$  and  $T_{\min}$  interchanged. Case 3 can be considered a combination of the two cases as shown in Fig. 2-8. The importance of the geometric effect is that even without any local temperature fluctuations, the airglow OH rotational temperature shows an apparent oscillation due to the temperature difference

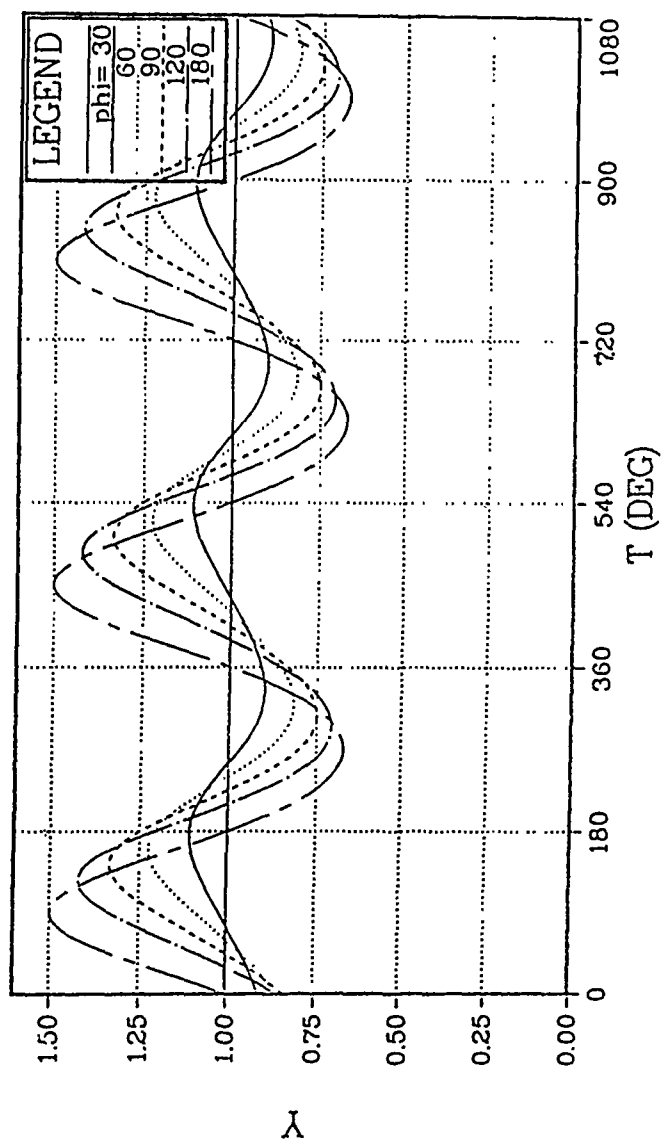


Fig. 2-7. Function Y

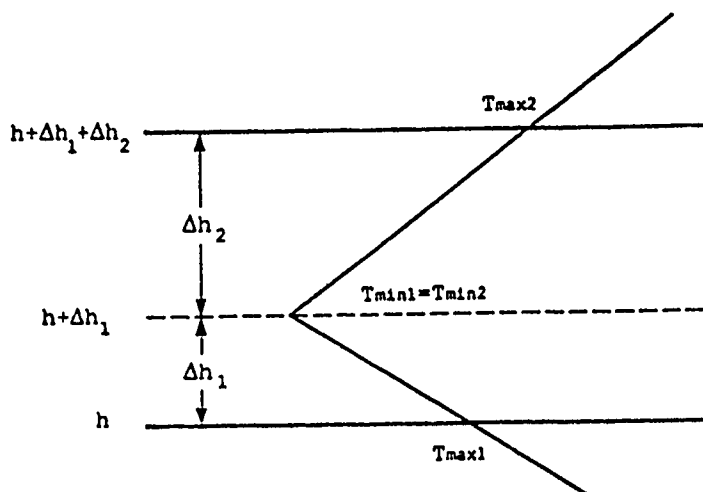


Fig. 2-8. Relation between temperature models

with respect to altitude within the emitting layer. This suggests that when there is a local temperature change due to an IGW, such a change will be observed with the geometric effect "modulation." Therefore, it is necessary to consider the geometric effect when analyzing temperature distributions with respect to altitude.

The previous simple examples present the general geometric effect; however, several assumptions were made in Fig. 2-6 which could be too limiting. The first such assumption is that the

emission layer is approximated by an uniform horizontal slab. This is equivalent to assuming that the layer has a uniform volume emission rate throughout an entire layer with sharp top and bottom boundaries.

The second assumption is that the layer is time invariant while the IGW passes through. This is equivalent to ignoring both temperature and concentration changes due to an adiabatic process. Because some chemical models of the layer are available, including the model using MSIS [21], more detailed simulation of the geometric effect will be presented in chapter IV.

#### Krassovsky's Parameter Eta

This section discusses the parameter introduced by Krassovsky [4] and since used in several mesospheric infrared emission studies [7], [11], denoted with the character  $\eta$  (eta) of the Greek alphabet. An attempt will be made to extend the concept of eta.

##### 1. First Definition of eta

Krassovsky's definition of eta is [4]:

$$\eta = \frac{\Delta I/I}{\Delta T/T} \quad (\text{unitless}) \quad (2.45)$$

where  $I$  is the volume emission rate,  $T$  is the temperature and  $\Delta I$  and  $\Delta T$  are the respective oscillation amplitudes. Theoretical works to explain the value and the temporal behavior of eta with regard to the physical conditions of the hydroxyl layer can be generalized into two major groups. The first group is represented by the work

of Krassovsky [4]. In this model it is assumed that the adiabatic change of an air parcel is caused by internal gravity waves. Here, the vibrationally excited molecule  $XO_2^*$  is assumed to be formed according to the reaction:



where X denotes either O or H atoms. The reaction rate coefficient  $R_X$  is expressed as:

$$R_X = \alpha T^{-n} \quad (2.47)$$

where the value of the exponent  $n$  depends on each particular X. Krassovsky gave  $n=4$  for X being O and  $n=1.3$  for X being H [4]. The number  $N$  of newly formed  $XO_2^*$  in a volume  $V$  is:

$$N = V[X][O_2][M]\alpha T^{-n} \quad (2.48)$$

where  $[A]$  denotes the concentration of the element A ( $\text{cm}^{-3}$ ). If we assume that the reaction takes place in an isothermal region of the atmosphere, the concentrations can be represented as:

$$[X] = (X)/V, \quad [O_2] = (O_2)/V, \quad [M] = (M)/V \quad (2.49)$$

where the element symbols in round brackets denote the number of that element in volume  $V$ . The equation for  $N$  can be rewritten as:



$$N = (X)(O_2)(M)\alpha T^{-n}v^2 \quad (2.50)$$

This equation together with the thermodynamic equation (2.30) becomes:

$$N = C_N T^{\left(\frac{2}{\gamma-1} - n\right)} \quad (2.51)$$

where  $C_N$  is a constant and  $T$  is the temperature. By incrementally differentiating this equation, the results are:

$$\frac{\Delta N}{N} = \left[\frac{2}{\gamma-1} - n\right] \frac{\Delta T}{T} \quad (2.52)$$

Note that in the expression the incrementals  $\Delta N$  and  $\Delta T$  are used in place of differentials  $dN$  and  $dT$ . This expression is intentionally used after the Krassovsky method in which the oscillation amplitudes of the corresponding entities are referenced. This method is discussed in detail in section 3.

From (2.45) and (2.52),  $\eta$  can be represented as:

$$\eta = \frac{2}{\gamma-1} - n \quad (2.53)$$

Note that  $\eta$  is a real number in this model. Krassovsky gave the value of  $\eta$  as unity when  $X$  is an oxygen atom and 3.7 when  $X$  is a hydrogen atom. However, he reported observed values of  $\eta$  between 4

to 5 [4]. Krassovsky attempted several explanations for the cause of this discrepancy, one of them being the need to consider the effect of quenching and the exclusion of other chemical reactions not included in the set.

This simple model has limited application to the wave dynamics of the mesospheric airglow. One of the limitations is that the measured quantity is not actually the volume emission rate at a spatial point, but is in fact an integrated value over a volume along the line of sight [11]. This model is further limited by the assumption that the concentration of each chemical species, including the hydroxyl, is in equilibrium. This assumption is valid only if the chemical reactions that determine the concentration proceed in a much shorter time period compared with the period of the IGW under investigation. However, several chemical reactions with reaction time constants of 5 to 20 minutes [3] must be considered when studying an IGW of less than one hour, resulting in the introduction of a phase factor into  $\eta$  [11]. This extension of  $\eta$  from an algebraically real number to a complex entity with phase as well as magnitude is discussed in the following section.

The work of Weinstock [22], [23] represents the second group of theoretical modeling relating IGWs to the apparent oscillation in the mesospheric infrared airglow. Weinstock's model is a nonlinear treatment of the internal gravity wave. This model is an attempt to assess some apparent nonlinear phenomena to the observations; however, the present dissertation does not include an implementation of any nonlinear model.

The most obvious difference between the two models is the dependence of  $\eta$  upon the scale height of related species, especially atomic oxygen [11], [23]. Hines pointed out the difficulties with the nonlinear model and suggested that the apparent nonlinearity could be a result of geometric effects [11].

## 2. The Complex $\eta$ Model

The following theoretical calculation of  $\eta$  is based upon that of Hines and Tarasick [11] - an adiabatic linearized model of atmospheric IGW dynamics. This model provides a more detailed consideration of the observables than the work of Krassovsky [4]. This means that in ground-based optical observations, the observed value is the line integral of the emission intensity along the line of sight within the field of view of the instrument. As a result, when the line of sight is to the zenith, the horizontal component of an incoming wave differs from the vertical component. This difference occurs because the horizontal component of the wave can introduce additional species into the observed column while the vertical component does not. This is the same effect as the geometric effect discussed in the previous section. To derive  $\eta$ , a monochromatic, small-amplitude sinusoidal wave of frequency  $\omega$  is used as an input. Thus, the linearization based upon the following formulae can be used:

$$u(x, z, t) = u_0 + u' \exp(i(\omega t - k_x x - k_z z)) \quad (2.54)$$

$$\frac{\partial u}{\partial t} = i\omega u' \quad (2.55)$$

$$\frac{\partial u}{\partial x} = -ik_x u' \quad (2.56)$$

$$\frac{\partial u}{\partial z} = -ik_z u' \quad (2.57)$$

where  $u$  is a physical entity such as velocity,  $u_0$  is the constant part of  $u$ ,  $u'$  is the amplitude of the sinusoidal oscillation of  $u$  with the frequency  $\omega$ , the horizontal wavenumber  $k_x$  and the vertical wavenumber  $k_z$ . The derivation of the complex  $\eta$  is based upon the ozone formation reaction (2.2):



Assuming that the concentration of the emitting species hydroxyl is instantaneously proportional to the concentration of ozone, the observed emission intensity is the integration of the volume emission rate along the line of sight. Therefore:

$$I = C \int_0^{\infty} k^* (n_0 + n') (N_0 + N')^2 dz \quad (2.58)$$

where  $k^*$  is the reaction rate coefficient for the reaction (2.2),  $n'$  is the wave-induced perturbation of the concentration  $[O]$  from its unperturbed value denoted by  $n_0$ ,  $N'$  is the wave-induced perturbation of the concentration of  $M$  from its unperturbed values  $N_0$ . Here, the concentration of  $O_2$  is assumed to be proportional to  $N$  at any time

with a ratio  $C$ , so that  $[O_2] = CN$ . Equation (2.58) can be rewritten as:

$$I = C \int_0^{\infty} k^* n_o N_o^2 \left(1 + \frac{n'}{n_o}\right) \left(1 + \frac{N'}{N_o}\right)^2 dz \quad (2.59)$$

The measurable temperature,  $T_m$ , will be taken as the brightness-weighted average of the actual local temperatures along the vertical line of sight. This can be represented as:

$$T_m = \frac{\int_0^{\infty} k^* n_o N_o^2 T_o \left(1 + \frac{n'}{n_o}\right) \left(1 + \frac{N'}{N_o}\right)^2 \left(1 + \frac{T'}{T_o}\right) dz}{\int_0^{\infty} k^* n_o N_o^2 \left(1 + \frac{n'}{n_o}\right) \left(1 + \frac{N'}{N_o}\right)^2 dz} \quad (2.60)$$

where  $T'$  is the wave-induced perturbation of  $T$  from its unperturbed value  $T_o$ . The reaction rate  $k^*$  is actually a function of temperature which can be linearized as:

$$\begin{aligned} k^*(T) &= k_o^* \left(\frac{T}{T_o}\right)^{-A} \\ &\approx k_o^* \left(1 - A \frac{T'}{T_o}\right) \end{aligned} \quad (2.61)$$

where  $k_o^*$  is the rate constant at temperature  $T_o$  and  $A$  is a constant. With the use of equation (2.61), equation (2.59) can be linearized and normalized to  $I_o$  as:

$$\begin{aligned} \frac{I'}{I_0} &= \frac{I - I_0}{I_0} \\ &= -\frac{1}{I_0} \int_0^{\infty} k_0^* n_0 N_0^2 \left( \frac{n'}{n_0} + \frac{2N'}{N_0} - \frac{AT'}{T_0} \right) dz \end{aligned} \quad (2.62)$$

where

$$I_0 = \int_0^{\infty} k_0^* n_0 N_0^2 dz \quad (2.63)$$

is the unperturbed observed intensity. The unperturbed observable temperature is:

$$T_m^0 = \frac{\int_0^{\infty} k_0^* n_0 N_0^2 T_0 dz}{\int_0^{\infty} k_0^* n_0 N_0^2 dz} \quad (2.64)$$

Note that the  $T_0$  in the integrand of the numerator is a function of  $z$ . The fractional perturbation of the measured temperature is, by (2.60) and (2.61),

$$\begin{aligned} \frac{T_m'}{T_m^0} &= \frac{T_m - T_m^0}{T_m^0} = \frac{T_m'}{T_m^0} + \\ &= \frac{\int_0^{\infty} k_0^* n_0 N_0^2 (T_0 - T_m^0) \left( \frac{n'}{n_0} + 2\frac{N'}{N_0} - A\frac{T'}{T_0} \right) dz}{\int_0^{\infty} k_0^* n_0 N_0^2 T_0 dz} \end{aligned} \quad (2.65)$$

where

$$\frac{T_w}{T_m} = \frac{\int_0^\infty k_0^* n_0 N_0^2 T' dz}{\int_0^\infty k_0^* n_0 N_0^2 T_0 dz} \quad (2.66)$$

The quotient of the integrals shown explicitly in (2.65) is the term that causes the observed temperature an apparent nonlinear behavior when the unperturbed temperature  $T_0$  is not a constant with respect to altitude  $z$ . This is another way to represent the geometric effect.

The next step in the derivation of  $\eta$  is the linearization of the continuity equation, here represented for the specimen  $n$ :

$$\frac{\partial n}{\partial t} = -n \nabla \cdot \underline{v} - \underline{v} \cdot \nabla n \quad (2.67)$$

where  $\underline{v}$  is the wave-induced velocity vector of an air parcel,  $\cdot$  denoting the inner product of two vectors. This can be linearized with the assumed input form of (2.54) into:

$$\begin{aligned} i\omega n' &= -n_0 \nabla \cdot \underline{v} - w \frac{dn_0}{dz} \\ &= -n_0 \nabla \cdot \underline{v} + w \frac{n_0}{H_n} \end{aligned} \quad (2.68)$$

where  $w$  is the  $z$  component of  $\underline{v}$  and  $H_n$  is the scale height of the  $n$  species that is defined as follows:

$$H_n = - \frac{1}{d(\ln n_0)/dz} \quad (2.69)$$

When  $n$  is atomic oxygen, for instance,  $H_n$  is about  $-3$  km, just under the OH airglow layer [11]. Because the observables are integrals of appropriate physical entities along the line of sight, the Lagrangian method is more suitable than the Eulerian [11]. In other words, each entity is referred to with respect to its own stationary coordinates and values. For example, consider an air parcel currently at a height  $z$ . It has moved from its unperturbed rest level at height  $\zeta = z-h$  with the height increment of  $h=h(t)$ . If we assume that all species move together, then the ratio  $n(z)/N(z)$  is the same as the unperturbed ratio  $n_0(\zeta)/N_0(\zeta)$ . This gives:

$$n_0(z) + n'(z) = (N_0(z) + N'(z)) \frac{n_0(\zeta)}{N_0(\zeta)} \quad (2.70)$$

If the linearization is appropriate in modeling the travelling wave, the same is true for the dominant species, namely,

$$N_0(z) + N'(z) = N_0(\zeta) + h \frac{dN_0(\zeta)}{d\zeta} + N'(\zeta) \quad (2.71)$$

where any difference between  $N'(z)$  and  $N'(\zeta)$  is of second order at most. Since  $w \ll h$  by (2.54), (2.71) can be simplified as:



$$N_0(z) + N'(z) = N_0 \left(1 + \frac{i}{\omega} \nabla \cdot \underline{v}\right) \Big|_{\zeta} \quad (2.72)$$

where the whole quantity of the right-hand side is evaluated at the height  $z=\zeta$ .

A similar form for the kinetic temperature is:

$$T_0(z) + T'(z) = T_0 \left(1 + \frac{i}{\omega} (\gamma-1) \nabla \cdot \underline{v}\right) \Big|_{\zeta} \quad (2.73)$$

where the adiabatic state and mass continuity equations were used. The detailed linearization of these equations is given in Appendix C. Using these results, the rate coefficient  $k^*$  can be represented as:

$$\begin{aligned} k^*(z) &= k_0^*(z) + k'(z) = k_0^*(\zeta) + h \frac{dk_0^*(\zeta)}{d\zeta} + k'(\zeta) \\ &= k_0^*(\zeta) + \left[ h \frac{dT_0(\zeta)}{d\zeta} + T'(\zeta) \right] \left[ \frac{dk^*}{dT} \right] \Big|_{T=T_0(\zeta)} \\ &= k_0^* \left[ 1 - \frac{i}{\omega} A(\gamma-1) \nabla \cdot \underline{v} \right] \Big|_{\zeta} \end{aligned} \quad (2.74)$$

Then from (2.58) with (2.74),

$$I_0 + I' = \int_0^{\infty} k^*(z) [n_0(z) + n'(z)] [N_0(z) + N'(z)]^2 dz$$

$$- \int_0^{\infty} k_o^* \left[ 1 - \frac{1}{\omega} A(\gamma-1) \nabla \cdot \underline{v} \right] N_o^3 \left[ 1 + \frac{1}{\omega} \nabla \cdot \underline{v} \right]^3 \left[ \frac{n_o}{N_o} \right] \Big|_{\zeta} dz \quad (2.75)$$

From the relation:

$$dz = \left( \frac{dz}{d\zeta} \right) d\zeta = \left( 1 + \frac{\partial h}{\partial \zeta} \right) d\zeta = \left( 1 - \frac{1}{\omega} \frac{\partial w}{\partial \zeta} \right) d\zeta \quad (2.76)$$

then (2.75) can be rewritten as the integration over  $\zeta$  as:

$$I_o + I' = \int_0^{\infty} k_o^* n_o N_o^2 \left[ 1 + \frac{1}{\omega} (3-A(\gamma-1)) \nabla \cdot \underline{v} - \frac{1}{\omega} \frac{\partial w}{\partial \zeta} \right] d\zeta \quad (2.77)$$

which yields:

$$\frac{I'}{I_o} = \frac{\frac{1}{\omega} \int_0^{\infty} k_o^* n_o N_o^2 \left[ (3-A(\gamma-1)) \nabla \cdot \underline{v} - \frac{\partial w}{\partial \zeta} \right] d\zeta}{\int_0^{\infty} k_o^* n_o N_o^2 dz} \quad (2.78)$$

A similar linear form can be calculated for the temperature according to the following procedure. With (2.74), the numerator of (2.60) is:

$$\int_0^{\infty} k_o^* n_o N_o^2 T_o \left[ 1 + \frac{1}{\omega} (3+(\gamma-1)(1-A)) \nabla \cdot \underline{v} - \frac{1}{\omega} \frac{\partial w}{\partial \zeta} \right] d\zeta \quad (2.79)$$

and the denominator is the same as that of (2.78). As a consequence, equation (2.60) can be represented in a normalized form with two parts as:

$$\frac{T'_m}{T_m^0} = \frac{T_m^c}{T_m^0} + \frac{T_m^v}{T_m^0} \quad (2.80)$$

where

$$\frac{T_m^c}{T_m^0} = \frac{\frac{i}{\omega} \int_0^\infty k_o^* n_o N_o^2 T_o (\gamma-1) \nabla \cdot \underline{v} \, d\zeta}{\int_0^\infty k_o^* n_o N_o^2 T_o \, dz} \quad (2.81)$$

$$\frac{T_m^v}{T_m^0} = \frac{\frac{i}{\omega} \int_0^\infty k_o^* n_o N_o^2 (T_o - T_m^0) \left( 3 - A(\gamma-1) \nabla \cdot \underline{v} - \frac{\partial w}{\partial \zeta} \right) \, d\zeta}{\int_0^\infty k_o^* n_o N_o^2 T_o \, dz} \quad (2.82)$$

The first part, (2.81), is the only contributor to  $T_m$ , or in other words, to  $T'/T_o$ , when  $T_o$  is a constant for all  $z$ . When  $T_o$  is allowed to vary with altitude, the second part, (2.82), works as an additional contributor to  $T_m$ . Equation (2.81) is the contributor in both cases.

The final step in deriving a theoretical complex parameter  $\eta$  is

to introduce a linearized relationship between  $\nabla \cdot \underline{v}$  and  $\partial w / \partial z$ . Hines gives such a relationship [11], [13], namely,

$$u \approx k_x C^2 \left[ k_z - i \frac{(1-\gamma/2)g}{C^2} \right] \quad (2.83)$$

$$w \approx \omega^2 - k_x^2 C^2 \quad (2.84)$$

for a wave of the form  $\exp[z/2H + i(\omega t - k_x x - k_z z)]$ , where  $g$  is the gravitational acceleration,  $C$  is the speed of sound and  $H$  is the scale height of the dominant species,  $H = C^2 / \gamma g$ . The horizontal coordinate is chosen so that the  $y$  component of  $\underline{v}$  vanishes. Incorporation of these relations results in the relation:

$$\begin{aligned} \frac{\partial w}{\partial z} &= \frac{(k_x^2 C^2 - \omega^2)(-ik_z + 1/2H)}{k_x^2 g + ik_z \omega^2 - \omega^2 / 2H} \nabla \cdot \underline{v} \\ &= (\mu + i\nu) \nabla \cdot \underline{v} \end{aligned} \quad (2.85)$$

where  $\mu$  and  $\nu$  are real and, under the assumptions made in this model, is independent of altitude. With the inclusion of (2.85) in (2.78),

$$\frac{I'}{I_0} = \frac{\frac{i}{\omega} \int_0^\infty k_0^* n_0 N_0^2 [3 - \mu - i\nu - A(\gamma - 1)] \nabla \cdot \underline{v} \, dz}{\int_0^\infty k_0^* n_0 N_0^2 \, dz} \quad (2.86)$$

For the case of  $T_0$  constant with  $z$ , (2.81) and (2.86) together produce:

$$\frac{I'}{I_0} = \left[ \frac{3-\mu-i\nu}{\gamma-1} - A \right] \frac{T_m^c}{T_m^o} \quad (2.87)$$

$$= [\eta_R^c + i\eta_I^c] \frac{T_m^c}{T_m^o} \quad (2.88)$$

Equation (2.88) is the desired complex parameter  $\eta = \eta_R^c + i\eta_I^c$ .

In the derivation of (2.88), it was assumed that the unperturbed temperature  $T_0$  is constant for all altitudes. This assumption is not valid in the OH airglow layer region [1]. Hines and Tarasick introduced a modification of  $\eta$  for the case of slowly changing  $T_0$  with altitude [1]. His calculations were based upon the WKB approximation of the wave in a varying medium. This approach requires the following condition:

$$qH \gg 1 \quad (2.89)$$

where  $q$  is equivalent of the wavenumber  $k_z$  under the condition of spatially variable temperature, and  $H$  is the scale height. Unfortunately, this condition is satisfied by waves which are likely to be unobserved by ground-based passive optical instruments.

### 3. Complications of Eta

In deriving the complex  $\eta$  in equation (2.88), it was assumed that the unperturbed temperature,  $T_0$ , is constant with respect to

altitude in the region of interest. In a better model,  $T_0$  should be allowed to vary with altitude. This can be accomplished, as was pointed out by Hines and Tarasick [11], with the use of a WKB approximation to the wave; however, even with this improvement, only those waves that are unlikely to be observed by the ground-based optical instrument satisfy the condition (2.89) required by the WKB approximation [11]. As is shown by (2.89), those fluctuations which satisfy (2.89) are the waves whose vertical wavelengths are much shorter than the scale height. Hence, these waves are subject to serious cancellation in the ground-based passive optical observations, since the layer thickness is on the order of the scale height.

The use of  $\eta$  involves another problem. Fig. 2-9 contains sample data taken by optical equipment described in Chapter IV. These airglow measurements clearly show oscillation. Yet from the figure, it is not possible to confidently ascertain either  $I_0$  or  $I$ . The situation is even worse for the rotational temperatures  $T_0$  or  $T'$ .

The difficulties described above should not be ascribed to the definition of the eta as given in equation (2.45), but are attributable to the interpretation of each element within the equation. From the calculation of the values of  $\eta$  leading to the equation (2.53),  $\Delta I$  and  $\Delta T$  in (2.45) are incremental fluctuations of the emission intensity and the temperature, and  $I$  and  $T$  are their absolute values just before the fluctuations take place. In other words,  $\Delta I$  and  $\Delta T$  can be treated as differentials  $dI$  and  $dT$ .

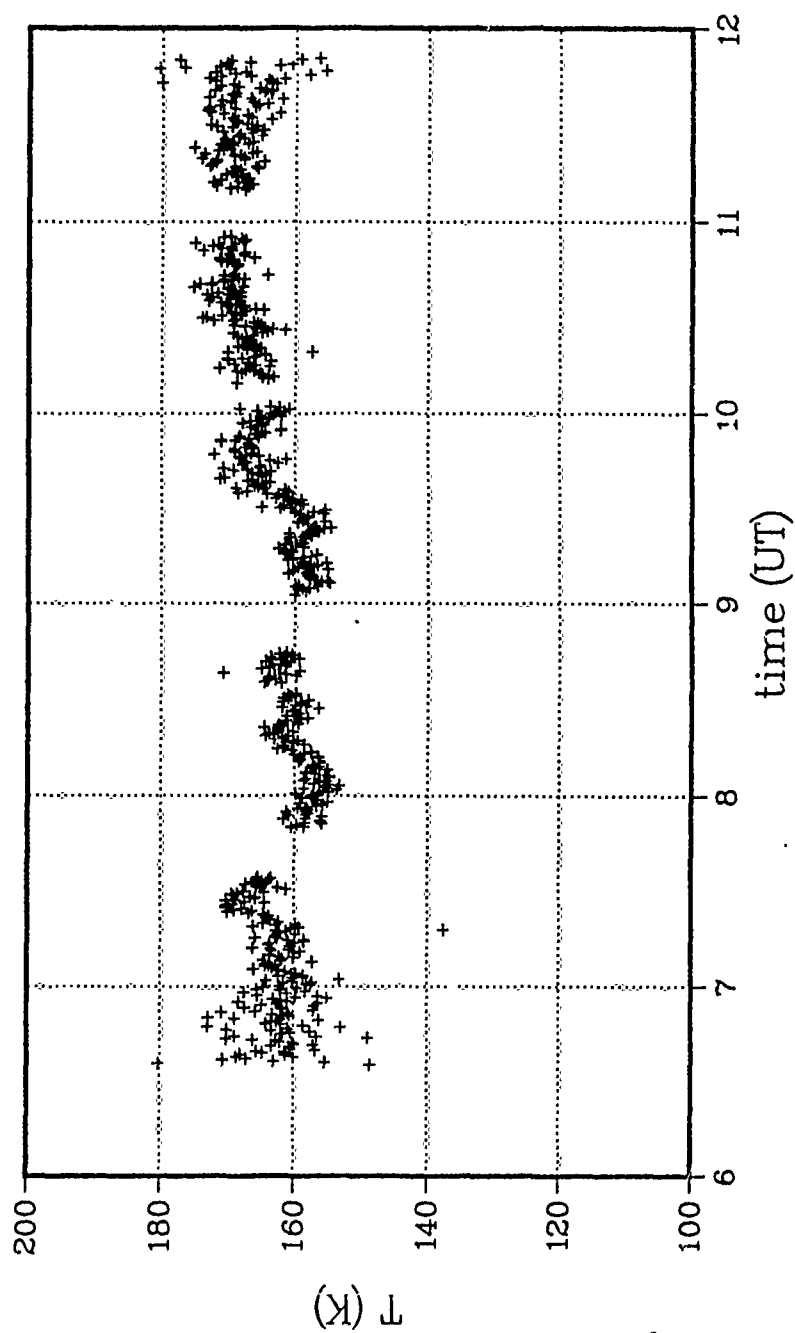


Fig. 2-9. Example of measured data

Instead, in previous studies, they were interpreted as the amplitudes of the assumed sinusoidal oscillations of the corresponding quantities. By interpreting them differently, data could be processed without clear definition of  $\Delta I$ ,  $\Delta T$ ,  $I_0$  and  $T_0$ , as discussed in detail in Chapter VI.

In case of discrete data, these derivatives are approximated by the increments from data point to data point. A similar argument holds for  $I$  and  $T$ , indicating that the new interpretation is naturally compatible with the discrete nature of the data.

On the other hand, the departure from the assumption of a sinusoidal input on constant average values is undesirable. It was this assumption that caused the cancellation of the geometric effects in both the emission intensity and the observed temperature by the relationship between  $\nabla \cdot \mathbf{v}$  and  $w$ , that is, equation (2.85).

One way to treat the nonsinusoidal input without constant background is a direct numerical calculation. The chemical model established in the section B in Chapter II can be used as a part of such a model. A numerical model for the internal gravity wave is discussed in Chapter III. More detailed treatment of the geometric effect is discussed in Chapter IV. Conditions required for experimental data to be useful for the study of the emission layer are discussed in Chapter V.



## CHAPTER III

## DYNAMIC MODEL

A numerical dynamic model based upon the analytical models developed in Chapter II is presented in this chapter. These methods include the use of MSIS model atmosphere [21] used in some mesospheric studies [11], [15]. The chemical-dynamic model, developed in Chapter II, is used in conjunction with the MSIS atmospheric model to calculate infrared emission from the mesospheric airglow. The internal gravity wave is used as the input to the model. Hines' method introduced in Chapter II is used in this chemical-dynamic model. Long-range dynamical characteristics of gravity waves are treated in order to derive the expected observables. A model which demonstrates that the often assumed monochromatic sinusoidal wave is not likely to be observed in the mesospheric airglow emission is examined for this purpose. This leads to the development of an optimal signal processing system, which is the subject of Chapter V.

Computational Dynamic Model

The chemical-dynamic model introduced in Chapter II can be used with an atmospheric model that provides the variable concentrations of several species which form an emission layer model. One such model can use the Mass Spectrometer and Incoherent Scatter (MSIS) model [21] which offers stationary concentrations of  $N_2$ ,  $O_2$ ,  $O$ ,  $H$  and the average mass density  $\rho$ , as functions of altitude. MSIS also provides the temperature for each altitude. Although MSIS was designed for thermo-

spheric modeling and may not be the ideal model for the mesospheric study, the following example shows that MSIS produces values close to the values of the US Standard Atmosphere [1]. MSIS has been used in several mesospheric studies [6], [11], providing one common reference for a comparison of these models. Fig. 3-1 shows some examples in which MSIS produces the desired output for a specific date.

Using the output from a model such as MSIS which gives the stationary quantities for the concentrations of chemical species and the temperature, the next step is to calculate the concentration of the hydroxyl using the chemical model developed in Chapter II. Fig. 3-2 demonstrates results of several such calculations. The altitude and the shape of the layer are consistent with observational data shown in Fig. 3-3 [10], [24].

The next step of the modeling is calculating the dynamic effects of the internal gravity wave. As a first-order approximation, the wave can only be assumed to change the concentrations of the major species,  $N_2$  and  $O_2$ . As a second order approximation, the adiabatic change of state due to IGW is also included. Once the change of state is calculated, the chemical model can be used to recalculate the concentration of the hydroxyl under the new condition.

In this study, a fully detailed computation of all equations is not always necessary to simulate the layer emission intensity and observational rotational temperature. The reduction method of measured airglow data is given in Chapter V. It is necessary to develop means of approximation based upon the analytical model developed by Hines, and introduced in Chapter II [11]. In this model

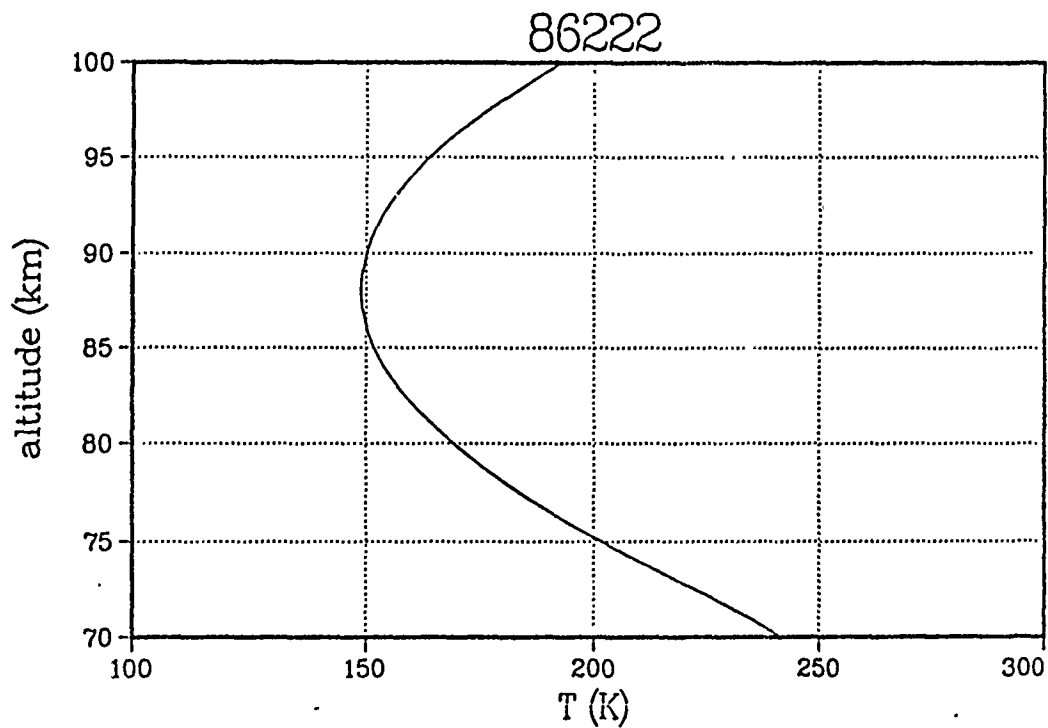
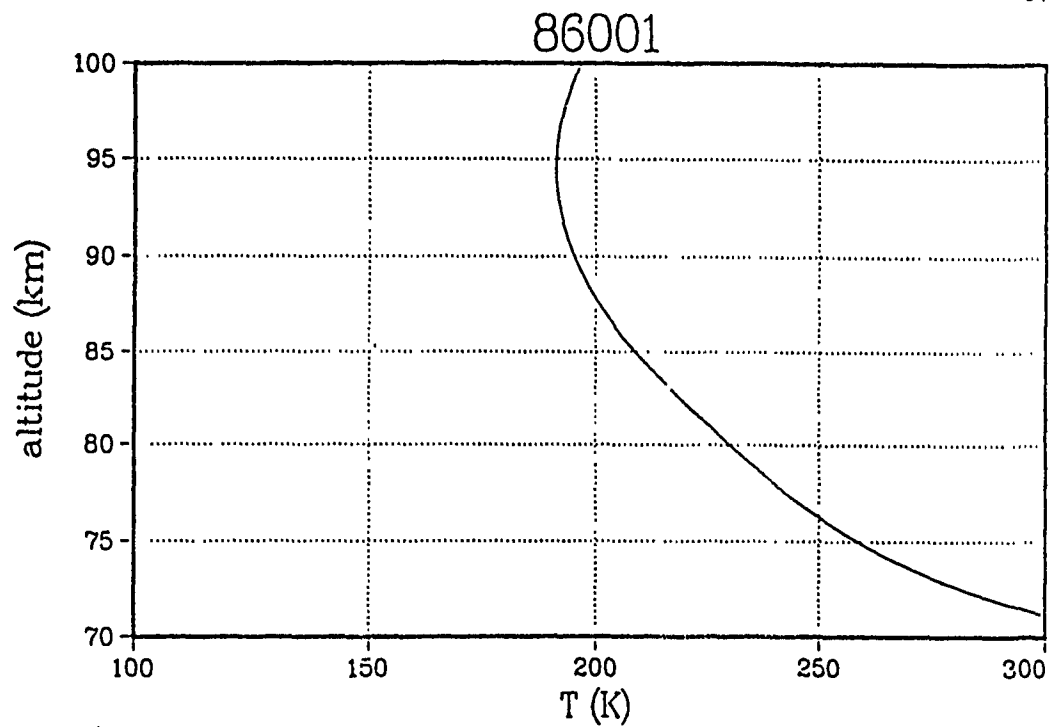


Fig. 3-1. MSIS model results for various entities: day 001 and 222 of 1986 were used as representatives for the winter and summer respectively. (a) temperature (K)

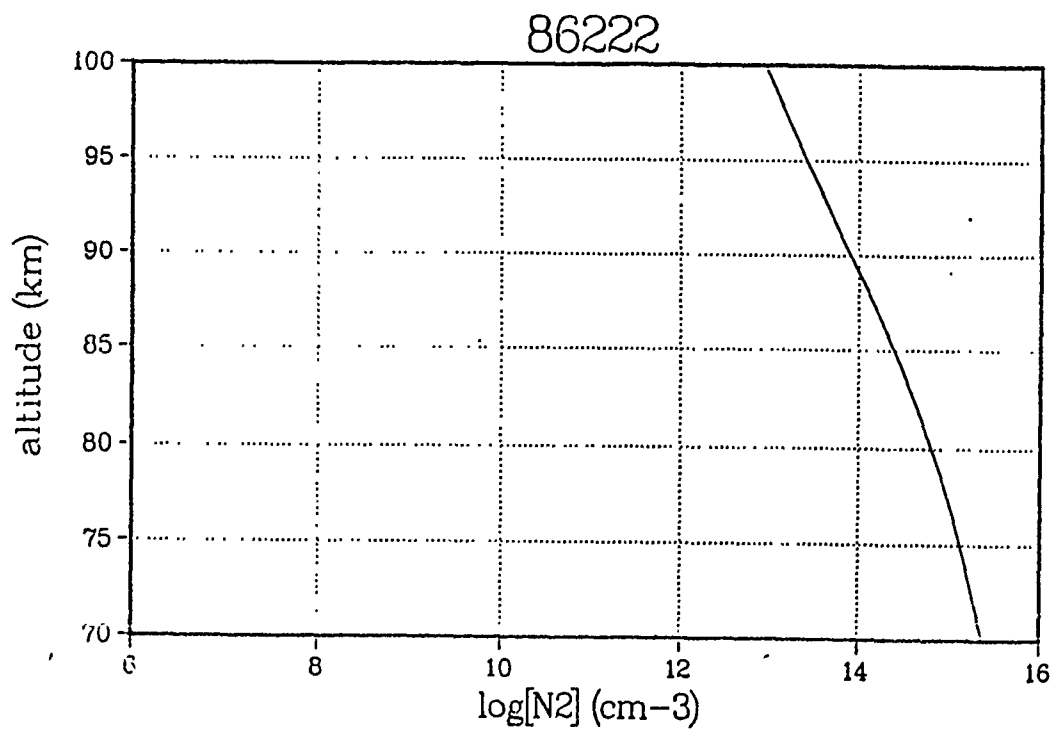
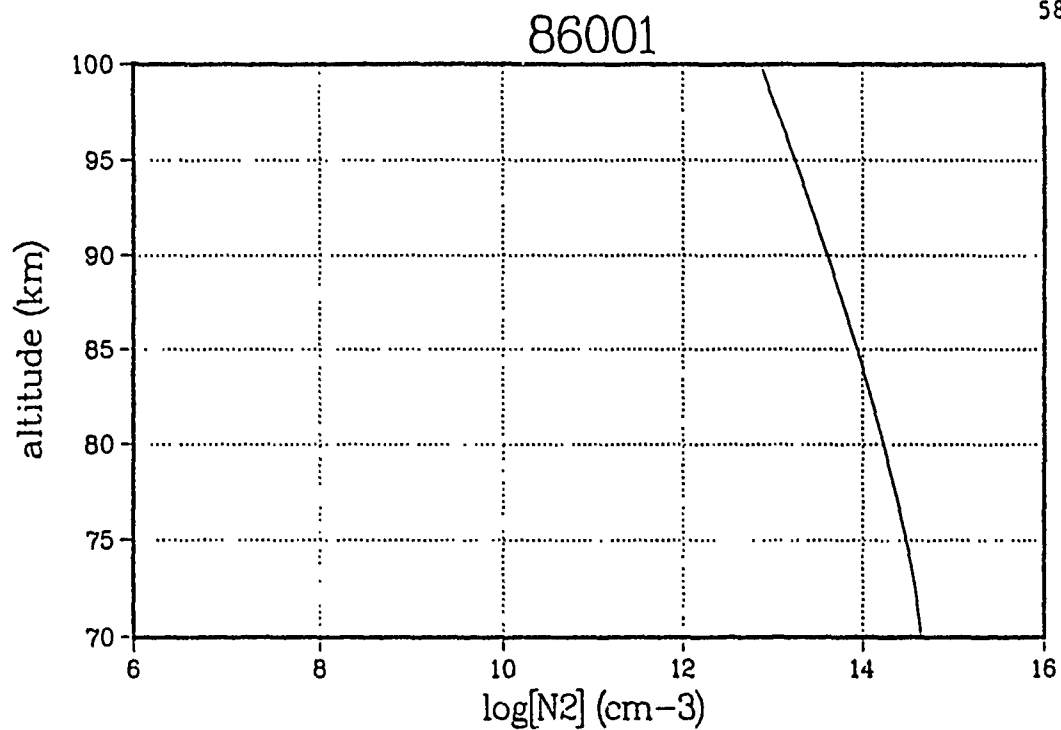


Fig. 3-1. (b) Sample MSIS model results: [N<sub>2</sub>]

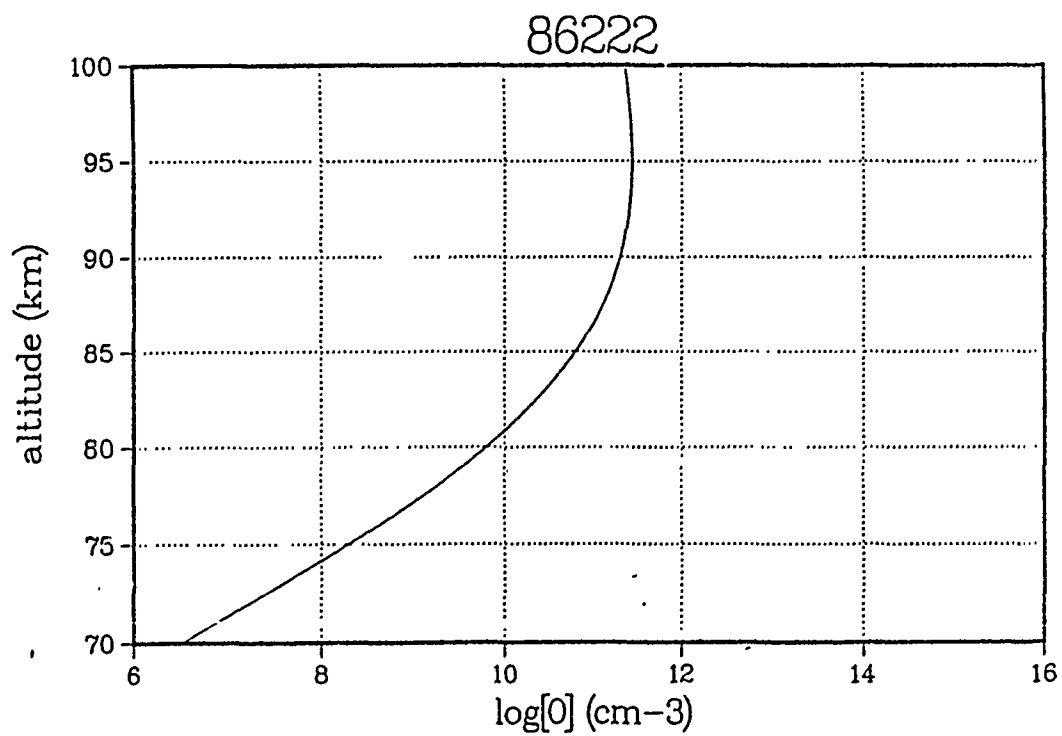
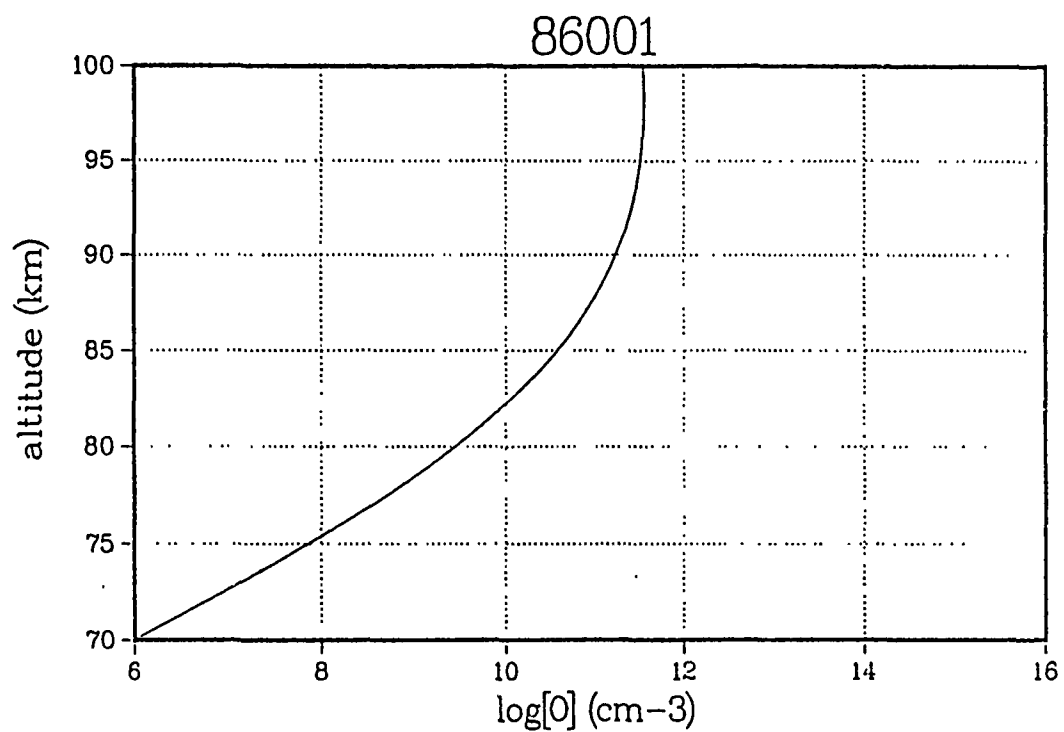


Fig. 3-1. (c) Sample MSIS model results: [O]

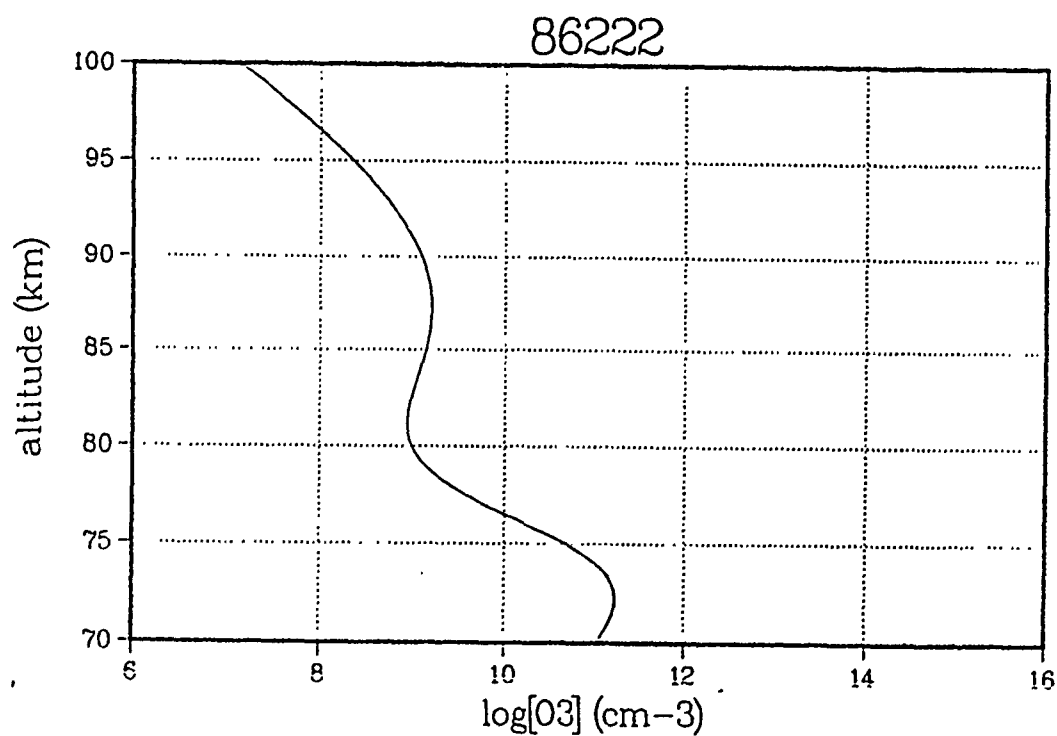
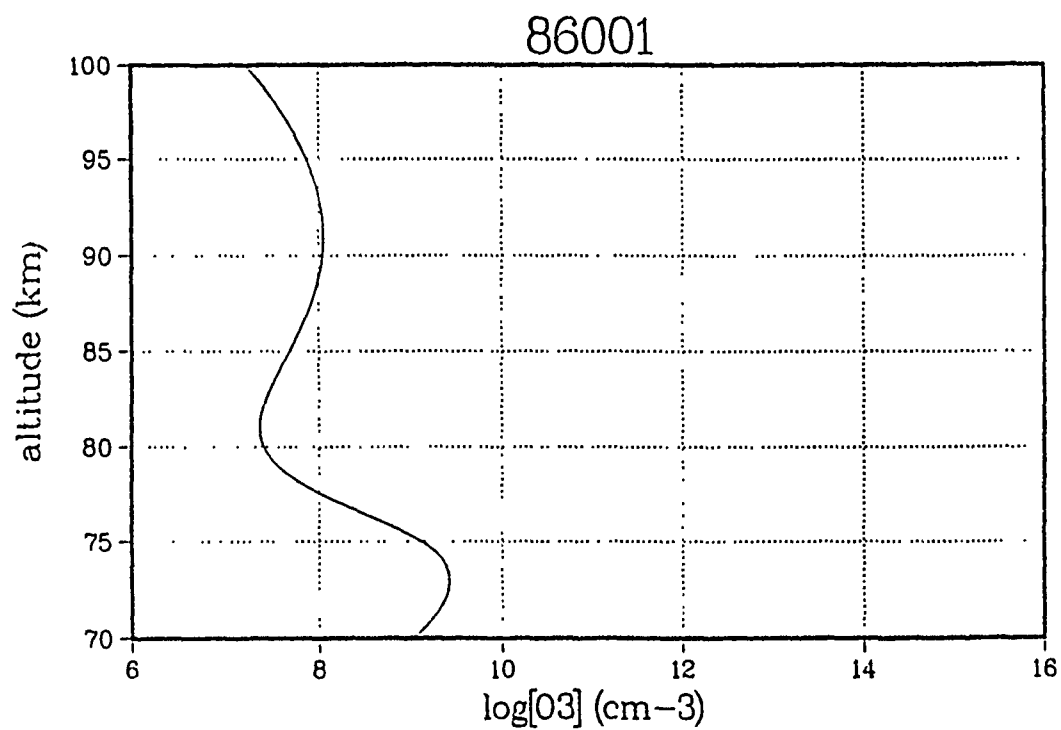


Fig. 3-1. (d) Sample MSIS model results: [O<sub>3</sub>]

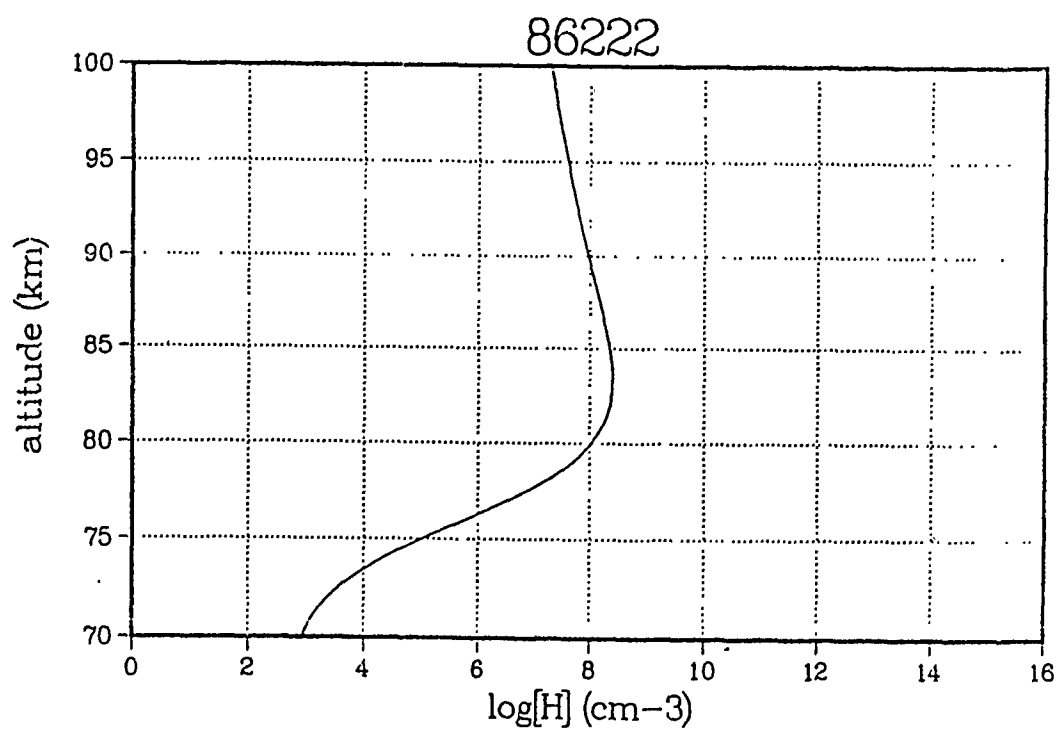
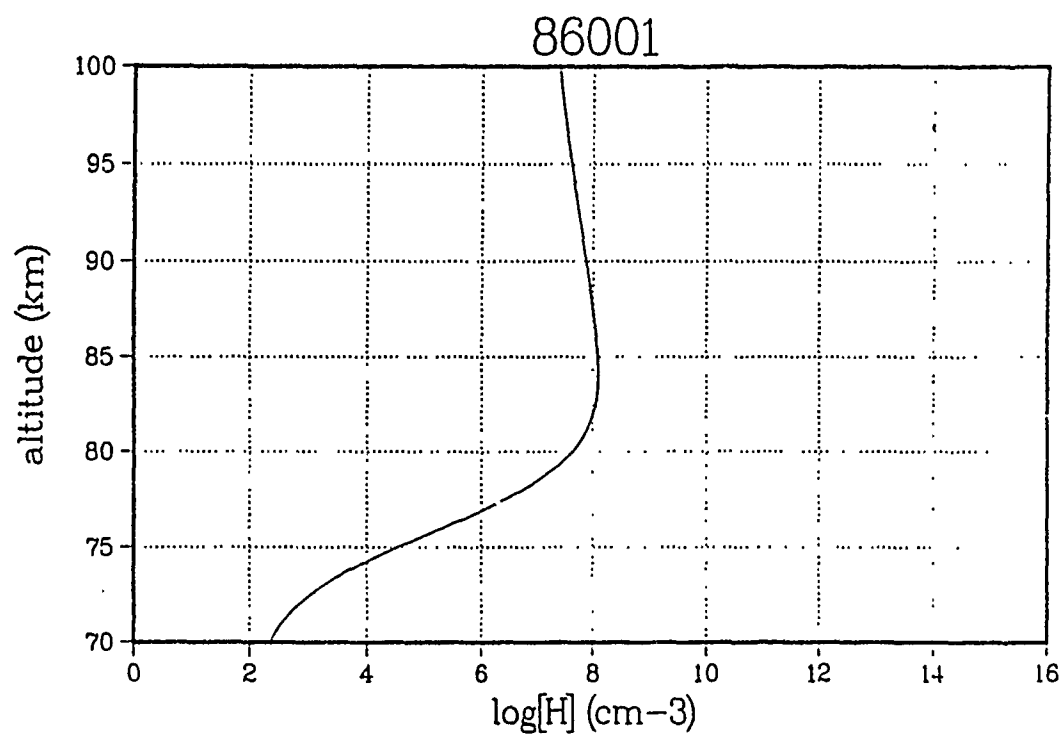


Fig. 3-1. (e) Sample MSIS model results: [H]

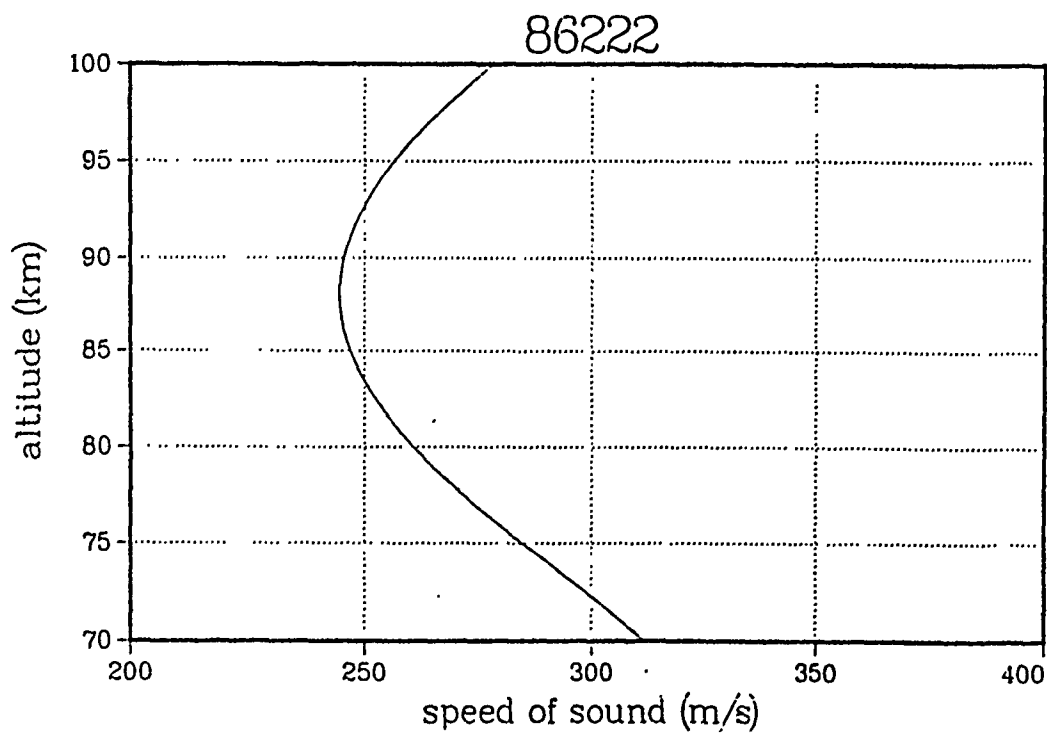
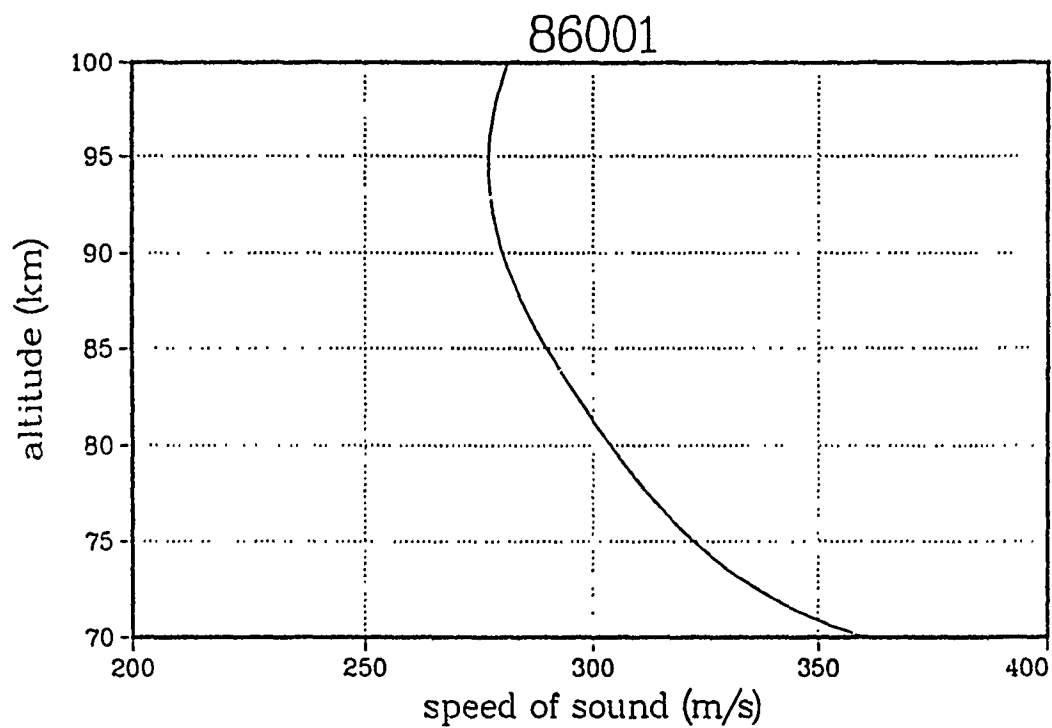


Fig. 3-1. (f) Sample MSIS model results: speed of sound (m/s)



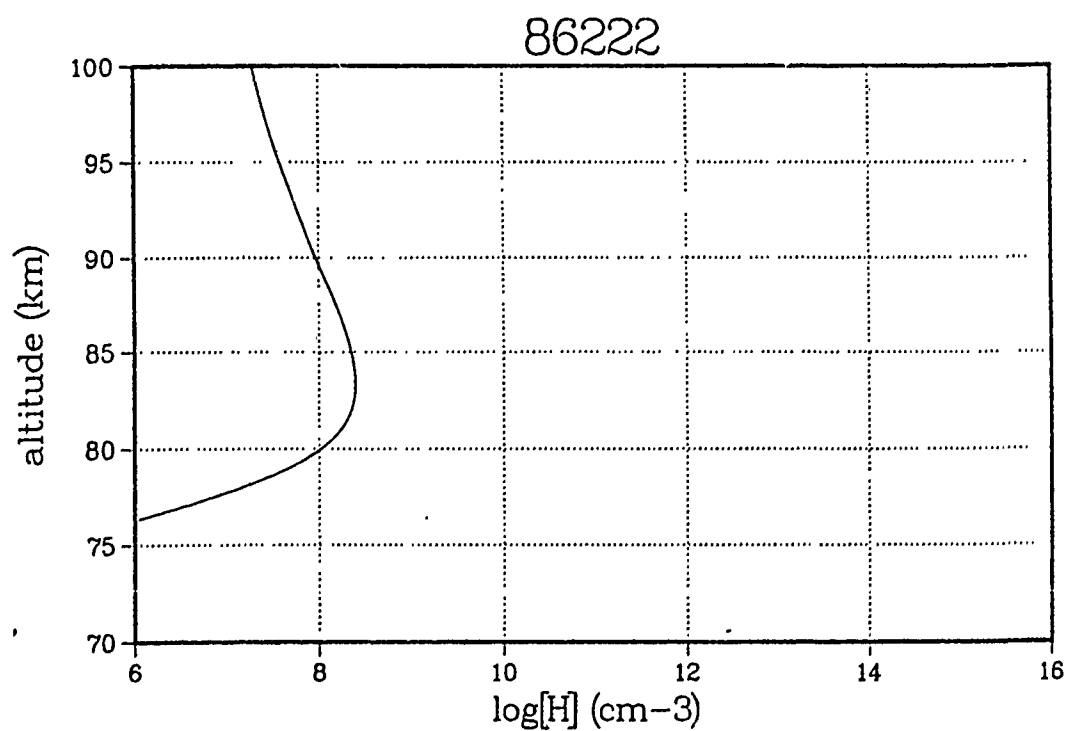
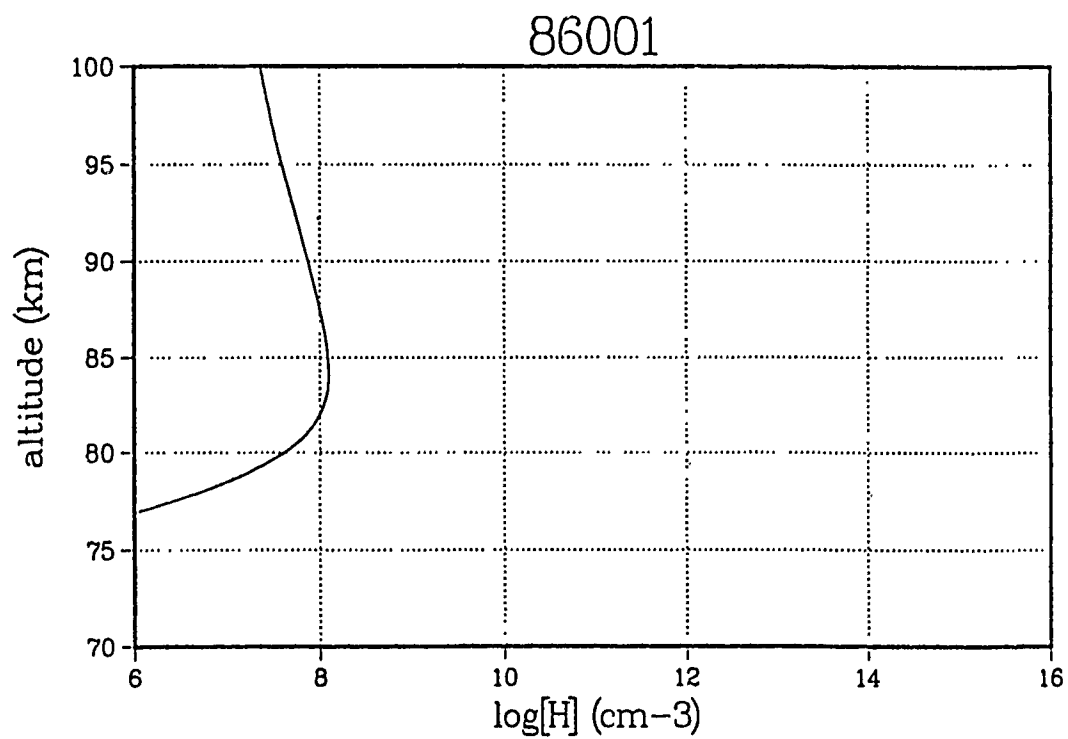


Fig. 3-1. (g) Sample MSIS model results: Brunt-Vaisala period

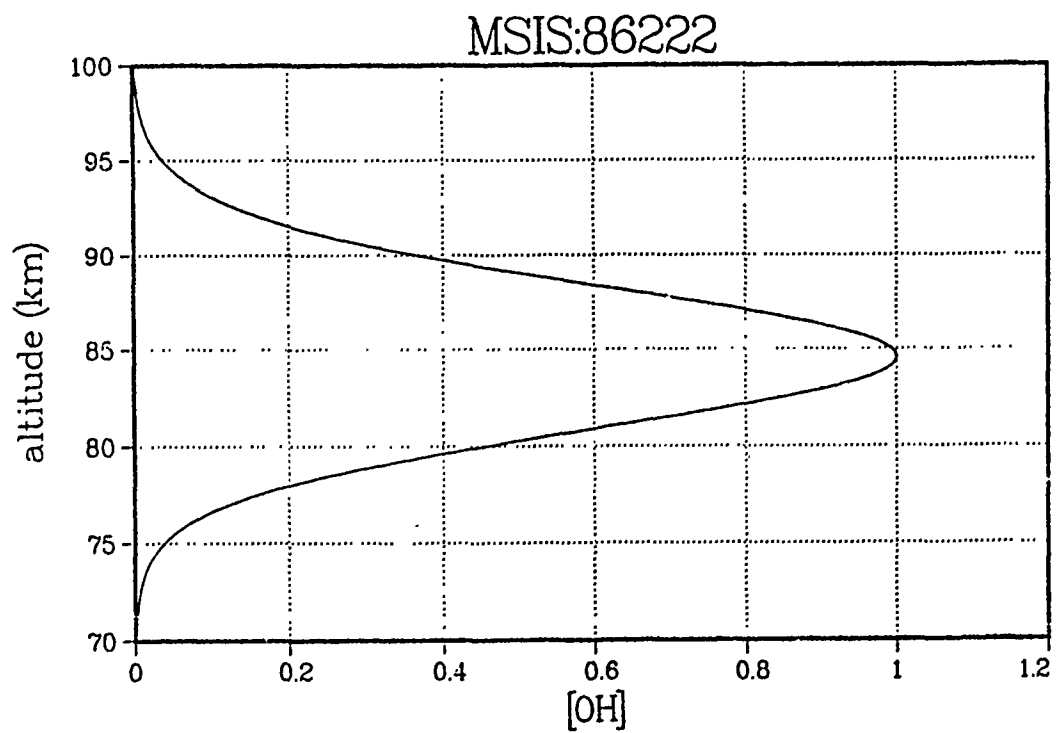
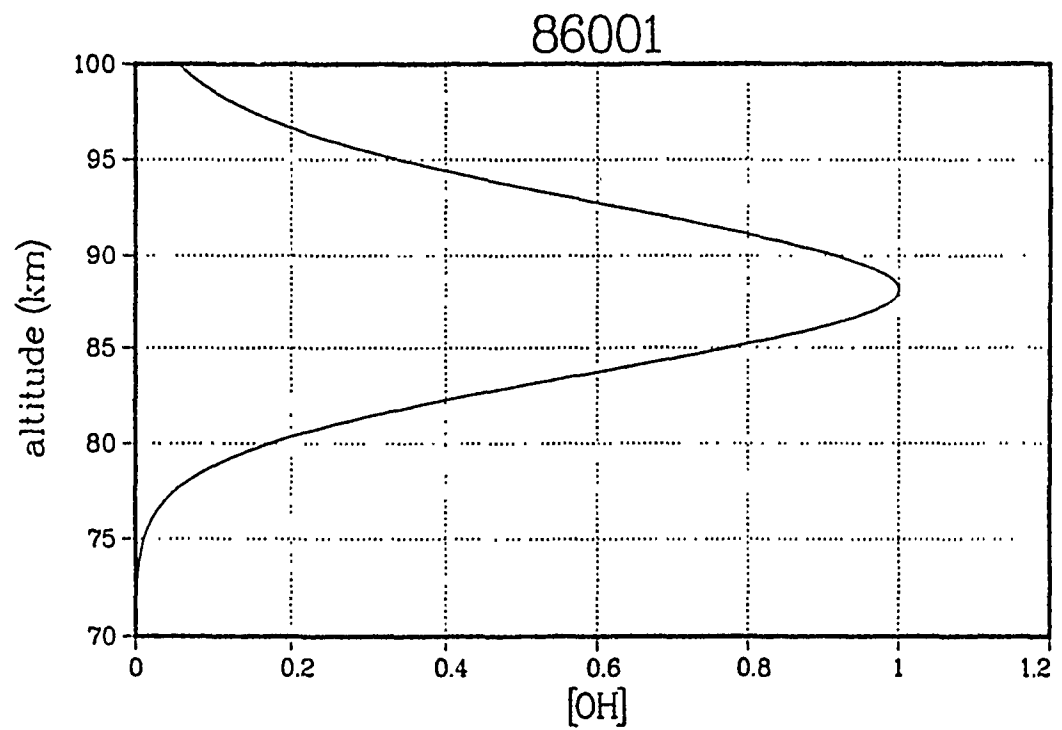


Fig. 3-2. Airglow layer model results

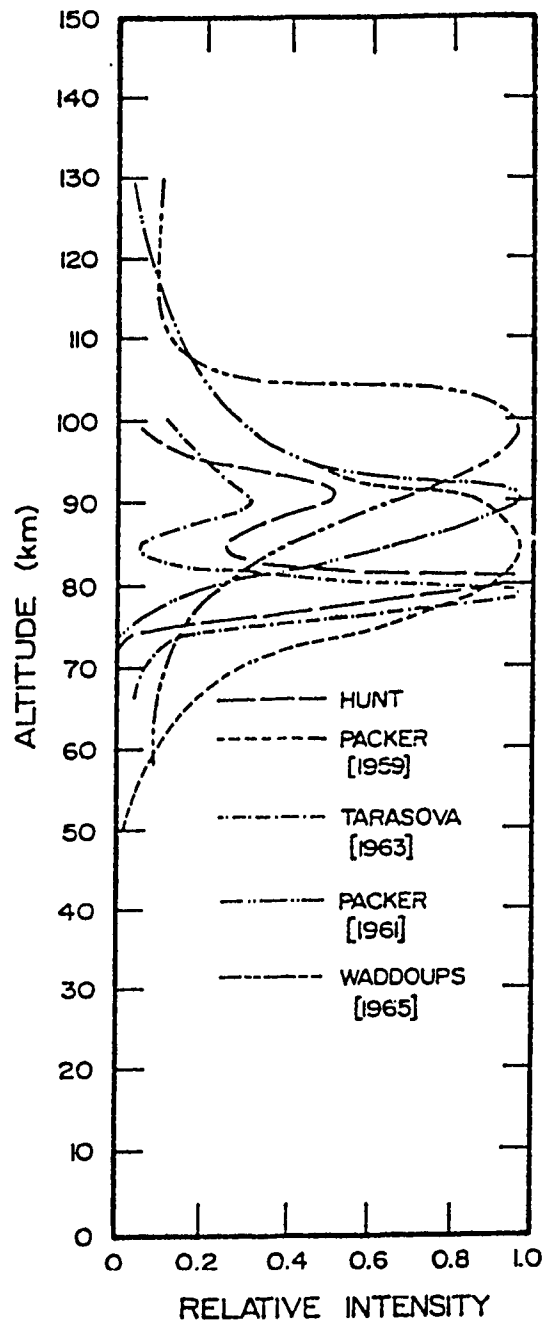


Fig. 3-3. Measured airglow layer profile (a) [10]

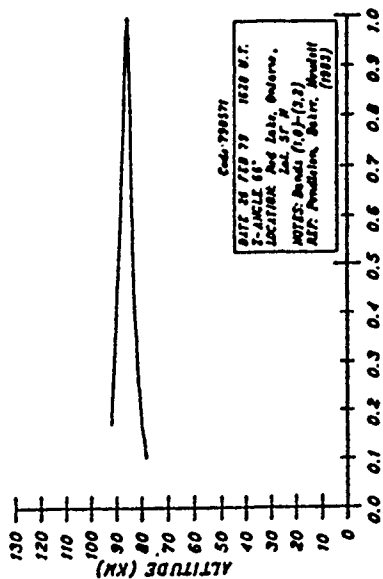
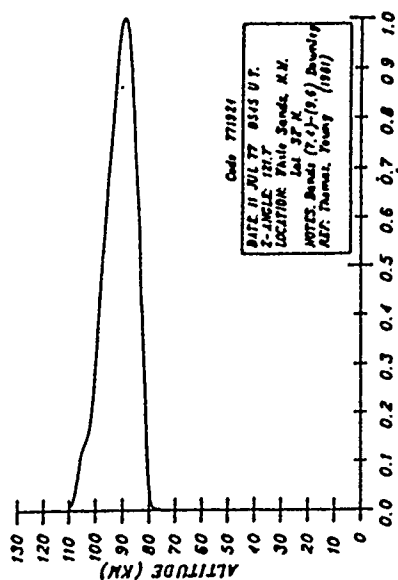
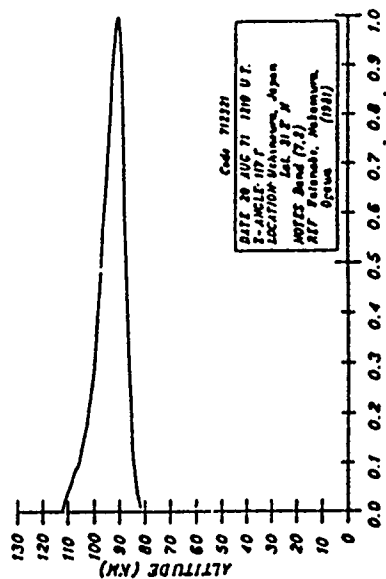
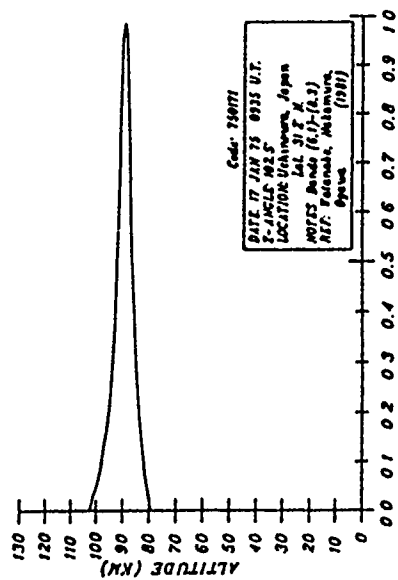


Fig. 3-3. Measured airglow layer profile (b) [24]

it is assumed that the observation is vertical, that is, the line of sight is toward the zenith. Further consideration for the geometric effect is given in detail in Chapter IV. The model developed in this chapter can be easily modified to include the geometric effect for off-zenith observations. Such an extended model is useful for investigating airglow data when using infrared imagers which favor off-zenith observations, using the optical brightness gain for optically thin airglow layers [5].

#### Approximation of Fluid Dynamics

Among the three major steps in calculating infrared emissions, fluid dynamics is the most difficult. Calculating fluid dynamics demonstrates the effect of internal gravity waves on the chemical-dynamic atmospheric model by calculating the temporal changes in the concentration of major species and also in the temperature over small volumes. This approach solves three equations simultaneously. These equations are:

$$\frac{\partial \rho}{\partial t} = -\rho \nabla \cdot \underline{v} - \underline{v} \cdot \nabla \rho \quad (3.1)$$

$$\rho \left( \frac{\partial \underline{v}}{\partial t} + (\underline{v} \cdot \nabla) \underline{v} \right) = -\nabla p + \rho \underline{g} \quad (3.2)$$

$$\frac{\nabla p}{\rho} = \gamma \frac{\nabla \rho}{\rho} \quad (3.3)$$

where  $\rho$  is the mass density,  $p$  is pressure,  $\underline{v}$  is wind velocity,  $g$  is the acceleration of the earth's gravity at the altitude of interest and  $\gamma$  is the specific heat ratio of the air as is defined in Chapter II. The underscored entity is a vector. These equations represent, respectively, the continuity equation, the momentum equation and the (adiabatic) state equation. The fluid dynamic equation set, or the three simultaneous equations, has not been solved in general form. In one-dimensional case, some properties of the solution have been studied [25] and numerical calculation methods for general applications have been developed [26], [27]. In two-dimensional case, a numerical method for general use is not readily available [28]. Internal gravity waves, as the name suggests, naturally involve two particular spatial directions: the propagation direction and the direction of the gravitational force. Unlike the acoustic wave, the gravity wave treatment employs non-isotropic geometry in which there is one particular direction - the direction of the gravity force - that renders space non-isotropic. In order to numerically simulate internal gravity waves, the model must be at least two-dimensional. The consequence is that none of the existing numerical algorithms for the one-dimensional case are applicable. Development of a two-dimensional numerical fluid-dynamics model is a subject requiring intensive study beyond the scope of this dissertation. Therefore, the analytical model developed in Chapter II is applied to numerical calculations in this chapter.

Using this method, the original partial-differential equations,

(3.1), (3.2) and (3.3), are converted into a set of algebraic equations with the assumption that the input wave is a small-amplitude, monochromatic, sinusoidal signal. This was completed in Chapter II adding the assumption that only a single chemical reaction is responsible for the formulation of the emitting layer. The results are cited as equations (2.80), (2.81), (2.82), (2.86) and (2.88). In this chapter, the integrations in those equations are accomplished numerically using a more realistic stationary model generated by MSIS. The equations are numerically calculated under discrete temporal and spatial steps. The atmosphere is divided into small "cells" that represent local physical entities such as temperature, pressure and species concentration. They are represented by (2.72), (2.73) and (2.74). In Chapter II, they were used to introduce (2.78), (2.81) and (2.82). Instead, (2.72), (2.73) and (2.74) can be used to perform the equivalent numerical integration. This is the method used in this chapter.

Although it is not necessary to carry out the full detailed numerical calculations in order to study mesospheric airglow-emission oscillations, some consideration which is related to the full scale model and necessary for the adopted simple model is presented here. This involves the empirical determination of the space and the time step-size of the cell used in the numerical model.

The first consideration is the speed of sound in the mesospheric region, as shown in Fig. 3-1(f). The speed of sound is the speed at which the displacement of pressure from its stationary value propagates. This is the fastest speed at which any disturbance propagates.

Therefore, the ratio of the spatial step to the time step should be kept on the order of the value of the sound speed.

The next consideration is the wind speed in the region. Many observational data record a wind speed of as much as 50 to 100 m/s around the emitting layer altitude [5], [13]. Therefore, the spatial step can be several hundred meters to a few kilometers.

The third consideration is the typical oscillation period of an internal gravity wave. Theoretically, as explained in Chapter II, the period of a linearized atmospheric IGW is longer than the Brunt-Vaisala period, which is about 5 minutes in the mesospheric region, as shown in Fig. 3-1(g). Consequently, the time-step could be as long as several minutes. With these considerations, the spatial step of one kilometer and the time step of 5 to 10 seconds could have been selected. However, as Fig. 3-1 shows, the values of most of the stationary background quantities can change significantly in one kilometer. Also, as Fig. 3-2 and 3-3 indicate, the infrared emission layer is about 7 km thick; therefore, a spatial step of much less than one kilometer, such as 100 meters, is a more desirable choice. This causes the corresponding time step to be about one second. Note that this process of cell-size determination is also valid for full-scale numerical simulation of the original differential equations, (3.1), (3.2) and (3.3).

In the case of small-amplitude IGW's observed in the mesosphere, the wave can be considered quasi-monochromatic. The justification is that such waves are believed to be generated at low altitudes and are then propagated through the stratosphere and lower mesosphere [13].



In these regions of IGW propagation, there exist temperature inversions. There is also a dispersion relation between the wave period and the propagation direction [18]. These two conditions result in a "window" for the wave frequencies allowed in the mesopause. As a result, an IGW generated at low altitude is expected to produce close to a monochromatic wave in the upper mesosphere. This justifies the assumption that locally monochromatic waves exist in the mesosphere. Note, however, that this assumption is valid only when the amplitude of the wave is small enough so that the linearization of the fluid-dynamic equations are valid. When the wave has a large amplitude, the lower atmosphere may no longer act as a band-pass filter, possibly allowing non-monochromatic, or even non-sinusoidal, waves to reach the mesosphere. The linear model is inadequate to describe such waves of great amplitude. Such cases need a nonlinear treatment which is beyond the scope of this dissertation. As pointed out in Chapter VII, solitary waves, or "solitons", and a mathematical chaos model are among possibilities to be studied in future. IGW dynamics leading to quasi-monochromasy in the mesosphere are discussed in subsequent sections.

#### Approximation of Chemical Model

The chemical model equations (2.4)-(2.6) described in Chapter II may be used to perform a numerical calculation using sufficiently small time-step  $\Delta t$ . Obviously, the  $\Delta t$  selected must be much shorter than the time constant of the fastest chemical reaction involved in this calculation. The fastest chemical reaction, represented by equation (2.5), has a time constant of tens of milliseconds. Conse-

quently,  $\Delta t$  was selected to be less than or equal to one millisecond. With a time step of one millisecond, it takes one million calculation steps to simulate ten minutes in real time.

Another method is available to calculate the chemical reactions (2.4)-(2.6), based upon the following assumptions:

- 1] Diffusion of all species is insignificant.
- 2] The concentrations of the major species remain almost constant within the IGW period.
- 3] The chemical reactions which determine the concentrations of the active minor species take place in a time scale much shorter than the time scale of interest. Therefore, the concentrations can be regarded as in equilibrium.

In other words, the effects of the transient behavior of the active minor species are assumed to be negligible within the IGW period. Based on these assumptions, the concentrations of the chemically active minor species of interest are represented as functions of the concentrations of the major species. This form puts forth the desired concentrations in terms of stable and/or measurable values. Therefore, a "hybrid" approach, the combination of the direct numerical simulation and the equilibrium value model, is feasible. When combined with the dynamic numerical model introduced previously, the equilibrium-value approach significantly reduces the amount of the total calculation. Furthermore, if the concentration of the hydroxyl alone is assumed to be in equilibrium, the next fastest reaction is that of ozone, (2.3), with a time constant of tens of minutes. This

means that even if the transient behavior of the ozone concentration is to be calculated, the time step may be set as long as tens of seconds. As a consequence, the total number of calculations is reduced by a factor of ten thousand, that is, from one millisecond to ten seconds for  $\Delta t$ . The  $\Delta t$  was selected at about one second in the dynamical model, a value which is also appropriate for the chemical model used in the above manner.

In most cases, the calculation of equilibrium values of minor species, assuming that long-lifetime species concentration is quasi-constant, is sufficiently accurate compared to the direct numerical calculation. However, it fails to produce accurate results in cases where the system is not in equilibrium, such as at twilight [3]. In other words, this hybrid approach should be used when the time period of interest is about 30 minutes or longer. When the time period of interest becomes shorter than about 30 minutes, equation (2.3) should be numerically calculated for each  $\Delta t$ .

#### Geometric Effect

The geometric effect plays a very important role in modeling of the observables of the mesospheric airglow. To include this effect in the numerical models introduced thus far, the most straight-forward method is the numerical integration of appropriate quantities along the line of sight. Since the chosen spatial step of 100 meters is small enough to assume that most relevant physical quantities are constant within one cell, the approach can be further simplified. Instead of numerical integrations, appropriate quantities are summed. It has been found (Chapter II) that the geometric effect has

significant influences on many observables, a more detailed analysis of the effect is needed. Because off-zenith angle observations are often exercised, the geometric effect of oblique observations should also be examined. These considerations are detailed in the next chapter.

### Model Calculation Examples

In this section, several results of calculations utilizing the hybrid model introduced in the previous section are presented. The background physical quantities obtained by the MSIS model are used and the linearized equations (2.80), (2.81), (2.82) and (2.86) are numerically calculated. Outputs consist of integrated infrared emissions and intensity-weighted temperature along the vertical line of sight. The geometric effect for the vertical observation, therefore, is already taken into account. Note that the discussion of  $\eta$  which led to the equations (2.87) and (2.88) requires no numerical calculation with respect to time, since the integration involving the  $\exp(i\omega t)$  term is cancelled and does not appear in the latter equations. Calculations reported here demonstrate typical signal forms that are expected to be observed according to the numerical model.

The integration is implemented by adding the real part of the complex integrands in (2.80), (2.81) and (2.86), since the real part represents the physical entity. The phase term  $\exp i(\omega t - k_x x - k_z z)$  changes as time progresses, and, for the vertical line of sight,  $x$  is constant for all  $z$  so that, without a loss of generality,  $x$  can be set to 0. This term is now simply:

$$\nabla \cdot \underline{V} = (\cos(\omega t - k_z z) + i \sin(\omega t - k_z z)) \quad (3.4)$$

This equation plays a major role when off-zenith observations are simulated using the same numerical model. This is explained in detail in Chapter IV.

Fig. 3-4 presents several results. These examples demonstrate the geometric effect on the intensity fluctuation. The thickness of the hydroxyl layer is determined by the scale height of related chemical species, which is a function of temperature. The ratio of the layer's thickness to the vertical wavelength of an IGW dictates the modulation occurring in the integrated emission intensity. The modulation in temperature, however, is not affected in the same manner. The temperature fluctuation is influenced by the value of the stationary temperature, not by the ratio of the layer thickness to the IGW wavelength. This example demonstrates the geometric effect introduced in Chapter II under more realistic conditions. However, the result is consistent with the simplified model of Chapter II.

#### Long Range Dynamics of IGW

Because the origins of IGW's are believed to be distant from the mesospheric region where the observational data are taken, it is important to examine the characteristics of the excitation and the long range propagation of IGWs. Such an analysis will assist in predicting signal characteristics for ground-based optical observations. The models developed so far use monochromatic sinusoidal waves as input. It will be demonstrated in this section that waves found in

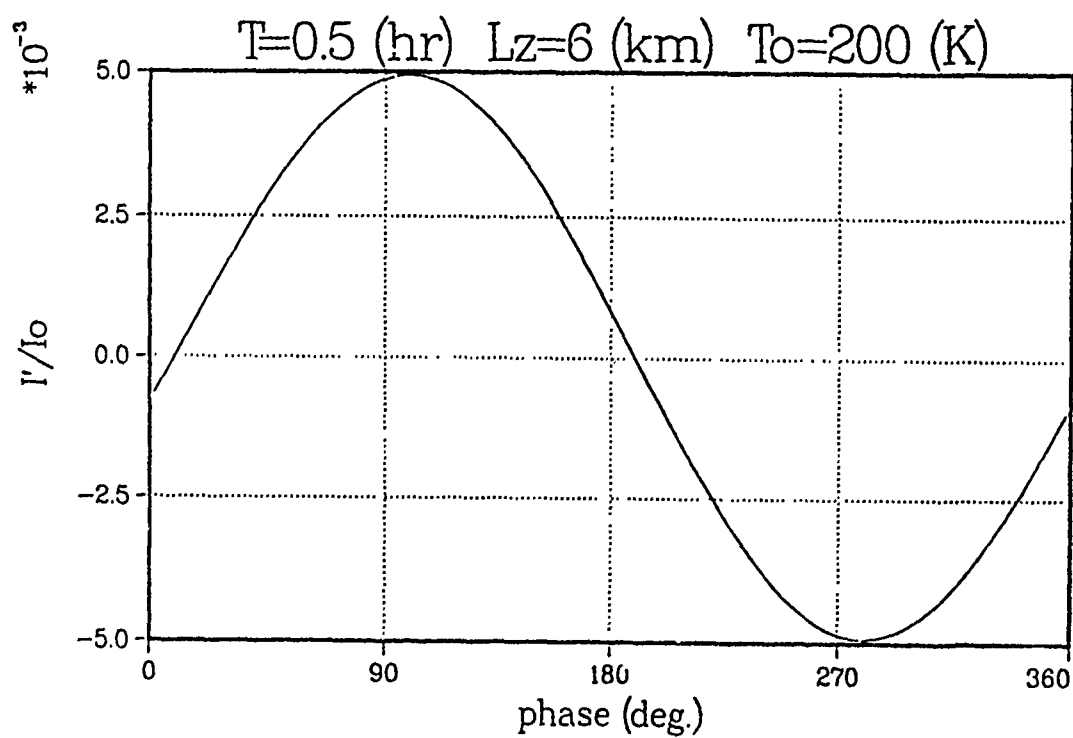
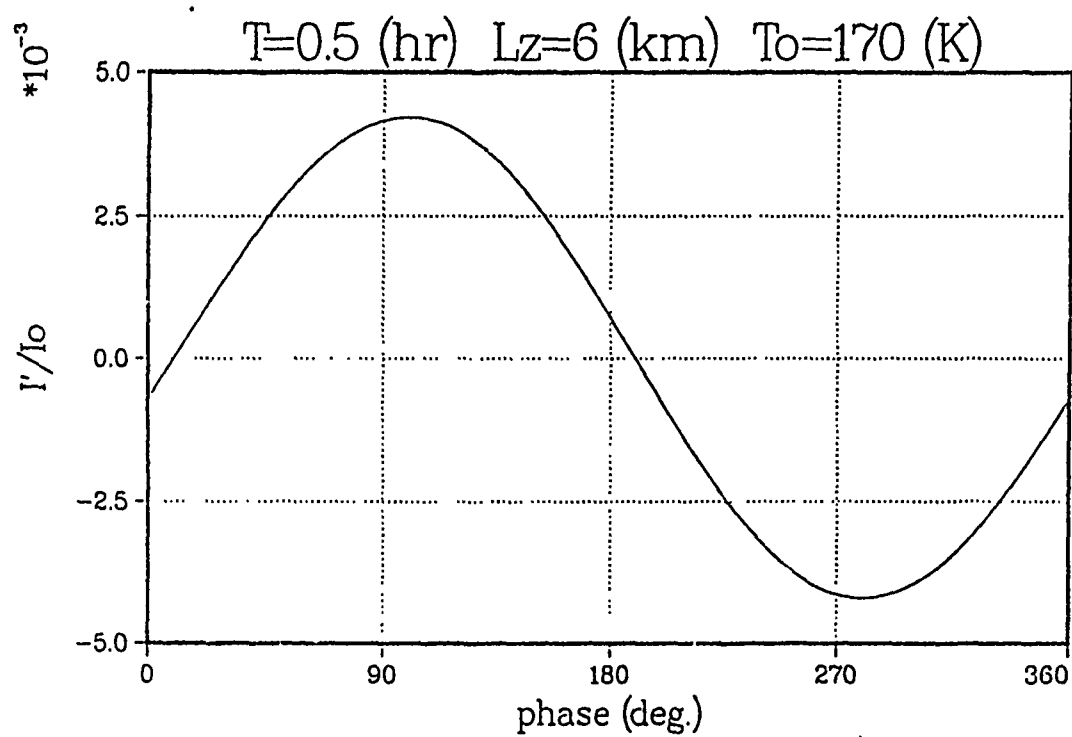


Fig. 3-4. Numerical model calculation

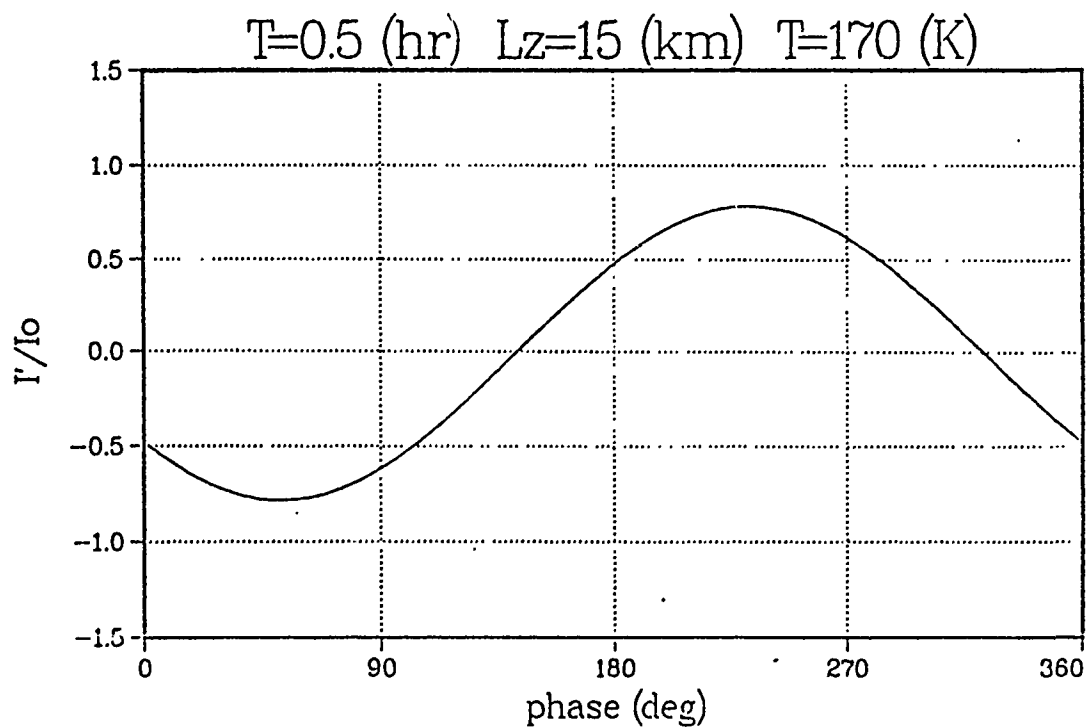
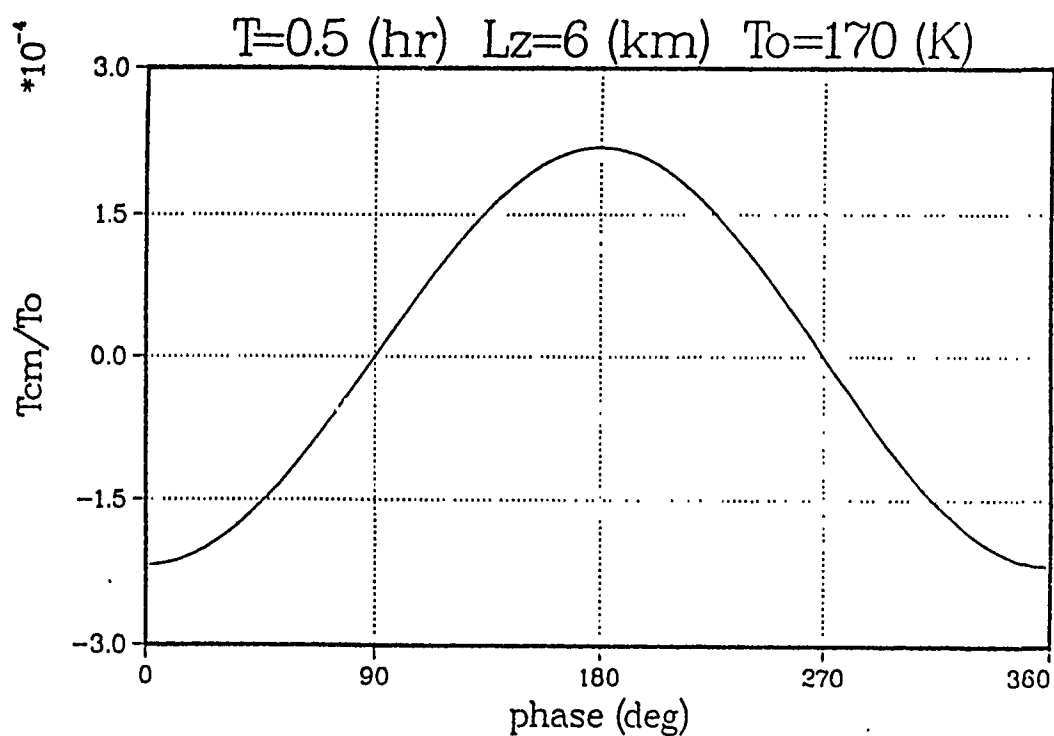


Fig. 3-4. Numerical model calculation (continued)

the mesospheric region are not likely to be monochromatic, unless the source of the IGW is a monochromatic sinusoidal oscillator. The signal characteristics are determined by the dynamics of the IGW generation and propagation, as well as by the geometrical configuration of the observation.

In this section, the effect of the dynamic propagation of an IGW is discussed by showing that the expected signal is chirp sinusoidal as a result of these mechanisms. Details of the geometric effect are left to Chapter IV.

The propagation of linearized IGWs summarized by Hines [18] is presented in Appendix A. Only the results are used here. In this model, the source of IGW is assumed to be in lower atmosphere - the upper troposphere or the lower stratosphere. In many cases, this source appears in the form of an atmospheric discontinuity, such as a front system, a (thunder) storm or strong winds colliding with tall mountains [5]. Once an atmospheric disturbance is generated, its energy propagates through the atmosphere at the packet velocity (Appendix A). In the course of propagation, the dispersion relation represented by equation (A.4) in Appendix A causes the wave packet to spread spatially. The separation occurs in the propagation packet speed according to the propagation direction and the oscillation frequency. Since the hydroxyl layer at the stationary state can be modeled to be flat at a constant altitude, the observable of ground-based optical measurement is the intersection of such a horizontal layer with the propagating wave. Note, however, that such an interaction can be observed as the local phase velocity. The packet



velocity can not be measured using a ground-based optical instrument with a small (1 degree or so) field of view. As shown in Appendix A, in cases in which IGWs are generated at low altitudes propagating with an upward packet velocity, the phase velocity is downward and the phase speed is greater than the packet speed. Consequently, the cross section of the airglow layer interacting with the IGW should appear as shown in Fig. 3-5. The slanted phase-plane interacting with an airglow layer, whose thickness is comparable with the vertical wavelength  $\lambda_z$ , causes the geometric effect.

Since the origins of many IGWs are forms of discontinuities, the generated signal is likely to contain broad-band frequency components. As depicted in Fig. 3-6, each frequency component has a unique "resonant direction," i.e. a direction towards which energy propagates faster than in other directions. The equations upon which the figure is based are introduced in the following section.

For each direction, a particular wave frequency component propagates faster than other frequency components, as depicted in Fig. 3-7 [18]. These properties indicate that after travelling several hundred kilometers, a wave packet which has close frequency components is likely to develop. The center frequency of each packet is a function of the direction of propagation.

Such wave frequency components are subject to the filtering effect of the temperature inversion, as described in Chapter II. Thus, only certain frequency components propagate through a temperature inversion and ultimately reach the airglow layer. Fluctuations produced by such wavepackets in the airglow layer are sinusoidal-like

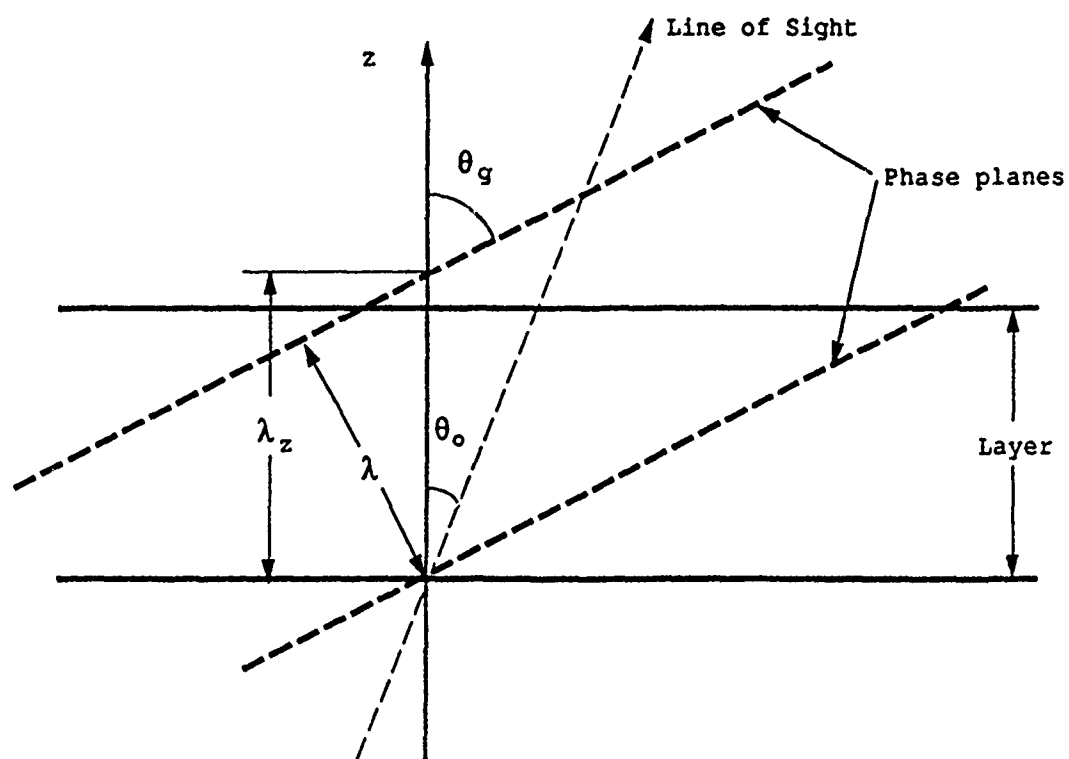


Fig. 3-5. IGW phase plane

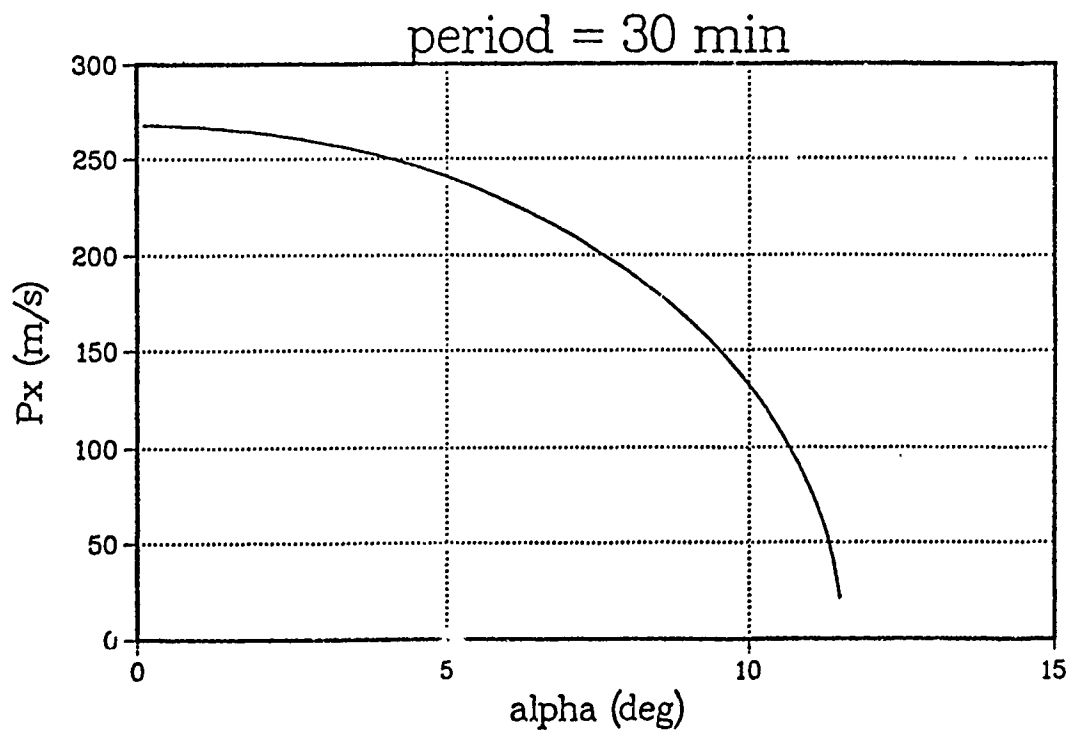
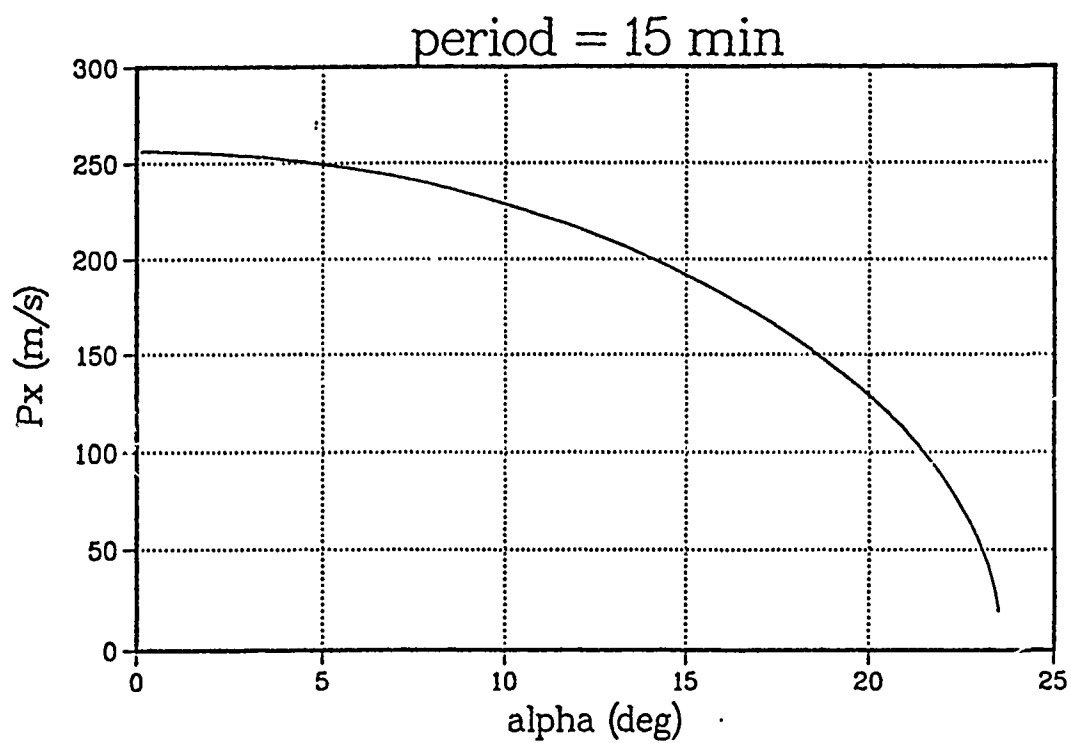


Fig. 3-6. Packet velocity vs. elevation angle

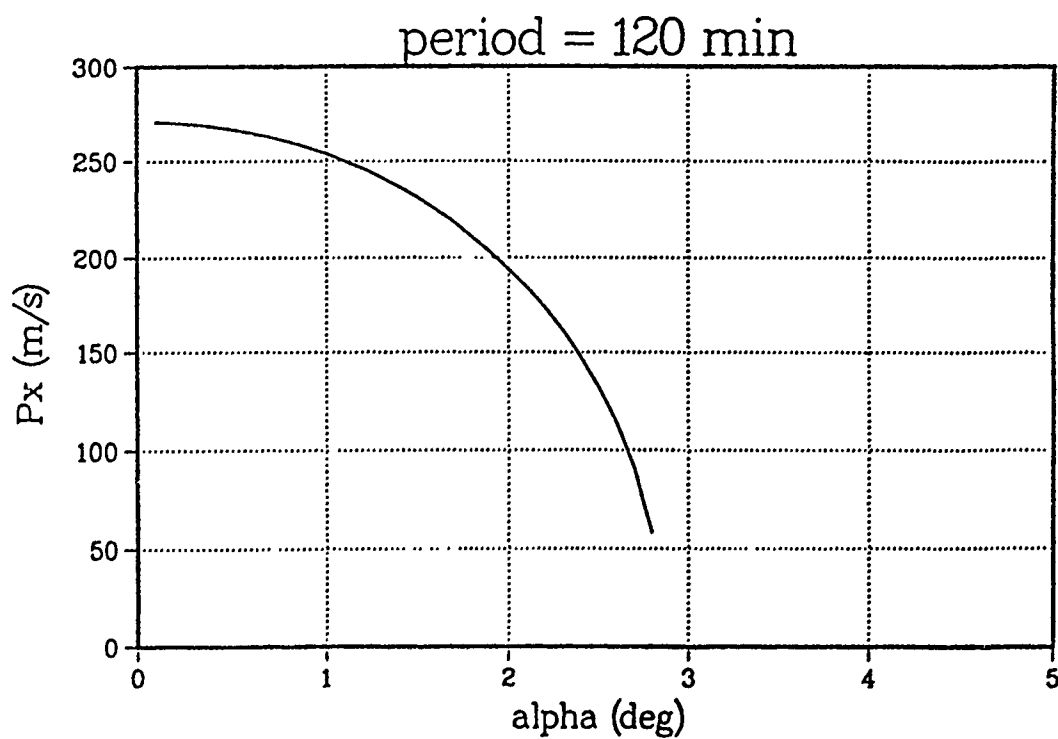
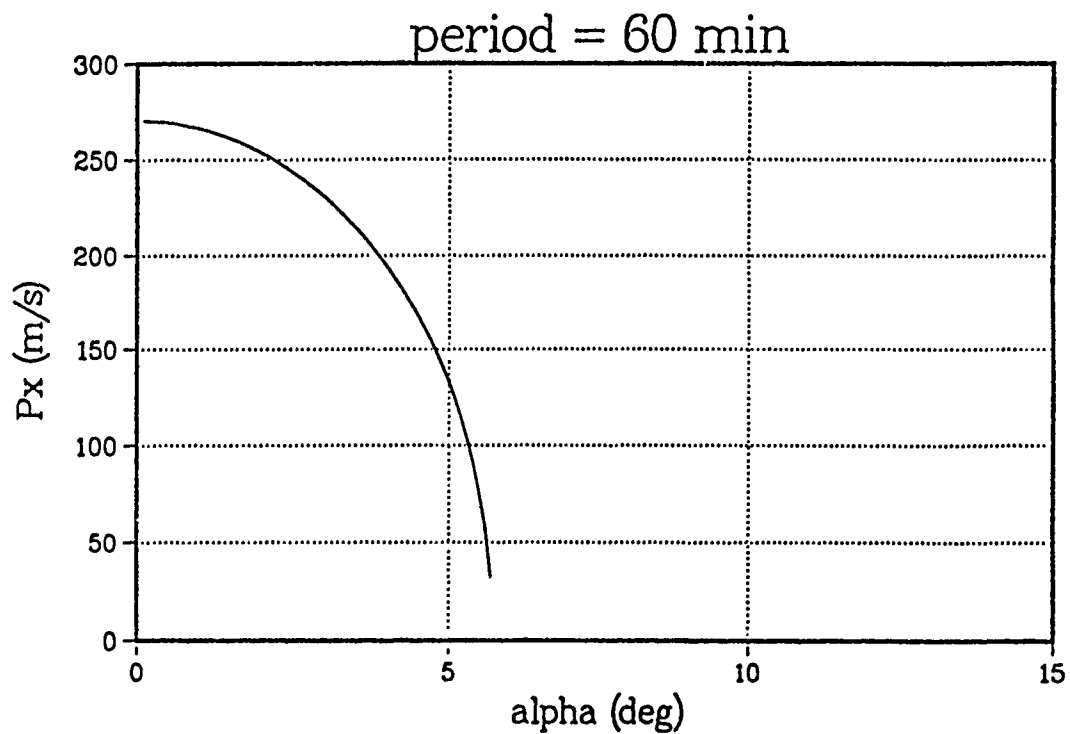
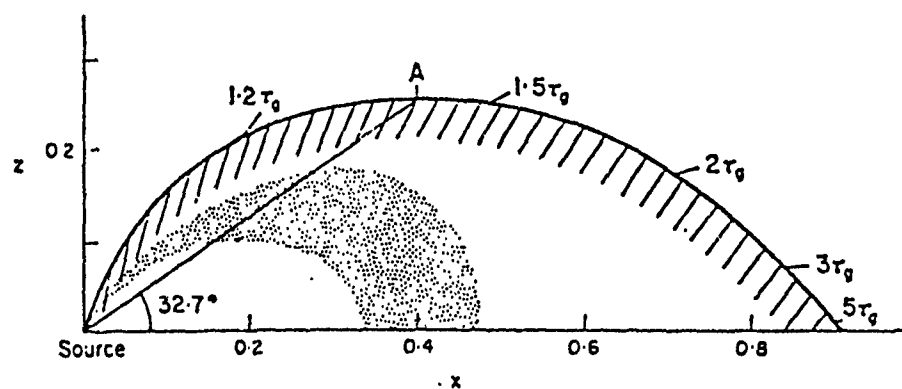


Fig. 3-6. Packet velocity vs. elevation angle (continued)



$\alpha$	$\omega/\omega_g$	$\Phi_A/C$	$\Phi_v/C$	$F_x/C$	$F_z/C$	$F/C$	$F_A/C$	$F_v/C$
0.0°	0.00	0.90	-1.22	0.90	0.00	0.90	0.00	1.22
0.4°	0.10	0.90	-1.21	0.90	0.01	0.90	0.90	1.13
1.8°	0.20	0.89	-1.19	0.88	0.03	0.88	0.91	1.02
4.3°	0.30	0.87	-1.16	0.85	0.06	0.85	0.92	0.89
7.7°	0.40	0.84	-1.12	0.80	0.11	0.80	0.94	0.74
13.7°	0.50	0.79	-1.09	0.71	0.17	0.73	1.00	0.58
21.3°	0.60	0.73	-1.06	0.58	0.23	0.63	1.32	0.41
32.7°	0.714	0.64	-1.05	0.40	0.26	0.48	$\pm \infty$	0.26
43.1°	0.80	0.56	-1.05	0.25	0.24	0.34	-0.51	0.16
58.3°	0.90	0.42	-1.10	0.09	0.16	0.18	-0.06	0.06
90.0°	1.00	0.00	-1.22	0.00	0.00	0.00	-0.00	0.00

Fig. 3-7. IGW dispersion relation [18]

oscillations with slowly changing frequency, often referred to as chirp signals (Fig. 3-8). Note that the quasi-monochromatic wave model can be still used cautiously in many cases, because the frequency usually changes only a few percent during one cycle. Also, experimental data are obtained only for a few cycles - in other words, the amount of observational data is small enough to be treated as monochromatic. Such slow frequency shifts are reported from observations [5].

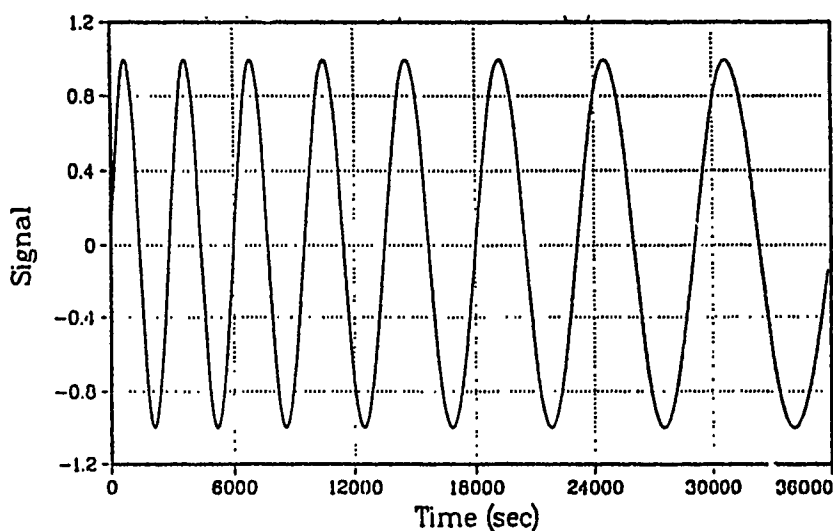


Fig. 3-8. Chirp signal

#### Model Results

The packet velocity  $\underline{P}=(P_x, P_z)$  at which a wave packet of frequency  $\omega$  propagates is:

$$P_x = \frac{\omega k_x (\omega^2 - \omega_g^2)}{\frac{\omega^4}{C^2} - k_x^2 \omega_g^2} \quad (A.14)$$

$$P_z = \frac{k_z \omega^3}{\frac{\omega^4}{C^2} - k_x^2 \omega_g^2} \quad (\text{A.15})$$

When this wave packet is propagating with the elevation angle  $\alpha$ , the following equation is also satisfied:

$$\tan \alpha = \frac{k_z}{k_x} \frac{\omega^2}{\omega^2 - \omega_g^2} = \frac{P_z}{P_x} \quad (\text{A.16})$$

When a wave packet has a constant propagation angle  $\alpha$ , the equation (A.14) can be used to calculate  $P_x$ , and then use of the relation  $P_z = P_x \tan \alpha$  yields  $P_z$ . In order to calculate  $P_x$  for a given  $\omega$ ,  $k_x$  needs to be known. This can be accomplished by solving equations (A.4) and (A.16), which yields:

$$(\omega^2 - \kappa \omega_g^2) \frac{\omega^2}{C^2} + \omega_g^2 k_x^2 - \omega^2 k_x^2 \left( 1 + \frac{(\omega^2 - \omega_g^2)^2}{\omega^4} \tan^2 \alpha \right) = 0 \quad (3.5)$$

where  $\kappa = \omega_a / \omega_g \approx 1.225$  [18]. For a given  $\omega$ ,  $k_x$  is calculated numerically using (3.5), and with the  $\omega$  and resultant  $k_x$ , (A.14) can be calculated numerically. Solving (3.5) for  $k_x$  yields:

$$k_x^2 = \frac{\omega^4}{C^2} \frac{(\omega^2 - \kappa \omega_g^2)}{(\omega^2 - \omega_g^2)(\omega^2 + (\omega^2 - \omega_g^2) \tan^2 \alpha)} \quad (3.6)$$

For an IGW,  $\omega < \omega_g$ . Therefore, for  $k_x$  to be algebraically real,  $\omega^2 + (\omega^2 - \omega_g^2) \tan^2 \alpha > 0$ . This can be rewritten, in terms of the wave period  $T = 2\pi/\omega$  and  $T_g = 2\pi/\omega_g$  as:

$$T^2 < T_g^2 \left( 1 + \frac{1}{\tan^2 \alpha} \right) \quad (3.7)$$

This constraint indicates that for a given wave propagation angle there is a maximum possible oscillation period, or minimum frequency, for physically allowed IGW. Fig. 3-9 plots the maximum period given

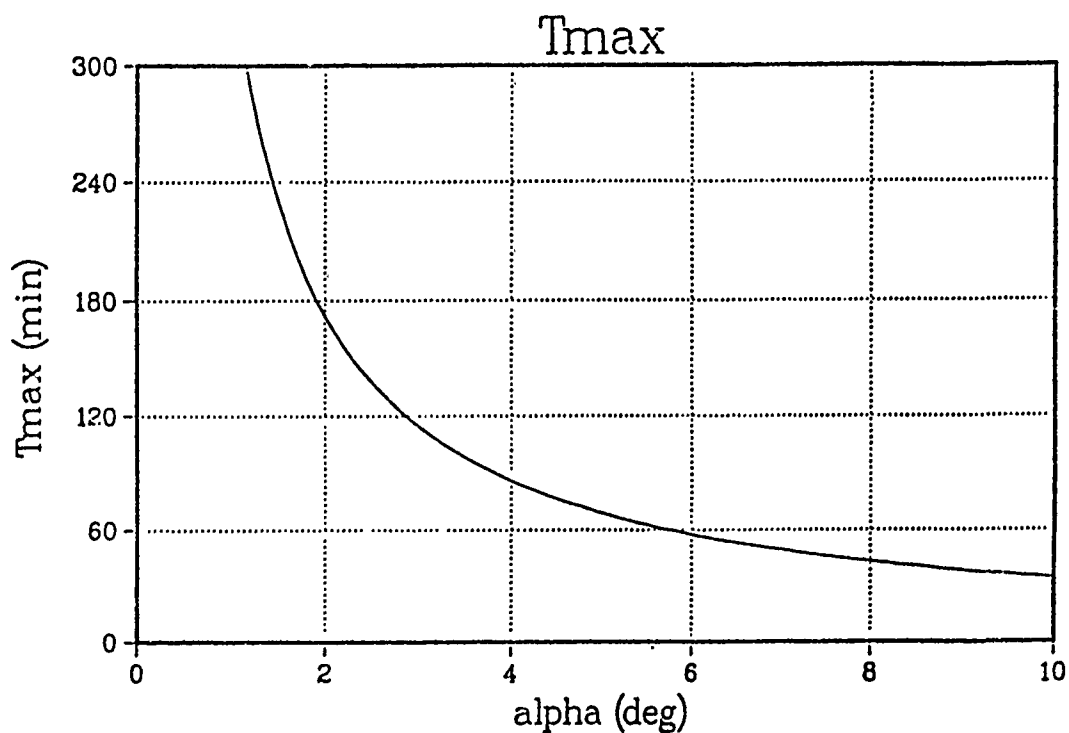


Fig. 3-9. Limiting period and elevation angle



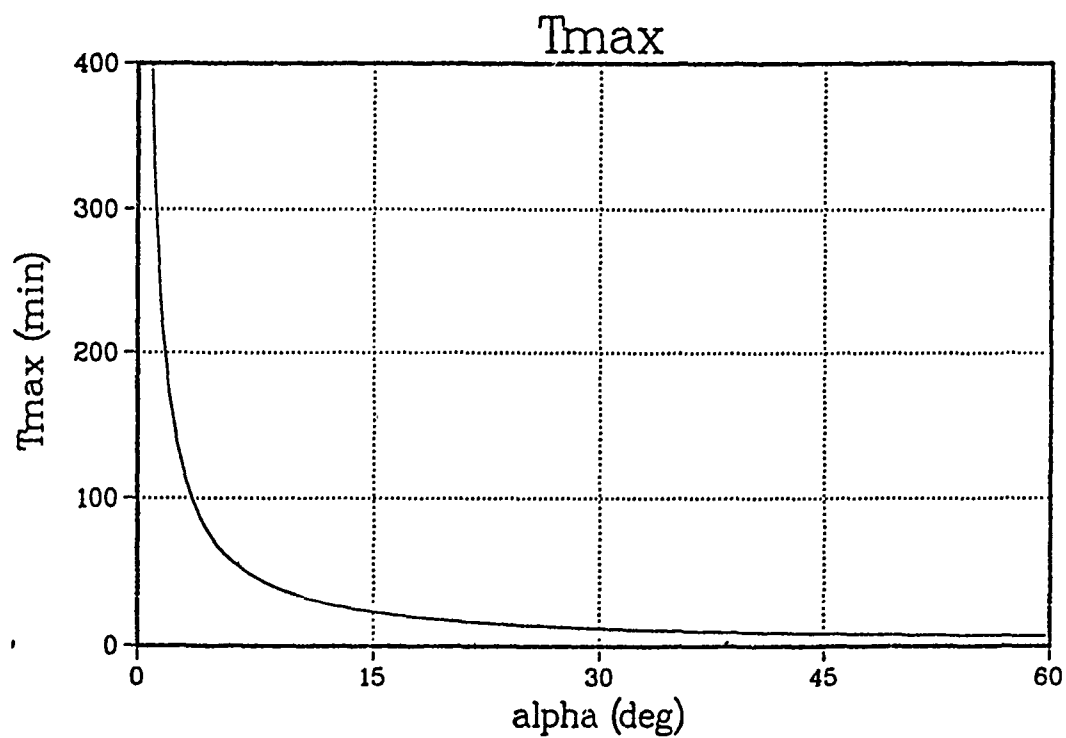
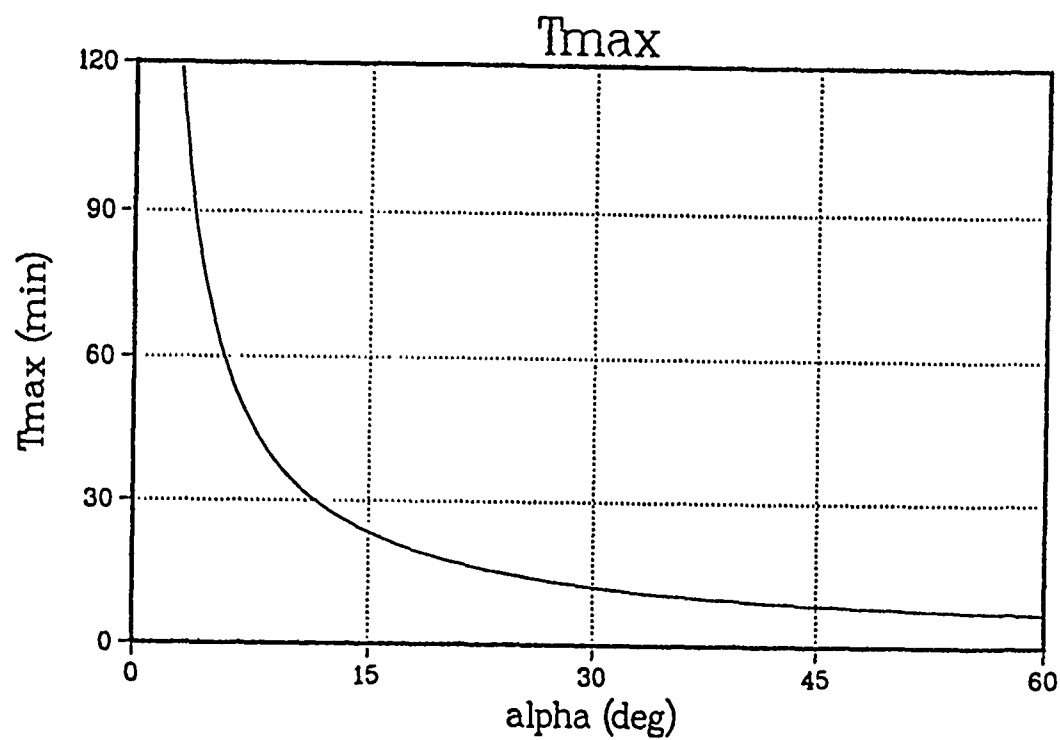


Fig. 3-9. Limiting period and elevation angle (continued)

by the right hand side of equation (3.7),  $T_{\max}$ , versus  $\alpha$ ; the same function is plotted in several different scales. For each  $\alpha$ , any wave component with a period smaller than  $T_{\max}$  can propagate. Any wave component with a period larger than  $T_{\max}$  can not propagate at the angle  $\alpha$ . In other words, all frequency components have upper limits of elevation angle  $\alpha$ , represented in the right hand side of equation (3.7).

Fig. 3-10 shows several calculated values of  $P_x$ . Each frame is a plot of wave packet speed  $P_x$  as a function of wave frequency, represented in period  $T=2\pi/\omega$ . The ascent angle  $\alpha$  varies from frame to frame.

The time  $T_x$  for a wavepacket with speed  $P_x$  to reach at distance  $L_x$  is  $L_x/P_x$ . The observation of an IGW takes place at a layer of altitude  $h$ . Using the right hand side of equation (3.7), the distance between the wave source and the observation location can be calculated by  $L_x=h/\tan \alpha$ . Table VIII is an example of  $\alpha$  and calculated  $L_x$ .

Fig. 3-11 is a plot of the frequency variation resulting from the interaction between an IGW and a horizontal layer at an altitude of 85 km. One important feature is that at each moment, there are two  $\omega$  values. This indicates that, except for the frontal frequency (i.e. the frequency that reaches to the observation location first) a pair of frequencies may be observed.

Also, the frequency change rate is a function of frequency (Fig. 3-11). For each  $\alpha$ , there are two cut-off frequencies: the Brunt-Vaisala frequency at the short period limit and the limiting frequency corresponding to the limiting period  $T_{\max}$  represented by the

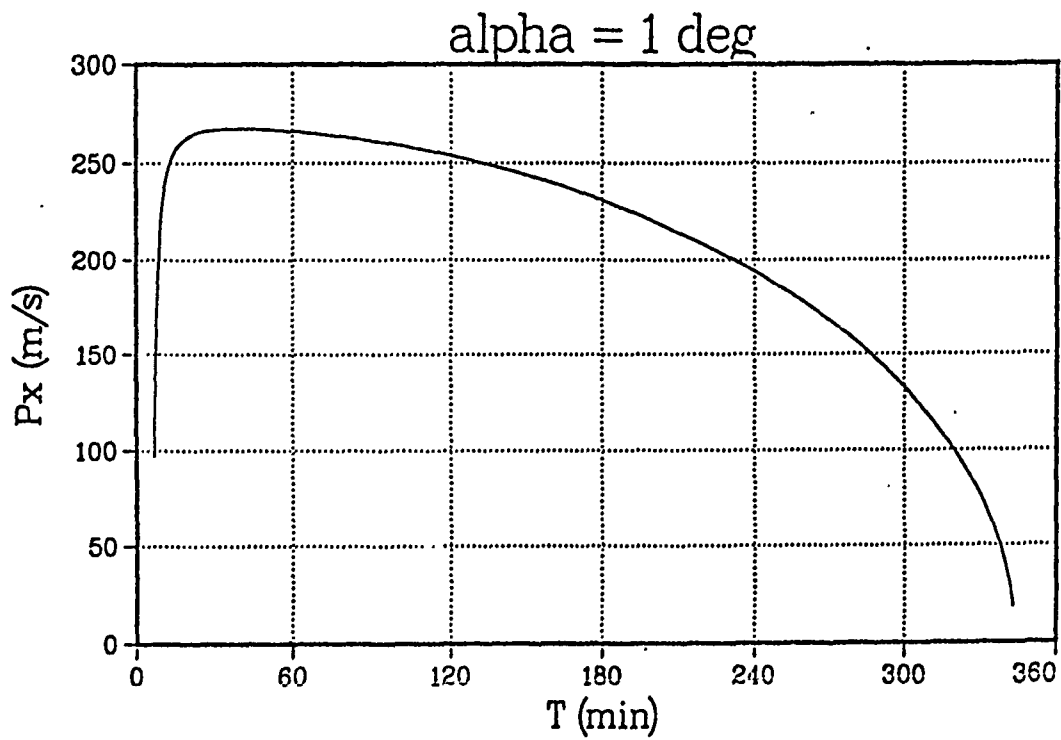
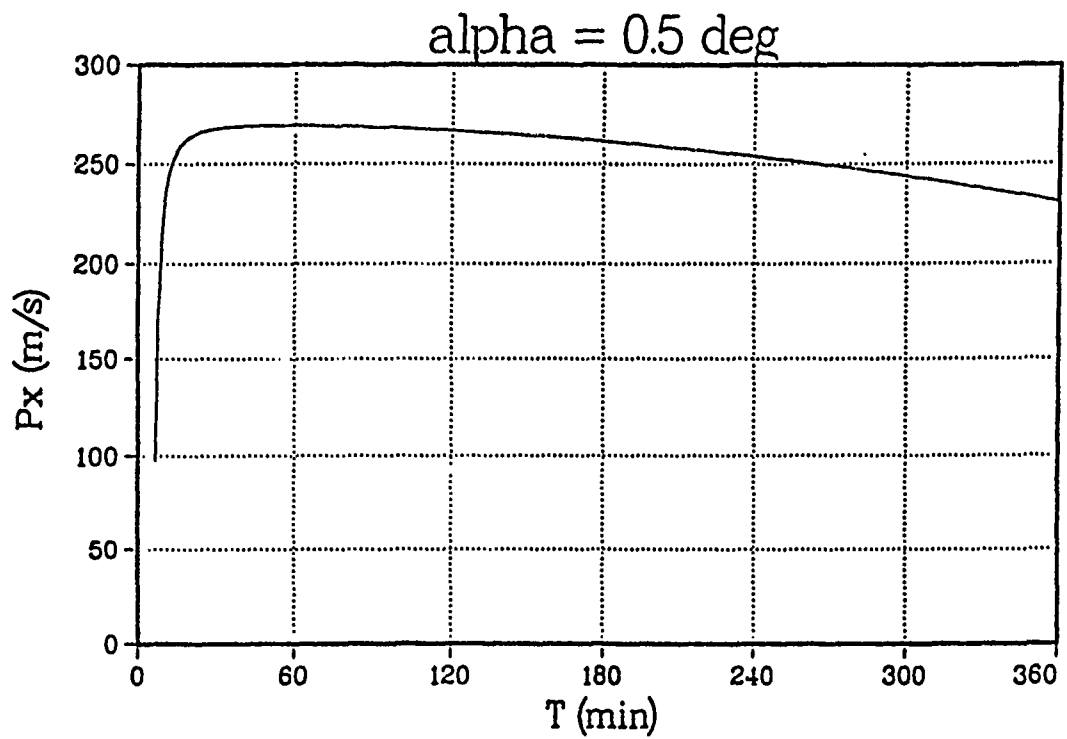


Fig. 3-10. Packet velocity

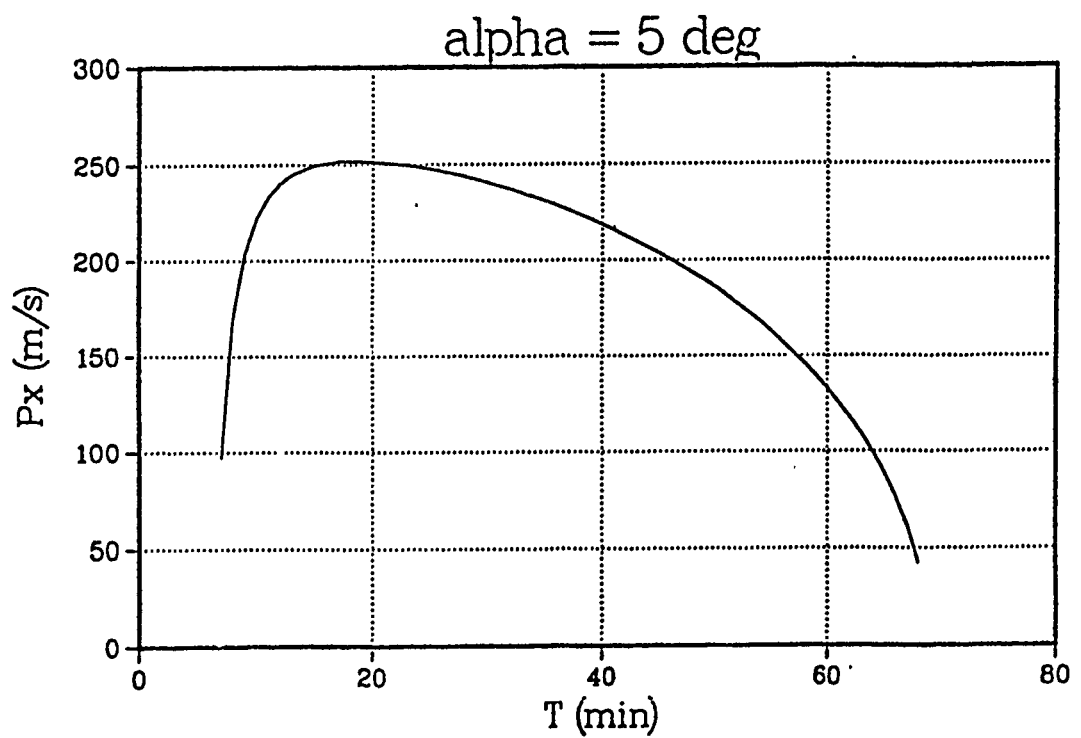
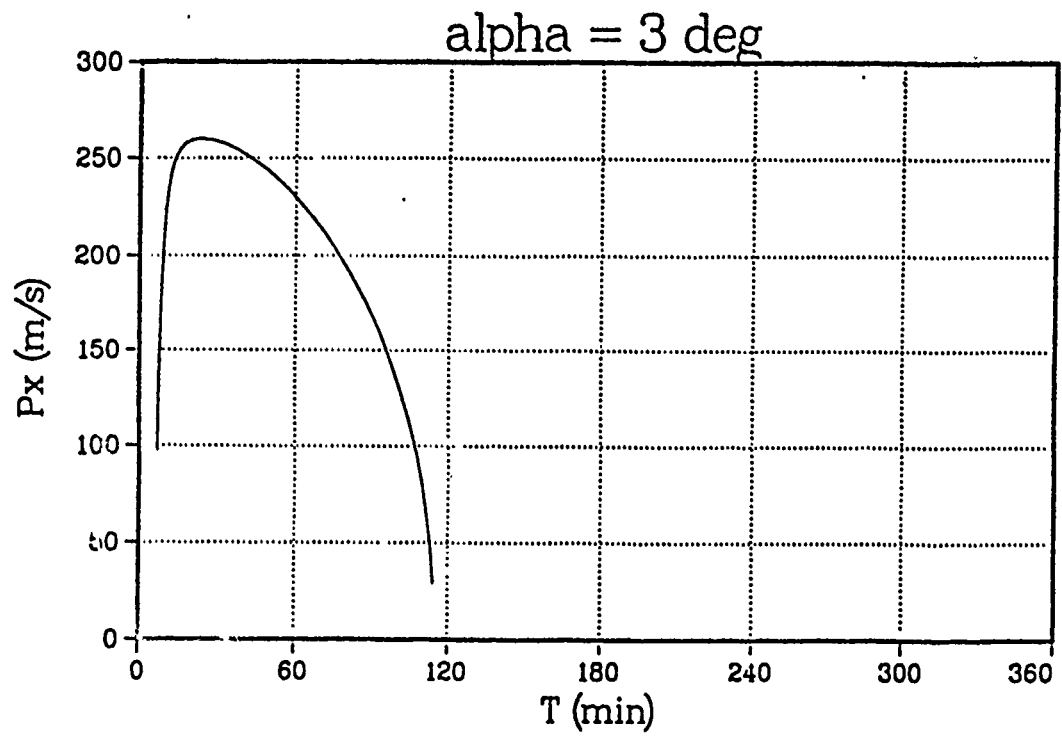


Fig. 3-10. Packet velocity (continued)

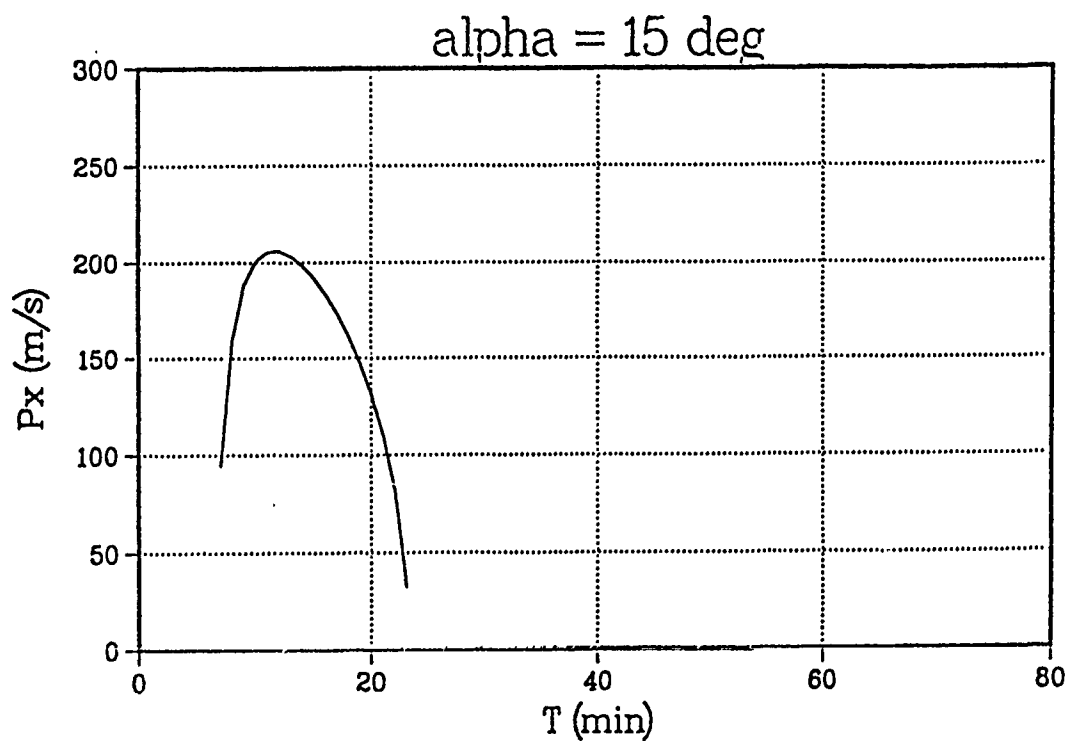
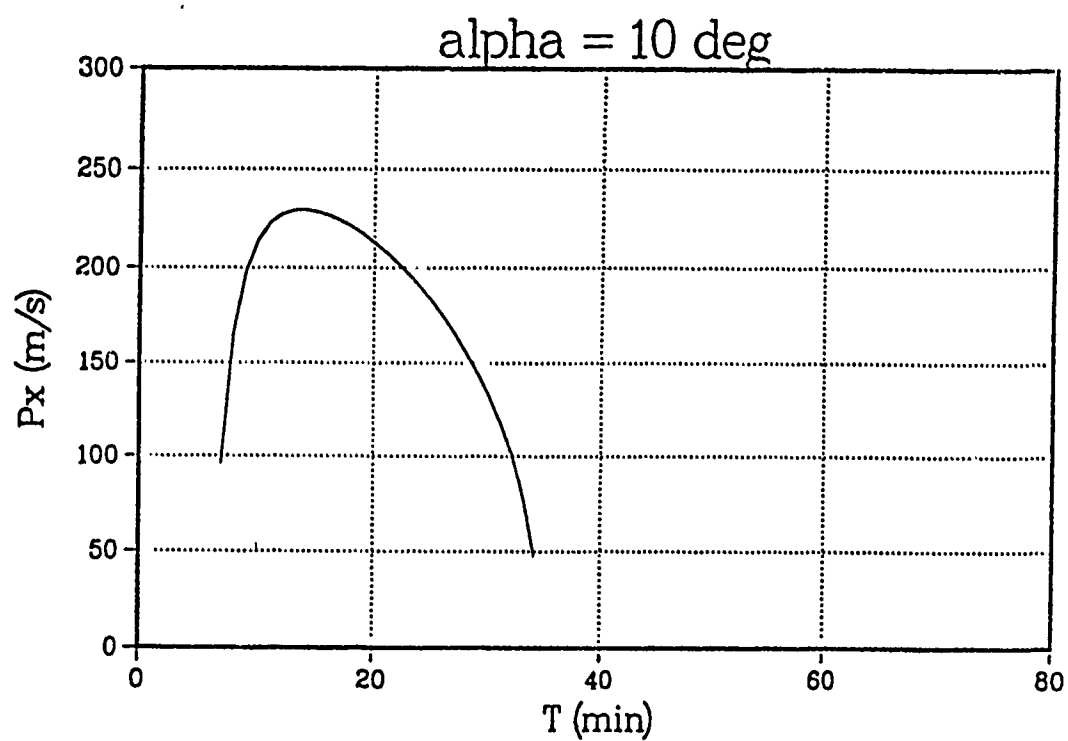


Fig. 3-10. Packet velocity (continued)

TABLE VIII  
Limiting T and  $L_x$  as a Function of  $\alpha$

$\alpha$ (deg)	limiting T (min)	$L_x$ (km)
15	23	317
10	34	482
5	68	972
4	86	1216
3	114	1622
2	171	2434
1	343	4870
0.5	687	9740

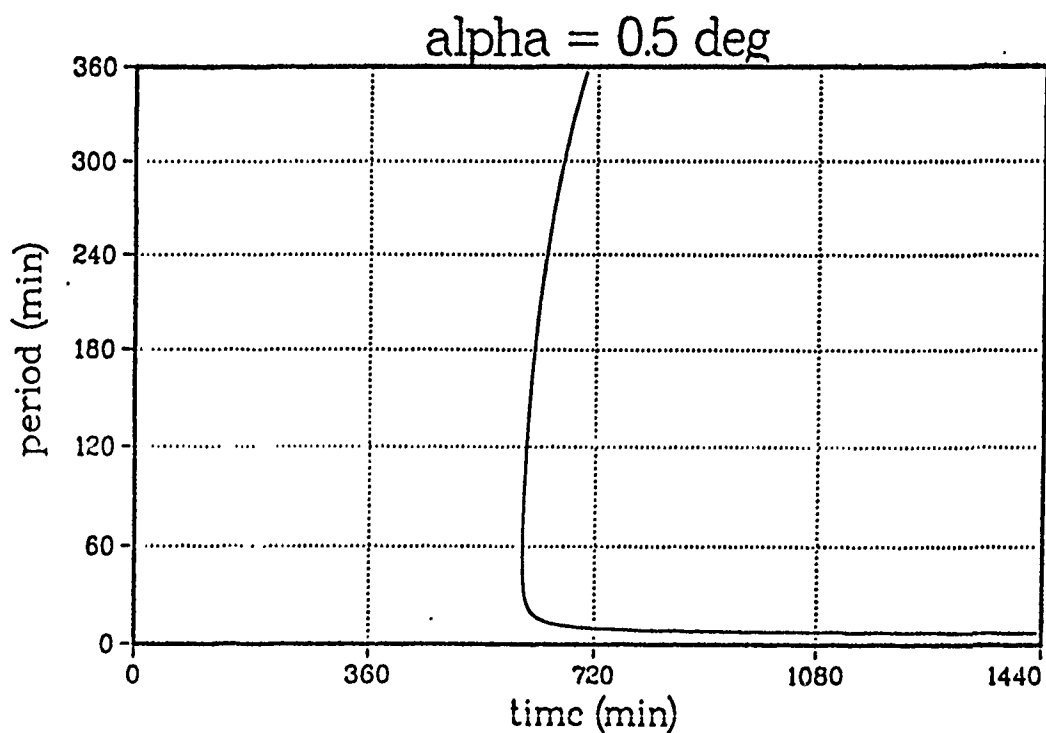


Fig. 3-11. Frequency chirp (shown with period)

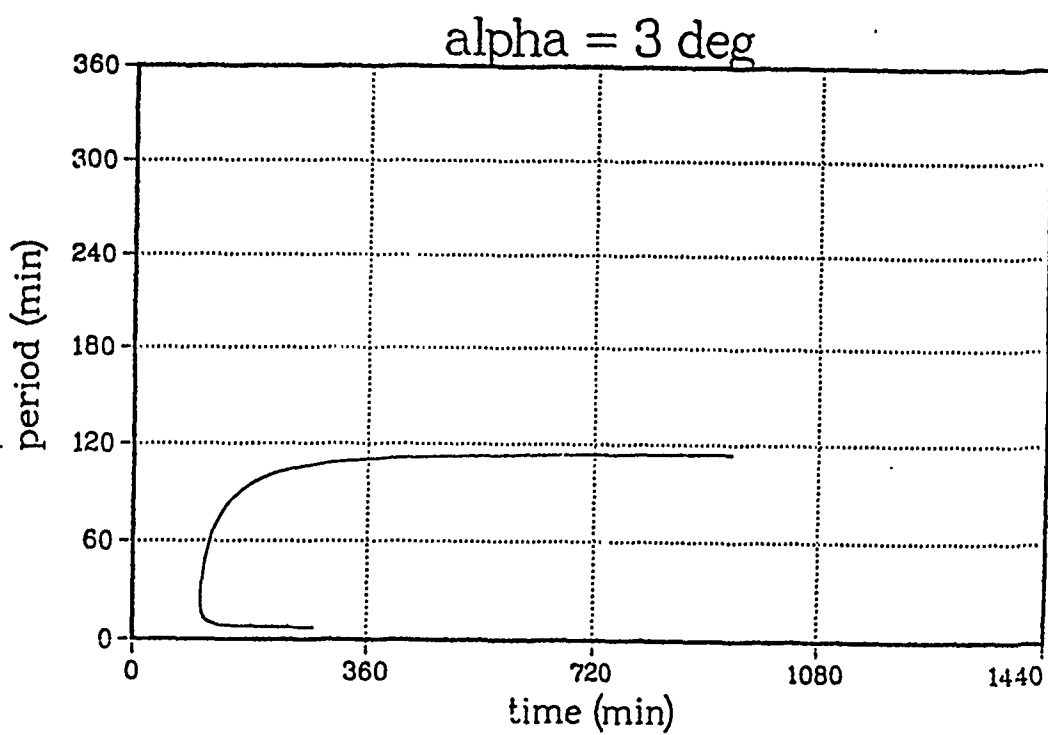
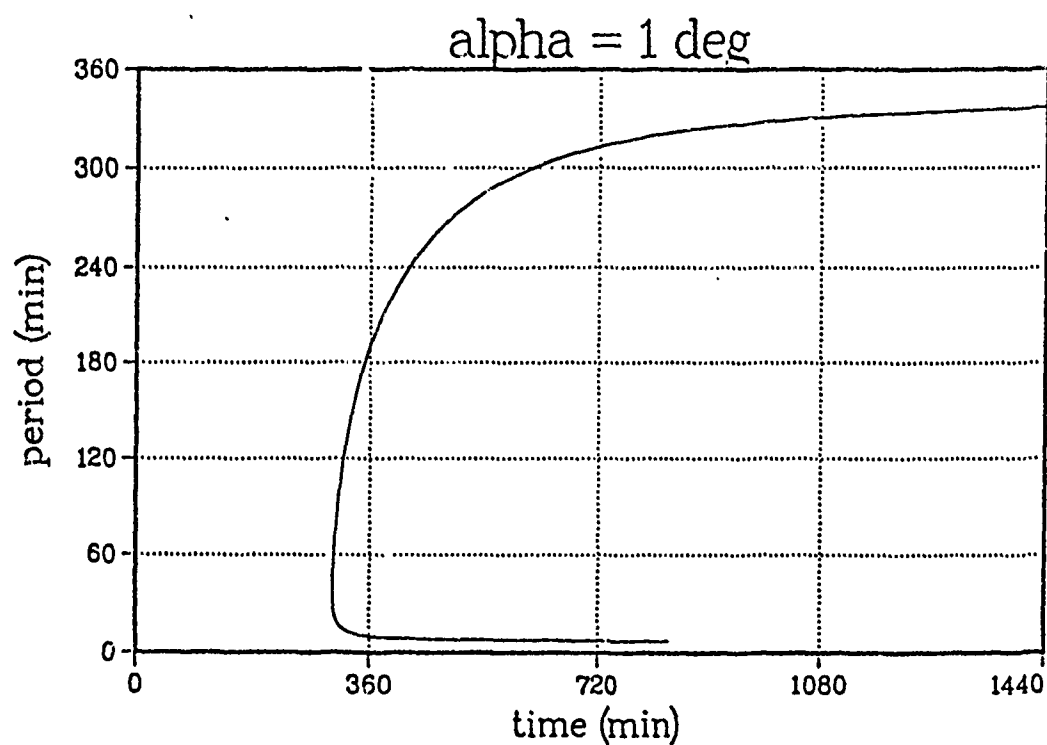


Fig. 3-11. Frequency chirp (shown with period) (continued)

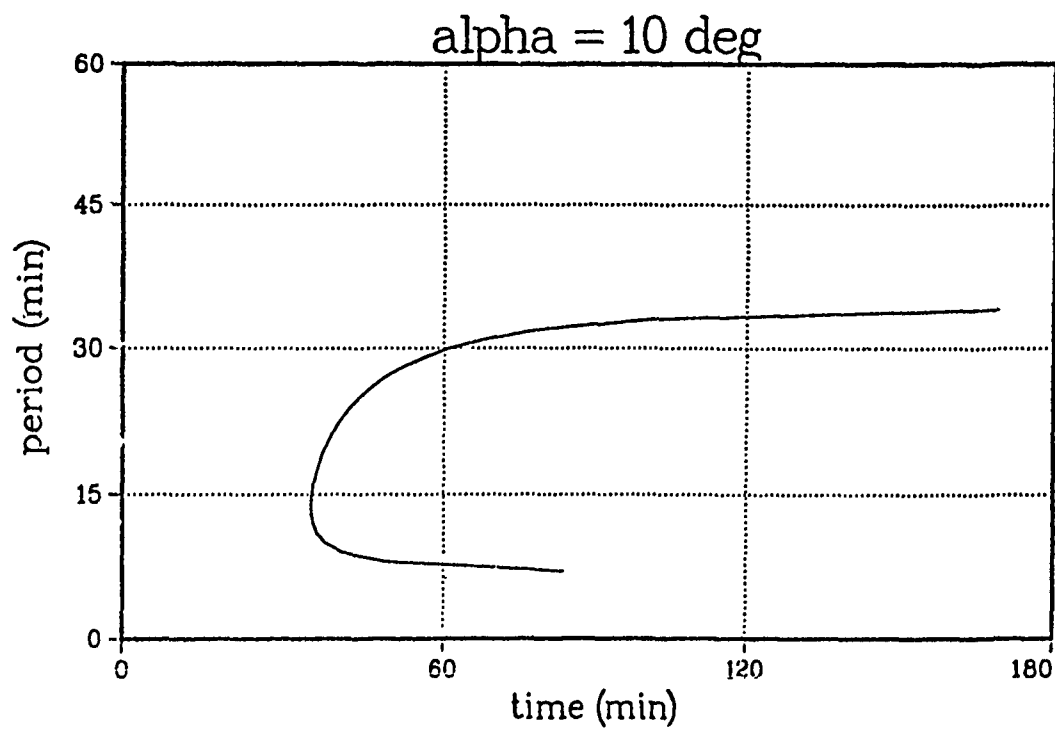
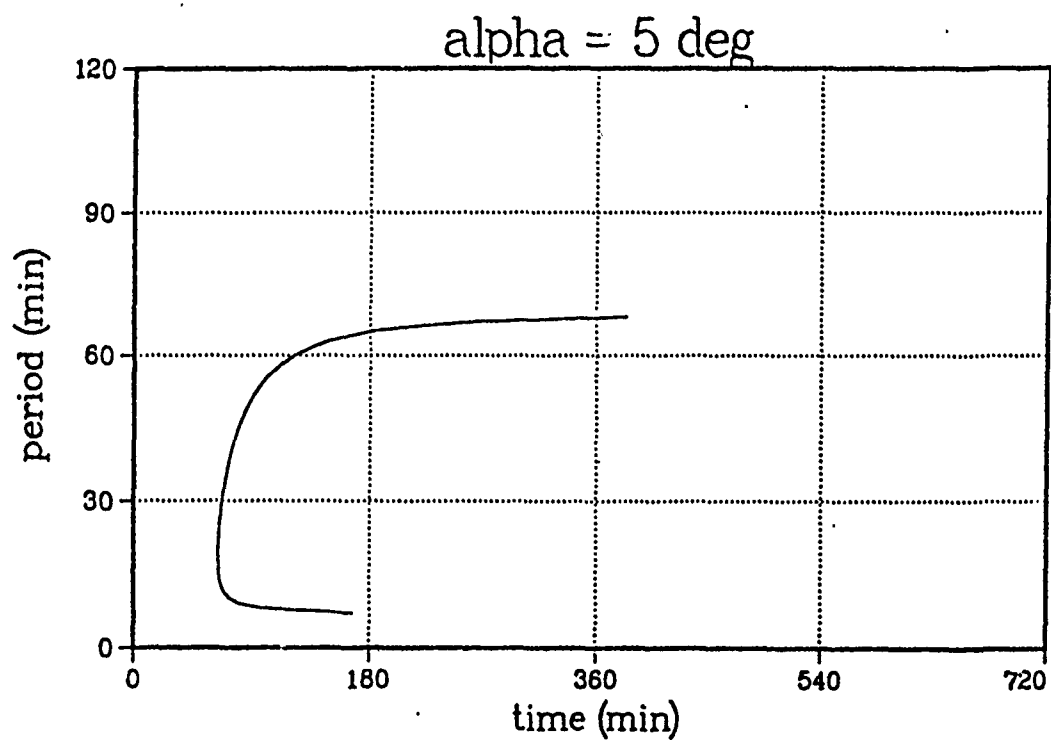


Fig. 3-11. Frequency chirp (shown with period) (continued)



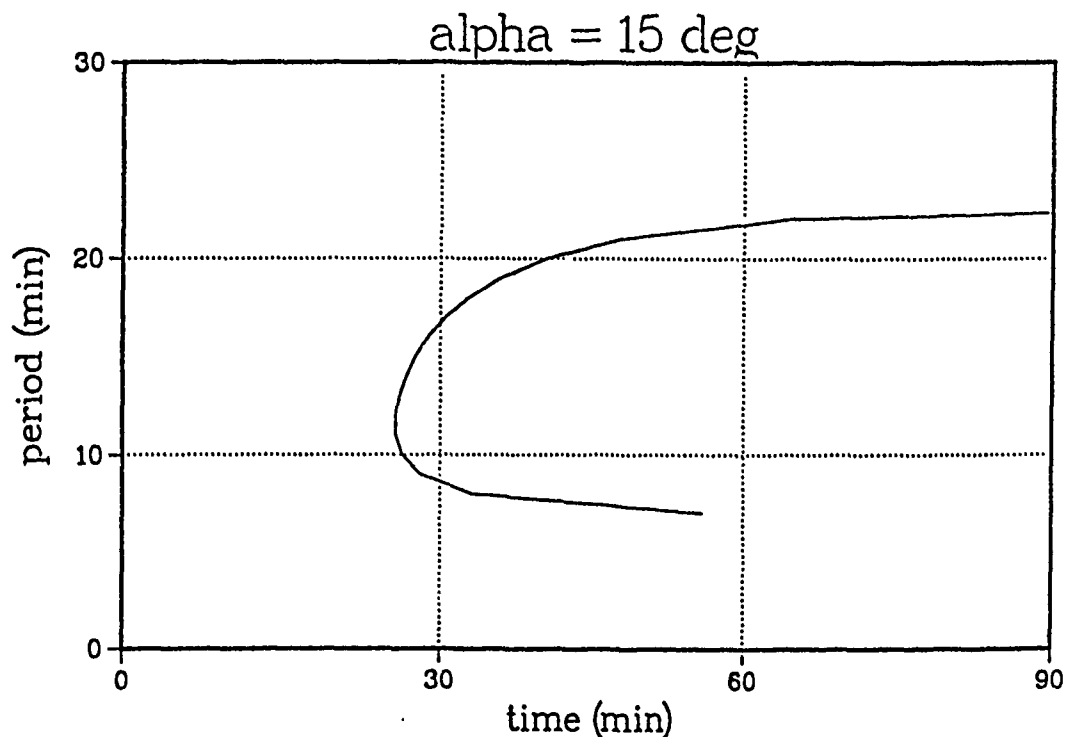


Fig. 3-11. Frequency chirp (shown with period) (continued)

right hand side of equation (3.7), as plotted in Fig. 3-9. The frequency change rate is maximum at the frontal frequency and becomes moderate at its neighboring frequencies. As time passes, the frequencies become almost constant, corresponding to low and high limiting frequencies.

These results indicate that an IGW which was generated in a distant low atmosphere and has propagated to the mesosphere is likely to chirp. It is therefore necessary to construct a system which will process such signals. Such a system is developed in Chapter V, and evaluated in Chapter VI.

## CHAPTER IV

## GEOMETRIC EFFECT

In this chapter, the geometric effect is studied in detail. This effect, introduced in Chapter II in a very simplified manner, has been shown to have a significant effect on observables; the airglow emission intensity and the rotational temperature. Also included in this chapter is the geometric effect of the off-zenith observation.

Geometric Effect Model

Among the several ways to calculate the observables of interest using a model with geometric effect taken into account, one straightforward method involves the numerical integration of appropriate quantities along the line of sight. The two observables of interest are the infrared airglow emission intensity, or the radiance, and the rotational temperature (Chapter V and Appendix B). The rotational temperature can be assumed to be identical to the kinetic temperature of the major species of the emission layer region, if the time scale of interest is at least a few seconds. When integrated through altitude, however, the observed kinetic temperature is not always identical to the observed rotational temperature. This occurs because the rotational temperature is calculated from the observed distribution of intensities of the vibrational-rotational spectral lines, and each spectral line is integrated through the line of sight independently. The rotational-line intensity is a function of the total emission intensity and kinetic temperature. Since the airglow layer

density and kinetic temperature change independently in real atmosphere, distribution of the integrated line intensity does not correspond to any total intensity and kinetic temperature combination. For comparison purpose, both the observed kinetic temperature and the rotational temperature are calculated according to the geometric effect. The discrepancy between the two temperature is then demonstrated.

The formulae for the integration through altitude are:

$$I_{\text{obs}}(t) = \int_0^{\infty} I(z,t) dz \quad (4.1)$$

$$I(z,t) = \sum_{i=1}^9 ([OH_i^*(z)] \sum_{j=1}^{i-1} A(i,j)) \quad (4.2)$$

$$T_{\text{obs}}^{\text{kin}}(t) = \int_0^{\infty} T(z,t) I(z,t) dz \quad (4.3)$$

where "kin" stands for kinetic, "obs" stands for observable, or observed. These formulae represent the same principle used in the introduction of the geometric effect in Chapter II.

The method of extending the calculations for the above formulae to off-zenith observation cases is based upon the Hines model introduced by equations (2.72) and (2.73). The basic principle was to convert the variable from the actual altitude  $z$  to its stationary altitude  $\zeta$ . This method assumes monochromatic sinusoidal gravity wave input. The

first step involves calculating amplitudes of the fluctuation in the concentration of the major species and the kinetic temperature for each  $\zeta$  using the Hines model. Using those amplitude and the desired vertical wavenumber, the temperature and the concentration for each  $\zeta$  at time  $t$  are calculated. This can be done by multiplying the term:

$$\exp(i(\omega t - k_x x - k_z z)) \quad (4.4)$$

to the integrand for each  $\zeta$  derived by the model, then adding the real parts of the resultant complex values according to equations that are converted from (4.1), (4.2) and (4.3), changing  $z$  to  $\zeta$  to obtain the desired quantities. The equations are (2.80), (2.81), (2.82) and (2.86). The theoretical  $\eta$  can be calculated by (2.88). Later sections demonstrate that this method allows a simple extension of the Hines model to a case of off-zenith observation.

#### Geometric Effect on Rotational Temperature

There are several ways to calculate the rotational temperature from the spectral line data. One of such methods is to fit a temperature to two of such line data according to the following formulae [10]:

$$T_{\text{obs}}^{\text{rot}}(t) = \frac{(hc)(E_{j1} - E_{j2})}{\ln\left(\frac{I_{j1} A_{j2}}{I_{j2} A_{j1}}\right)} \quad (4.5)$$

$$I_{ji} = \int_0^{\infty} A_{ji} [OH_{v'ji}]^* dz \quad (i=1,2) \quad (4.6)$$

$$A_{ji} = A_{v'ji v''ji} \quad (i=1,2) \quad (4.7)$$

where  $I_{ji}$  is the rotational line intensity of the emissive transition from  $(v'ji)$  to  $(v''j'')$ ,  $E_{ji}$  is the energy level of the  $v'ji$  state represented in the unit of  $\text{cm}^{-1}$ .  $A_{ji}$  is its Einstein coefficient for the emissive transition and  $j1$  and  $j2$  are two different rotational levels with the same upper vibrational level. These formulae are based upon the theoretical spectral form of [9], [10]:

$$I(N_{v'}, T, \nu_{ii'}) = \frac{N_{v'} \nu_{ii'}^3 S_{ii'}}{\sum_{j=1/2} (2j+1) \exp(-E_j/\kappa T)} \exp(-E_i/\kappa T) \quad (4.8)$$

where  $I$  is the volume emission rate (Rayleigh) of the emission line of the wavenumber  $\nu_{ii'}$  ( $\text{cm}^{-1}$ ),  $i$  and  $i'$  denote the upper and lower rotational state, at temperature  $T$  (K) with the number density of the upper vibrational state hydroxyl  $N_{v'}$  ( $\text{cm}^{-3}$ ).  $S_{ii'}$  is the line strength and the denominator of (4.7) is the partition function for the upper vibrational state. Theoretical values with the corrections using the observed data should be used for parameters  $\nu_{ii'}$ ,  $S_{ii'}$  and  $E_j$ . Such data are available from several sources [9], [29], [30]. In this study, the data developed at Utah State University based upon Meis model is used [29].

Another way to calculate the rotational temperature is to fit a temperature to more than three pairs of  $E_{j'}$  and  $\ln(I_{j'}A_{j'})$  where  $j'$  represent different rotational levels of the same upper vibrational level  $v'$ . The fitting of the temperature can be done with the least-square technique [31]. This section demonstrates that a large fitting error could result even from data with a high signal to noise ratio, when the geometric effect is taken into account.

The least-square fitting of form  $y=ax+b$  to the data  $(x_i, y_i)$  with the standard deviation error for  $(y_i)$  being  $(\sigma_i)$  ( $i=1, N$ ) has a form [32]:

$$a = \frac{S_{xx}S_y - S_xS_{xy}}{\Delta} \quad (4.9)$$

$$b = \frac{SS_{xy} - S_xS_y}{\Delta} \quad (4.10)$$

with the standard deviation error estimate

$$\sigma_a = \frac{S_{xx}}{\Delta} \quad (4.11)$$

$$\sigma_b = \frac{S}{\Delta} \quad (4.12)$$

where

$$\Delta = SS_{xx} - (S_x)^2 \quad (4.13)$$

$$\begin{aligned}
S &= \sum_{i=1}^N \frac{1}{\sigma_i^2} & S_x &= \sum_{i=1}^N \frac{x_i}{\sigma_i^2} & S_y &= \sum_{i=1}^N \frac{y_i}{\sigma_i^2} \\
S_{xx} &= \sum_{i=1}^N \frac{x_i^2}{\sigma_i^2} & S_{xy} &= \sum_{i=1}^N \frac{x_i y_i}{\sigma_i^2} & & (4.14)
\end{aligned}$$

In case of the rotational temperature calculation, the data pair (x,y) should be  $x=hcE_j/k$  and  $y=\ln(I_j/\nu_{jj}'S_{jj}')$ . The linear fitting can then provide appropriate temperature-error estimates.

Both the two-lines method and the least-square fit method assume that the rotational emission lines are results of infrared emitting hydroxyl volume of a single temperature. This is not the case in a ground-based passive observation, when there is a temperature difference within the emitting layer. This is apparent from (4.6) and (4.8) combined into the following formula:

$$\begin{aligned}
I_{ji} &= \int_0^\infty I(N_{v_i}(z), T(z), \nu_{ji}) dz \\
&= \int_0^\infty \frac{N_{v_i}(z) \nu_{ji}^3 S_{ji}}{\sum_{j=1/2}^\infty (2j+1) \exp(-E_j/\kappa T(z))} \exp(-E_j/\kappa T(z)) dz & (4.15)
\end{aligned}$$

For comparison, both the brightness-weighted temperature and the rotational temperature calculated from the integrated rotational lines are presented in the next section.

The significance of the temperature change in the emission layer and the emission layer profile, represented by  $T(z)$  and  $N_v(z)$  in the numerator of (4.15), is demonstrated using the computer model. This model provides the integrated line intensities for each rotational line according to (4.15) and the rotational temperature estimate according to the least square fit. The model also provides the intensity weighted kinetic temperature according to (4.3). For the emission-layer profile, the results of the Gaussian distributions with different variance above and below the peak and the distributions derived from MSIS are compared. The kinetic temperature profile, parabolic profile with different coefficients and profile derived by MSIS are used and compared. The resultant geometric effects are shown quantitatively.

In this model, the volume emission rate profile is defined as:

$$[OH(z)] = \exp\left(-\frac{(z-z_0)^2}{\sigma^2}\right) \quad (4.16)$$

for the simple Gaussian profile with the peak altitude  $z_0$  and thickness parameter  $\sigma$ , or

$$\begin{aligned} [OH(z)] &= \exp\left(-\frac{(z-z_0)^2}{\sigma_L^2}\right) & (z \leq z_0) \\ &= \exp\left(-\frac{(z-z_0)^2}{\sigma_U^2}\right) & (z \geq z_0). \end{aligned} \quad (4.17)$$



for the Gaussian with different thickness parameters  $\sigma_l$  and  $\sigma_u$ , below and above the peak altitude  $z_0$ , respectively. Examples shown in Fig. 4-1 and 4-2 provide close approximations to the MSIS model introduced in Chapter III, shown here for comparison purposes.

The temperature profile is defined as:

$$T(z) = T_0 + \Delta T(z-z_t)^2 \quad (4.18)$$

for a simple parabolic profile with the minimum temperature  $T_0$  at altitude  $z_t$  and a parameter  $\Delta T$ . To make this model closer to MSIS model, the following model is used:

$$\begin{aligned} T(z) &= T_0 + \Delta T_l (z-z_t)^2 & (z \leq z_t) \\ &= T_0 + \Delta T_u (z-z_t)^2 & (z \geq z_t) \end{aligned} \quad (4.19)$$

which is a parabolic profile with the minimum temperature  $T_0$  at altitude  $z_t$  and different parabolic parameters  $\Delta T_l$  and  $\Delta T_u$  for below and above  $z_t$ , respectively. Examples shown in Fig. 4-3 and 4-4 provide close approximations to the MSIS model presented in Chapter III and included in the figure.

In these models, each rotational line emission intensity for each altitude is calculated using equation (4.8). The resultant intensities are added according to:

$$I_{\text{obs}}(j,k) = \Delta z \sum_{i=0} I(N_i, T_i, \nu_{jk}) \quad (4.20)$$

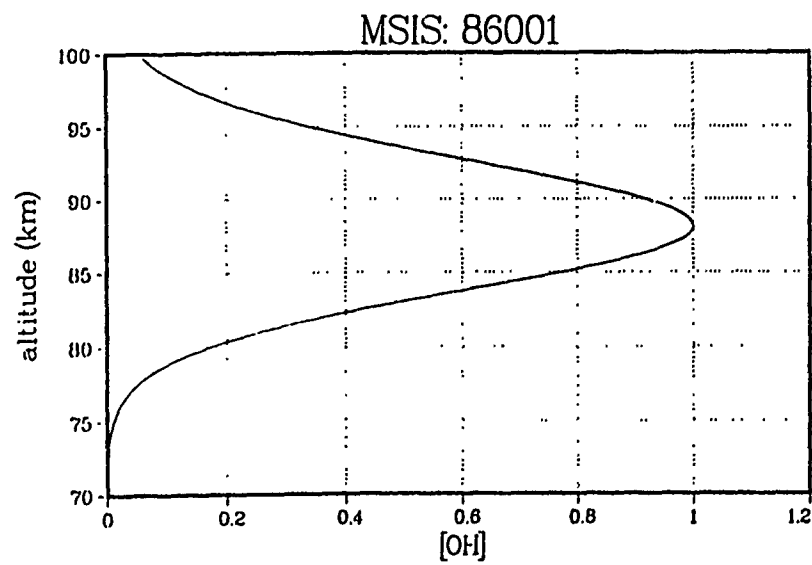
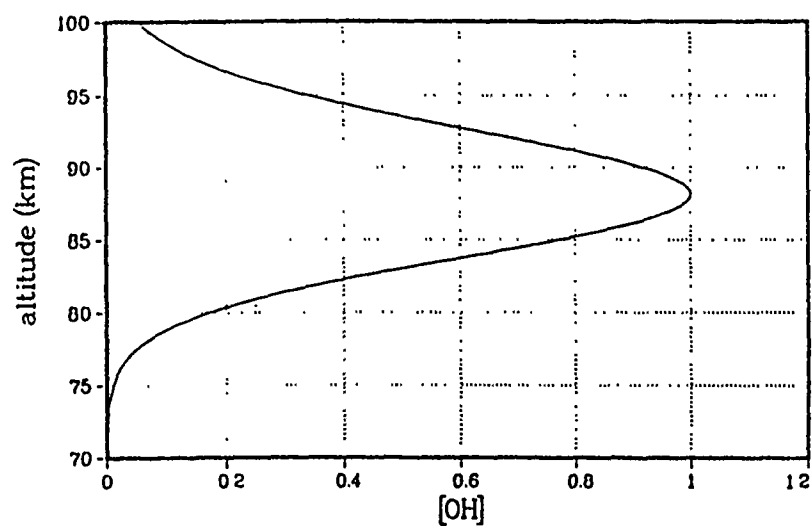


Fig. 4-1. Layer model (day 86001)

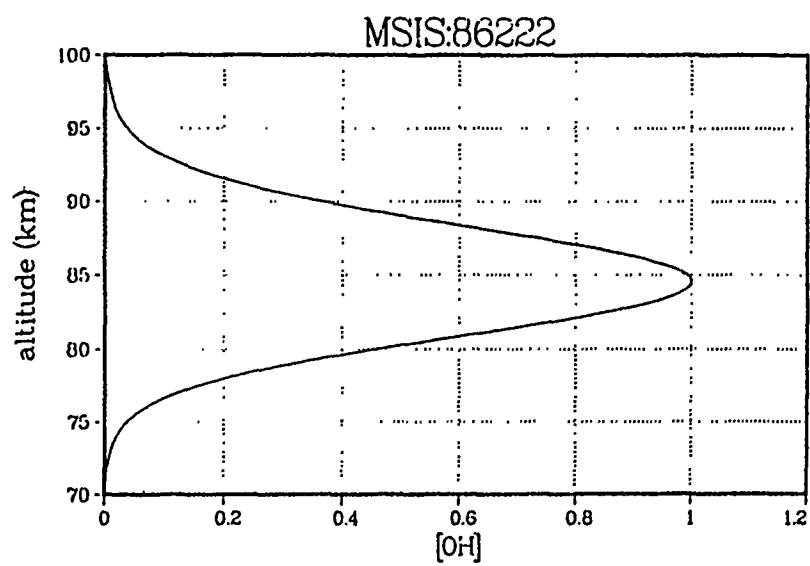
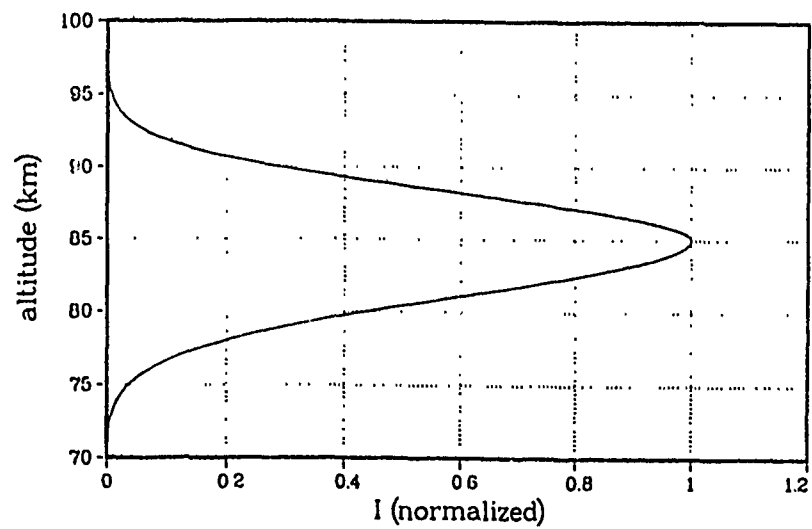


Fig. 4-2. Layer model (day 86222)

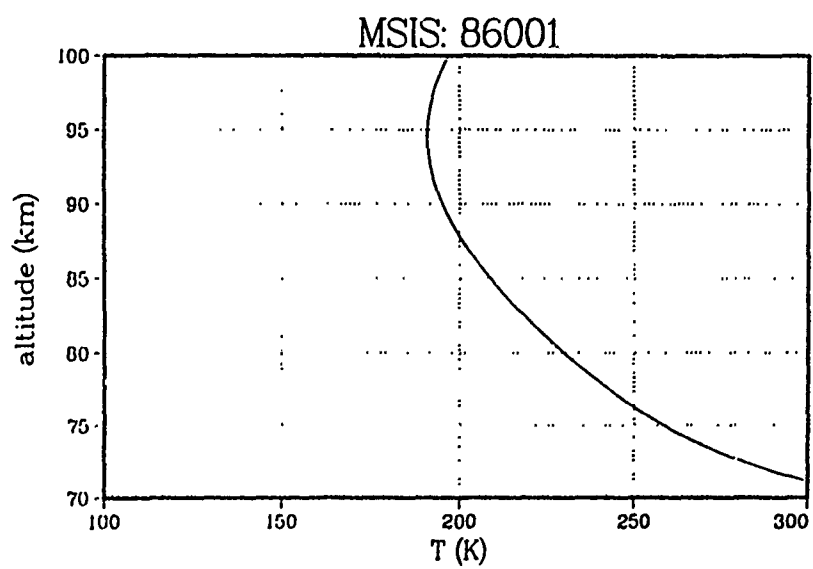
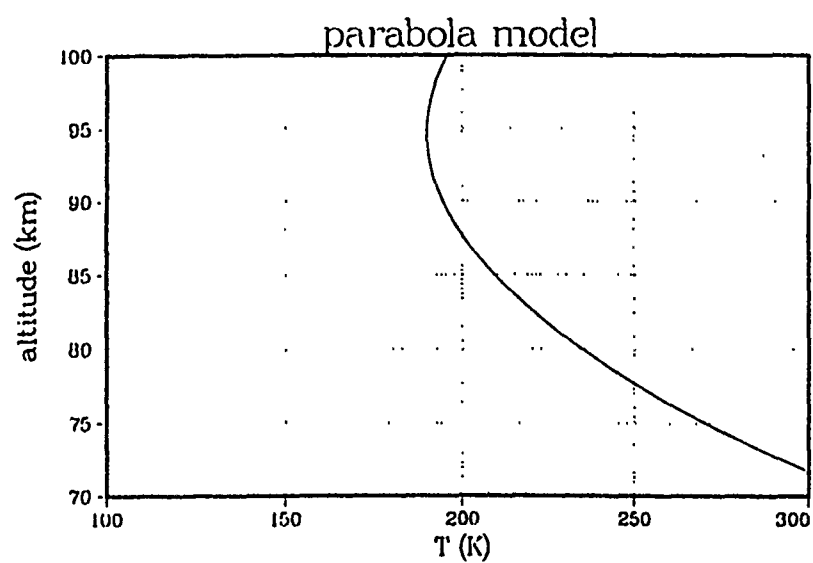


Fig. 4-3. Temperature model (day 86001)

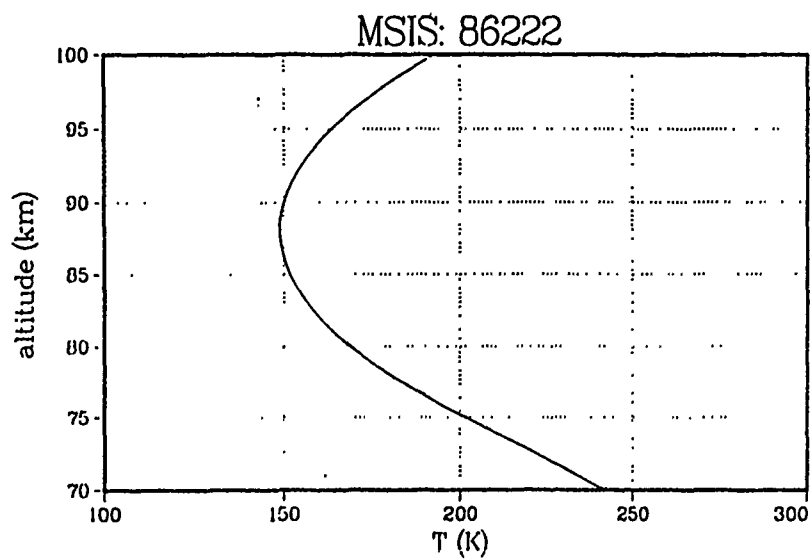
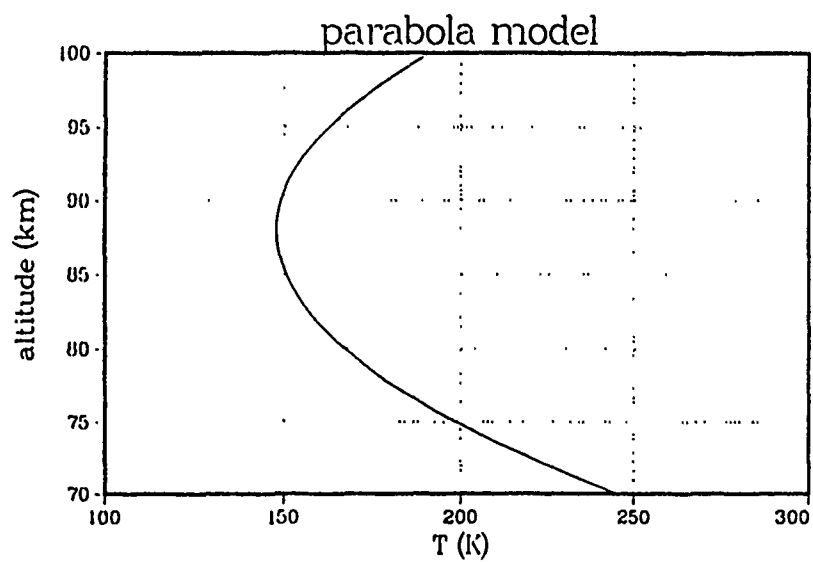


Fig. 4-4. Temperature model (day 86222)

where  $j$  and  $k$  denote rotational levels,  $N_i$  and  $T_i$  denote the concentration of hydroxyl at the upper vibrational level  $v'$  and temperature at altitude  $z_i$ , and  $z_i = z_b + i\Delta z$ . In the following examples,  $z_b$  is set to 70 km,  $\Delta z$  is 0.1 km and  $i$  runs from 0 to 301, resulting  $z_i$  from 70 to 100 km.  $I(N_i, T_i, \nu_{jk})$  is, therefore, the local volume emission rate of wavenumber  $\nu_{jk}$  at altitude  $z_i$ .

Results of this model are provided in Fig. 4-5 and Table IX. Fig. 4-5 contains plots of  $E_i(j)$ , the energy of the initial rotational level  $j$ , and natural logarithm of  $I_{\text{obs}}(j)/\nu_{jk}S_{jk}$ , where  $\nu_{jk}$  denotes wavenumber and  $S_{jk}$  denotes the line strength of the rotational emission line  $\nu_{jk}$ . Table X lists parameters of several emission lines ordered by their energy. Table XI contains the estimated intensity and temperature with their error estimates, corresponding to Fig. 4-5. Table XI also includes the integrated intensity weighted kinetic temperature. Note that the rotational and kinetic temperatures are close but not identical in most cases. Fig. 4-6 provides rearrangement of the emission intensity and temperature. Instead of functions of altitude, the intensity at each temperature is accumulated for all altitude and plotted the apparent intensity weight of each temperature. If there is a passive optical instrument which can measure kinetic temperature, such instrument will measure the intensity distribution as a function of temperature, similar to this figure. It is clear that the distribution is far from gaussian in many cases. Those cases with small temperature error estimates somehow retain symmetry and/or small variances, while those with large error estimate are asymmetric and/or have large variances. This

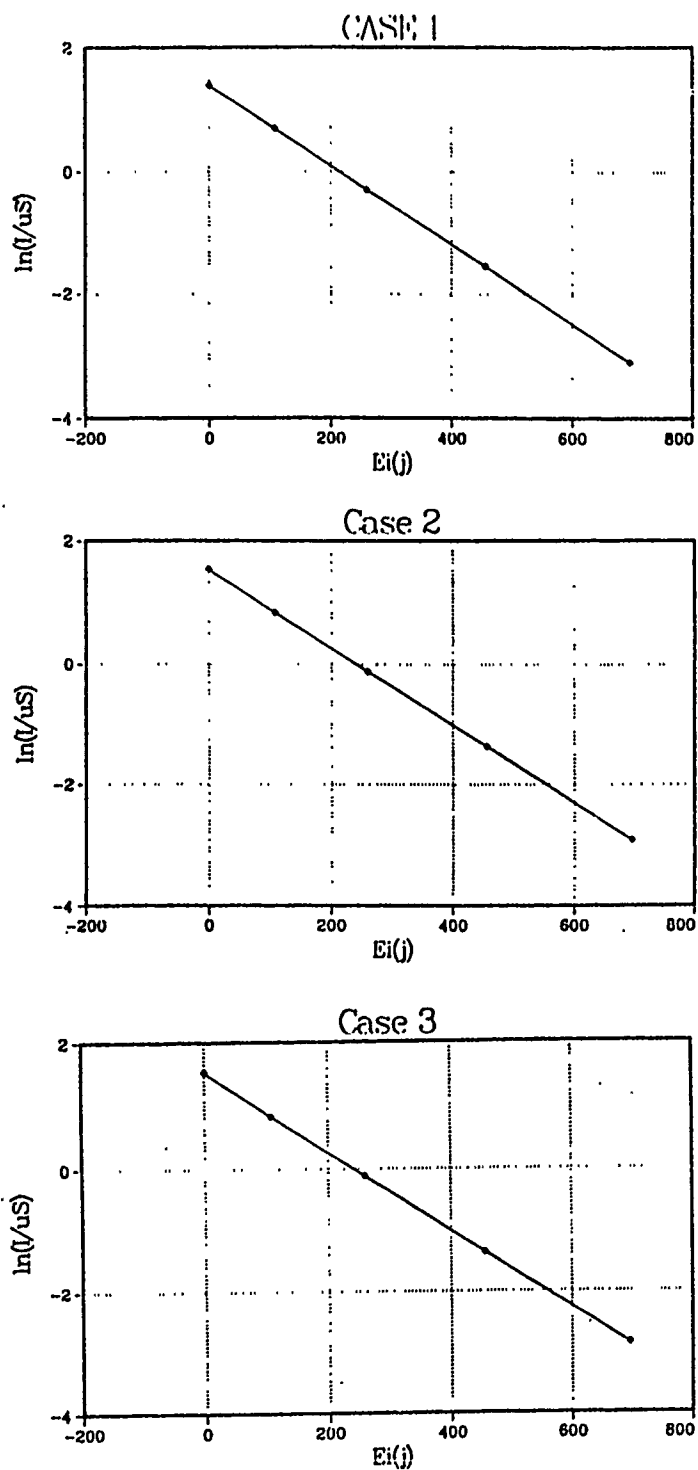


Fig. 4-5. Rotational temperature fit

TABLE IX  
Rotational Temperature Fit Statistics

	j	$E_i(j)$	$\ln(I/\nu_{jk}S_{jk})$
CASE 1:	1	0.0	1.38540
	2	107.477	0.68924
	3	259.126	-0.29077
	4	455.375	-1.55459
	5	696.371	-3.09882
CASE 2:	1	0.0	1.54621
	2	107.477	0.85288
	3	259.126	-0.12264
	4	455.375	-1.37978
	5	696.371	-2.91419
CASE 3:	1	0.0	1.53226
	2	107.477	0.84781
	3	259.126	-0.11533
	4	455.375	-1.35669
	5	696.371	-2.87224



TABLE X  
Rotational Line Parameters

	Energy ( $\text{cm}^{-1}$ )	$E-E_0$ ( $\text{cm}^{-1}$ )	J
$E_0 \rightarrow$	10172.28	0.0000000E+00	2
	10172.32	4.2968750E-02	2
	10246.99	74.71387	3
	10247.15	74.87305	3
	10300.34	128.0635	1
	10300.48	128.1992	1
	10352.27	179.9873	4
	10352.63	180.3477	4
	10354.09	181.8135	2
	10354.32	182.0420	2
	10443.17	270.8896	3
	10443.42	271.1387	3
	10488.46	316.1797	5
	10489.11	316.8291	5
	10566.93	394.6475	4
	10567.11	394.8301	4
	10655.80	483.5186	6
	10656.82	484.5400	6
	10724.70	552.4229	5
	10724.73	552.4331	5
	10854.37	682.0898	7
	10855.84	683.5654	7
	10915.67	743.3926	6
	10915.88	743.5996	6
	11084.14	911.8574	8
	11086.14	913.8633	8
	11139.37	967.0898	7
	11139.89	967.6143	7
	11344.96	1172.680	9
	11347.57	1175.290	9
	11395.30	1223.021	8
	11396.22	1223.940	8
	11636.61	1464.327	10
	11639.89	1467.614	10
	11682.96	1510.683	9
	11684.35	1512.071	9
	11958.78	1786.498	11
	11962.81	1790.532	11
	12001.85	1829.568	10
	12003.78	1831.498	10
	12351.44	2179.160	11
	12353.98	2181.700	11

TABLE XI  
Estimate for Fig. 4-5

	$\int I \, dz$	$\Delta(\int I \, dz)$	$T_{\text{rot}}$	$\Delta T_{\text{rot}}$
CASE 1:	97.5	0.302	155.3	0.191
CASE 2:	115.1	0.429	156.1	0.232
CASE 3:	115.1	0.408	158.1	0.225

$z_t = 88\text{km}$  for all cases:

	$\sigma_L$	$\sigma_U$	$T_0$	$\Delta T_L$	$\Delta T_U$
CASE 1:	5.5	5.5	148.0	0.3	0.3
CASE 2:	6.0	7.0	148.0	0.3	0.3
CASE 3:	6.0	7.0	150.0	0.3	0.3

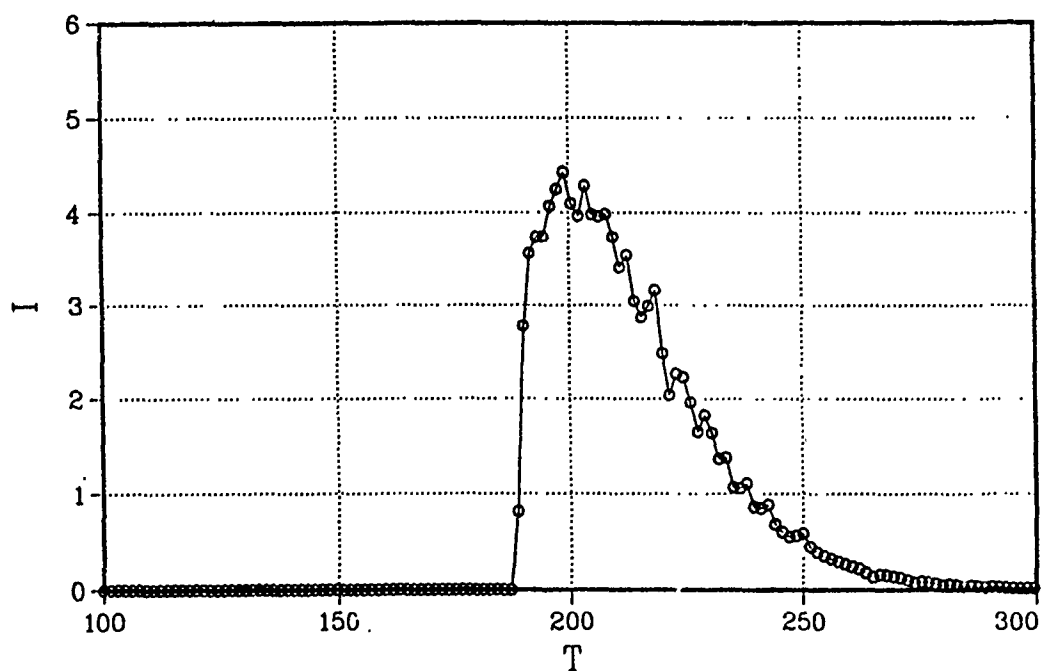
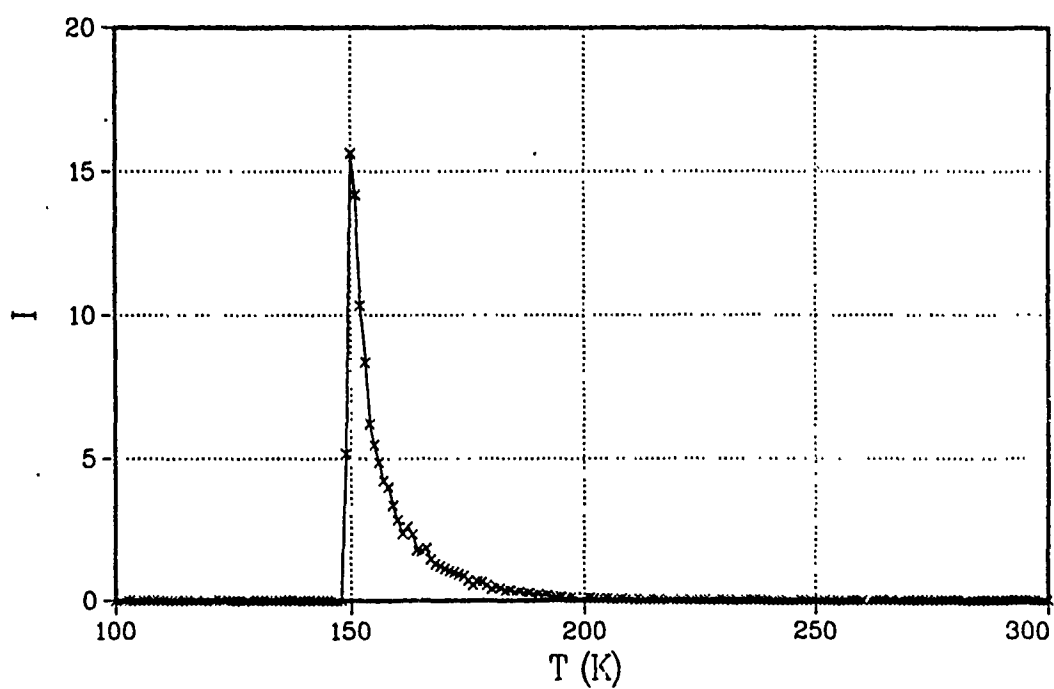


Fig. 4-6. Intensity distribution as a function of temperature

is natural because the least-square fit assumes the distribution similar to Gaussian.

### Geometric Effect for Vertical Observations

The discussion so far devoted to the "stationary geometric effect," that is, the geometric effect with the finite thickness layer at rest. Another aspect of the geometric effect is the "dynamic geometric effect," becoming the basis for the off-zenith geometric effect as well as the vertical observation with the emitting layer moving according to the incoming internal gravity wave. This is indeed a restatement of the discussion carried out by Hines and other people [7], [11], but should clarify the concept of the dynamic geometric effect. Of particular interest to the geometric effect are called "polarization relations" by Hines [13], because they define phase as well as amplitude relations between changing physical quantities. According to Hines, the air parcel travels at the wind velocity of [13]:

$$U = \omega K_x C^2 (k_z - i \frac{(1 - \gamma/2)g}{C^2}) \quad (4.21)$$

$$W = \omega(\omega^2 - k_z^2 C^2) \quad (4.22)$$

where U and W are phasers for horizontal and vertical speed respectively. From these equations it is obvious that u, the horizontal wind speed, and w, the vertical wind speed, have a phase shift. This makes the trajectory of the air parcel an ellipse rather than a line.

Since there is also a common factor,  $\exp(z/2H)$ , not explicitly represented in the polarization relations, the true trajectory is an oval, asymmetric ellipse with a larger radius at higher altitude. It is this unusual air parcel trajectory that causes the dynamic geometric effect, both in vertical and off-zenith observations. The geometric effect for  $\theta_0=0$  is already given in Chapter II and III.

#### Geometric Effect For Off-Zenith Observations

The extension of the dynamic models introduced so far allows the simulation of the observable of interest when the line of sight is off to the zenith. It is shown that a small modification of those model is enough for the extension, accounting for the geometric effect.

There is a simple relationship between  $x$  and  $z$  for the line of sight. When the line of sight has a zenith angle  $\theta_0$ , where the small  $o$  indicates 'observation', the relation between  $x$  and  $z$  along the line is:

$$x = z \tan \theta_0 \quad (4.23)$$

By substituting (4.23) to (4.4), the phase factor becomes:

$$\exp i(\omega t - k_x x - k_z z) = \exp i(\omega t - K_0 z) \quad (4.24)$$

where

$$K_0 = -k_x \sin \theta_0 + k_z \cos \theta_0 \quad (4.25)$$

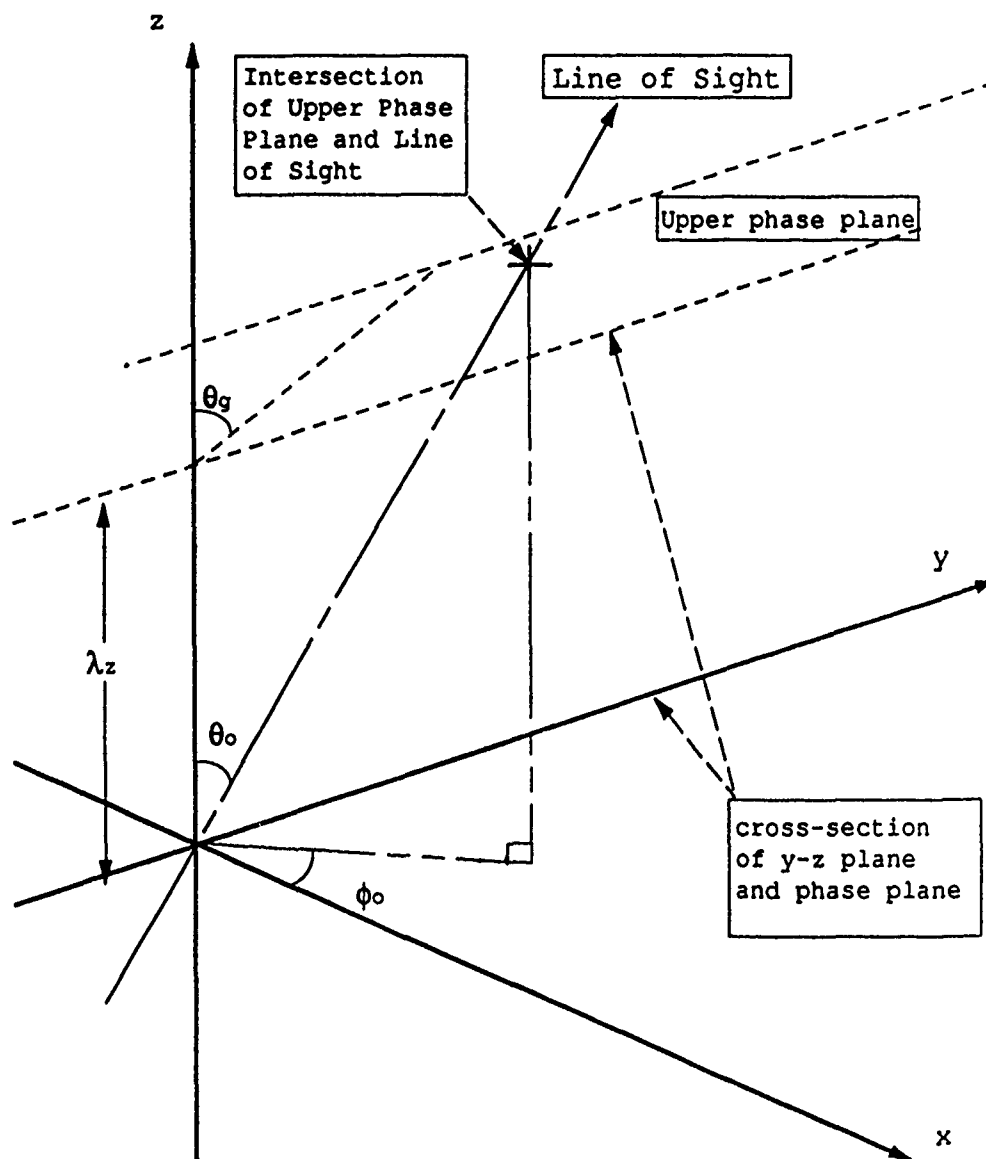
This indicates that the effect of the off-zenith observation is the apparent wavelength change described by (4.25). It should be noted, however, that the derivation of (4.25) assumes that the line of sight is still in the x-z plane; in other words, parallel to the wave vector in x-y plane. Further geometric considerations allows cases of the line of sight not to be parallel to the wave vector. If the line of sight has an azimuth angle of  $\varphi_0$  with respect to the wave vector, the equation (4.25) is modified to (refer to Fig. 4-7):

$$K_0 = -k_x \sin \theta_0 \cos \varphi_0 + k_z \cos \theta_0 \quad (4.26)$$

Modifying the apparent wavenumber, or the apparent wavelength, allows the previous dynamic models for the vertical observations to be used in the same manner in off-zenith observation simulation. The only change occurs when multiplying the time varying term (4.24),  $K_0$  should be used instead of  $k_x$  and  $k_z$ . Note that the  $k_x$  and  $k_z$  must still be used to calculate other parts of the integrand, because those parts are determined by the physically meaningful quantities  $k_x$  and  $k_z$ , instead of the  $K_0$  which is only a result of the geometric effect. Therefore  $K_0$  should be included only in the oscillation term, (3.4) or (4.24).

Using the relation:

$$\tan \theta_0 = \frac{k_z}{k_x} \quad (4.27)$$



Line of sight: $z \tan \theta_0 = x / \cos \phi_0$	
Phase plane : $z \tan \theta_g = x$	: Lower plane
Phase plane : $(z - \lambda z) \tan \theta_g = x$	: Upper plane

Fig. 4-7. 3D Geometric effect

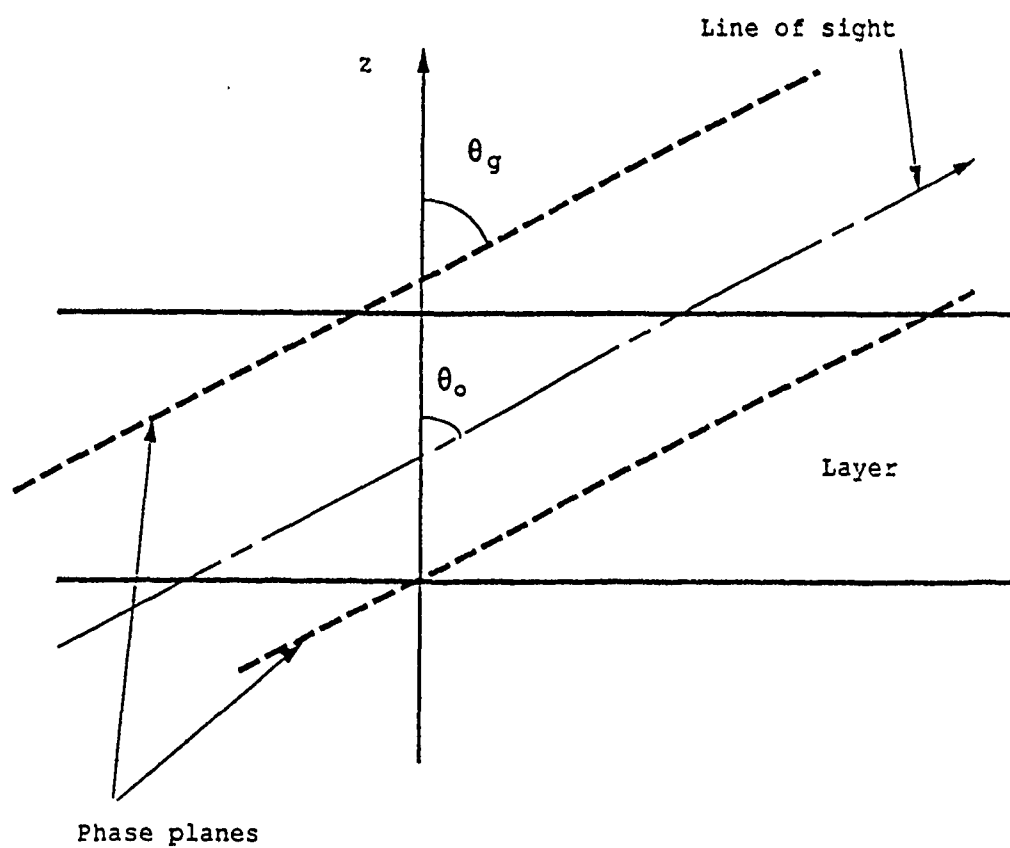
where  $\theta_g$  is the angle of the wave propagation direction to the zenith, (4.25) and (4.26) becomes, respectively:

$$K_o = k_z \cos \theta_o \left(1 - \frac{\tan \theta_o}{\tan \theta_g}\right) \quad (4.28)$$

$$K_o = k_z \cos \theta_o \left(1 - \frac{\tan \theta_o}{\tan \theta_g} \cos \varphi_o\right) \quad (4.29)$$

A simple but interesting property of this modifications was briefly introduced in Chapter II. When  $\theta_o = \theta_g$ , equation (4.29) leads to an interesting conclusion when  $\varphi_o = 0$ , which is (4.28). As is seen from (4.25) and (4.26),  $K_o = 0$ , the apparent wavelength along the line of sight becomes infinity (Fig. 4-8). Since the line of sight is parallel to the wave plane on which all parts have the same phase, the oscillation is observed in its full magnitude. This means that the geometric effect, the cancellation of the different phase, does not occur, since there is no phase change along the line of sight. On the other hand, any geometrical configuration in which the wave in the layer along the line of sight exercises an integer multiple of 360 degree phase change, as in the simple slab-layer model, no oscillation will be observed when there is actually an oscillation. In case of more realistic layer geometry where the intensity within the layer is not uniform, such cancellation will not be perfect and some oscillation will be observed. However, serious attenuation in apparent oscillation amplitude is expected. Note that the oscillation energy corresponding to those attenuated amplitude does not disappear, but is





$$\theta_o = \theta_g, \quad \varphi_o = 0$$

Fig. 4-8. Special case geometric effect

"transferred" into the apparent "DC" component of the emission, or a constant brightness representing the average brightness. This effect is especially notable with an infrared imager with a relatively wide field of view. The same wave packet with the same physical characteristics, such as wavelength, oscillation frequency and amplitude, will produce entirely different signals depending upon the geometrical relation between the line of sight and the wave propagation direction. This modification of the true wave into an apparent wave can be described according to the following equation:

$$I_{obs}(t) = \int_0^{\infty} [OH_0(z)] \exp(i(\omega t - K_0 z)) dz \quad (4.30)$$

where 'Re' denotes the real part,  $[OH_0(z)]$  is the stationary concentration of hydroxyl at altitude  $z$ , and  $K_0$  is given by (4.26) or (4.29).

When  $[OH_0(z)]$  is approximated with a constant  $C$  between  $z=z_L$  and  $z=z_U$ ,  $z_L < z_U$ , and 0 elsewhere, equation (4.30) becomes:

$$I_{obs}(t) = \frac{C}{K_0} [ \sin(\omega t - K_0 z_L) - \sin(\omega t - K_0 z_U) ] \quad (4.31)$$

$$= \frac{2C}{K_0} \cos\left(\frac{K_0(z_U - z_L)}{2}\right) \sin\left(\omega t - \frac{K_0}{2}(z_U + z_L)\right) \quad (4.32)$$

This result is similar to the oscillation part of equation (2.36).

The replacement of the true wavelength by the apparent wavelength along the line of sight is necessary and sufficient for the description of the off-zenith geometric effect.

## CHAPTER V

## DATA PROCESSING TECHNIQUE

Dynamic airglow signal processing systems intended for a detection of internal gravity waves are presented. Selection of the analysis method and choice of parameters for the selected method depends upon the a priori knowledge of the input signal, rather than the signal-processing theory alone.

Data Reduction System

This section describes data of the mesospheric infrared radiation measured by the interferometer spectrometer. A description and the theory of operation of the instrument can be found in a literature [33]. The method used to calculate the relative emission intensity and the rotational temperature using the observational data is described in Chapter IV and Appendix B. Most attention is focused in an introduction of a method to calculate IGW parameters such as time-resolved power spectral density out of the observational data. These parameters are used in the discussion of the IGW dynamics and the chemical and thermodynamic modeling of the infrared emission source, the mesospheric hydroxyl layer.

Michelson Interferometer Spectrometer

The interferometer used in the so-called Fourier transform spectroscopy is an instrument based upon the same interference principle used in the historical Michelson-Morley experiment in the 1880's. The theory of operation is found in literature [33], [34].

## Data Reduction

After the spectrum of the incoming infrared light is calculated, the emission intensity and the rotational temperature for a specified emission band are calculated as functions of time. In the present case, developed by Espy using a least-square fitting of synthesized spectral lines of one vibrational band to the measured spectral lines of the same band was used [35]. This method also provides the estimation of emission intensity and error estimates of these values. The least-square method is described in Chapter IV and Appendix B [31], [35]. These values are analyzed as time series with the spectral-analysis techniques. Here, the word "spectrum" refers to the spectrum in the temporal oscillation of the emission intensity and the rotational temperature, rather than to the optical emission spectrum as referred to previously.

## Spectral Analysis Techniques

### Introduction

Once the temperature and intensity data are prepared, the power spectral densities of both rotational temperature and emission intensity fluctuations can be calculated. These frequency domain spectra are useful in studying theoretical characteristics of IGW's in their frequency domain representations.

One frequency domain analysis techniques is the adoption of a Fourier transformation and its application, a short-time Fourier analysis [36]. Another is the maximum entropy method (MEM) [37]. This section devotes to the two techniques.

### Fourier Analysis

There are several methods of estimating the power spectral density. One commonly used method is calculating the Fourier transform of the original signal. More precisely, the power spectral density of the signal is obtained by the Fourier transform of the signal's auto correlation [38]. This method does not provide a well defined spectrum when the original signal contains only a few cycles of the oscillation. Most experimental data contain no more than 3 to 7 cycles: most observations last 45 minutes to a few hours at a time, and the IGW's to be studied have periods of tens of minutes to several hours. Under such conditions, the best estimate of the oscillation frequency has the uncertainty  $\Delta f$  of:

$$\Delta f = \frac{2\pi}{T_L} \quad (\text{radian/second}) \quad (5.1)$$

where  $T_L$  is the total data length. The given condition makes the value of the peak frequency comparable to the half width of the main lobe. When data have a DC component, or a constant, this causes an interference of DC and the signal of interest. Such problems may be avoided by carefully removing DC, as are discussed in the following sections. Also, the Fourier analysis fails to provide a peak when data contain less than one cycle of oscillation. In such case, even DC removal does not work properly.

Also, the Fourier transform technique produces the spectral function with significant sidelobes [38]. The sidelobes of nearby frequencies interfere with each other, making the Fourier signal

analysis inaccurate. As equation (5.1) indicates, this is a serious problem when the data contain only one or two cycles. In such case, the sidelobe of the data window, the DC component, can interfere with the main lobe of the signal.

#### Short-Time Fourier Analysis

It is necessary to use a signal processing technique that can cope with limitations such as short data duration. Moreover, the expected signal is not monochromatic sinusoidal. Some observational data actually show such chirp oscillations, as shown in Fig. 5-1. This is real IRFWI data taken in the summer of 1986 in Fairbanks, Alaska. The expected signal does not contain an oscillation of a single frequency (monochromatic wave), so the limited signal duration problem cannot be solved even with any instrumental or experiment operation improvement, such as longer observation time. This invalidates a use of the simple Fourier analysis.

With such a limitation, one technique, a short-time Fourier analysis, can be an appropriate method to estimate the IGW signal characteristics [36]. This technique provides a means to estimate instantaneous frequencies constantly changing. This method is described in applicable literature [36]. With this technique, a spectrograph of the signal can be derived. "Spectrograph" was originally used in speech analysis as a graphic representation of the short-time Fourier spectrum [36]. When possibility exists for a frequency variation in the signal, the use of the short-time Fourier analysis may be considered with careful choice of the window length which should be longer than the signal frequency (period) of interest.

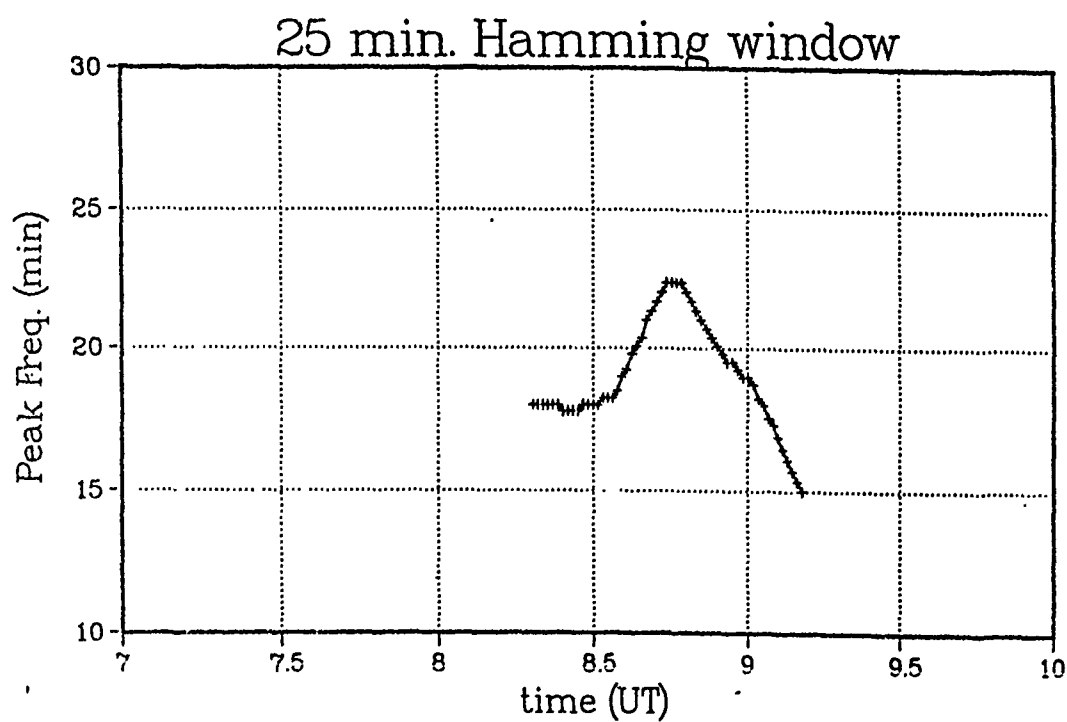
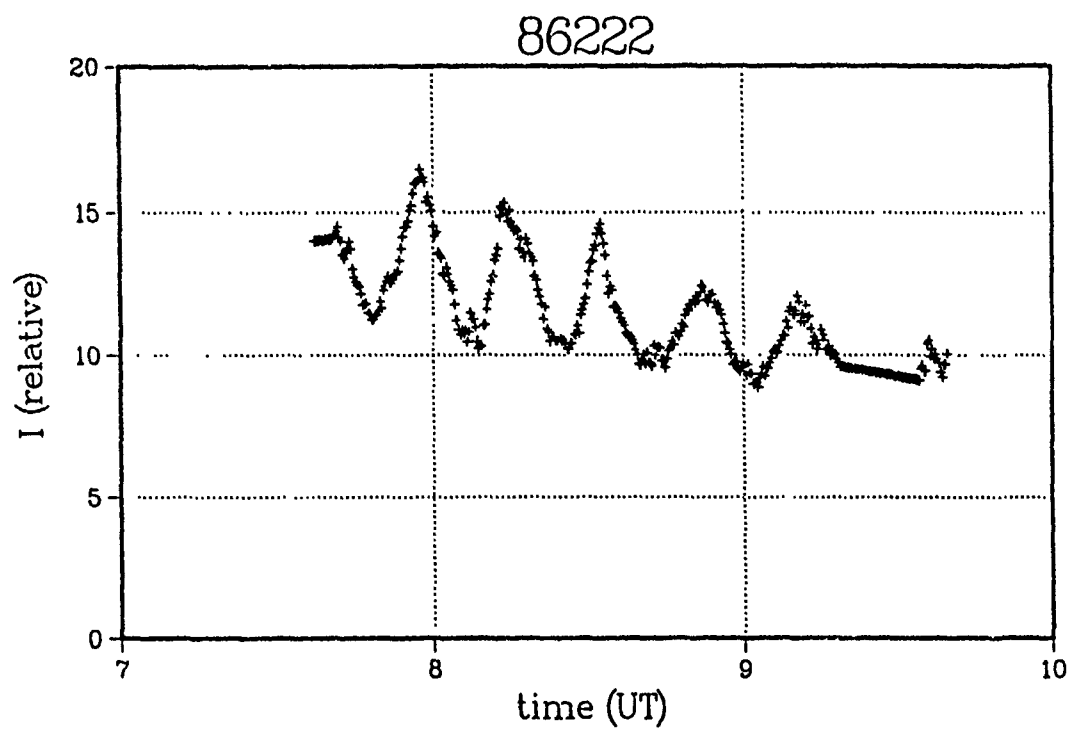


Fig. 5-1. Observed chirp in airglow emission



This technique is stable compared to the maximum entropy method, especially in presence of noise. It will be shown that, unlike the short-time Fourier analysis technique, the maximum entropy method is not stable in presence of a noise.

#### Maximum Entropy Method

A technique called maximum entropy method (MEM) was developed within last 23 years and described often in related literature [37]. This method has the following advantage:

1. There is no need for a window function. MEM provides very sharp peak with no sidelobes. This is due to the fact that in MEM, the spectral lines are approximated by a function of the form  $1/(\epsilon^2 + (\omega - \omega_0)^2)$  where  $\epsilon$  is a parameter [37].
2. Very high frequency resolution can be achieved using very small amounts of data, often less than a complete cycle.

However, MEM has the following problems [37]:

1. An interference can occur between spectral lines. Unlike the similar interference due to sidelobes in the Fourier transform technique, such interference produces a peak at a wrong frequency (frequency shift) in MEM. As described later in this chapter, this problem may be avoided by use of an appropriate filter.
2. MEM assumes sharp, or narrow, spectral lines. In case of a broad band signal, such as a chirp signal which does not have a sharp peak, MEM can produce faulty spectrum with several sharp peaks. This problem can sometimes be avoided if enough high order is

used in the calculation of MEM spectrum. When the amount of data is too small, this remedy can not be applied.

3. The magnitude of the resultant spectrum does not necessarily represent any physical quantity of the signal. Even their relative magnitude in the resultant spectrum may not represent their relative physical magnitude. A better mathematical understanding of MEM is needed.
4. MEM is susceptible to noise. A weak noise can cause splitting of the spectral line [37]. A strong noise can cause a shift in the spectral line. The severity of such effects depends on the phase and duration of the signal in data, which further complicates the problem. It is known that this problem can not be cured by increasing the amount of data.

Several results of real data processing are presented in the last section of this chapter. Results of the two methods, short-time Fourier analysis and MEM, are compared.

### Digital Filter

#### Introduction

The interferometer produces one interferogram per single scanning of the moving mirror, or the prism in case of IRFWI. The airglow emission intensity and the rotational temperature are calculated for each scanning frame. Because of the way data are reduced, the input signal to the analysis program is discrete by nature. Therefore, the application of the digital filter technique is a natural choice to design filters to remove the effect of a noise and other interfere-

nces. A filter is needed to limit the signal frequency higher than the corresponding frequency of the window length. This is needed for (short-time) Fourier analysis to remove the interference of the window. As will be shown, MEM can also produce better results if enough low frequency components are removed. The high frequency removal has some effect on MEM, but usually not in Fourier analysis. The highest IGW frequency component of interest is limited by the Brunt-Vaisala frequency, so to assist a time domain analysis, a use of a low pass filter may be effective. The FIR filter technique is most suitable in processing this type of data.

#### IIR and FIR Filter

The conventional analog filters transformed into discrete signal forms are called infinite impulse response filters or IIR filters [39], because the IIR filter uses its output signal as the feedback signal to the input, resulting in an infinite length response to an impulse input. Because of the feedback, IIR filters are sometimes called recursive filters [39]. This type of filter has the advantage of simple design: usually one can design this type of filter with a calculator. It has several disadvantages which cause serious problems to the IGW signal analysis. One problem is the nonlinear phase characteristics of the filter, especially near the cut-off frequency. This is a serious disadvantage, since the phase difference between the intensity and the temperature oscillations is one of the quantities of interest. Another problem is that an IIR filter can be unstable. Because the IIR has a feed back loop, a significant impulse response can last for a long period of time. This can introduce a faulty

oscillation to the signal.

Another type of filter, called finite impulse response filters or FIR filter, can be designed with linear phase shift characteristics while maintaining the desired amplitude property [39], although it usually requires a large number of data points to obtain the superior phase characteristics. This causes truncations of data on both ends. Since the number of data points from the instrument are usually very limited, the FIR filters are useful only when enough amount of continuous oscillations are recorded. If such problems are overcome, FIR filters are superior to IIR filters, effective in studying IGW oscillations with periods of 30 minutes or less. For signals with longer periods, a simple DC removal sometimes works better.

The effect of a high-pass filter and a band-pass filter on the maximum entropy method is demonstrated in Fig. 5-2. Fig. 5-2(a) is one of the IRFWI data taken in Alaska. Fig. 5-2(b) is several spectra obtained by the maximum entropy method. The high-pass filter has a cut-off frequency represented in period of 30 minutes. The band-pass filter has the same low cut-off frequency and a high cut-off frequency of 3.3 minutes. The resultant spectra are quite different, both in amplitude and location (frequency) from that of the raw data.

An effect of a low pass filter is demonstrated in Fig. 5-3. Fig. 5-3(a) shows a sample data taken by IRFWI. Fig. 5-3(b) shows its spectrum derived by MEM. The low-pass filter has a cut-off frequency, represented in the period, of 3.3 minutes. As shown, the resultant spectra are quite different with and without the filter, as well as DC removal, indicating the instability of the MEM.

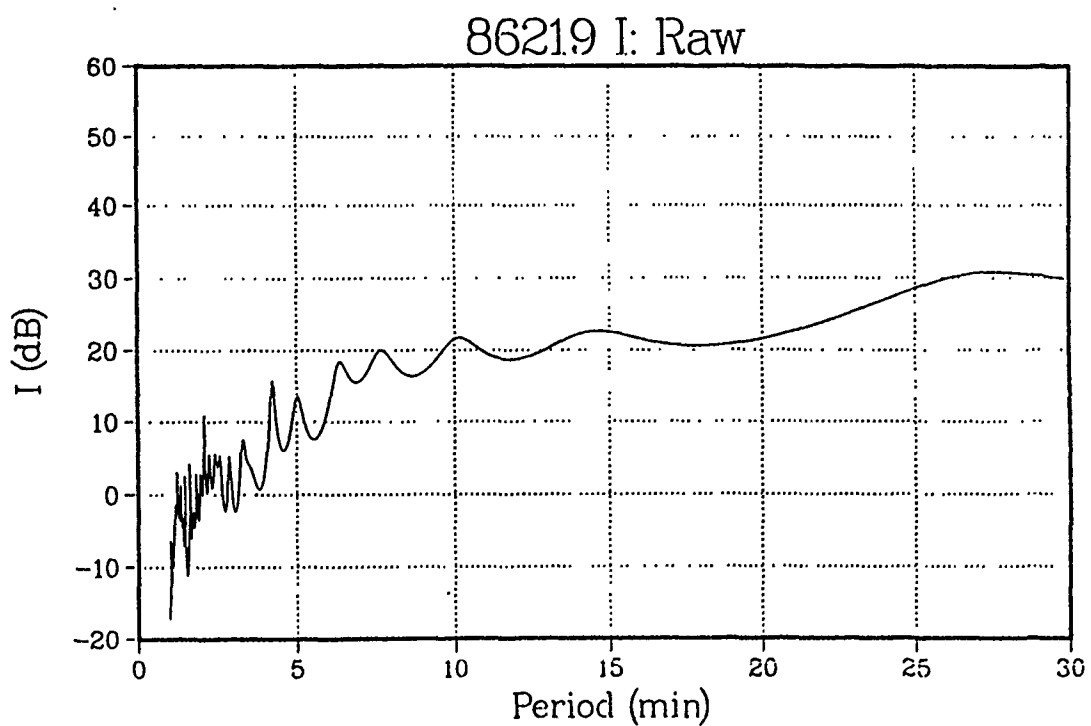
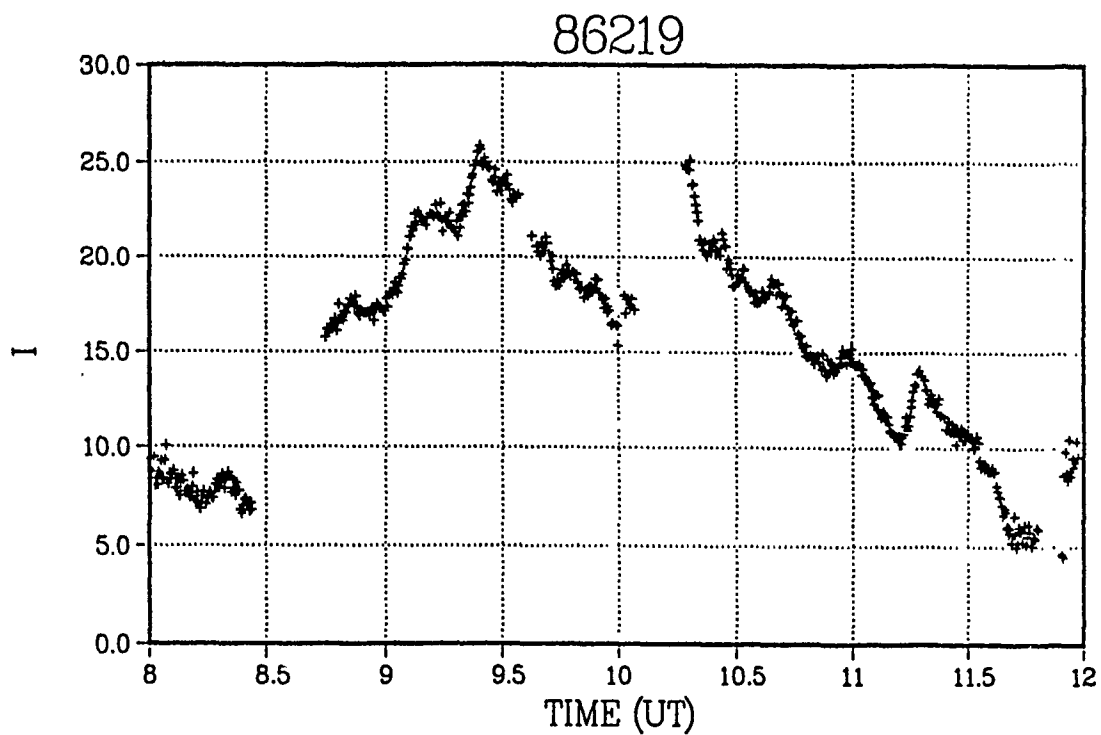


Fig. 5-2. Effect of high-pass filter: (a) data

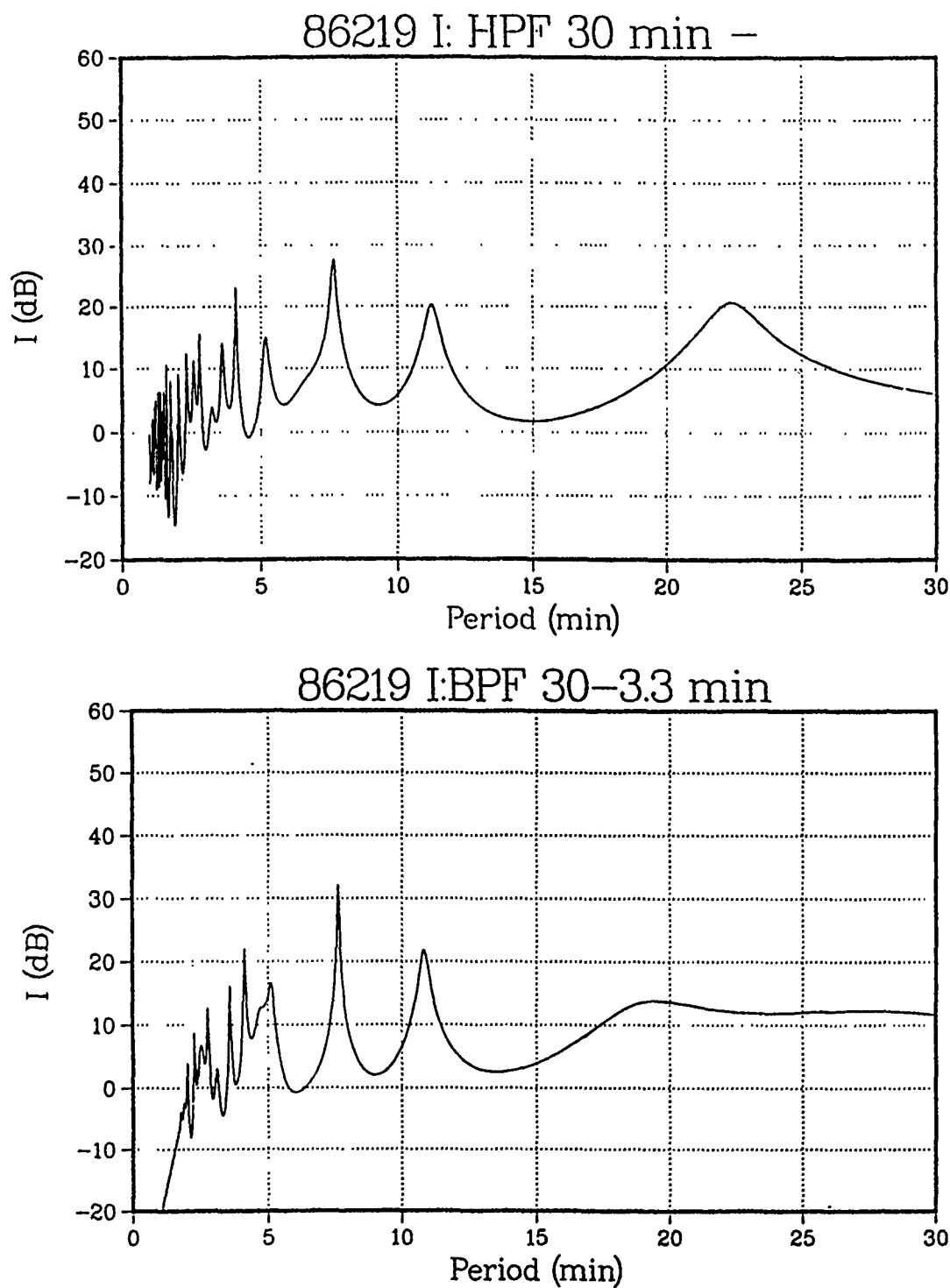


Fig. 5-2. Effect of high-pass filter: (b) MEM spectrum

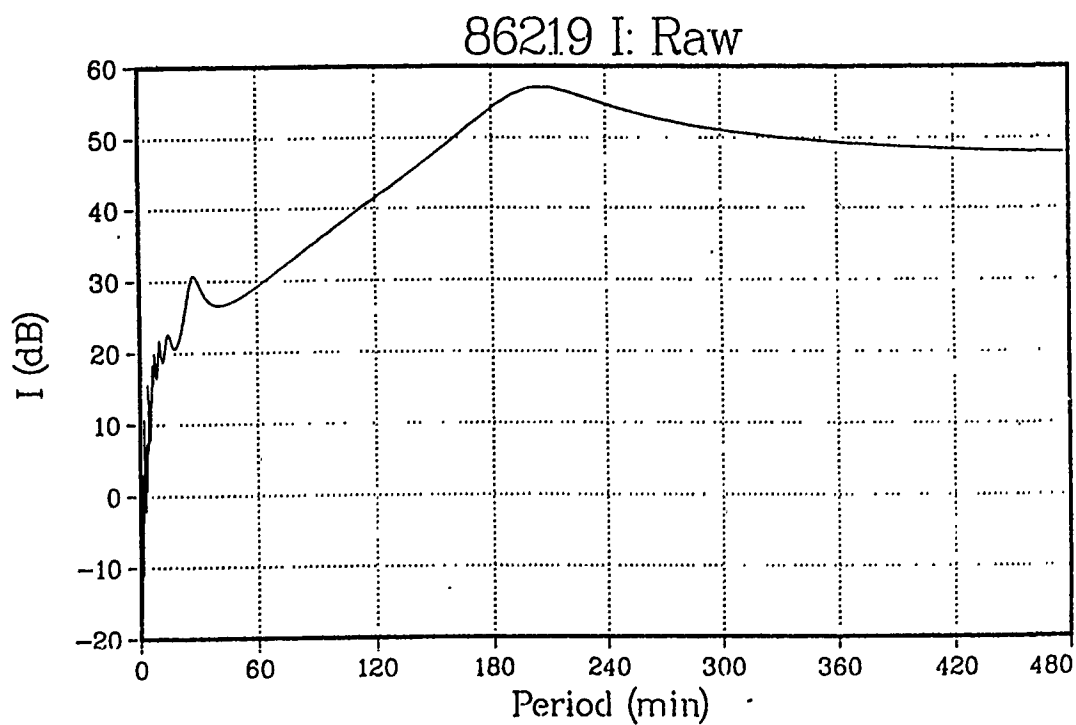
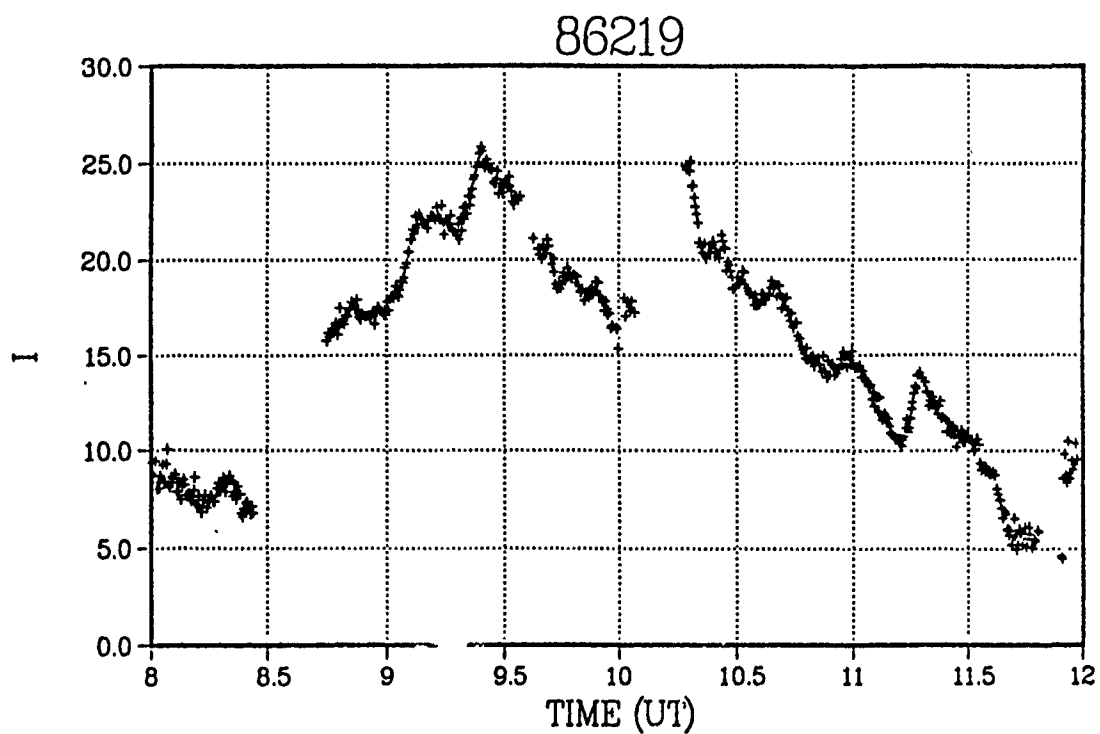


Fig. 5-3 Effect of low-pass filter; (a) data

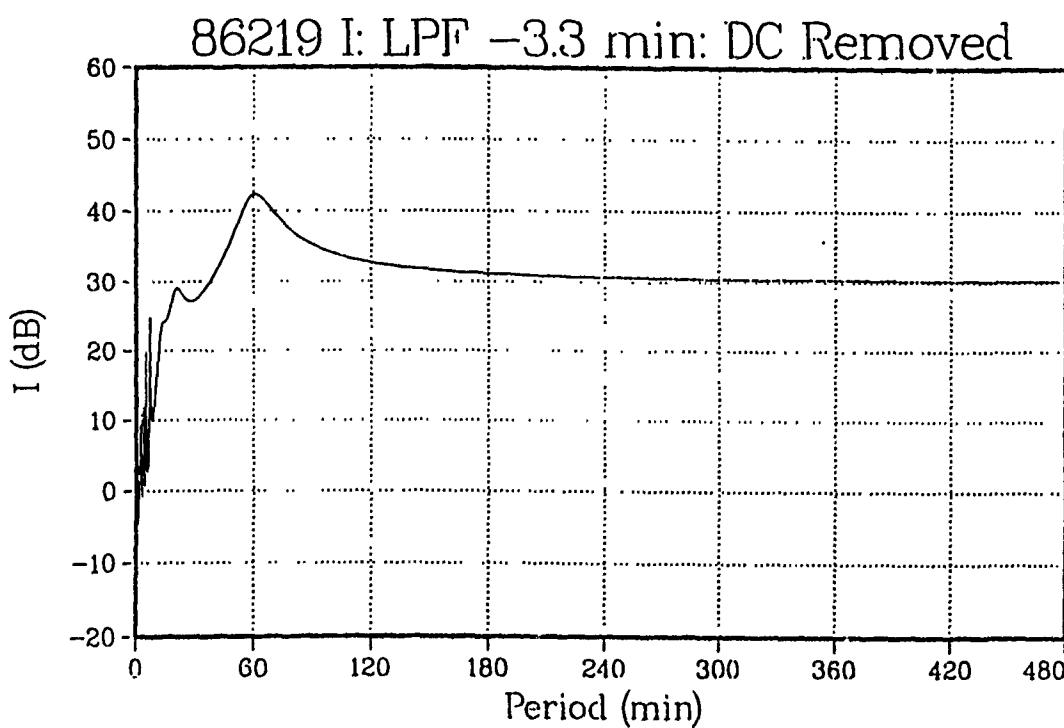
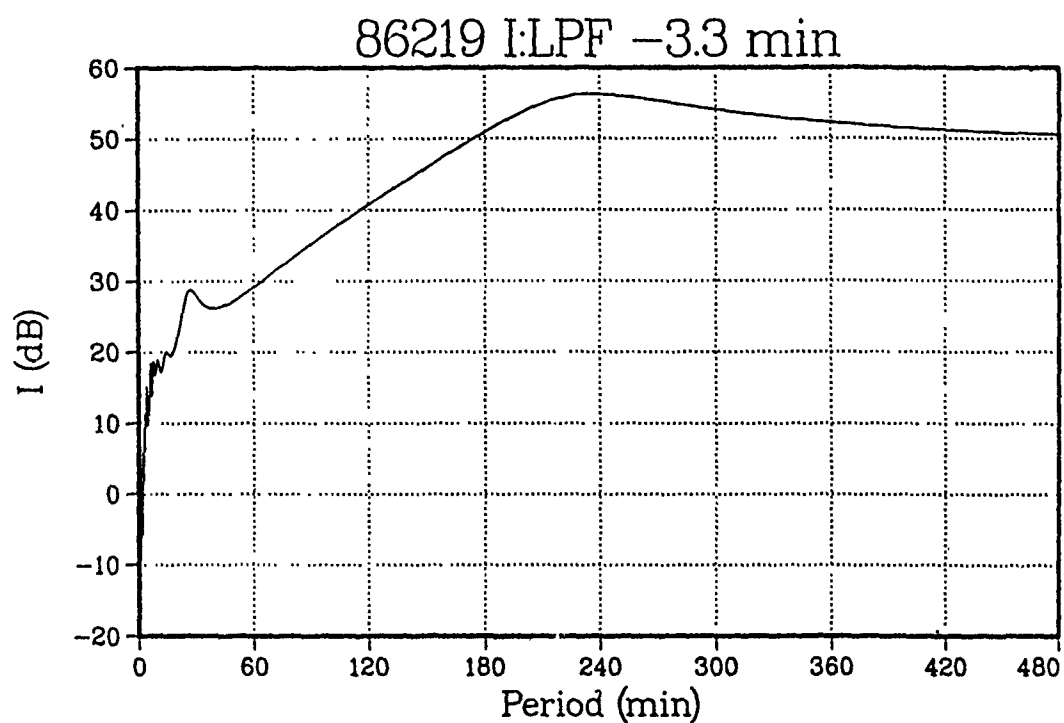


Fig. 5-3 Effect of low-pass filter: (b) MEM spectrum



Another use of the low pass filter is demonstrated in Fig. 5-4. This effect is a suppression of the apparent oscillation at the sampling interval period due to the sampling of data with error and noise. Since IGW has longer period than Brunt-Vaisala period theoretically, such spurious spectrum may be removed. If the differential of the signal is of interest, for instance, numerical differentiation can give good results only after such noise is removed. Fig. 5-4(a) is another data from Alaska. Fig. 5-4(b) is the output of a low pass filter. Fig. 5-4(c) shows the results of numerical differentiation taken from the original and filtered signal.

#### Time Domain Analysis

Several limitations make the frequency domain analysis of the IGW data with properties such as short duration and frequency chirp inaccurate and difficult to implement. These limitations are:

1. Missing data due to instrument calibration or some other reasons. Data are truncated during these periods. Frequency domain analysis results in broadened main lobe in Fourier spectrum due to averaging. The short-time Fourier technique gives lower than true frequency in some cases.
2. Usually only few cycles of oscillations are included in one set of data even without any data truncation. The oscillation period of interest is usually 15 to 60 minutes while the continuous measurement duration at a time is few hours. This causes a large uncertainty in the frequency estimate.
3. Frequency domain analysis does not always properly process signals

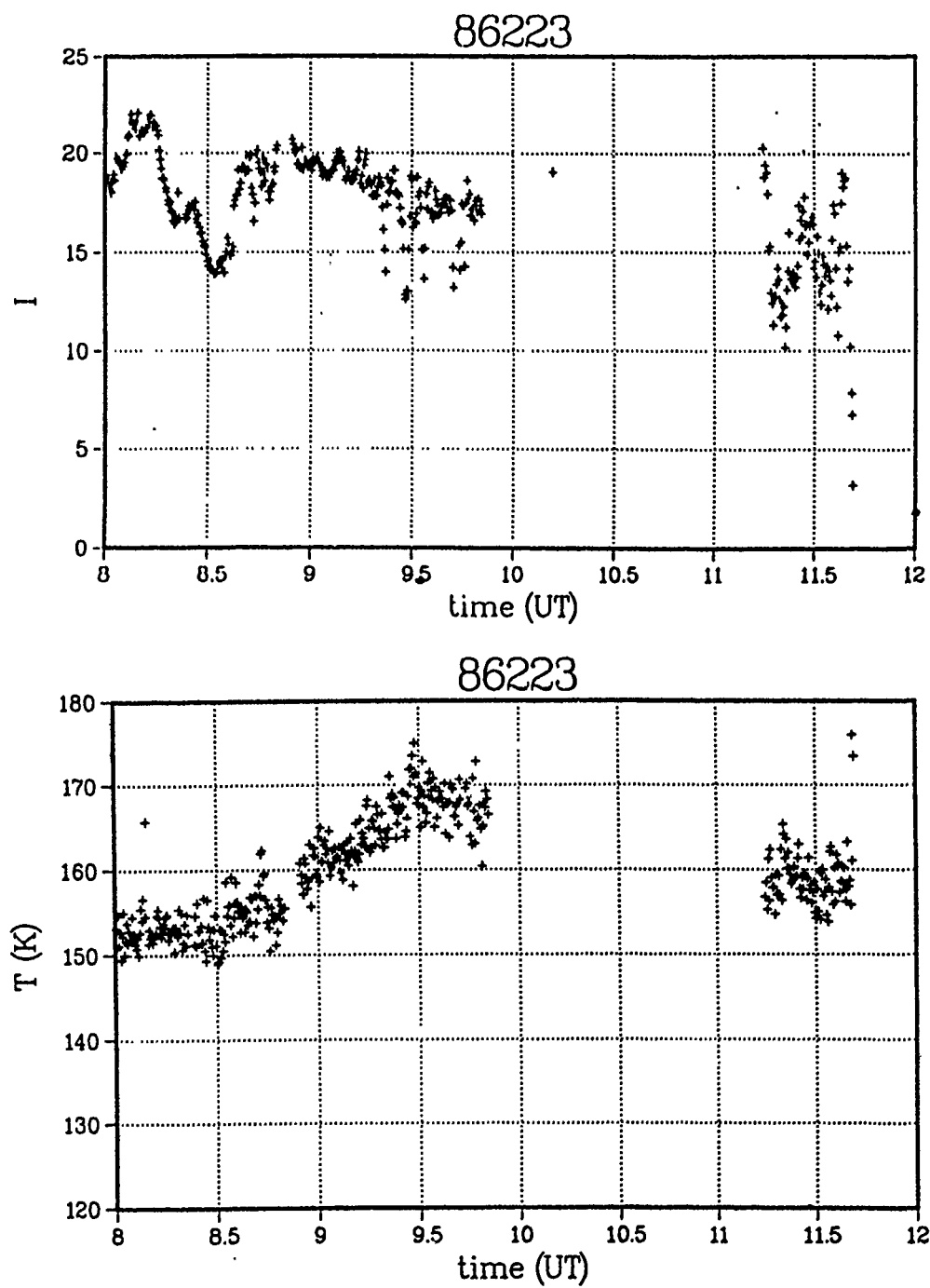


Fig. 5-4. Time domain analysis: (a) data

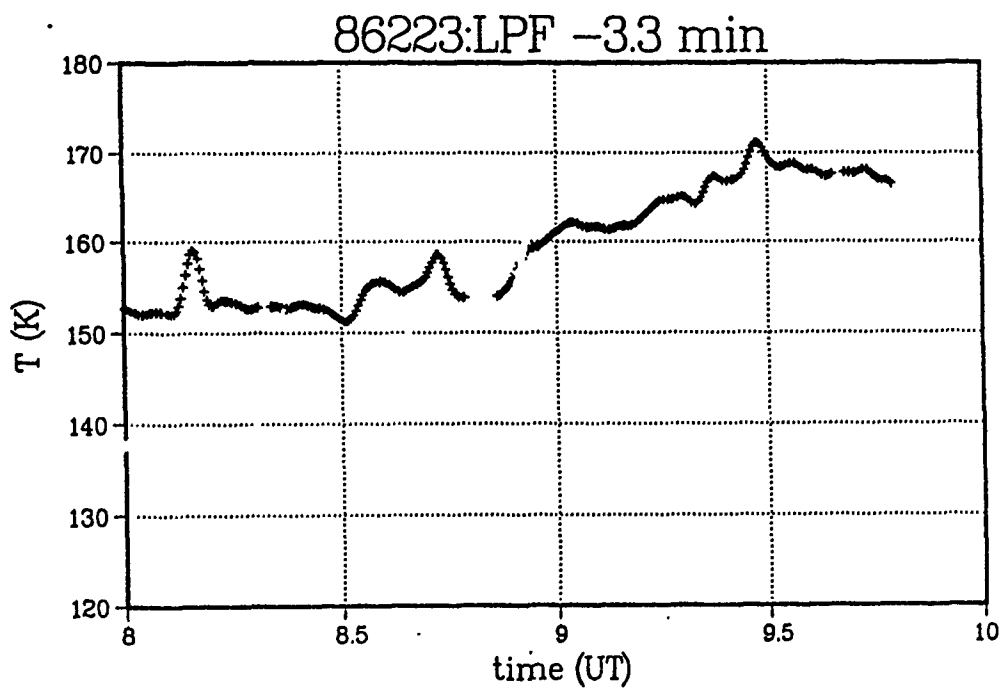
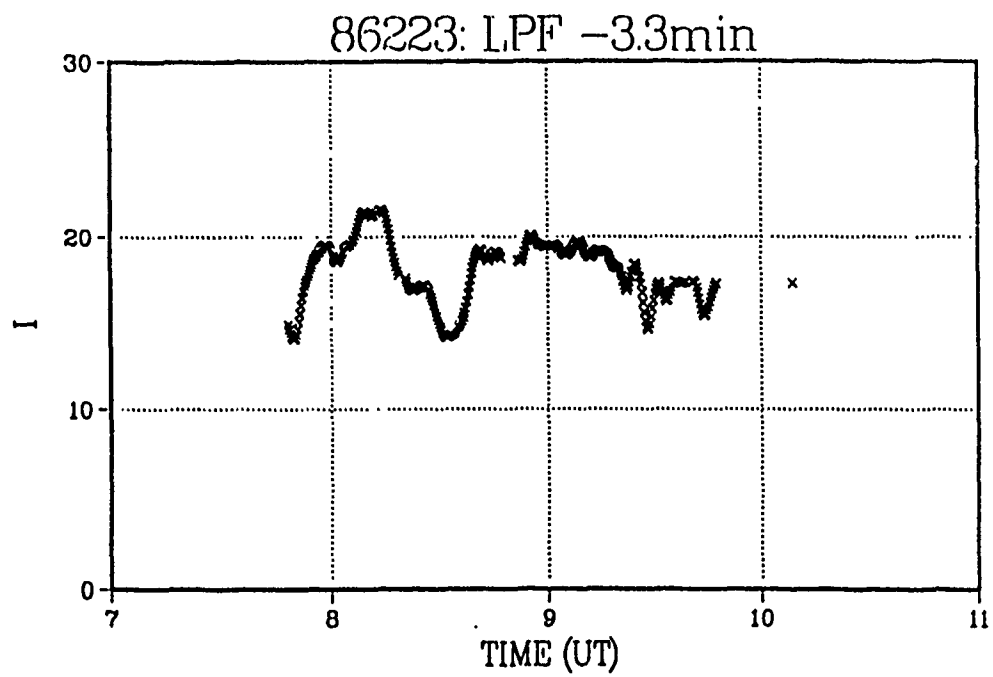


Fig. 5-4. Time domain analysis: (b) low-pass filter output

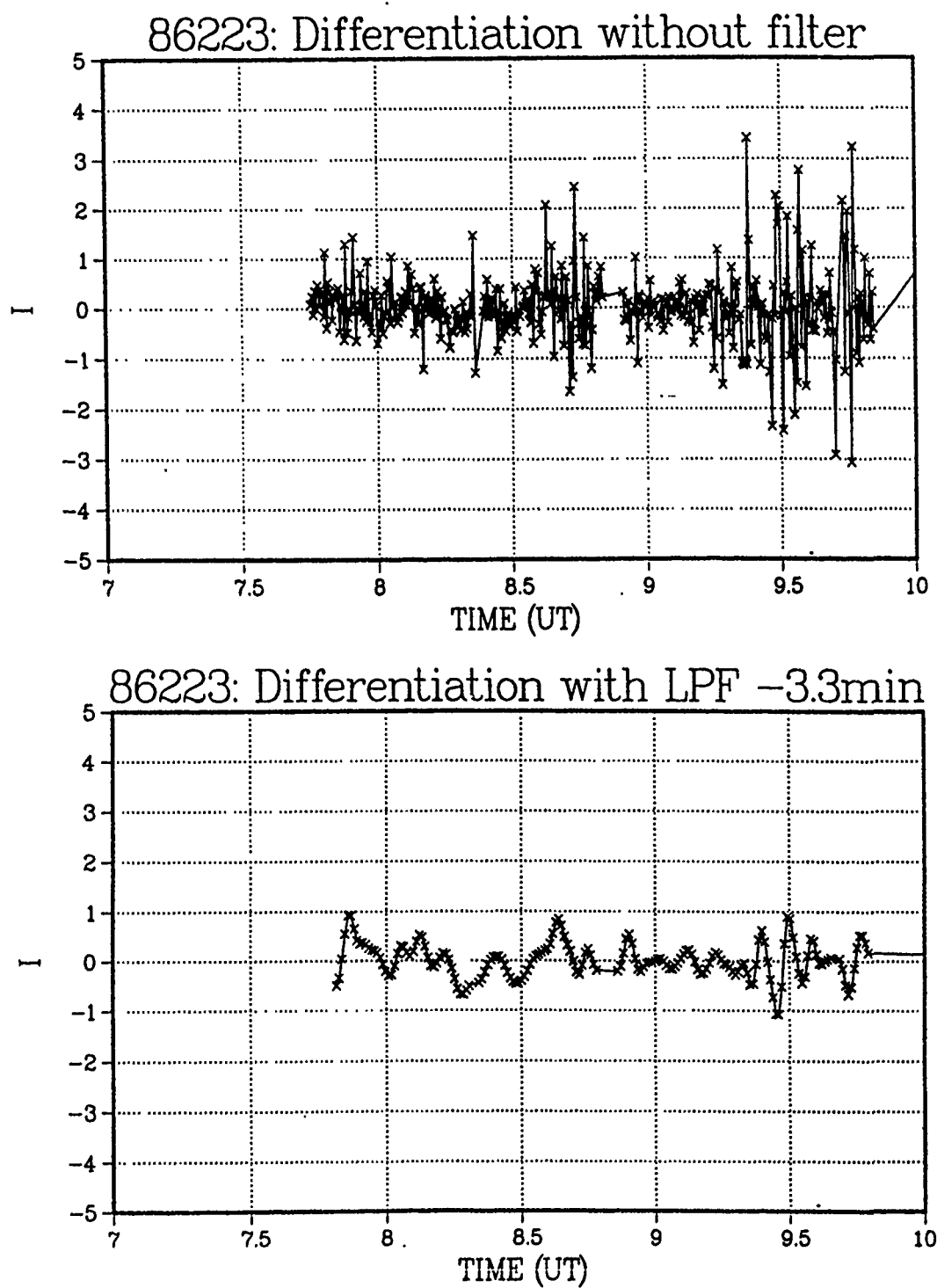


Fig. 5-4 Time domain analysis: (c) numerical differentiation

from wave packets whose durations are limited. The frequency domain analysis for such wave packets does not work properly, even if all other problems, such as data truncation and limited observation time, do not occur, because the original wave lasts only a few periods and varies its frequency rather than monochromatic. Use of the short-time Fourier analysis technique offers a limited solution to these problems. MEM may provide a better solution to overcome these limitations, but its own problems need to be resolved before MEM can be applied with confidence.

When the data are not long enough and/or signal to noise ratio is not good enough, the frequency cannot be determined from the data, even if the signal is monochromatic. Time domain analysis would work with such quality of data with fewer problems encountered in the frequency domain analysis. Since the short-period oscillation can be processed with the short-time Fourier analysis technique, the time domain analysis may be considered to process oscillations with long period, such as a few hours.

In the time domain analysis involving long period oscillations, use of a proper low pass filter is essential. This is especially true with the rotational temperature data with smaller signal to noise ratio and most noise has high frequency components. The linear phase shift property of the FIR filter is very significant for the time domain analysis because the phase relation between the emission intensity and the rotational temperature is the quantity of interest.

The output of a low-pass filter, or a band-pass filter if DC removal is needed, can be examined directly in time domain. Often the

data length is not sufficient to deduce the frequency, but the existence of wave activity may be identified. This technique may be useful when there is a large and slow change in the average emission intensity and/or the rotational temperature of the airglow.

In Fig. 5-4, the output of a low-pass filter can be used to determine the average quantity. Average quantities may be used to evaluate Krasovsky's  $\eta$  or the background stationary quantity in a study of oscillations with much shorter periods.

#### Example Data Analysis

In this section, the short-time Fourier analysis technique, the MEM and the time domain analysis technique are applied to experimental data taken by IRFWI in Pokerflat, Alaska during the summer of 1986. The dates are presented in their universal time (UT) format: the last two digits of the year followed by three digits representing the day in the year starting January 1st being 001. Time and date represents values at the longitude 0. The emission intensity is the band intensity for (3,1) band, and value is the direct output from the IRFWI data processing system developed by Espy [35]. The rotational temperature is reduced by the same system.

Fig. 5-5(a) presents the raw data and the same data with the linear interpolations and the simple DC removals. Fig. 5-5(b) presents their Fourier spectrum. Fig. 5-5(c) is the results of MEM on these data. The effect of a simple DC removal is demonstrated in these examples. The DC is removed by simply subtracting the average value of all data after they are interpolated with a straight line connecting the edge data of the truncated intervals.

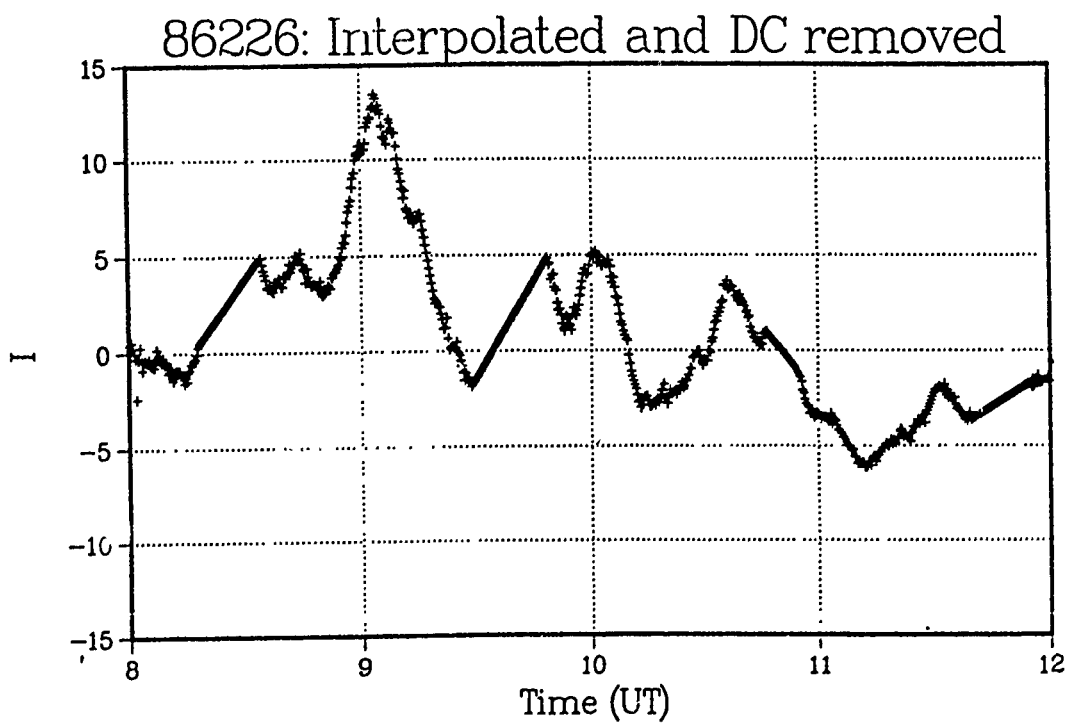
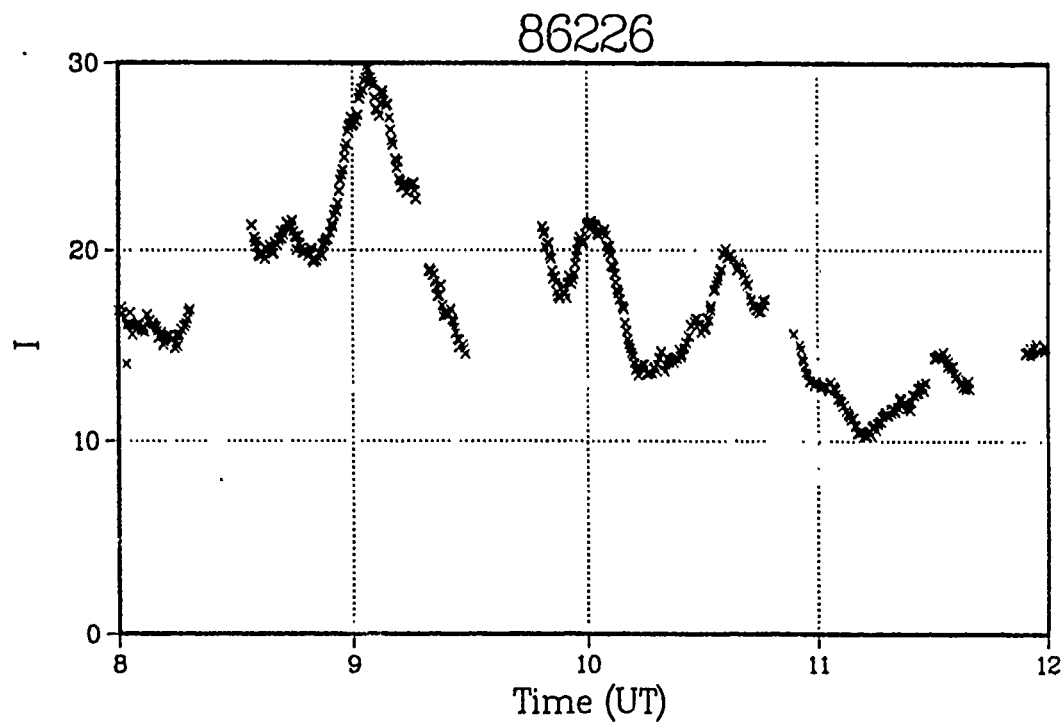


Fig. 5-5. Signal processing: (a) data

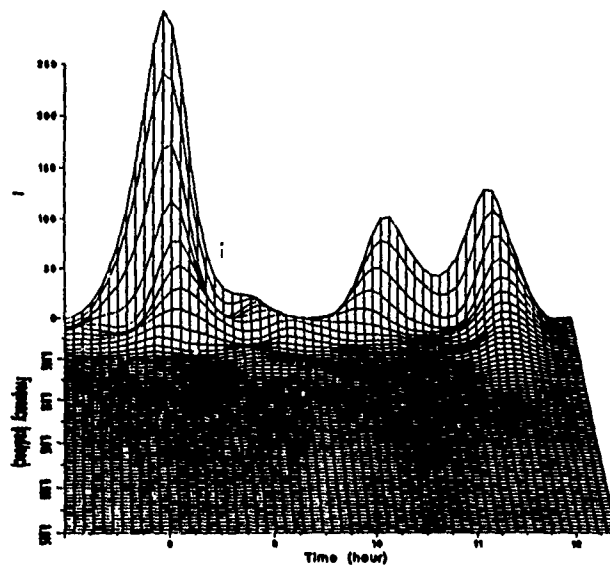
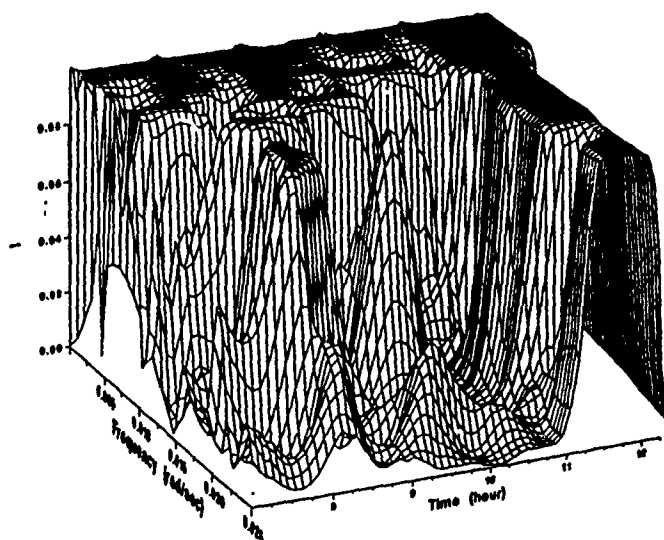
**86226 I:Hamming 85min****86226 I:Hamming 85min**

Fig. 5-5. Signal processing: (b) Fourier spectrum



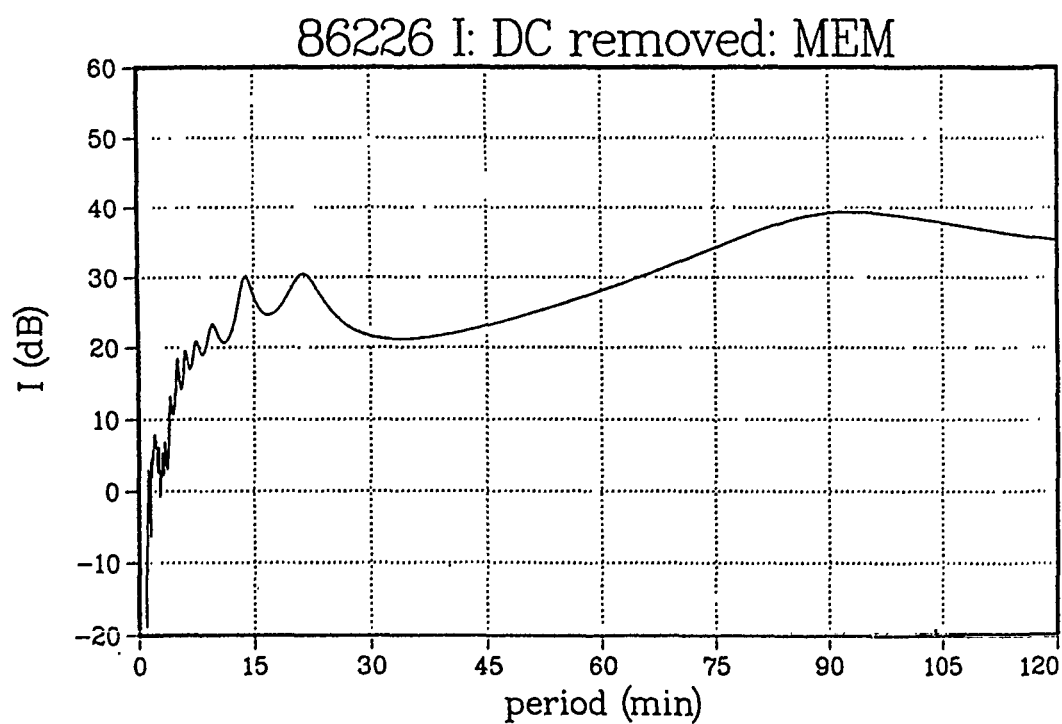
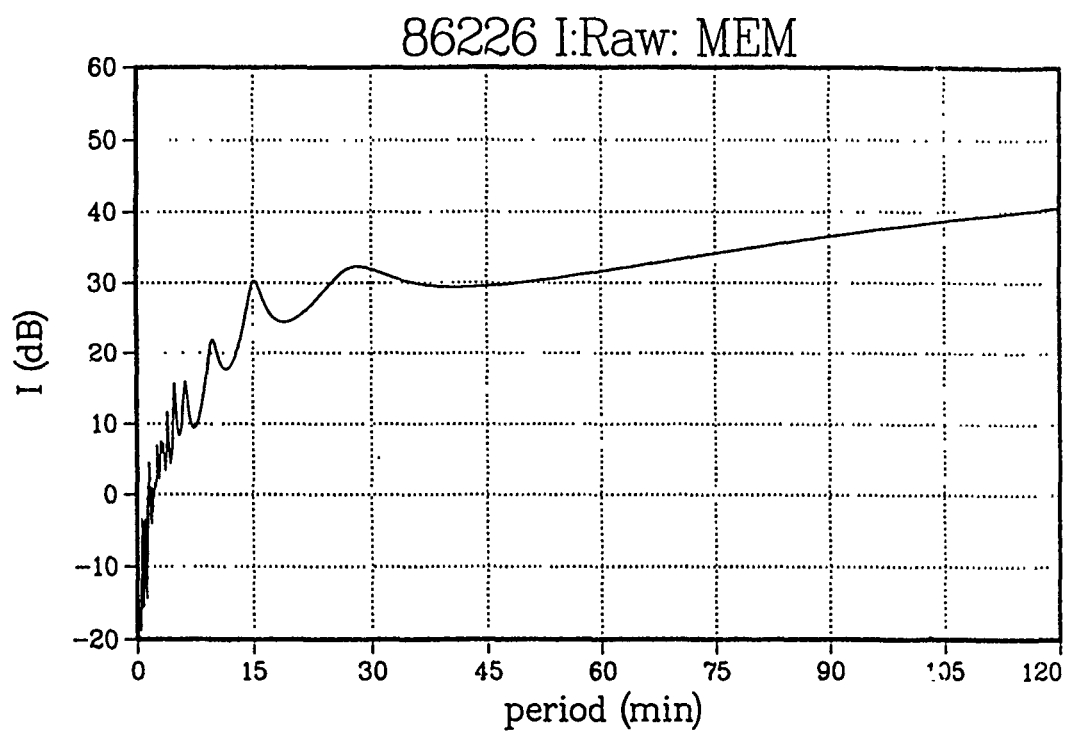


Fig. 5-5. Signal processing: (c) MEM spectrum

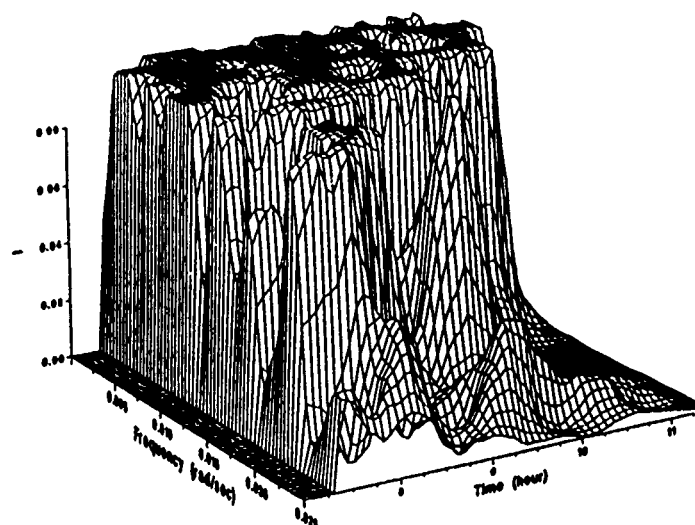
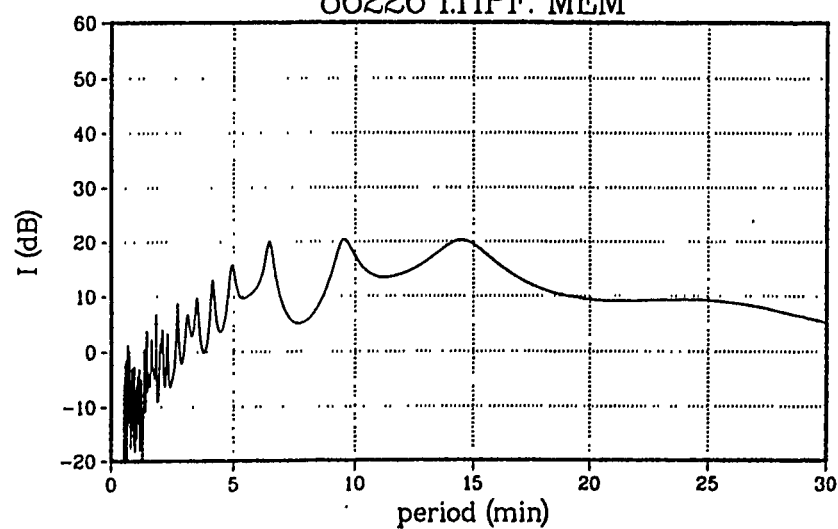
**86226 I:HPF:Hamming 85min****86226 I:HPF: MEM**

Fig. 5-5. Signal processing: (d) spectrum of output of high-pass filter (HPF)

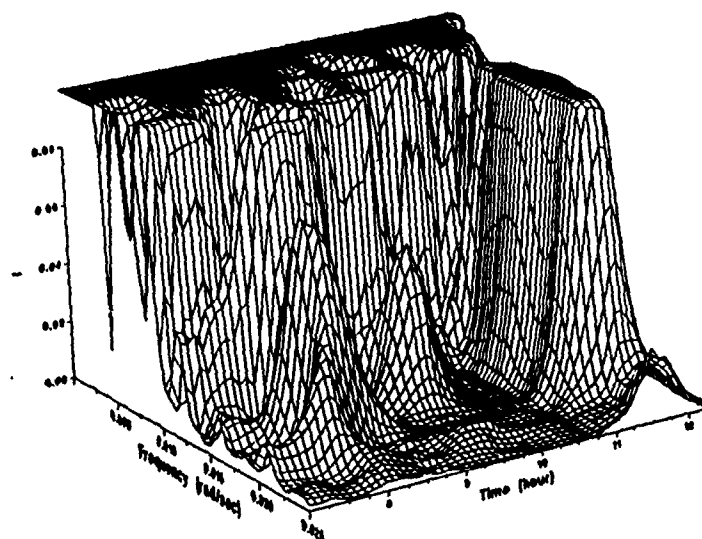
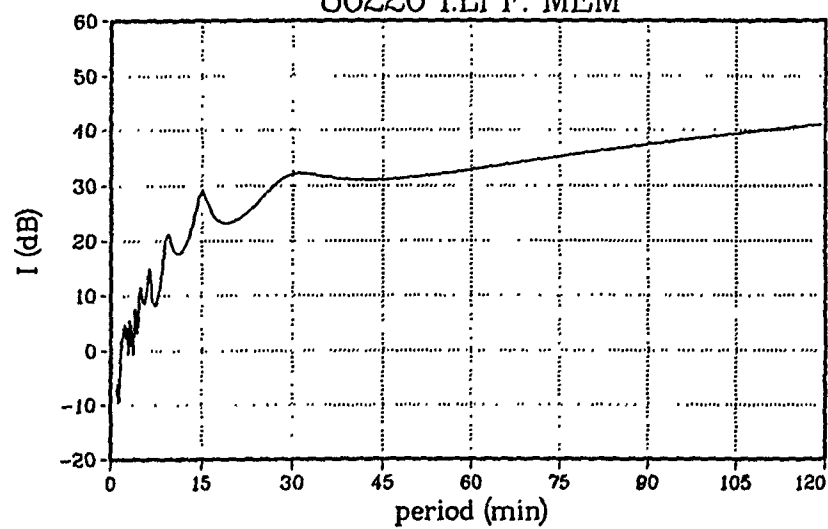
**86226 I:LPF:Hamming 85min****86226 I:LPF: MEM**

Fig. 5-5. Signal processing: (e) spectrum of output of low-pass filter (LPF)

# 86226 I:BPF:Hamming 85min

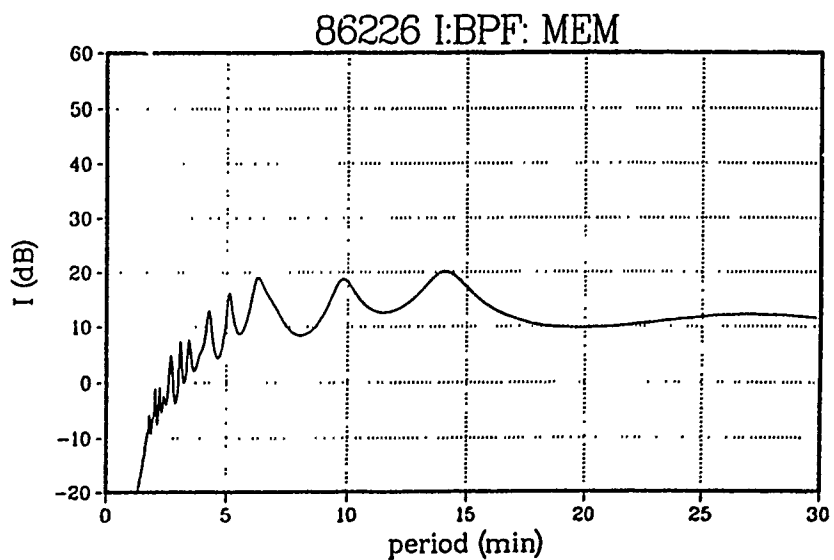
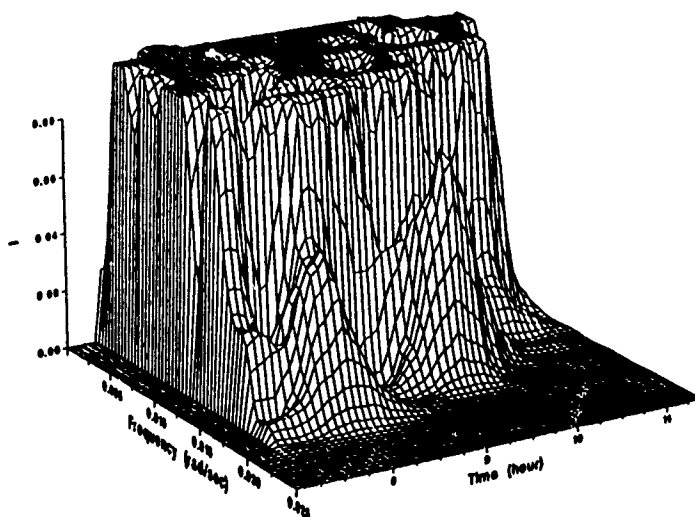


Fig. 5-5. Signal processing: (f) spectrum of output of band-pass filter (BPF)

The spectrograph can be plotted from any direction. The viewing angle of the plots can be chosen to optimize the sight for spectral peaks which have interesting features. Fig. 5-5(b) contains one such example, indicated by an arrow.

Fig. 5-5(d) demonstrates the effect of a high pass filter. The comparison reveals a major difference from the simple DC removal, especially in MEM. This figure includes the combination of the use of the filter and the DC removal, in this order. The effect of the DC removal is again significant in MEM.

Fig. 5-5(e) shows the effect of a low-pass filter. Since the raw signal contains many high frequency components, the effect is very significant in MEM. The DC removal causes great differences in all cases, especially with MEM.

Fig. 5-5(f) is the result of the use of a band pass filter. The results are combinations of the high and low pass filters. Again, the MEM demonstrates the most significant effect.

From these examples, the following conclusions about the signal processing techniques are derived:

1. DC removal is effective in all cases to distinguish long period signals and minimizes the interference of the DC sidelobe to short period signals.
2. Use of MEM is not recommended because it is too susceptible to data modification such as filtering and DC removal.
3. Long period signals become hard to detect once the window becomes shorter than the signal period. Therefore, window length should be as long as the amount of data allows.

4. Hamming windows perform reasonably in most cases. Use of Blackman windows may be considered when the interference becomes as large as the signal of interest.

## CHAPTER VI

## DISCUSSION

In this chapter, results of both theoretical models and experimental techniques are analyzed and interpreted. First, the data processing system developed in Chapter V is evaluated, comparing performances of different data processing techniques. Interpretation of the chirp signal detected by the signal processing system using the dynamic IGW model is demonstrated, providing the basis for the conclusions presented in Chapter VII. Secondly, observables for ground-based optical measurements are further analyzed. Finally, the validity and utility of Krassovsky's  $\eta$  parameter are discussed further, and the extension and limitations of  $\eta$  are discussed.

Data Processing and Interpretation

In Chapter V, several signal processing techniques were introduced and applied to different frequency ranges. These techniques were categorized as 1) high (30 minutes or shorter), 2) low (30 minutes to the inverse of the data duration) and 3) trends longer than the observation window. This incrementation is based upon the relationships between the oscillation period, the data length, and the window length used in the short-time Fourier analysis. These relationships affect both the choice of an appropriate filter and the performance of the signal detection technique.

Accordingly, this section is divided into three parts. The first part treats high frequency signal processing; the second part is the

low frequency signal case, and the third part is the long trend case. Design specifications of the finite impulse response (FIR) filters used and performances of the short-time Fourier analysis technique and the maximum entropy method (MEM) are included. Note that the value of 30 minutes used to differentiate the high and low frequencies is arbitrary and may be adjusted according to the data length. Longer data streams make longer boundaries, 45 minutes or more, possible. This boundary value is chosen to distinguish the frequency range which exhibits different characteristics of the interference with the data window.

#### High Frequency Signal Case

Relatively high frequency signals, with a period of 30 minutes or shorter, can be detected relatively easily compared to lower frequency signals because the data duration is usually much longer than the signal oscillation period so that a suitable window length for the short-time Fourier analysis can be easily chosen. The same condition also makes possible straightforward design of appropriate filters, although it has been found that no filter is necessary in most cases to detect high frequency signal.

Filters are not needed as long as the magnitude of the signal of interest is much larger, such as a factor of 10, than the sidelobes of the undesired frequency peak in the low frequency range. When a low frequency or DC signal is so strong that its sidelobes may interfere with the high frequency signal, a high pass filter must be used. Any filter, including an FIR filter, has some ripples in its pass band characteristics, so the use of a filter can attenuate the desired



signal as well as the unwanted low frequency signal. Results with and without a filter need to be compared when the frequency of the signal of interest is close to the filter cut-off frequency. Also, by using windows with different lengths, which produces sidelobes at different frequencies, the distinction between a sidelobe and a faint signal may be made. It is within this frequency range that most of the chirp is detected with the short-time Fourier analysis technique of Chapter V.

In case of high-pass filters, an additional DC blocker may introduce a spurious low frequency component as well as removing DC, but a simple clipping of such large components revealed that they do not spoil the high frequency signal, as long as their sidelobes are at least 10 times smaller than the signal of interest. Since an IGW spectrum is limited by the Brunt-Vaisala frequency, an appropriate band-pass filter may be used for visual clarification in time domain analysis without masking possible signals produced by the IGW. The Brunt-Vaisala frequency in the mesosphere corresponds to a 4 to 8 minutes period depending upon the temperature (Appendix A).

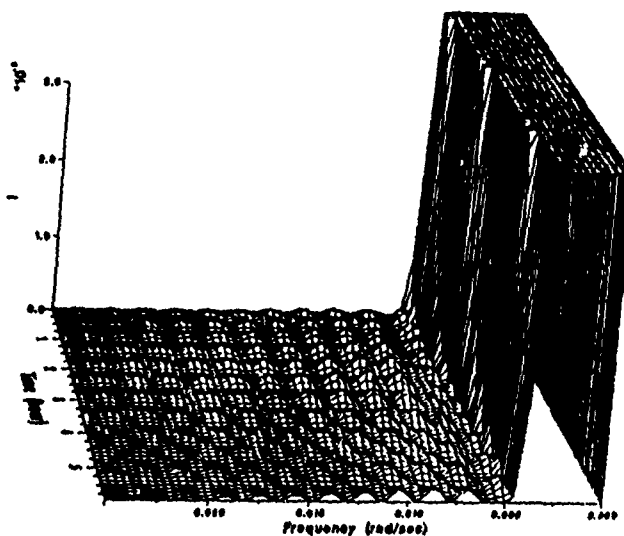
Although use of a filter does not affect the output of the short-time Fourier analysis, it alters the magnitude of spectral peaks for all frequencies in MEM output. Also in MEM, locations of some peaks shift as a result of filtering. Because of such instabilities, the MEM should be used only as an auxiliary method to other technique such as the short-time Fourier technique. Similar frequency shifts and magnitude variations are reported as a result of noise [37]. In some case, a single peak splits into two in the presence of weak noise for

reasons not fully understood [37].

It may be necessary to remove the DC component, slow trends and low frequency signals when these signals are large, causing significant sidelobes in high frequency region which can directly interfere with high frequency signals. With the use of an appropriate window function which produces small sidelobes, this difficulty may be avoided without removing a low frequency signal. Fig. 6-1(a) shows several window sidelobes in a three-dimensional spectrogram of the generated chirp signal used in Chapter III (Fig. 3-8). The peak of the signal has a magnitude of 4, and it is noted that the figure has a scale of order of  $10^{-3}$ . Comparison with the example in Fig. 5-5 suggests that the small peaks in Fig. 5-5(b) are real signals, not sidelobes of lower frequency signals. These peaks are almost 100 times larger than the expected sidelobe magnitudes for the Hamming window. Without such a window function, the sidelobes would be comparable, or even larger, than the small high-frequency signals.

Another way to distinguish the sidelobe of a low-frequency signal and a true signal in high-frequency domain is the use of windows with different length. Figure 6-1(b) represents the same spectrograph in Figure 5-5(b) with a different scale of signal amplitude. They are the same data with three different windows, 60, 75 and 85 minutes long. All of the resultant spectrograph shows small peaks in UT-10-11 at  $\omega \approx 0.01$ . The magnitude and height of the peaks change, but the frequency remains the same. This indicates that these peaks represent true signal, because the sidelobes of different length windows have different frequencies.

Hamming 60min



Hamming 85min

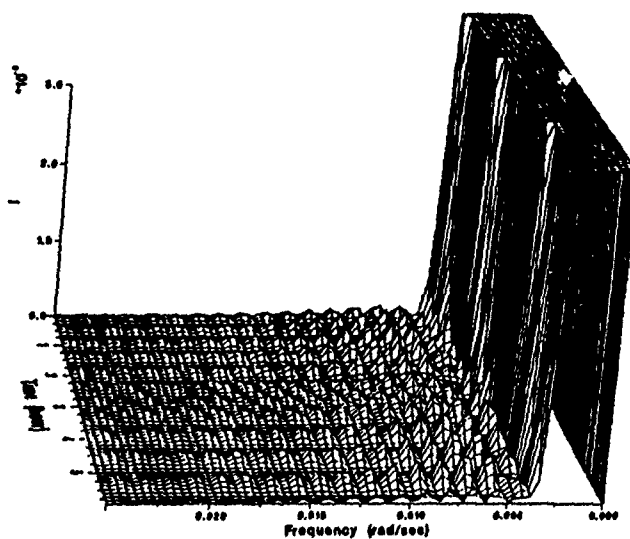
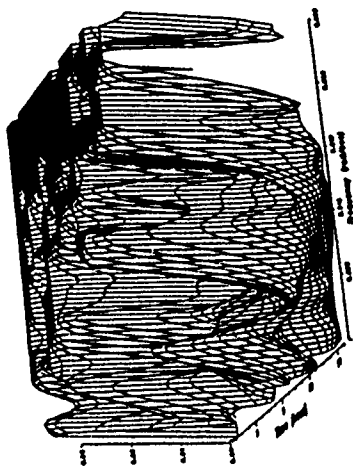
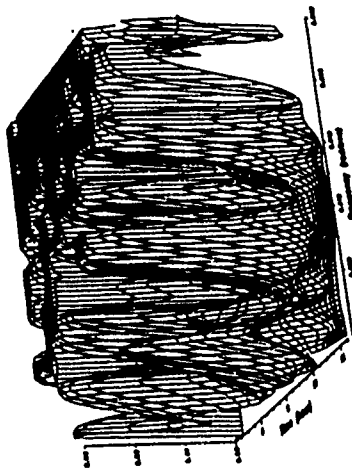


Fig. 6-1. Effect of windows of different lengths: (a) Sidelobes with Hamming windows of different length

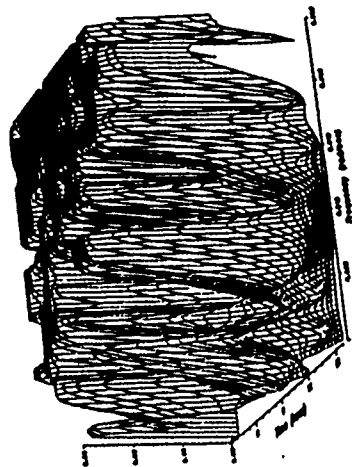
86226 I:HPF:Hamming 60min



86226 I:HPF:Hamming 75min



86226 I:HPF:Hamming 85min



86226 I:HPF:Blackman 85min

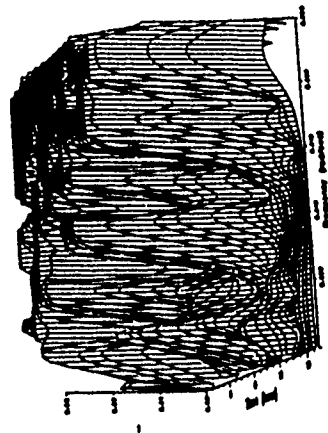


Fig. 6-1. Effect of windows of different lengths: (b) Magnified spectrograph with several windows

Because it is possible to detect high frequency signals under presence of rather strong low-frequency signals using the short-time Fourier analysis technique, use of a filter may be avoided since a filter truncates the data. The high pass filter used in Fig. 5-5 requires 180 data points to calculate an output value and truncates half of the required points, 90 points, or 30 minutes worth of data at the beginning and end (20 second sampling interval multiplied by 90 equals 30 minutes). In the intensity data of UT date 86226, the use of the filter causes the loss of signal after 12 UT which contain significant peaks found in the non-filtered data.

In summary, the short-time Fourier analysis technique works without any major problems in the study of high frequency signals. The FIR filter may be useful in time domain studies but is not needed in short-time Fourier analysis. Because the use of filter truncates both ends of time domain data, the use of filter should be avoided in the short-time Fourier analysis. Chirp signals are expected to change their amplitude as well as frequency as functions of time, so careful study of the spectrograph is needed to detect them.

#### Low Frequency Signal Case

Oscillations with longer than 30 minute periods are subject to a serious interference with the data window. Thus, the removal of DC is necessary and can be accomplished by subtracting the average from each data. MEM sometimes detects a peak at very low frequency, even longer than the data period. It is known that MEM is capable of detecting signals with periods longer than the duration of the observed data. However, in the presence of noise, operations such as

the removal of DC or use of filters of all kinds, may cause faulty peaks at all frequencies [37], and therefore may not be completely accurate. The use of the time domain analysis may be used to test the result of MEM.

If more than one signal cycle is included in the data, with DC removal, the short-time Fourier analysis technique can be used. Since the uncertainty in frequency is comparable with the oscillation frequency, the detection of the frequency variation as a result of chirp may not be performed well in this frequency range.

As the example in Fig. 6-1(a) indicates, the resultant spectrum of the short-time Fourier analysis varies according to the phase of the signal within the window. Similar effects of the signal phase is reported for MEM [37]. The time domain signal analysis is needed to assess the result of frequency domain analysis by observing such phase characteristics.

### Trends

In this study, the word "trend" refers to a slow signal variation caused by a very long period oscillation or a slow change due to some other factor. The Fourier transform technique may not be applied to a signal when data contain less than a single cycle of the signal. MEM is capable of detecting a peak in such cases, but the resultant spectra are subject to noise and the phase of signal in data [37]. The effect of filtering may be interpreted as a result of redistribution of noise by such filters. Therefore, the results of MEM analysis need to be analyzed with an aid of some other method. One such method used in this dissertation is the representation of signal in

the time domain. The low pass filter may be used to clarify the low frequency variation (Fig. 5-4). Fig. 6-2 represents the MEM spectrum of the same data, detecting a peak at about 70 minutes. The visible trend in the time domain representation is slightly longer than an hour, giving consistent results (Fig. 5-4).

It is noted that whether a signal frequency is "low" or "high" is determined only with respect to the window length, and not related to any physical characteristics of IGWs. Several windows with various lengths may be used for different frequency range analysis. The three dimensional spectrograph will help such overall approach.

#### Source Distance Estimation

The distance between the source of an observed IGW and the observed location can be estimated using the spectrograph and the dynamic IGW model presented in Chapter III.

Fig. 6-3 shows two days of IRFWI data taken in Pokerflat, Alaska (147.5 W 65.1 N), during the summer of 1986. Fig. 6-3(a) and (b) are spectra of the intensity and the temperature of the UT day 216, and Fig. 6-3(c) and (d) are spectra of the intensity and the temperature of the UT day 223 respectively.

These examples contain several peaks indicated by the arrows in which frequencies change with time. It is expected in the result obtained in Chapter III that the high frequency IGW signals are likely to chirp towards higher frequency. The series of peaks in the spectrograph of the temperature data on day 223 are consistent with the model prediction. Signals longer than one hour are likely to chirp towards a lower frequency at a rate indicated in Fig. 3-11.

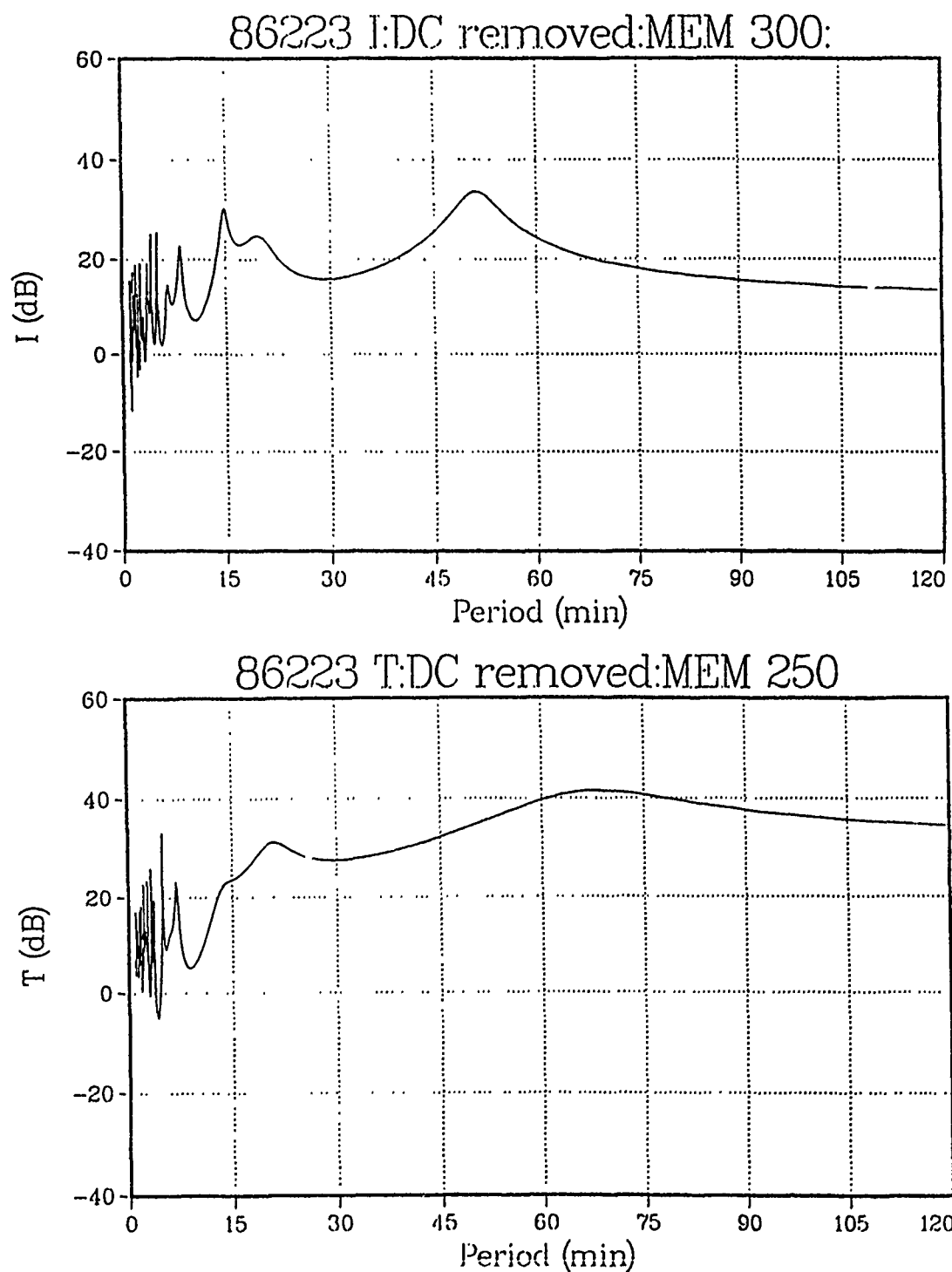
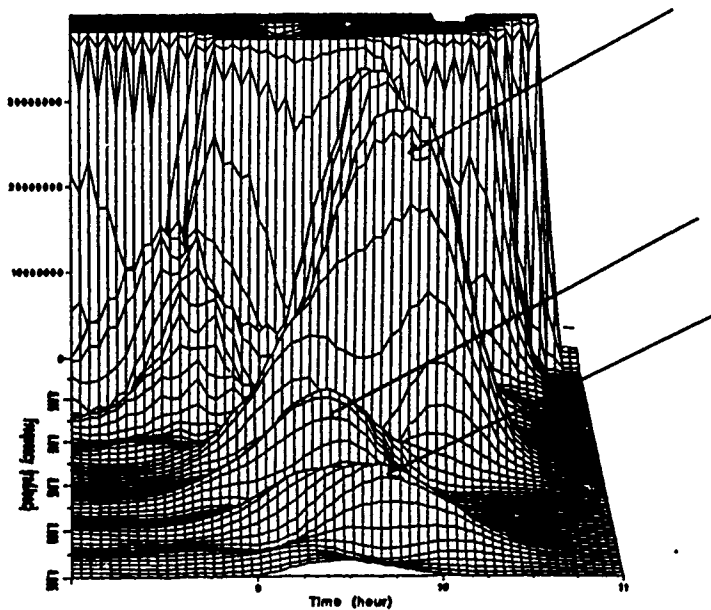


Fig. 6-2. Time domain data and MEM spectrum



### 86216 I:Hamming 85min



### 86216 I:Hamming 85min

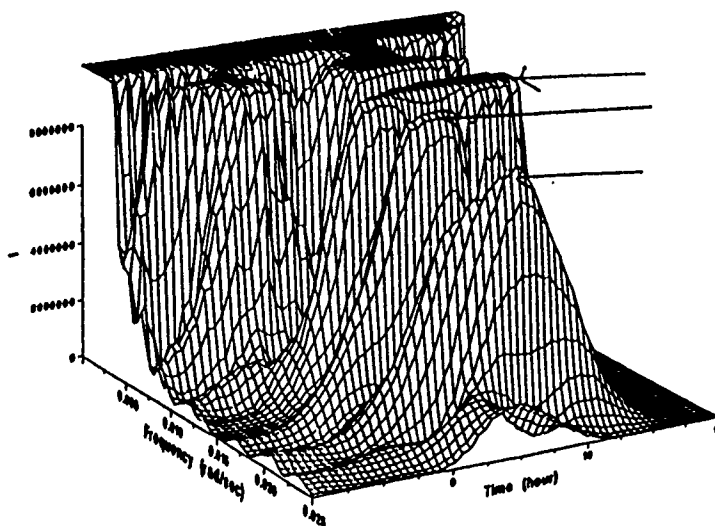


Fig. 6-3. Fourier spectrum: (a) Intensity: day 86216

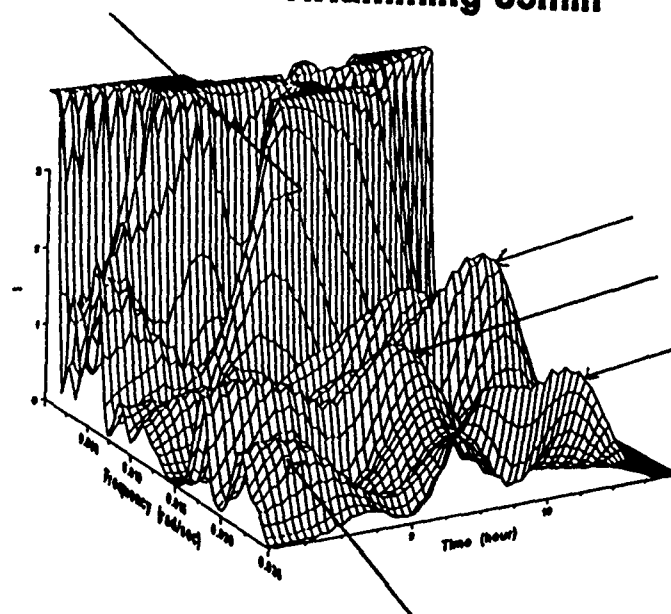
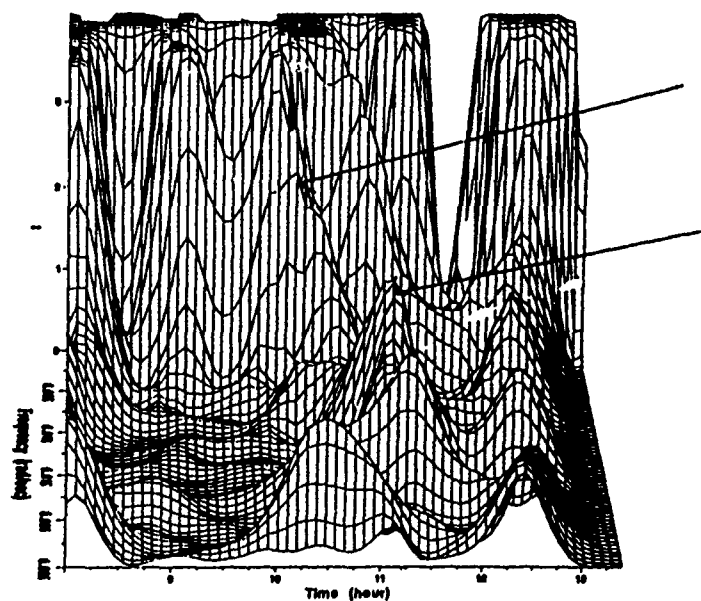
**86216 T:Hamming 85min****86216 T:Hamming 85min**

Fig. 6-3. Fourier spectrum: (b) Temperature: day 86216

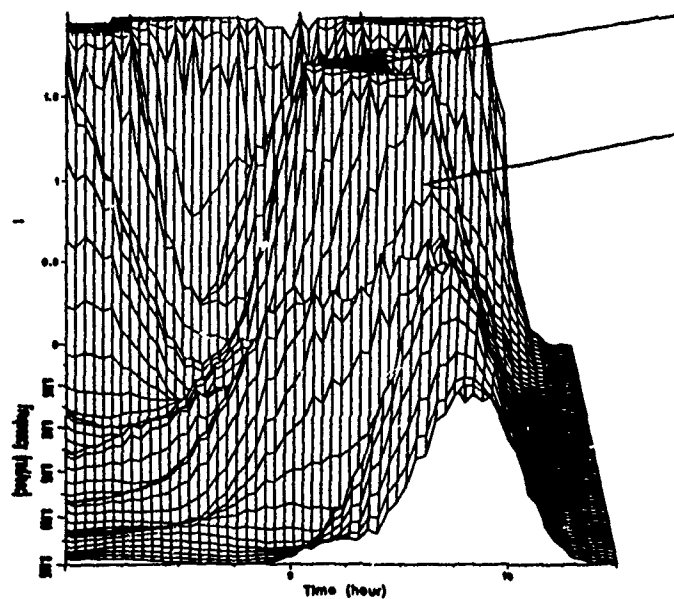
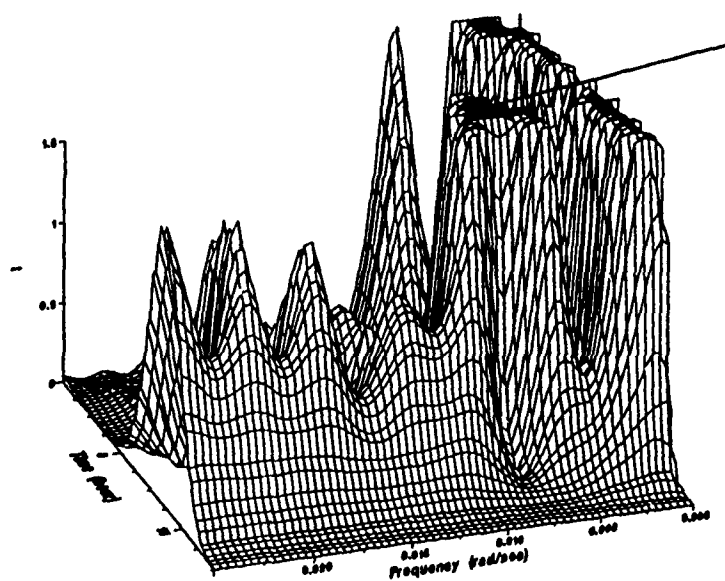
**86223 I:Hamming 85min****86223 I:Hamming 85min**

Fig. 6-3. Fourier spectrum: (c) Intensity: day 86223

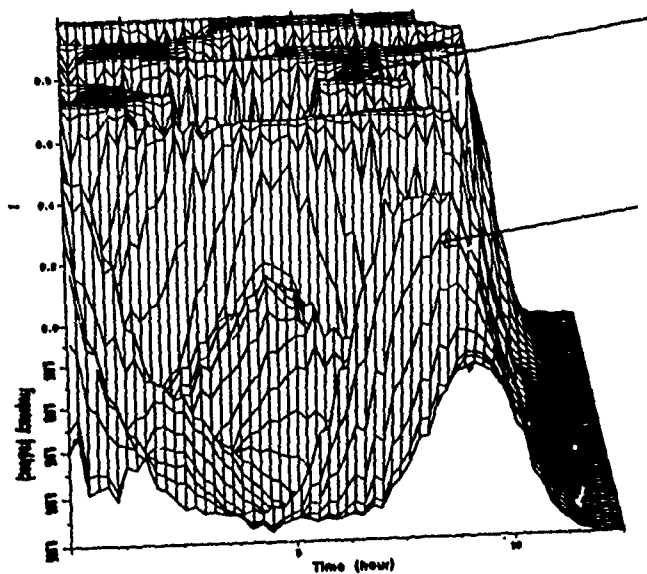
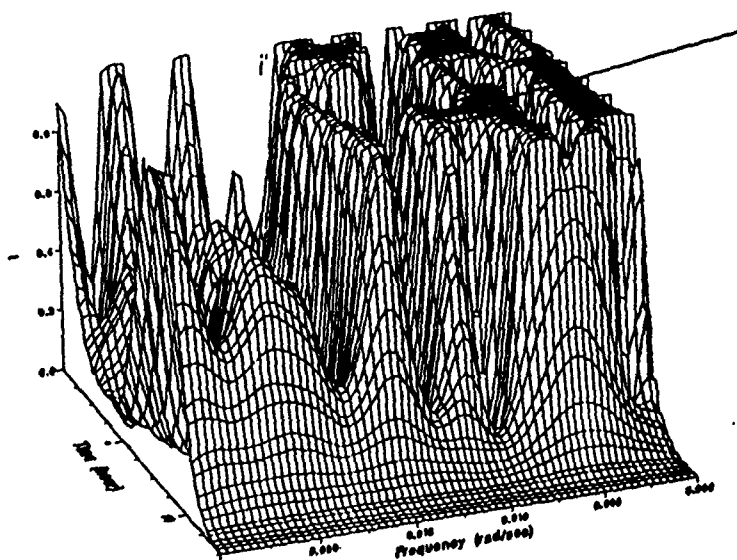
**86223 T:Hamming 85min****86223 T:Hamming 85min**

Fig. 6-3. Fourier spectrum: (d) Temperature: day 86223

The interference of the window and low frequency signal, as well as such frequency change, makes the detection of a chirp at low frequency difficult.

The temperature contains a more complex spectral structure than the intensity due to the geometric effect explained in Chapter IV, where it was demonstrated that the observable intensity is subject to different cancellation mechanisms from the observable rotational temperature, resulting in more serious cancellations. In the day 223 measurement, the large, low frequency peak in the intensity spectrum at 9.6 UT is not observed in the temperature spectrum. This can be also seen in the time domain representation in Fig. 6-2(a). The temperature curve is almost flat after rising significantly. This may not be a part of a sinusoidal wave.

According to Fig. 3-11, for each IGW elevation angle  $\alpha$ , certain frequency components travel at the fastest speed, and the chirp starts towards both high and low frequency from this particular frequency. The low frequency component has an asymptotic value given by equation (3.7) and Fig. 3-9 for each  $\alpha$ . The high frequency limit is always the Brunt-Vaisala frequency. Near the fastest travelling frequency, the frequency variation rate is much larger than near the both limiting frequency (Fig. 3-11).

It is possible to estimate  $\alpha$ , therefore the distance of the IGW source, using the frequency variation rate. A fast frequency variation indicates that the observed frequency is close in value to the fastest travelling frequency. A slow frequency change rate observed in the low frequency branch indicates that the observed

frequency is close in value to the limiting frequency. By estimating either the fastest travelling frequency or the limiting frequency, the elevation angle  $\alpha$  may be estimated. This is a useful technique by which the distance of the ICW source may be estimated. This model may be tested by measuring both the fastest and limiting frequencies and testing if the  $\alpha$  obtained by the two methods are consistent.

There is another way to estimate  $\alpha$  if a chirp signal is found in the frequency range between both limiting frequencies and near the fastest travelling frequency. The fastest travelling frequency can be determined whether it is lower or higher than the observed frequencies by the direction of the frequency chirp, as shown in Fig. 3-11. This also allows for an estimate of the fastest travelling frequency. Therefore, the distance of the ICW source can be estimated.

In the example of Fig. 6-3(a) and (b), the day 86216, the three peaks at UT=9 to 10 and  $\omega \approx 0.026$ , 0.016 and 0.012 (rad/sec), or  $T \approx 4$ , 6.5 and 8.5 (minutes), exhibit chirp towards higher frequency. This example also has a peak at UT=8.8 to 9.5 and has  $\omega \approx 0.006$ , or  $T \approx 17$  (minutes), chirping towards a lower frequency which is visible in the temperature spectrograph but not in the intensity. According to Table VII and Fig. 3-9, this indicates that  $\alpha$  is less than 20 degrees, and the distance to the source can be estimated longer than 240 kilometers.

In the example of Fig. 6-3(c) and (d), on the day 86223, a few small peaks at high frequency are also seen, but there are two large peaks of particular interest (only one is visible in the intensity spectrograph). They appear as the fastest travelling frequency

components followed by chirps towards both high and low frequencies. Their fastest travelling frequency components are 0.008 and 0.005 (rad/sec), or  $T=13$  and 21 minutes. They correspond to, according to equation (3.7) and Table VII,  $\alpha=28$  and 17 (deg) and  $L_x=170$  and 290 (km).

Such distance estimation will help to identify the source, especially if combined with the directional information. In the above examples, the direction was not available.

### Observables

The geometric effect significantly influences observed emission oscillations, especially in the high frequency components which is associated with short vertical wavelengths. The effect on the observed rotational temperature can be significant, but the magnitude of the effect was found to be on the same order of uncertainties caused by other mechanisms such as instrument error, noise in instrument, noise in signal and water vapor absorption. The geometric effect upon the rotational temperature is two-fold: 1) cancellation in oscillation amplitude and 2) non-gaussian distribution of brightness-weighted temperature. Further study is needed to reduce, or if possible to remove, these uncertainties.

Using the off-zenith geometric effect model, it is possible to estimate IGW parameters with a measurement covering a wide viewing angle. The IGW parameters such as  $\omega$ ,  $k_x$  and  $k_z$  can be reduced using the off-zenith geometric effect model, provided that the apparent wavelength can be measured. To observe the wavelength, it is necessary to measure a wide field of view (fov) that extends more

than one apparent spatial wavelength at sufficient resolution. The resolution must be at least half the apparent wavelength to satisfy the sampling theorem. Because the direction of propagation needs to be measured at the same time, to avoid aliasing, the resolution within the fov should be much higher than the Nyquist frequency. For an IGW with the period of 15 minutes to several hours, the theoretical apparent wavelength is between a few tens to a few hundred kilometers. The packet speed of such wave is 150 to 250 m/s, using equations (A.14) and (A.15), so it takes about one hour for the wave to travel on the order of 500 kilometers. It is necessary to measure more than several periods of a wave without major interruptions. One measurement instrument which can satisfy such requirements is an infrared imager [5]. The use of an infrared all-sky camera will help evaluate data from instruments with smaller fov. As the viewing elevation angle decreases, closer to the horizon, the optical path becomes more involved with air refraction, scattering and water vapor absorption, as well as more serious geometric effect. Therefore, the low-angle observation should be limited to the emission intensity measurement, not the rotational temperature which is more sensitive to those interferences.

Using the Hines' IGW model, a relation between  $\omega$ ,  $k_x$ ,  $k_z$  and the distance from the IGW source and the observation location can be obtained. Equation (3.6) gives the  $k_x$ , or the horizontal wave length as a function of  $\omega$  and the elevation angle  $\alpha$  of the wave propagation.



$$k_x^2 = \frac{\omega^4}{c^2} \frac{(\omega^2 - \kappa\omega_g^2)}{(\omega^2 - \omega_g^2)(\omega^2 + (\omega^2 - \omega_g^2)\tan^2 \alpha)} \quad (3.6)$$

Assuming the height of the airglow layer, the distance of the wave source can be calculated using the elevation angle. Fig. 6-4 gives such relations for several oscillation period. Since the observed vertical wavelength is usually 8 to 15 km regardless of frequency, it seems that relatively small portion of possible waves are actually observed. From this relation, it may be possible to estimate the distance of the source using measured  $\omega$  and  $k_x$  or  $k_z$ . Because  $\lambda_x$ , the horizontal wavelength, is a steep function of the distance and  $\omega$ , it is practical to test the correspondence between  $\omega$  and  $\lambda_x$  first. Because the observed vertical wavelength is limited, the distance may be obtained from either  $\omega$  or  $\lambda_x$  alone since the two have almost one to one relation. More observational data including wavelengths need to be accumulated to test this method.

#### Discussion on Eta

In this section, the implementation and utility of Krassovsky's parameter  $\eta$  is further discussed. As was shown in previous chapters, experimental data would seldom, if at all, be appropriate to calculate eta as originally defined. Instead, signal processing techniques suitable for the likely data characteristics were developed.

The original  $\eta$  is defined under the assumption that the airglow layer is much thinner than the vertical wavelength of an IGW. Therefore, in case of long period oscillations with long wavelengths,

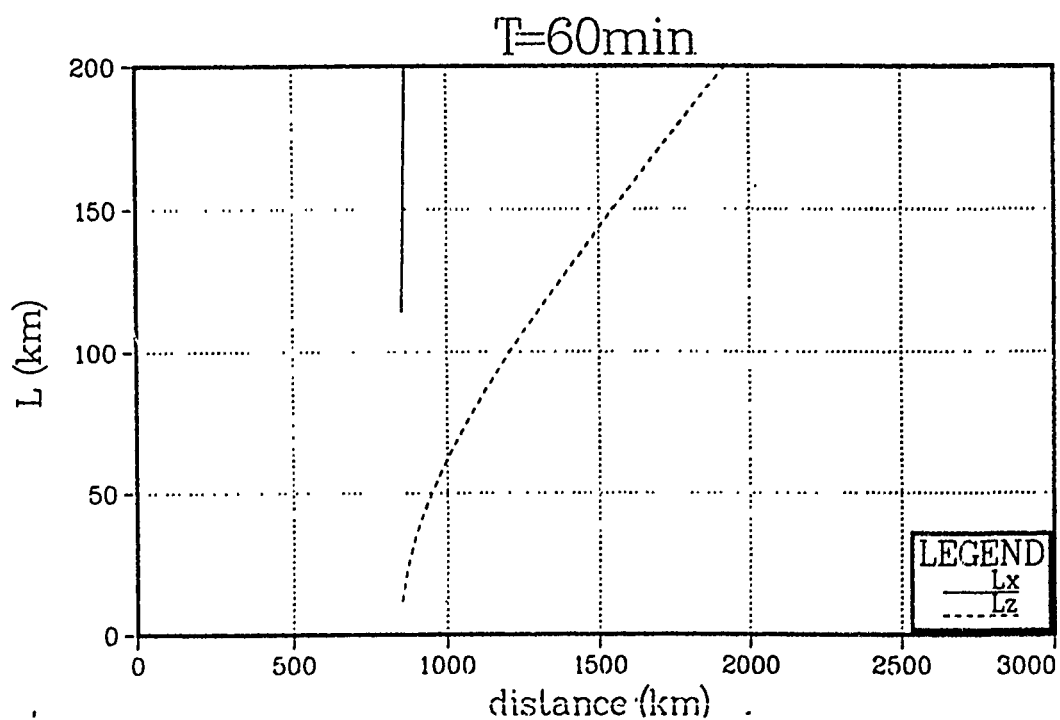
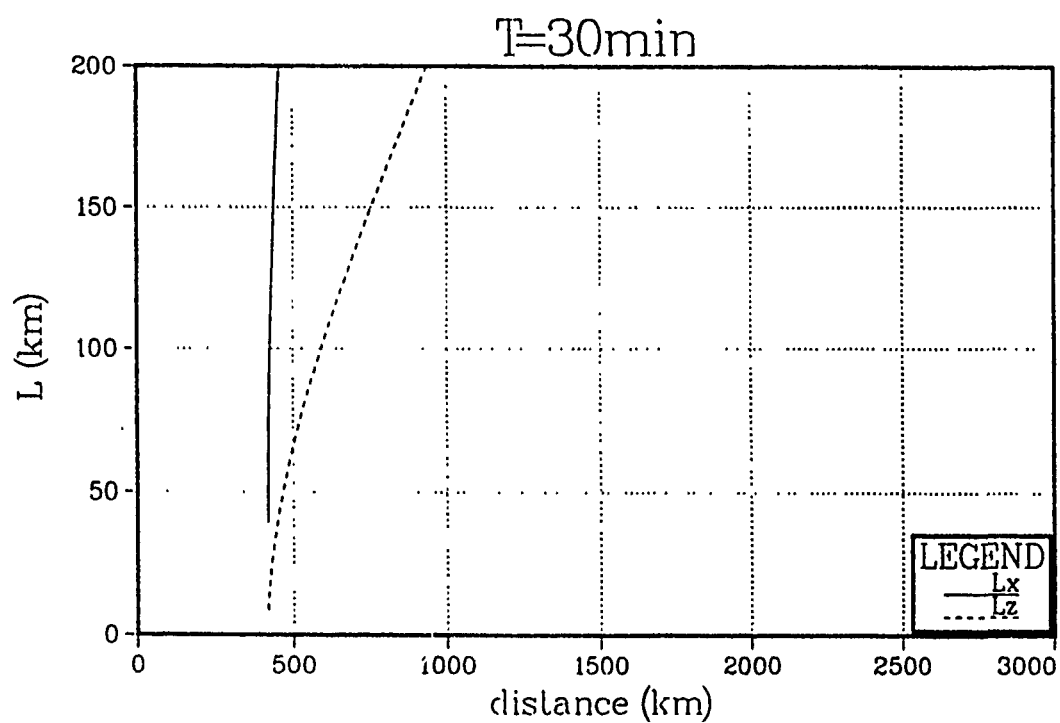


Fig. 6-4. Wavelength, frequency and travel distance

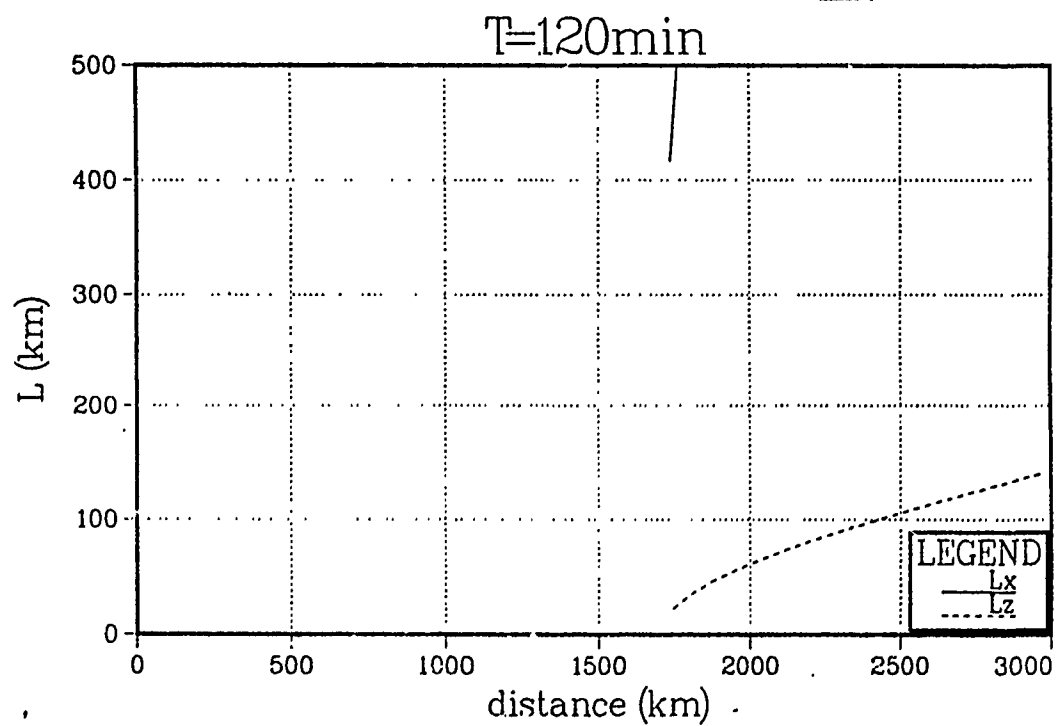
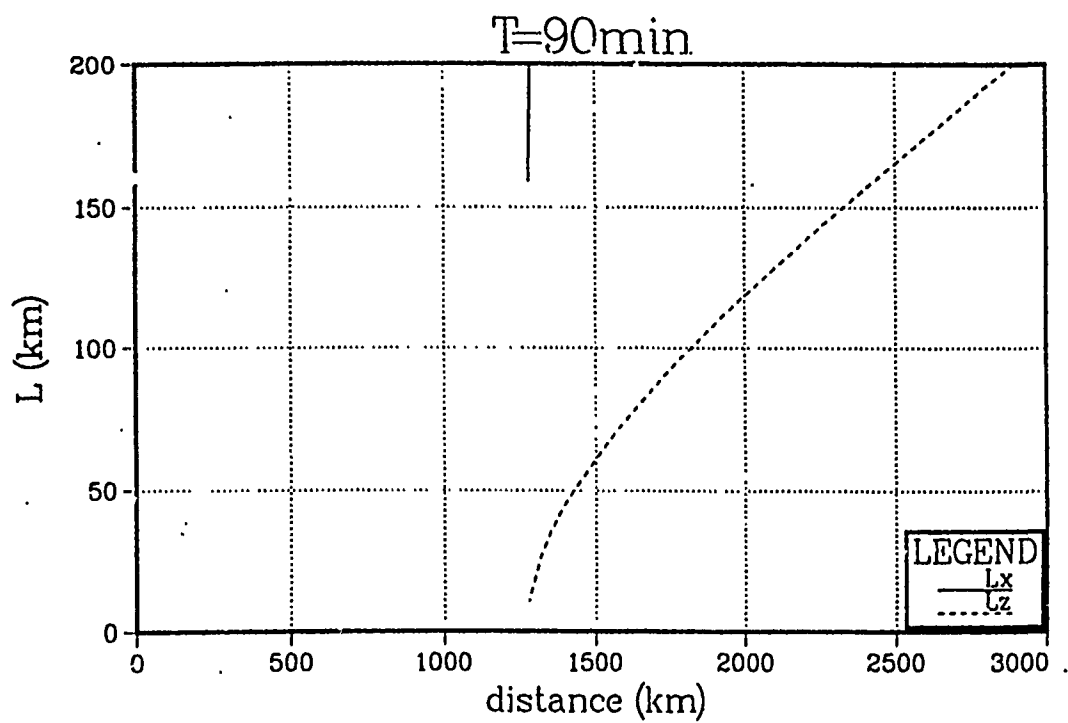


Fig. 3. Length, frequency and travel distance (continued)

such as a few hours with longer than 500km horizontal wavelength, the  $\eta$  may still be calculated using the original definition. Such observational data conditions require several hours of continuous measurement with the use of a low-pass filter. The applicability of the time domain signal processing is most suitable in this kind of study, since it is a similar method used by Krassovsky in his introduction of  $\eta$ .

The concept of  $\eta$  may be utilized in the case where  $\eta$  is not limited to a quasi-sinusoidal wave with constant background for both the emission intensity and temperature. As was suggested in Chapter II,  $I$  and  $T$  can be instantaneous values and  $dI$  and  $dT$  can be the time derivatives of the emission intensity and the temperature respectively. The resultant  $\eta$  should be of the same value according to (2.53). The derivation by Krassovsky did not include the geometric effect introduced in the present study, and as a consequence, (2.53) is limited in accuracy of values of  $\eta$  in model calculations.

In computing both intensity and temperature, as is shown in Fig. 6-5(a), each data point has an error, or uncertainty. The central values exhibit discontinuities, resulting in the large signal component at the frequency corresponding to the time interval between data points. Since this component caused by the sampling is spurious, an optimal filtering process is necessary. Because of the phase property, an FIR digital filter is desirable, provided that sufficient data points are available. Without filtering, calculating  $dT$  as:

$$dT = T(t+\Delta t) - T(t) \quad (6.1)$$

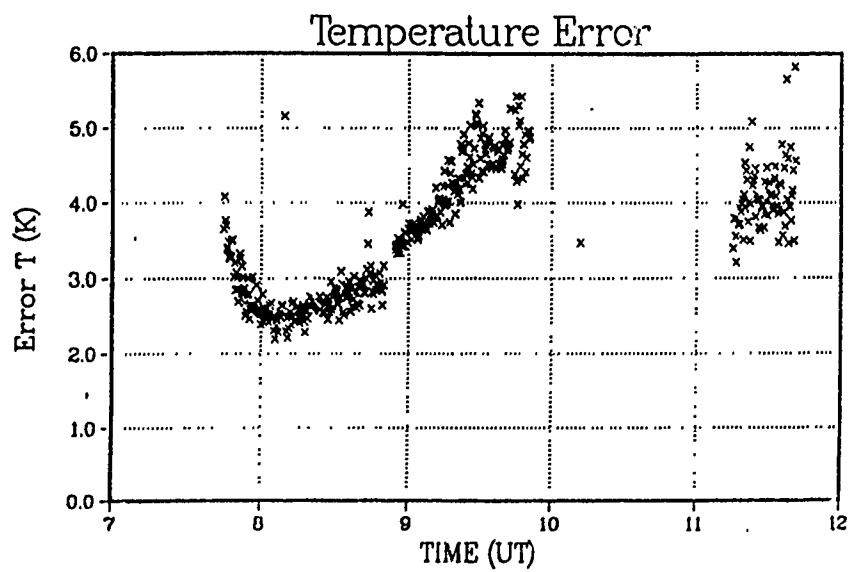
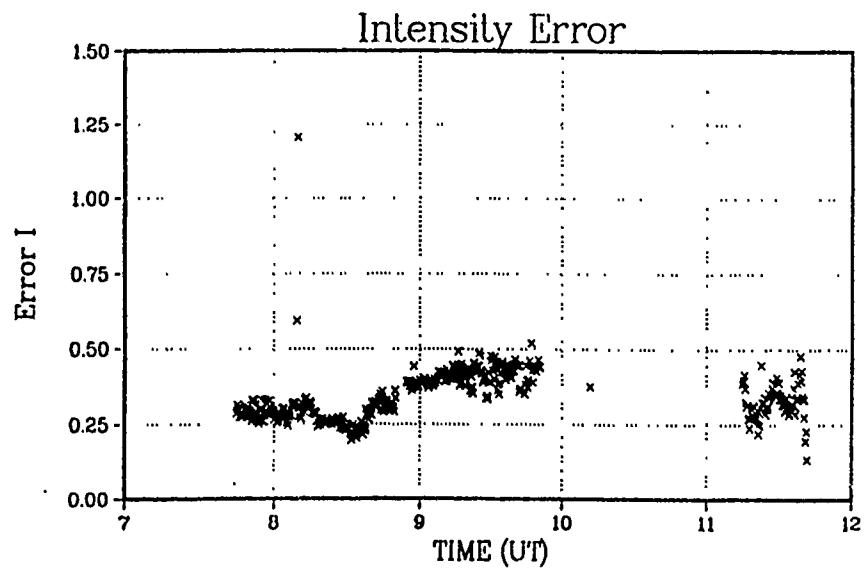


Fig. 6-5. Time domain analysis: (a) Time domain data error estimate

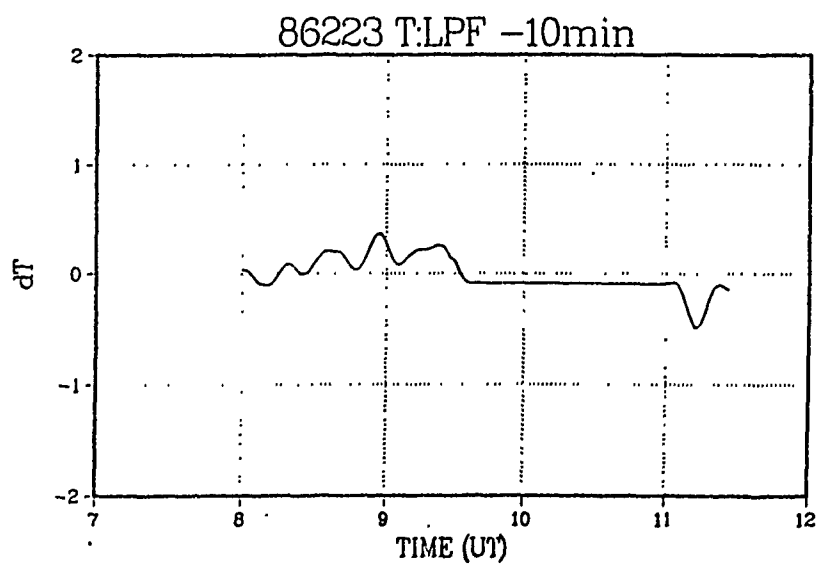
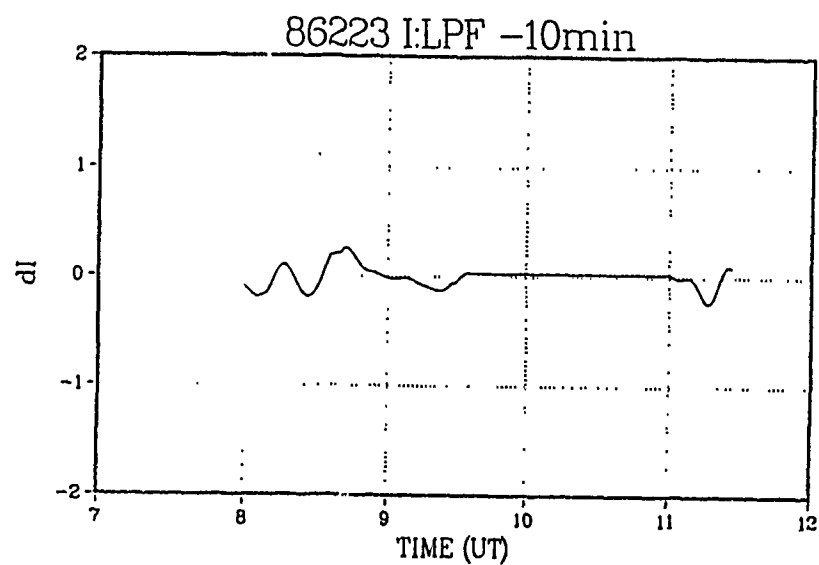


Fig. 6-5. Time domain analysis: (b) Numerical differentiations

will result in a large value for  $dT$  that renders such calculations useless for evaluating  $\eta$ . Some of the outputs of low-pass filters and their numerical differentiations are given in Fig. 6-5(b).

Another consideration is, as expected from the theoretical calculation and some observed value of  $\eta$ , that the fluctuations in temperature,  $dT$ , are usually very small. The observational  $\eta$  is reported to be between 5 to 10 in many cases [4], [6]. This makes  $dT/T$  much smaller than  $dI/I$  so that expected value for  $dT$  is often undetectably small. Quite often, possible fluctuations in temperature are smaller than the error estimate, or even the small jump in each data point caused by discrete measurements. In such cases, because the signal can be smaller than noise, the filter eliminates not only noise but also the signal. Because the frequency components of the sampling induced noise and of the noise associated with the error estimate are on the same order as the sampling frequency, long period fluctuations could be detected with an appropriate low-pass filter. In case of a sampling period of about 20 seconds, long-period fluctuations, such as hours, could be detected, provided that at least one entire cycle is recorded.

Most observations report the  $\eta$  to be about 5 to 10 [4], [6]. Thus the intensity fluctuations are much larger than the temperature fluctuations, so this problem is at least 5 to 10 times less serious in the intensity data. One possible method to overcome this problem in temperature data is using the filtered intensity signal as a reference to detect temperature fluctuations using, say, the coherent detection. Since a theoretical relation between observed intensity

and temperature is available, comparison between expected and observed temperature fluctuations using such model may be possible.

As the short-time Fourier analysis revealed, the temperature data exhibits more oscillations of a variety of frequencies than the intensity. The theoretical model, the geometric effect, also predicts that the temperature and the intensity are subject to different cancellation mechanisms. It was shown in Chapter II that when there is a temperature variation within the emission layer, temperature may exhibit some oscillation while the intensity oscillation is attenuated significantly. Such conditions also make  $\eta$  less useful, particularly for IGW's with short vertical wavelengths, namely, comparable with the airglow layer thickness.

Also, not all fluctuations are necessarily caused by IGWs. The characteristics of the airglow fluctuations caused by IGWs can be predicted using theoretical models, as is introduced in previous chapters. Therefore, fluctuations in observed data that do not satisfy those properties could be considered to have other origin. The long period trend need not be a part of a sinusoidal oscillation, for instance. This paper does not deal with any of the airglow fluctuations caused by something other than the linear IGW's. However, the result of this study can be used to reject the possibility of IGW-induced fluctuations on certain data which do not satisfy the predicted characteristics.



## CHAPTER VII

## CONCLUSIONS

Summary

The major achievements of this study are summarized as follows:

1. Developed a systematic formulation of a photochemical model of the mesospheric hydroxyl layer. The model can be used to calculate airglow emission line intensities with IGW parameter inputs for comparison with airglow observations.
2. Summarized the dynamics of the IGW in a form appropriate for the estimation of ground-based observations of mesospheric airglow emissions. It was found with a realistic model atmosphere that the fluctuations in the airglow emissions do not necessarily represent the amplitude nor the phase of the IGW oscillation. Only the wave frequency is represented correctly.
3. Found that the IGW propagation elevation angle is limited by a function of the IGW frequency. With this finding, it is possible to estimate a minimum distance of the source of an observed IGW using its frequency.
4. Found that IGW's are likely to be quasi-sinusoidal, often referred to as "chirp", after travelling a long distance into the mesospheric region. As a result, IGW-induced fluctuations in the mesospheric airglow emissions are likely to be variable frequency sinusoidal. This is similar to whistler mode electromagnetic wave propagation in the ionosphere. However, the changing rate of the

frequency was found to be small, so observations exhibiting a cycle or two oscillation can be treated as monochromatically sinusoidal.

5. Summarized the geometric effect of ground-based optical observation. This effect was used in conjunction with the dynamics of the IGW to evaluate the zenith-aspect observational data. It was found that the brightness-weighted kinetic temperature, integrated along the line of sight, is likely to depart from a gaussian distribution. Since the rotational temperature is related to the kinetic temperature, this departure affects the apparent rotational temperature. Use of the least square fitting technique to estimate the rotational temperature is therefore in question. A systematic error in the rotational temperature estimation is likely to occur; however, this error is usually less than 1 K when using rotational lines with the rotational level  $j < 6$ . This would be significant for rotational temperature estimates of about 1 K or less uncertainty. As the temperature estimate accuracy and precision are improved, the geometric effect on rotational lines will become increasingly significant.
6. Analyzed off-zenith observations as an extension of the zenith observation geometric effect. The result can be used to optimize both experimental planning and data analysis. The off-zenith observation can be unambiguous only if the background conditions, such as the stationary kinetic temperature and the concentrations of related chemical species, are uniform horizontally along the line of sight.

7. Developed signal processing techniques optimized for the detection of IGW-induced chirp oscillation. The expected chirp-like frequency change appears to occur frequently, and the short time Fourier transform technique works without problem when analyzing data containing more than two complete cycles of oscillation. As the amount of data becomes smaller, approaching only a single oscillation period, the technique gives lower than actual frequency. When measurement window contains less than one oscillation period, this technique does not detect a spectrum peak for that signal.
8. Found that the Krassovsky's  $\eta$  is useful only to limited cases. Such cases need to satisfy the following conditions:
  - a) a stationary background in emission intensity and temperature,
  - b) several cycles of oscillations are recorded in both emission intensity and rotational temperature data and c) noise and error estimates of both data are smaller than their signal amplitude.

### Conclusions

The following conclusions are derived from this study:

1. It was found that the temperature dependence of the rates of the chemical reactions responsible for the formation of the hydroxyl layer can have a significant effect in the translation of the IGW and the observable in the passive ground-based optical measurement. The significance of this effect varies, and can only be evaluated with knowledge of the vertical distribution of physical parameters, such as concentrations of related chemical species and

temperature. As a result of this effect, oscillations observed in hydroxyl airglow do not accurately represent IGW amplitude.

2. The distance between the source and the observation site of an IGW may be deduced from the observed oscillation frequency and its changing rate. The estimation becomes more accurate if the low limiting frequency of the chirp is observed, since the low limiting frequency is a unique function of the IGW propagation elevation angle.
3. The relation between frequency and horizontal wavelength may be used to estimate the distance to the source.
4. If the physical parameters such as temperatures along the IGW path are known, the spectrum of the wave source may be estimated using the observed oscillation spectrum and wavelengths. In turn, if the spectrum of the source is known, such physical parameters along the wave path may be estimated using observational data.
5. Off-zenith observations can be evaluated using a geometric effect model. According to the model, aiming at a particular angle implicitly sets up spatial filtering due to the slanted nature of the IGW phase plane. Waves are attenuated or amplified according to their frequency, wavelength and propagation direction with respect to the line of sight for each observation angle, resulting in favored range in frequencies and wavelengths for that direction, similar to a band-pass filter.
6. The use of the maximum entropy method (MEM) is not recommended in a study of the mesospheric airglow oscillations.
7. The application of Krassovsky's  $\eta$  upon experimental data has

several limitations. Such limitations are: 1) the numerical differentiation of data is heavily affected by the characteristics of the preconditioning filters, 2) the temperature fluctuation is usually very small, making  $\eta$  very sensitive to a numerical error, because this small value is in denominator.

8. The application of Krassovsky's  $\eta$  may be appropriate for some cases. Such cases include long period IGWs, more than several hours to a few days, which tend to have vertical wavelengths much longer than the hydroxyl layer thickness, approaching to the assumption in the definition of the  $\eta$ .
9. Off-zenith angle observation may help in some cases where such geometrical configuration causes amplifications to some range of signals. This gain has a penalty of attenuations to signals outside of the gain range, due to the same geometric effect. This range is a function of the viewing elevation angle.

#### Recommendations

Based on the findings of this study, the following recommendations are presented:

1. Because the volume emission rate varies over the hydroxyl layer, future studies require depth data to be obtained in order to compare the theoretical model with experimental data. Some methods to obtain such data are: a) use of ranging instruments, such as RADAR (Radio Detection And Ranging) and LIDAR (Light Detection And Ranging), b) stereoscopic observations by use of a single instrument which scans the sky or multiple count instru-

ments at distant locations. The recommendation for the range of each instrument is presented in part 4. The distance between different instruments for multiple site observation needs to be large enough for the geometric effect to be observable. This is related to the range of each instrument. Separation of 100 to 1000 km is recommended for observation of oscillations over a few hour period. These waves have low propagation elevation angle, 10 degrees or fewer, so the longer distance may be adopted. Shorter period oscillations may need to be observed with shorter separation, such as 100 to 300 km, because such wave may propagate at larger elevation angle, 30 degrees or so. With the acquisition of stereoscopic data, the wave dynamic model can be tested more accurately, and the location of the source may be calculated.

2. Once the dynamic model is verified, some depth information may be deduced using a simple ground-based passive observation data and the geometric effect model. Therefore, further improvement of the IGW dynamic model, especially nonlinear model, is recommended.
3. Some of the techniques for modeling the geometric effect may be applied to a modeling of other types of observations, such as satellite-based passive optical observation. Further study in this area is recommended.
4. Because IGWs are likely to be in the form of spatially limited chirp wave packets, observation of the same wave packet as it propagates through the atmosphere for long period of time is preferred over the observation of a fixed direction which provides data on a small fraction of the packet activity. Such observation

can be exercised by scanning a narrow field of view (fov) instrument, or using a wide fov instrument with high resolution such as an infrared imager [5]. IGWs with period of 15 minutes to several hours have horizontal wave length of 30 to 100 km, which translates into the span half angle of 10 degrees (30 km) to 30 degrees (100 km) for vertical observation. At least two data are needed to detect a wave; therefore, the resolution needs to be at least half of the span angle. Because there must be at least two spatial samples, the entire observation needs to occur at more than 10 to 30 degrees half angle. This translates into the recommended use of: a) scanning an instrument with the fov 5 degrees half angle or less scanning 30 degrees or larger half angle, b) use of an instrument with 30 degrees half angle or larger fov, with a spatial resolution of 5 degrees half angle or less. The numbers for fov need to be smaller for off-zenith observations according to the factor  $\cos\theta_0$ , where  $\theta_0$  is the angle of the line of sight with respect to the zenith.

5. A more theoretical study of the maximum entropy method is needed to overcome some of the problems. Its capability of working with very small amounts of data without the need for a window makes MEM suitable for the signal analysis of airglow oscillation data.

## REFERENCES

- [1] U.S.A.F. Air Research and Development Command, Handbook of Geophysics, Revised Edition. New York: Macmillan Co., 1961.
- [2] J.E.Frederick, D.W.Rusch, and S.C.Liu, "Nightglow emissions of OH( $X^2\pi$ ): comparison of theory and measurements in the (9-3) band," J.Geophys.Res., vol.83, no. A6, pp. 2441-2445, 1978.
- [3] Mark Allen, Jonathan I.Lunine, and Yuk L.Yung, "The vertical distribution of ozone in the mesosphere and lower thermosphere," J.Geophys.Res., vol.89, no. D3, pp. 4841-4872, 1984.
- [4] V.I.Krassovsky, "Infrasonic variations of OH emission in the upper atmosphere," Ann. Geophys., vol.28, pp. 739-746, 1972.
- [5] Michael John Taylor, "Observation and analysis of wave-like structures in the lower thermospheric nightglow emissions," Ph.D. dissertation, Univ. of Southampton, England, 1985.
- [6] V.I.Krassovsky, B.P.Potapov, A.I.Semenov, M.V.Shagaev, N.N.Shefov, V.G.Sobolev and T.I.Torshelidze, "Internal gravity waves near the mesopause and the hydroxyl emission," Ann. Geophys., vol.33, pp. 347-356, 1977.
- [7] R.L.Walterscheid, G.Schubert and J.M.Straus, "A Dynamical-chemical model of wave-driven fluctuations in the OH nightglow," J.Geophys.Res., vol.92, no. A2, pp. 1241-1254, 1987.
- [8] C.O.Hines, "Dynamical heating of the upper atmosphere," J.Geophys.Res., vol.70, pp. 177-183, 1965.
- [9] Gerhard Herzberg, F.R.S., Molecular Spectra and Molecular Structure. I. Spectra of Diatomic Molecules. New York:Prentice Hall, 1939.
- [10] Doran J.Baker, "Studies of atmospheric infrared emissions," Rep. AFGL-TR-78-0251, 1978. ADA072831
- [11] Colin O. Hines and David W. Tarasick, "On the detection and utilization of gravity waves in airglow studies," Planet.Space Sci., vol.35, no.7, pp. 851-866, 1987.
- [12] Alan W.Peterson and Gene W.Adams, "OH airglow phenomena during the 5-6 July 1982 total lunar eclipse," Appl.Opt., vol.22, pp. 2682-2685, Sept. 1983.



- [13] C.O.Hines, "Internal atmospheric gravity waves at ionospheric heights," Can. J. Phys., vol.38, pp. 1441-1481, 1960.
- [14] Mark Allen and Yuk L.Yung, "Vertical transport and photochemistry in the terrestrial mesosphere and lower thermosphere (50-120 km)," J.Geophys.Res., vol.86, no. A5, pp. 3617-3627, 1981.
- [15] I.C.McDade, E.J.Llewellyn, D.P.Murtagh and R.G.H.Greer, "ETON 5: Simultaneous rocket measurements of the OH Meinel Dv-2 sequence and (8,3) band emission profiles in the nightglow," Planet.Space Sci., vol.35, pp. 1137-1147, 1987.
- [16] T.F.Tuan, R.Hedinger, S.M.Silverman and M.Okuda, "On gravity wave induced Brunt-Vaisala oscillations," J.Geophys.Res., vol.84, no. A2, pp. 393-398, Feb. 1979.
- [17] C.O.Hines, "Observed ionospheric waves considered as gravity or hydromagnetic waves," J.Atmos.Terr.Phys., vol.30, pp. 1205-1216, 1974.
- [18] C.O.Hines, "Propagation velocities and speeds in ionospheric waves: A review," J.Atmos.Terr.Phys., vol.36, pp. 1179-1204, 1974.
- [19] David C.Fritts, "Gravity wave saturation in the middle atmosphere: a review of theory and observations," Rev. Geophysics and Space Physics, Vol.22, No.3, pp.275-308, 1984.
- [20] James Lighthill, Waves in Fluids. New York:Cambridge Univ. Press, 1978.
- [21] A.E. Hedin, "A global thermospheric model based on mass spectrometer and incoherent scatter data," J.Geophys.Res., vol.82, no.16, pp. 2139-2147, 1977.
- [22] J.Weinstock, "Nonlinear theory of gravity waves and enhanced diffusion in the atmosphere," Geophys.Res.Let., vol.2, no.10, pp. 453-456, Oct. 1975.
- [23] J.Weinstock, "Nonlinear theory of acoustic-gravity waves. 1. saturation and enhanced diffusion," J.Geophys.Res., vol.81, pp. 633-652, Feb. 1976.
- [24] Doran J. Baker and A.T. Stair, Jr., "Rocket measurement of the altitude distributions of the hydroxyl airglow," Physica Scripta, vol.37, pp. 611-622, 1988.
- [25] James Glimm, "Solutions in the large for nonlinear hyperbolic systems of equations," Communications on Pure and Applied Mathematics, vol.18, pp. 697-715, 1965.
- [26] Francois Thomasset, Implementation of Finite Element Methods for

Navier-Stokes Equations. New York:Springer-Verlag, 1981.

- [27] Bruce A. Fryxell, Paul R. Woodward, Phillip Colella and Karl-Heinz Winkler, "An implicit-explicit hybrid method for Lagrangian hydrodynamics," J. Comput. Phys., vol.63, pp. 283-310, 1986.
- [28] Phillip Colella and Paul R. Woodward, "The piecewise parabolic method (PPM) for gas-dynamical simulations," J. Comput. Phys., vol.54, pp.174-201, 1984.
- [29] Frederick H. Mies, "Calculated vibrational transition probabilities of OH( $X^2\Pi$ )," J. Molecular Spectroscopy, vol.53, pp.150-188, 1974.
- [30] David N. Turnbull, "An empirical determination of the electric dipole moment function and transition probabilities of OH( $X^2\Pi$ )," Ph.D. dissertation, Univ. of Western Ontario, Canada, 1987.
- [31] R. Hill, A. Mulac and D. Aeschliman, "Temperatures from rotational-vibrational Raman Q-branches," J. Quant. Spectrosc. Radiat. Transfer, Vol. 21, pp.213-220, 1979.
- [32] W. Press, B. Flannery, S. Teukolsky and W. Vetterling, Numerical Recipes. New York:Cambridge Univ. Press, 1986.
- [33] Peter R. Griffiths and James A. de Haseth, Fourier Transform Infrared Spectrometry. New York:John Wiley & Sons, 1986.
- [34] M.W. Mackenzie, Advances in Applied Fourier Transform Infrared Spectroscopy. New York:John Wiley & Sons, 1988.
- [35] C. L. Lawson and R. J. Hanson, Solving Least Squares Problems. Englewood Cliffs, NJ:Prentice Hall, 1974.
- [36] L.R. Rabiner and R.W. Schafer, Digital Processing of Speech Signals. Englewood Cliffs, NJ:Prentice Hall, 1978.
- [37] Edmond M. Dewan, "A Review of maximum entropy spectral analysis and applications to Fourier spectroscopy," Rep. AFGL-TR-85-0091, 1985. **ADA164698**
- [38] Robert W. Ramirez, The FFT Fundamentals and Concepts. Englewood Cliffs, NJ:Prentice Hall, 1985.
- [39] A. Oppenheim and R. Schafer, Digital Signal Processing. Englewood Cliffs, NJ:Prentice Hall, 1975.

**APPENDICES**

## Appendix A: Theory of the Internal Gravity Waves

### The Internal Gravity Waves

In this section, the theory of the atmospheric internal acoustic/gravity wave is described based upon a general theory of waves in fluids [13], [18]. In an atmospheric gravity wave, both compressional and gravitational forces (buoyancy) cause wave propagation. At the high frequency end of the spectrum, these waves approach to acoustic waves, while at the low frequency end approach to pure gravity waves such as the water surface wave.

The basic properties of the acoustic wave are: 1) Isotropic 2) Non-dispersive. The speed of sound in the air "c," for example, is given by:

$$c = \sqrt{\gamma P / \rho} = \sqrt{\gamma RT} \quad (A.1)$$

where

P = atmospheric pressure	(N/m <sup>2</sup> )
$\rho$ = atmospheric density	(kg/m <sup>3</sup> )
R = gas constant	8.314 (J/mol.K)
$\gamma = C_p/C_v \approx 1.4$	(for air below 100 km)

There are two types of propagating gravity waves: 1) surface waves and 2) internal waves. An example of a surface wave is a wave on the ocean surface. This type of wave can exist only at a boundary or discontinuity in the density of the medium. This wave is isotropic

in the horizontal direction which is the propagating direction, since the effect of gravity is the same for all directions. However, unlike acoustic waves, surface waves are dispersive. For example, the wave velocity of a long period sea wave " $c_s$ " is given by:

$$c_s = \sqrt{g\lambda_x / 2\pi} \quad (A.2)$$

where  $g$  is the acceleration of gravity and  $\lambda_x$  is the horizontal wavelength.

Internal gravity waves can exist in the atmosphere where the density decreases continuously with increasing altitude. This type of wave can freely propagate to all elevation angles, and is not limited to horizontal propagation as are surface waves. Since the restoring force due to gravity is always in a fixed direction, there is no reason for isotropy of propagation. Hence internal gravity waves are anisotropic and dispersive.

#### Properties of Internal Acoustic-Gravity Waves

The simplest model is based upon the assumption that the atmosphere is:

- a) continuously stratified and compressible,
- b) isothermal and uniform in composition,
- c) stationary in the absence of waves,
- d) inviscid (no dissipation of energy in the gas).

Because the actual atmosphere has non-uniform and variable nature, such model is not always appropriate.

This model also assumes that the wave motion is adiabatic and produces small variations with a period of less than one day. Exact solutions are found for two dimensional plane waves of the form  $\exp(i(\omega t - k_x x - k_z z))$ , where  $\omega$  is the angular frequency,  $k_x$ ,  $k_z$  are the real horizontal and vertical wave numbers. This form of waves can be the solution when these parameters satisfy the following dispersion equation [13]:

$$\omega^4 - \omega^2 c^2 (k_x^2 + k_z^2) + (\gamma - 1) g^2 k_x^2 - \frac{\gamma^2 g^2 \omega^2}{4c^2} = 0 \quad (\text{A.3})$$

This can be rewritten as:

$$\frac{(\omega^2 - \omega_A^2)}{c^2} \omega^2 - \omega^2 (k_x^2 + k_z^2) + \omega_g^2 k_x^2 = 0 \quad (\text{A.4})$$

where

$$\begin{aligned} \omega_A &= \gamma g / 2c \\ \omega_g &= \sqrt{\gamma - 1} \, g / c \end{aligned} \quad (\text{A.5})$$

The properties of the wave motion can be deduced from this relationship. For any pair of wave numbers  $(k_x, k_z)$ , two distinct values of  $\omega$  exist. Their asymptotic roots are:

$$\omega^2 = c^2 (k_x^2 + k_z^2) \quad (\text{A.6})$$

$$\omega^2 = \frac{\omega_g^2 k_x^2}{k_x^2 + k_z^2} \quad (\text{A.7})$$

Equation (A.6) represents the ordinary relationship of the non-dispersive property of sound waves, and is valid when  $\omega^2 \gg \omega_A^2$ . The equation (A.7) represents the dispersion relation of an internal gravity wave under the asymptotic condition  $\omega^2 \ll \omega_g^2$ .

The wave can propagate only if  $k_x$  and  $k_z$  are positive, which is true when  $\omega < \omega_g$ . Hence, internal atmospheric gravity waves can exist only at periods greater than a certain value  $T_g$  which is defined as:

$$T_g = 2\pi c / g\sqrt{\gamma-1} \quad (\text{A.8})$$

The value  $T_g$  is known as the Brunt-Vaisala period. This is the natural resonance period of a displaced parcel of air under the restoring force due to buoyancy alone.

Similarly, internal acoustic waves require  $\omega > \omega_A$ . Thus, internal atmospheric acoustic waves can exist only at periods smaller than a characteristic value  $T_A$ , which is defined as:

$$T_A = 4\pi c / \gamma g \quad (\text{A.9})$$

The value  $T_A$  is known as the acoustic resonance period. This is the resonant period of the whole atmosphere with the restoring force due only to compression.

Since the ratio  $\gamma = C_p/C_v$  is less than 2 within the homosphere then  $T_A < T_g$  and the two types of internal waves are completely decoupled. Fig. A-1 shows the permissible values of  $k_x$  and  $k_z$  for several different periods. The acoustic waves form a family of ellipses and the gravity waves form a set of hyperbolas. At periods less than one minutes, the ellipses are almost circular implying isotropic wave motion, or the regular acoustic wave, i.e. sound.

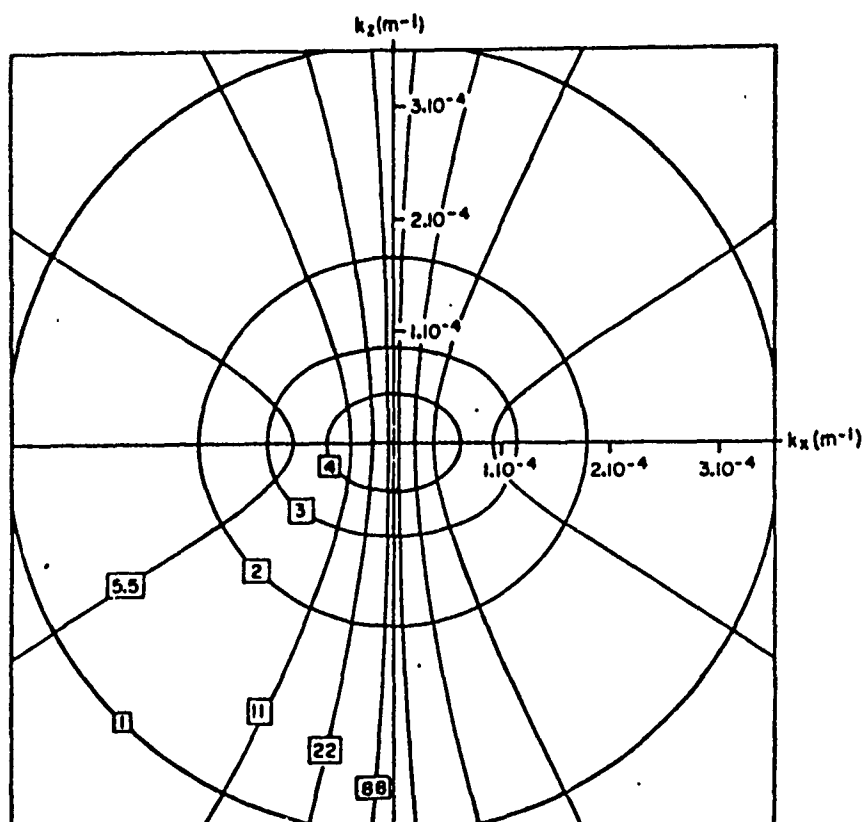
Internal gravity waves usually travel much slower than the speed of sound. In general, the shorter the period, the smaller the phase speed and the shorter the wavelength of the wave. Internal gravity waves also have a property that the direction of energy flow is different from that of the phase propagation. For a long period wave, both directions are almost normal to each other.

For shorter period gravity waves, the motion of the air parcel is not only transverse but is slightly elliptical, resulting from the combination of the longitudinal compressional forces and transverse buoyancy forces.

As a consequence of the conservation of energy flux in an inviscid atmosphere where density decreases exponentially, amplitude of waves increases exponentially with altitude.

Fig. A-2 shows the relationship between the horizontal wavelength and phase velocity for several phase propagation angle theta ( $\theta$ ) of IGW. The direction of phase velocity is given by  $\theta$  and shown to be downward. Using the equation (A.7),  $\theta$  satisfies:





The family of ellipsoids represents the acoustic-wave solutions to the equation (A.6). The family of hyperbolas represents the IGWs, solutions to equation (A.7). Each curve is marked by oscillation periods in minutes.

Fig. A-1. Permissible IGWs

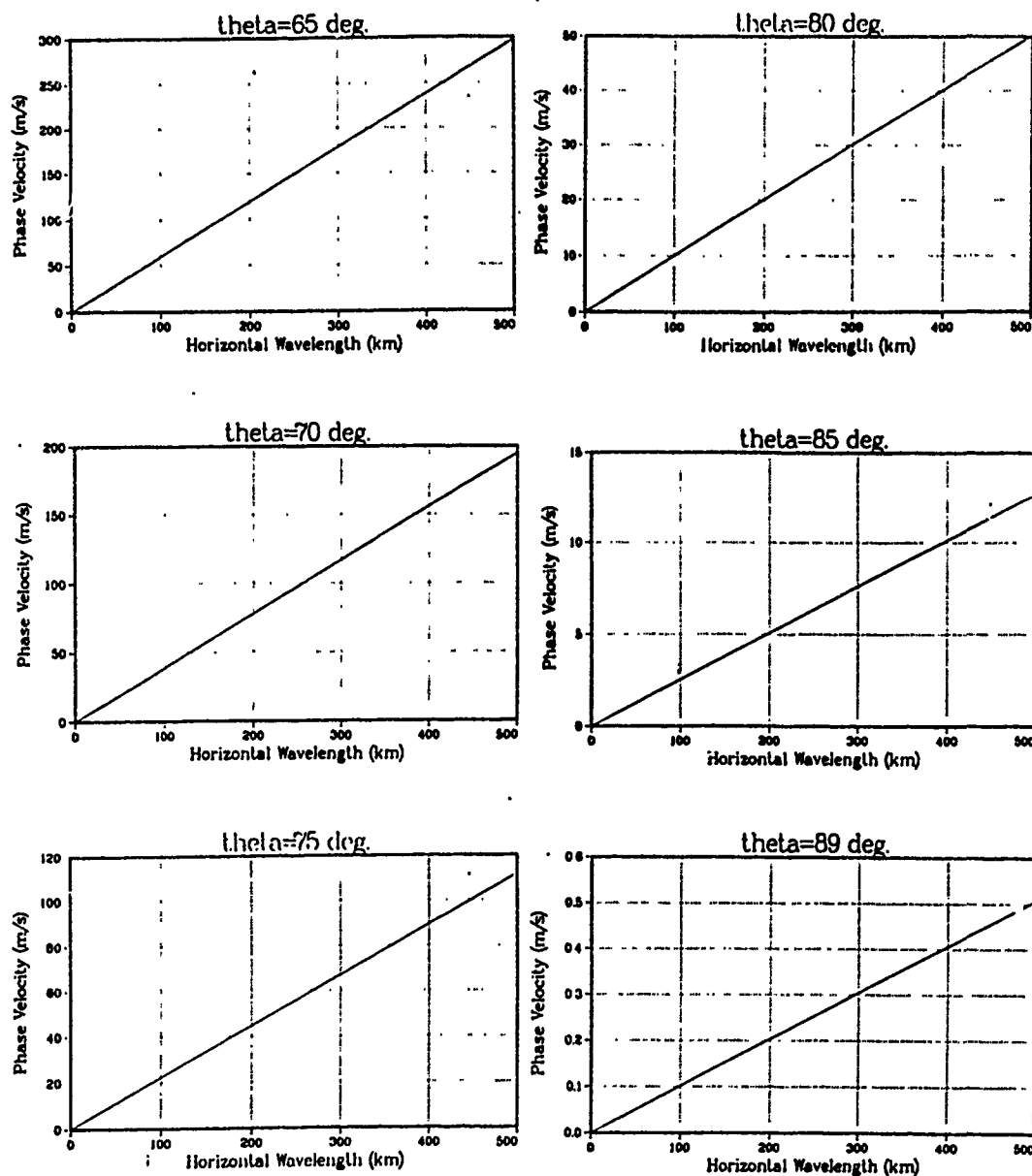


Fig. A-2. IGW topography

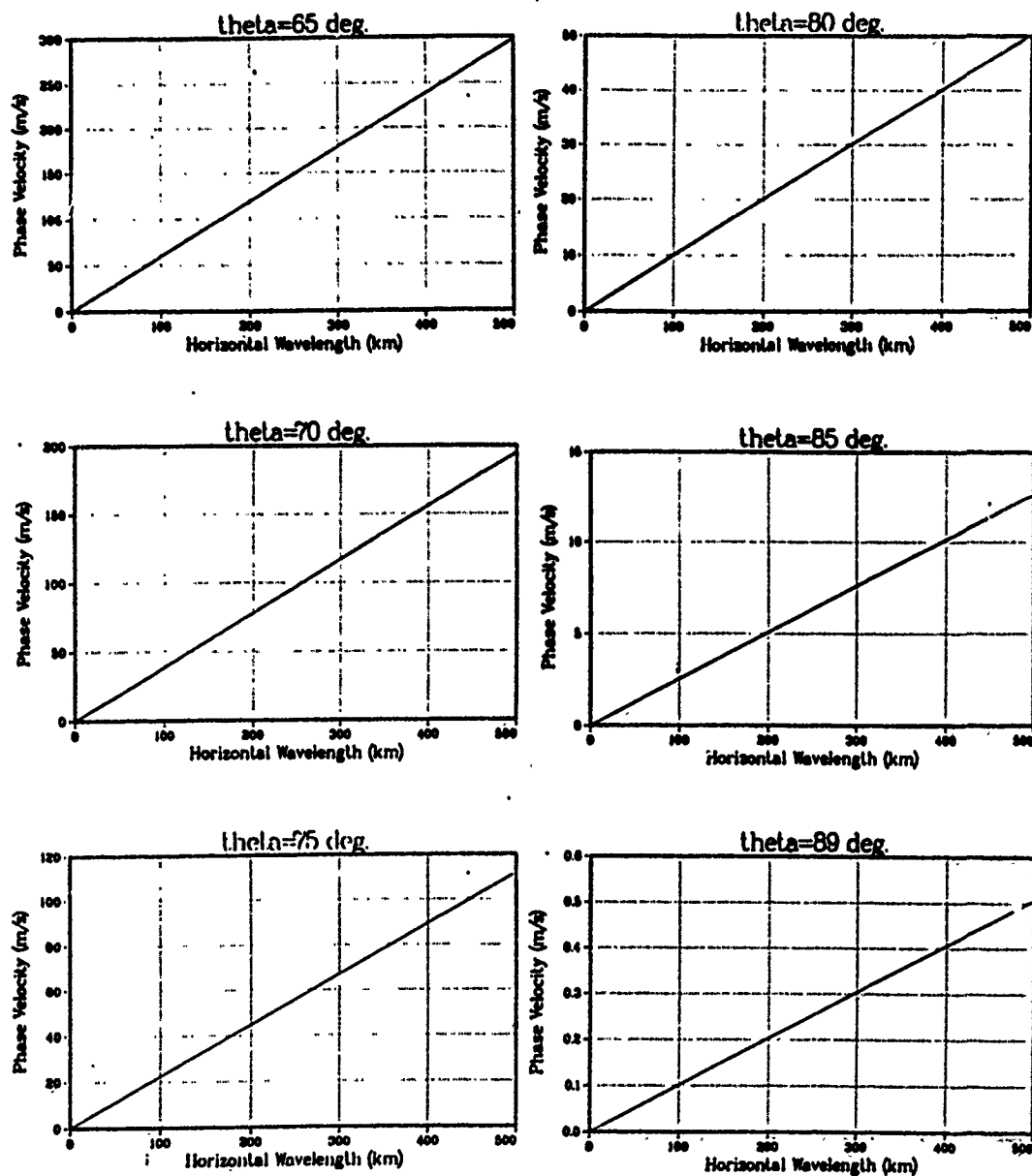


Fig. A-2. IGW topography

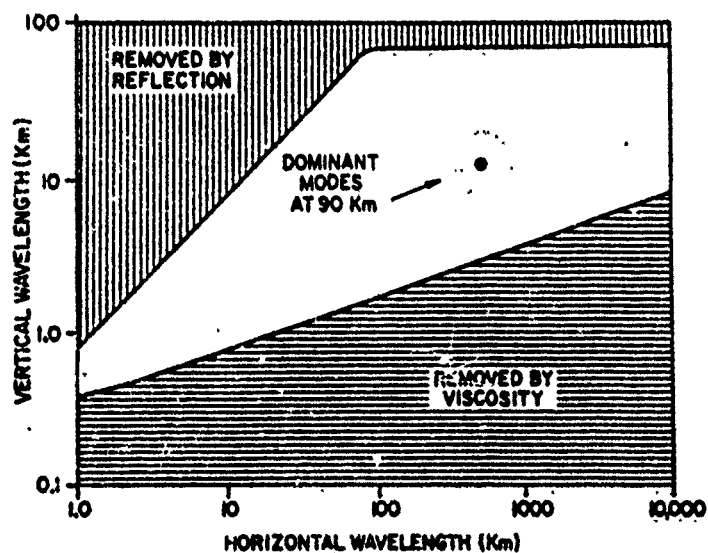


Fig. A-3. Filtering of IGW [13]

TABLE XII  
Polarization Relations [13]

$$P = \gamma \omega^2 [k_z - i(1 - \gamma/2)g/C^2]$$

$$R = \omega^2 k_z + i(\gamma - 1)gk_z^2 - i\gamma g\omega^2/2C^2$$

$$X = \omega k_z C^2 [k_z - i(1 - \gamma/2)g/C^2]$$

$$Z = \omega[\omega^2 - k_z^2 C^2]$$

$$f_G = \frac{(\omega^2 - \omega_A^2)}{c^2} \omega^2 - \omega^2(k_x^2 + k_z^2) + \omega_g^2 k_x^2 \quad (A.13)$$

is the left-hand side of the dispersion equation (A.4). Substituting (A.13) into (A.11) and (A.12) yields:

$$P_x = \frac{\omega k_x (\omega^2 - \omega_g^2)}{\frac{\omega^4}{c^2} - k_x^2 \omega_g^2} \quad (A.14)$$

$$P_z = \frac{\omega^3 k_z}{\frac{\omega^4}{c^2} - k_x^2 \omega_g^2} \quad (A.15)$$

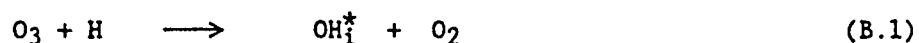
This is the relationship between the packet velocity [18] and the wave parameters. The elevation angle of the wave energy propagation,  $\alpha$ , may be specified with the following equation:

$$\tan \alpha = \frac{k_z}{k_x} \frac{\omega^2}{\omega^2 - \omega_g^2} = \frac{P_z}{P_x} \quad (A.16)$$

### Appendix B: Rotational Temperature

After the optical emission spectrum is obtained, the band emission intensity and the rotational temperature for a specified band are to be calculated. First, the definition of the rotational temperature is presented.

The hydroxyl can be modeled as a dipole consisting of two mass points with positive and negative charge connected by a "massless spring" as in Fig. B-1. When generated by the chemical reaction:



where  $i$  denotes the vibrational level. Energy for hydroxyl in this reaction is 3.3 eV [10] which is too small for the electronic state to be excited, so they remain at the ground state. This energy is large enough to excite the vibrational level whose quantum number is less than or equal to nine. These vibrational levels are associated with rotational levels. These rotational levels cause the rotational emission lines in the emissive vibrational level transitions. As a result, those transition emissions produce emission bands that are made by numerous rotational lines. The distribution of emission intensity among the rotational lines within a single band is a function of temperature. In this context, "temperature" is the kinetic temperature of hydroxyl that can be assumed identical to the kinetic temperature of the major species as long as the time scale of interest is larger than the inverse of the collision frequency which is on the order of few milliseconds. With this method, the tempera-

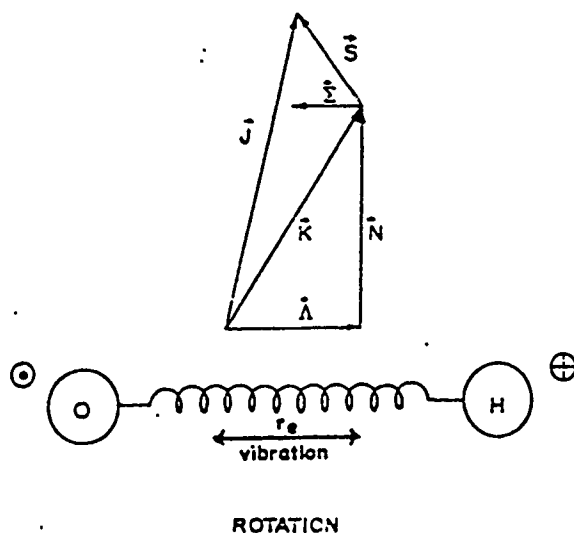


Fig. B-1. Hydroxyl model [10].

ture can be calculated from the distribution of several rotational line intensities. Theoretically, only two rotational lines are necessary and sufficient to calculate the temperature. But with real data this method is too sensitive to any error in the line intensities including the effect of noise. The theoretical ratio of rotational lines in a band for given hydroxyl concentration and temperature can be calculated as follows. Let  $v'$  and  $v''$  denote the initial and final vibrational states, thus making  $(v', v'')$  band. Let  $j'$  and  $j''$  denote the initial and final rotational states. The concentration of the initial state is given as  $N_{v'}$ . Then the concentration of each rotational state  $j'$ ,  $N_{v'j'}$  is represented as [9]:

$$Nv'j' = \frac{Nv'}{Q_r} (2j'+1) \exp\left(-\frac{Bj'(j'+1)hc}{kT}\right) \quad (B.2)$$

$$B = \frac{h}{8\pi^2 c I} \approx 16.28 \text{ (cm}^{-1}\text{)} \quad [9] \quad (B.3)$$

$$Q_r = \sum_{j=0}^{\infty} (2j+1) \exp\left(-\frac{Bj(j+1)hc}{kT}\right) \quad (B.4)$$

where  $T$  is the temperature,  $Q_r$  is the partition function,  $B$  is the rotational constant,  $h$  is the Planck constant,  $c$  is the speed of light and  $k$  is the Boltzmann constant. The emissive transition occurs only according to the selection rule. In this case the selection rule is  $\Delta j = 0, \pm 1$ ; the change of the rotational level is either none, plus one or minus one, corresponding to what are customary called Q, P and R branches. Each branch is divided into two smaller subsets. This is based on the two different total electronic angular momentum about the internuclear axis. It is represented by a quantum number  $\Omega$ , that can take either  $1/2$  or  $3/2$  [10]. Each branch of P, Q and R lines is denoted with a subscript of 1 or 2 depending whether  $\Omega=3/2$  ( $P_1$ ,  $Q_1$  and  $R_1$ ) or  $1/2$  ( $P_2$ ,  $Q_2$  and  $R_2$ ). The most straightforward method to calculate the rotational temperature is to use the rotational lines of a single branch. In case of (3,1) band of hydroxyl, the P branch is commonly used. This is because the Q branch lines are too closely spaced for the interferometer spectrometer to resolve, and the R branch falls into the



wavelengths that are in the water vapor absorption region. In practice, more than three lines are used to calculate the rotational temperature. Among those are the methods developed by Hill, Espy and Niple independently [31], [35] using the least square fitting of a synthesized spectral lines of one band to the experimental data of the spectral lines in the same band.

Appendix C: Linearization of the  
Adiabatic State Equation

This derivation of the linearized equation of adiabatic change of state is adopted from Hines [11]. This gives an important expression for the derivative of the vertical velocity component  $w$  of  $\underline{y} = [u, 0, w]$  with the assumed form:

$$w = W(z)\exp(i(\omega t - kx)) \quad (C.1)$$

The equation of horizontal acceleration yields:

$$i\omega\rho_0 u = ikxp' \quad (C.2)$$

or

$$\frac{p'}{\rho_0} = \frac{\gamma\omega u}{kxC^2} \quad (C.5)$$

with the speed of sound  $C = (\gamma p_0 / \rho_0)^{1/2}$ ,  $\rho_0$  and  $p_0$  being the unperturbed mass density and pressure and those with apostrophe being their perturbations. The Lagrangian derivative of the pressure is:

$$\begin{aligned} \frac{Dp}{Dt} &= \frac{\partial p'}{\partial t} + w \frac{dp_0}{dz} \\ &= i\omega p' - w \frac{p_0}{H} \end{aligned} \quad (C.4)$$

where  $H=H_p = -(d(\ln p_0)/dz)^{-1} = p_0/\rho_0 g = C^2/\gamma g$  is the pressure scale height,  $g$  being the gravitational acceleration. The equation of adiabatic change of state can be represented as:

$$\frac{\gamma}{\rho_0} \frac{D\rho}{Dt} = \frac{1}{p_0} \frac{Dp}{Dt} \quad (C.5)$$

and the continuity equation:

$$\frac{1}{\rho_0} \frac{D\rho}{Dt} = -\nabla \cdot \underline{v} = ik_x u - \frac{\partial w}{\partial z} \quad (C.6)$$

With (C.5) and (C.6), (C.3) yields:

$$ik_x u - \frac{\partial w}{\partial z} = iu \frac{\omega^2}{C^2} - \frac{1}{\gamma H} \frac{\partial w}{\partial z} \quad (C.7)$$

and so:

$$ik_x u = \frac{k_x^2 C^2}{k_x^2 C^2 - \omega^2} \left( \frac{\partial w}{\partial z} - \frac{w}{\gamma H} \right) \quad (C.8)$$

From (C.6) and (C.8),

$$\nabla \cdot \underline{v} = -ik_x u + \frac{\partial w}{\partial z} = \frac{-k_x^2 C^2}{k_x^2 C^2 - \omega^2} \left( \frac{\partial w}{\partial z} - \frac{w}{\gamma H} \right)$$

$$= \frac{1}{\omega^2 - k_x^2 C} \left( \omega^2 \frac{\partial w}{\partial z} - k_x^2 g w \right) \quad (C.9)$$

The adiabatic equation of state can also be written in the following form:

$$\frac{DT}{Dt} = i\omega T' + w \frac{dT_0}{dz} = \frac{(\gamma-1)T_0}{\rho_0} \frac{D\rho}{Dt} \quad (C.10)$$

(C.6) and (C.10) yield:

$$T_0(z) + T'(z) = T_0(z) \left( 1 + i \frac{\gamma-1}{\omega} \nabla_{\underline{v}} \right) \quad (C.11)$$

This is the equation (2.73). The associated equation for the change in density, (2.72), is derived as follows. From the continuity equation, the following form is derived:

$$i\omega N' = -N_0 \nabla_{\underline{v}} - i\omega h \frac{dN_0}{dz} \quad (C.12)$$

or

$$N' = -\frac{N_0}{i\omega} \nabla_{\underline{v}} - h \frac{dN_0}{dz} \quad (C.13)$$

since  $\nabla N = dN_0/dz$ , or  $N_0$  is constant for the same altitude with different  $x$  or  $y$  coordinates. Equation (C.13) leads to:

$$N_0(z) + N'(z) = N_0(\zeta) + h \frac{dN_0(\zeta)}{d\zeta} + \left( -\frac{N_0}{i\omega} \nabla_{\underline{v}} - h \frac{dN_0}{dz} \right) \Big|_{\zeta}$$

$$= N_0(\zeta) + h \frac{dN_0(\zeta)}{d\zeta} + \frac{i}{\omega} N_0 \nabla_{\underline{v}} \Big|_{\zeta} - h \frac{dN_0}{d\zeta}$$

$$= N_0(\zeta) \left( 1 + \frac{i}{\omega} \nabla_{\underline{v}} \right) \Big|_{\zeta} \quad (C.14)$$

which is the equation (2.73).